
Electronic Thesis and Dissertation Repository

9-29-2023 1:00 PM

Impinging Jet Flow and Hydraulic Jump of Newtonian and Viscoplastic Liquids

Wenxi Wang, *Western University*

Supervisor: Khayat, Roger E., *The University of Western Ontario*

A thesis submitted in partial fulfillment of the requirements for the Doctor of Philosophy degree in Mechanical and Materials Engineering

© Wenxi Wang 2023

Follow this and additional works at: <https://ir.lib.uwo.ca/etd>



Part of the [Applied Mechanics Commons](#)

Recommended Citation

Wang, Wenxi, "Impinging Jet Flow and Hydraulic Jump of Newtonian and Viscoplastic Liquids" (2023). *Electronic Thesis and Dissertation Repository*. 9671.
<https://ir.lib.uwo.ca/etd/9671>

This Dissertation/Thesis is brought to you for free and open access by Scholarship@Western. It has been accepted for inclusion in Electronic Thesis and Dissertation Repository by an authorized administrator of Scholarship@Western. For more information, please contact wlsadmin@uwo.ca.

Abstract

The steady laminar incompressible flow of an axisymmetric impinging jet of either a Newtonian fluid or a viscoplastic fluid of the Heschel-Bulkley type and the hydraulic jump of either a circular or polygonal shape on a solid disk is analyzed. The polygonal jump is induced by azimuthal dependence edge conditions: a non-circular disk or a circular disk with a variable edge film thickness. The thin-film and Kármán–Pohlhausen approaches are utilized as theoretical tools.

To cross the jump smoothly, a composite mean-field thin-film approach is proposed. The stress singularity for a film freely draining at the disk edge is found to be equivalent to an infinite film slope. The flow in the supercritical region is insensitive to the gravity strength, but is greatly affected by the viscosity. The existence of the jump is not necessarily commensurate with the presence of recirculation.

The disk size is found to can affect the film thickness in the subcritical region, vortex size and jump length significantly. The jump is relatively steeper with a stronger recirculation zone for a higher obstacle. Scaling laws for the jump properties, such as the jump radius and length, and edge film thickness, are proposed. The surface scaling separating the regions of existence/non-existence of the recirculation is found through numerical results.

The non-circular jump originated from the disk non-circularity or periodic edge film thickness is found. The balance of mass and momentum is established in the radial and azimuthal directions. The geometry of a non-circular disk has little influence on the jump shape. A small azimuthal variation in the edge thickness for a circular disk leads to a significant loss of axial symmetry. An increase in the number of peaks and valleys appears as the disk radius decreases.

The viscoplastic jump is found to occur closer to impingement, with growing height, as the yield stress increases; the subcritical region becomes invaded by the pseudo-plug layer. The viscosity does not influence sensibly the jump location and height except for small yield stress; only the yielded layer is found to remain sensitive to the power-law rheology for any yield stress.

Keywords

Impinging jet, circular continuous hydraulic jump, polygonal hydraulic jump, viscoplastic hydraulic jump, free surface flow, surface tension.

Summary for Lay Audience

The impinging jet and hydraulic jump is a phenomenon that can be observed in the kitchen sink daily. When opening the tap, a column of water from the faucet impacts the bottom of the sink, spreading radially outward, and a water film rises abruptly at a critical radial location, a hydraulic jump forms. Although it is simple at first glance, the impinging jet and hydraulic jump have a complex flow structure and extensive industrial applications, such as rinsing, cleaning, cooling and coating. The appearance of a hydraulic jump can significantly influence the characteristics of flow, and the performance of related applications. In industrial applications, the fluid employed may not be a common fluid such as water or oil, but a complex fluid such as mud, pastes and concentrated suspensions. The current thesis presents a theoretical investigation of the circular impinging jet of common and complex fluids, and the hydraulic jump of either a circular or polygonal shape on a solid disk. The polygonal jump is induced by azimuthally dependent edge conditions: a non-circular disk or a circular disk with a variable edge film thickness. To investigate the flow features at the jump level, a composite model for a continuous jump is proposed. The momentum balance equations are established in both the radial and azimuthal directions for a polygonal jump. The model that takes the rheology of complex fluid into account is also presented. It is found that a larger flow rate, smaller viscosity, and lower gravity level lead to a larger jump radius. The existence of the jump is not necessarily commensurate with the presence of recirculation. The geometry of a non-circular disk has little influence on the jump shape. A small azimuthal variation in the edge thickness for a circular disk leads to a significant loss of axial symmetry. The complex fluid jump is found to occur closer to impingement, with growing height compared with the common fluid.

Co-Authorship Statement

The current thesis is prepared in the Integrated-Article format consistent with the regulations of the School of Graduate and Postdoctoral Studies at the University of Western Ontario. Chapters 2-5 are papers based on the manuscripts that have been published in peer-reviewed journals or submitted to peer-reviewed journals for review. I, Wenxi Wang, am the first author of all manuscripts, and my supervisor, Dr. R.E. Khayat, is the co-author. Additionally, Abdelkader Baayoun contributed to the conceptualization and edition of Chapter 2 and Chapter 3, while Dr. J.R. de Bruyn assisted in conceiving Chapter 5.

Acknowledgments

I would like to sincerely express my deep gratitude to my supervisor, Dr. R.E. Khayat, for his unwavering support throughout my Ph.D. study. His continuous encouragement and guidance played a significant role in the completion of this work. Moreover, I am truly grateful to him for consistently pushing me to expand my knowledge and for guiding me through all the challenges encountered in this research. I am also immensely thankful to my advisory committee members, Dr. E. Savory and Dr. J.M. Floryan, for their invaluable insights and constructive suggestions. I extend my appreciation to Dr. J.R. de Bruyn for his cooperation, which greatly contributed to the advancement of this study.

Furthermore, I want to thank my former and current colleagues, Dr. Yunpeng Wang and Abdelkader Baayoun, for their thoughtful discussions.

Lastly, I owe a debt of gratitude to my parents and my wife for their unwavering support and encouragement throughout this journey. Their belief in me has been a constant source of motivation. I would like to express a special thanks to my wife, Zexiao Cai, whose love, understanding and comfort have been a pillar of strength for me during this entire endeavour.

Table of Contents

Abstract.....	ii
Summary for Lay Audience.....	iii
Co-Authorship Statement.....	iv
Acknowledgments.....	v
Table of Contents.....	vi
List of Tables.....	xi
List of Figures.....	xii
List of Appendices.....	xxiv
Chapter 1.....	1
1 Introduction.....	1
1.1 Background and applications.....	1
1.2 Methodologies.....	6
1.2.1 Boundary layer theory and thin-film approach for a Newtonian fluid.....	6
1.2.2 The Kármán–Pohlhausen approach for a Newtonian fluid.....	8
1.2.3 Herschel-Bulkley constitutive model and its influence on the methodologies.....	10
1.3 Literature review.....	14
1.3.1 The hydrodynamics of the impinging jet and circular continuous jump ..	14
1.3.2 The influence of azimuthally varying edge conditions on the hydraulic jump.....	21
1.3.3 The viscoplastic circular hydraulic jump.....	23
1.4 Objectives and Outline of the Thesis.....	28
1.4.1 The objectives of the thesis.....	28
1.4.2 The outline of the thesis.....	30
1.5 References.....	31

Chapter 2.....	41
2 A coherent composite approach for the continuous circular hydraulic jump and vortex structure.....	41
2.1 Introduction.....	44
2.2 The physical domain and problem statement.....	48
2.3 Formulation and solution strategy	52
2.3.1 The flow in the impingement zone and boundary-layer region ($0 < r < r_0$).....	53
2.3.2 The flow in the fully-developed viscous region ($r_0 \leq r \leq r_\infty$).....	56
2.3.3 Solution strategy	60
2.3.4 Upstream influence and the free-interaction problem	61
2.3.5 Asymptotic flows	64
2.4 Validation.....	65
2.4.1 Validation against numerical models.....	66
2.4.2 Comparison against experiment.....	71
2.4.3 The nature of the subcritical flow	78
2.5 Further results	79
2.5.1 The influence of the flow rate.....	79
2.5.2 The jump of type 0.....	84
2.6 Conclusion	90
2.7 References.....	91
Chapter 3.....	97
3 The characteristics of the continuous circular hydraulic jump	97
3.1 Introduction.....	100
3.2 Review of the physical domain and problem formulation.....	103
3.2.1 The physical domain and problem statement.....	103
3.2.2 The flow in the boundary layer region ($0 < r < r_0$)	107

3.2.3	The flow in the fully-developed viscous region ($r_0 \leq r \leq r_\infty$).....	108
3.3	The influence of the disk geometry	111
3.3.1	The influence of the disk size	112
3.3.2	The interplay between the flow rate and disk size	115
3.3.3	The influence of the obstacle height at the edge of the disk.....	121
3.4	Scaling analysis.....	125
3.4.1	The scaling law for the jump radius.....	126
3.4.2	The film thickness and velocity at the edge of the disk without an obstacle	130
3.4.3	The jump length and vortex size.....	134
3.4.4	The energy loss and conjugate depth.....	137
3.5	Further parametric assessment.....	147
3.5.1	Influence of the gravity.....	147
3.5.2	Influence of the viscosity	149
3.5.3	Existence of the jump and the recirculation zone	150
3.6	Concluding remarks	153
3.7	References.....	156
Chapter 4.....		161
4	The influence of azimuthally varying edge conditions on the hydraulic jump.....	161
4.1	Introduction.....	164
4.2	Physical domain and problem statement.....	167
4.3	The axisymmetric supercritical flow	170
4.4	The non-axisymmetric subcritical flow formulation	172
4.4.1	Conservation of momentum across the jump.....	172
4.4.2	Accounting for surface tension effect.....	173
4.4.3	The subcritical flow field and film height.....	176

4.5	Results and discussion	178
4.5.1	Validation.....	178
4.5.2	The non-circular jump on a non-circular disk.....	180
4.5.3	The non-circular jump on a circular disk, Imposed edge film thickness	189
4.6	Concluding remarks and discussion.....	195
4.7	References.....	198
Chapter 5.....		202
5	The viscoplastic circular hydraulic jump	202
5.1	Introduction.....	206
5.2	Physical domain and problem statement.....	211
5.2.1	The physical domain	213
5.2.2	Governing equations and boundary conditions.....	214
5.3	The influence of the yield stress on the supercritical flow	218
5.3.1	The depth-averaged formulation and velocity profile	218
5.3.2	The influence of the viscosity and yield stress	222
5.3.3	The limit of Newtonian supercritical flow and small B correction	227
5.3.4	The impingement zone.....	232
5.4	Formulation of the subcritical viscoplastic flow and the hydraulic jump.....	235
5.4.1	The flow in the subcritical region	235
5.4.2	Estimating the edge thickness and yielded layer height	236
5.4.3	Conservation of mass and momentum across the jump.....	239
5.4.4	The jump length for a Bingham fluid	240
5.5	The influence of the yield stress and viscosity on the hydraulic jump	242
5.5.1	The film and yielded layer profiles.....	242
5.5.2	The jump radius and height.....	246
5.5.3	Further parametric study	250

5.6 Concluding remarks and discussion.....	258
5.7 References.....	263
Chapter 6.....	274
6 Conclusion and recommendations for future works	274
6.1 Conclusion	274
6.2 Recommendations for future works.....	277
Appendices.....	278
Curriculum Vitae	282

List of Tables

Table 1: Typical rheological parameters for different viscoplastic fluids.	12
---	----

List of Figures

Figure 1-1: (a) Schematic illustration of an impinging jet and circular hydraulic jump, (b) a water jet and formed hydraulic jump in a kitchen sink..... 1

Figure 1-2: Planar hydraulic jump on the St. Joseph River in Niles, Michigan (from flickr) .. 2

Figure 1-3: Schematic illustration of different types of hydraulic jump structures..... 5

Figure 1-4: A schematic illustration of (a) the boundary layer, (b) the boundary layer separation and (c) the thin-film flow..... 8

Figure 1-5: Comparison of Watson’s (1964) similarity velocity profile against the parabolic and cubic velocity profiles for a thin-film flow..... 9

Figure 1-6: Some viscoplastic materials in different flow configurations. (a) A collapsed extrusion of toothpaste (Kamrin & Mahadevan 2012), (b) a ketchup splatter (Luu & Forterre 2009), (c) a dambreak of blue-coloured Carbopol on an incline (Cocharde & Ancey 2008), and (d) a mud volcano (Photograph from the USGS). 11

Figure 1-7: A schematic illustration of the stress-strain rate relationship for Newtonian and viscoplastic fluids..... 12

Figure 1-8: A schematic illustration of the thin-film flow for a viscoplastic fluid..... 14

Figure 1-9: A schematic illustration of the velocity profile of Bingham fluid for a Poiseuille flow. 25

Figure 2-1: Schematic illustration of the axisymmetric jet flow impinging on a flat stationary disk and the hydraulic jump of type I with one vortex downstream. Shown are the developing boundary-layer region ($0 < r < r_0$) and the fully-developed viscous region ($r_0 < r < r_\infty$). The fully-developed viscous region comprises a region ($r_0 < r < r_1$) where gravitational effects are moderate, and a second region where gravitational effects are strong ($r_1 < r < r_\infty$). All notations are dimensionless. In this case, the jet radius is equal to one. The film is allowed to fall freely over the edge of the disk where an infinite slope in the film thickness occurs, $h'(r = r_\infty) \rightarrow -\infty$. Shown in dashed-red curve is the schematic film-thickness profile

reflecting the approach of Wang & Khayat (2019), terminating with a singularity at a finite radius denoted here by r_s . The jump location coincides with $h''(r_j) = 0$, and $h(r_m) = h_{max}$.
 48

Figure 2-2: Influence of gravity and viscosity on the size of the impingement zone (distance between the origin and the point of intersection with the boundary-layer height). (a) Influence of Fr for $Re = 100$, and (b) influence of Re for $Fr = 4$. The horizontal lines are the thickness of the viscous layer in the impingement zone, and the curves are the boundary-layer profiles emanating from the origin..... 56

Figure 2-3: A sample case ($Re = 800$, $Fr = 5$ and $r_\infty = 25$), illustrating the shooting method and the effect of the upstream and downstream boundary conditions on the jump location (upstream influence). The distributions of film profiles (a) and the wall shear stress (b) are obtained for different initial conditions. The green solid and dashed curves correspond to the profiles of the film and boundary layer, respectively, in the developing boundary-layer region. Here, the transition location is at $r = r_0 = 4.18$. (green vertical line). The red curve corresponds to the variation of the film thickness in the moderate-gravity viscous region, obtained by solving the first-order equation (2.3.8), and exhibiting a singularity at $r = r_s = 12.3$ (red vertical line). The black and blue curves show branches of the solution for the film thickness variation in the strong-gravity viscous region obtained by solving the second-order equation (2.3.11). Depending on the value of r_1 (and consequently h_1) the solution may or may not reach the edge. The unique solution to the problem (blue curve), corresponding to an infinite slope at the edge of the disk, is obtained for $r_1 = 10.7931$ (blue vertical line). 62

Figure 2-4: (a) Comparison of the free-surface profile based on the present approach against the boundary-layer and Navier-Stokes profiles of Fernandez-Feria et al. (2019), as well as the depth-averaged based profile of Kasimov (2008) for $Re = 854.29$, $Fr = 97.19$ and $r_\infty = 80$. (b) Visualization of the flow field based on the present approach (U and τ_w distributions in inset).
 67

Figure 2-5: Comparison of the present approach (solid curves) against the numerical solution of the boundary-layer equations (open circles) of Fernandez-Feria *et al.* (2019) for the radial distributions of (a) the film profile, (b) the wall shear stress, (c) the gravity term and (d) the

radial momentum flux term in equation (2.3.7). Here the liquid is silicone oil with $Re = 164.98$, $Fr = 16.87$ and $r_\infty = 31$ 70

Figure 2-6: Comparison of the free-surface profiles between our present approach (black solid line) and the measurements (open blue circles) of Duchesne *et al.* (2014). The Navier-Stokes solution of Zhou & Prosperetti (2022) is also included (red solid line) as well as the lubrication solution (green dashed line). Arrows point to the jump heights $H_{J1} = h_{max}$ and H_{J2} based on the present and lubrication approaches, respectively. Here, $Re = 169.1$, $Fr = 16.87$ and $r_\infty = 93.75$ 72

Figure 2-7: Flow details corresponding to the profile in figure 2-6 using the present approach. Shown are the flow streamlines (a), the wall shear stress distribution (b) and the surface velocity distribution (c). The results are plotted in dimensionless form with $Re = 169.10$, $Fr = 16.87$ and $r_\infty = 93.75$. In (a), the red curve represents the supercritical free surface of the film, showing a singularity, predicted using the first-order model (2.3.8)..... 74

Figure 2-8: Influence of Fr (flow rate) on (a) the jump radius r_j (inset shows $r_j \approx 1.08Fr^{7/10}$), (b) the maximum film height h_{max} (inset shows $h_{max} \approx 1.32Fr^{4/25}$) and (c) the Froude number at the jump Fr_j over the experimental flow rate range of Duchesne *et al.* (2014), corresponding to $50.11 < Re < 551.25$ or $Ga = 100$. Theoretical results (black solid curves) are compared against the measurements (blue circles) of Duchesne *et al.* (2014). In (c), the open blue and red circles represent the Fr_j values based on the measured heights H_{J1} and the height H_{J2} (see figure 2-7). 76

Figure 2-9: Comparison of our approach (solid lines) for the jump radius with the measurements of Hansen *et al.* (1997) (open circles). Results for water ($Ga = 627840$) are in red, those for silicone oil ($Ga = 2790$) are in blue. The dash-dotted lines are the predictions of the spectral inertial-lubrication model developed by Rojas *et al.* (2010), and the dashed lines those of the Navier–Stokes simulations of Zhou & Prosperetti (2022). 77

Figure 2-10: Influence of the Froude number (flow rate) on (a) the film profile, (b) wall shear stress (inset shows amplification in the downstream vicinity of the jump) and (c) surface velocity (insets show local profile for $Fr = 5$ and amplification near the disk edge). Here, Ga

= 100 ($50.11 < Re < 551.25$) and $r_\infty = 93.75$, corresponding to the range of flow rate in the experiment of Duchesne et al. (2014). 81

Figure 2-11: Influence of Fr (flow rate) on the local Froude number Fr_j . Inset shows the distribution of the numerically predicted jump radius (black solid curve) and the critical radius (red dashed curve), as well as the experimental data of Duchesne et al. (2014) (open blue circles). Here, $Ga = 100$ and $r_\infty = 93.75$, corresponding to the experiment parameters. 83

Figure 2-12: Dependence of the vortex size and structure on Fr (flow rate). (a) The vortex length and height and (b)-(d) the vortex structure for $Fr = 5-55$ (vertical dotted lines delimit the jump region/length). Here $Ga = 100$ and $r_\infty = 93.75$, corresponding to the parameters in the experiment of Duchesne et al. (2014). 84

Figure 2-13: Influence of the Froude number (gravity) on (a) the free surface profile (solid curves) and the boundary-layer thickness (dashed curves), (b) the wall shear stress and (c) the local Froude number. The inset in (c) shows the distribution of the numerically predicted jump radius (black solid curve) and the critical radius (red dashed curve). (d)-(g) The streamlines for $Fr = 2, 5, 10$ and 15 . Here, $Re = 800$ and $r_\infty = 25$ 88

Figure 2-14: Influence of Re (viscosity) on (a) the free surface profile (solid curves) and the boundary-layer thickness (dashed curves), (b) the wall shear stress and (c) the local Froude number. The inset in (c) shows the distribution of the numerically predicted jump radius (black solid curve) and the critical radius (red dashed curve). (d)-(f) The streamlines around the jump region for $Re = 200, 400, 600$ and 800 . Here, $Fr = 10$ and $r_\infty = 25$ 90

Figure 3-1: Schematic illustration of the axisymmetric jet flow impinging on a flat stationary disk and the hydraulic jump of type I with one vortex downstream. Shown are the developing boundary-layer region ($0 < r < r_0$) and the fully-developed viscous region ($r_0 < r < r_\infty$). The fully-developed viscous region comprises a region ($r_0 < r < r_{j-}$) where gravitational effects are moderate, and a second region where gravitational effects are strong ($r_{j-} < r < r_\infty$). All notations are dimensionless. In this case, the jet radius is equal to one. The film is allowed to fall freely over the edge of the disk where an infinite slope in the film thickness occurs, $h'(r = r_\infty) \rightarrow -\infty$. The red dashed- curve is the schematic film-thickness profile reflecting the approach of Wang & Khayat (2019), terminating with a singularity at a finite radius denoted

here by r_s . The jump location coincides with $h''(r_j) = 0$, and $h(r_{j-}) = h_j$, and $h(r_{j+}) = H_j$. The downward arrow represents the gravitational acceleration. 104

Figure 3-2: Comparison of the free-surface profile based on the present approach against the Navier-Stokes profiles of Fernandez-Feria *et al.* (2019) for $Re = 854.29$, $Fr = 97.19$ and (a) $r_\infty = 53.33$, (b) $r_\infty = 80$ 113

Figure 3-3: Influence of the disk radius r_∞ on (a) the free surface profile (solid curves) the boundary-layer thickness (dashed curves), and (b) the wall shear stress. Shown in (c)-(e) are the streamlines for $r_\infty = 40, 50$ and 60 . The inset in (a) shows the dependence of the jump radius and maximum film height on the disk radius. Here, $Re = 854.29$, $Fr = 97.19$ are parameters used in Fernandez-Feria *et al.* (2019). 114

Figure 3-4: Influence of the Froude number (flow rate) on the film profile for three different disk sizes: (a) $r_\infty = 93.75$, (b) $r_\infty = 50$ and (c) $r_\infty = 25$. Here, $Ga = 100$ ($50.11 < Re < 551.25$), corresponding to the range of flow rate in the experiment of Duchesne *et al.* (2014). Dash-dotted curves in (a)-(c) represent the locus of the maximum film height. 116

Figure 3-5: Comparison of the free-surface profile in the supercritical and jump regions based on the present approach against the measurements of Duchesne (2014) for three different flow rates. Here, $Ga = 100$ and $r_\infty = 93.75$. The green curves are based on expressions (3.2.12a,b) and (3.2.13a), the red curve in (c) is from the Navier-Stokes solution of Zhou & Prosperetti (2022), the blue circles are from Duchesne (2014), and the black curves are from the present approach. 118

Figure 3-6: Influence of Fr (flow rate) for different disk sizes on the jump radius. Shown in (a) is the prediction based on the present approach, in (b) and (c) are the comparison between the present approach, the measurement of Duchesne (2014), and the present scaling (3.4.5) for $r_\infty = 93.75$ and 50 , respectively. Here $Ga = 100$, corresponding to the parameters in the experiment of Duchesne *et al.* (2014). 119

Figure 3-7: Influence of Fr (flow rate) for different disk sizes on (a) maximum film height, (b) jump length and (c) vortex length. Here $Ga = 100$, corresponding to the parameters in the experiment of Duchesne *et al.* (2014). 121

Figure 3-8: Comparison of the free-surface profiles between our approach (black solid line) and the Navier-Stokes solution of Askarizadeh *et al.* (2019) and (2020), shown in red symbols in (a) and (b), respectively, for $\sigma = 10$ and 45 mN/m, and corresponding obstacle heights of 1 and 0.05 mm. Predicted and simulated flow fields are shown in (c) and (d), respectively, with the inset in (c) depicting the surface velocity and wall shear stress distributions. In all cases, $Re = 381.97$, $Fr = 9.76$, $r_\infty = 16$ 123

Figure 3-9: Influence of the film thickness at the disk edge on (a) the free surface profile (solid curves) and the boundary-layer thickness (dashed curves), and (b) the wall shear stress. Shown in (c)-(e) are the streamlines for $h_\infty = 0.65$, 0.85 and 1.05 . The inset in (a) shows the dependence of the jump radius and maximum film height on the film thickness at the disk edge. Here, $Re = 381.97$, $Fr = 9.76$ and $r_\infty = 16$ are parameters corresponding to the simulation of Askarizadeh *et al.* (2019, 2020). 125

Figure 3-10: Comparison of scaling laws for the influence of the Froude number (flow rate) on the jump radius. Our scaling law (3.4.5) is compared in (a) against those of Bohr *et al.* (1993) and Duchesne *et al.* (2014), and in (b) against the scaling law of Rojas *et al.* (2013). Measurements of Duchesne *et al.* (2014) are added in (a) and those of Hansen *et al.* (1997) in (b) for reference. In (b), results for water ($\nu = 1cSt$) ($Ga = 627840$) are in red, those for silicon oil ($\nu = 15cSt$) ($Ga = 2790$) are in blue, and those for silicon oil ($\nu = 95cSt$) ($Ga = 70$) are in green. 129

Figure 3-11: Influence of Fr (flow rate) on film thickness h_∞ and surface velocity $Fr\langle u_\infty \rangle$ at the edge of the disk. Shown in (a) and (c) are predictions based on the present approach against expressions (3.4.8) and (3.4.9), and in (b) is the comparison between the present approach and the measurements in Duchesne (2014). Here, $Ga = 100$ ($50.11 < Re < 551.25$) and $r_\infty = 93.75$, corresponding to the range of flow rates in the experiment of Duchesne *et al.* (2014). 133

Figure 3-12: Influence of r_∞ (disk radius) on thickness h_∞ at the edge of the disk. Here, red curves and circle symbols correspond to $Re = 854$, $Fr = 97$, and blue curves and circle symbols correspond to $Re = 356$, $Fr = 194$. Simulation results come from the Navier-Stokes solutions of Fernandez-Feria *et al.* (2019). 134

Figure 3-13: Dependence of the jump length, vortex length and vortex height on the film thickness at the disk edge. Here, $Re = 381.97$, $Fr = 9.76$ and $r_\infty = 16$ are parameters corresponding to the simulation of Askarizadeh et al. (2019, 2020). 135

Figure 3-14: Influence of the Froude number (flow rate) on the jump and vortex lengths. Solid and dash-dotted curves based on our predictions and dashed curve based on expression (3.4.11). Here $Fr_j = 0.32$, $Ga = 100$ and $r_\infty = 93.75$, corresponding to the parameters in the experiment of Duchesne et al. (2014). 137

Figure 3-15: Influence of Fr (flow rate) on (a) the film depth immediately upstream and downstream of the jump, and (b) the conjugate depth ratio. Here $Ga = 100$ and $r_\infty = 93.75$, corresponding to the parameters in the experiment of Duchesne et al. (2014). Inset in (a) shows the experimental measurements of Craik et al. (1981) for $Re = 265.46 - 1238.44$, $Fr = 0.18 - 0.85$, and the grey dashed curve in the inset is included for visual guidance. 140

Figure 3-16: Influence of Fr (flow rate) on the Froude number (a) Fr_{j-} at the leading edge and (b) Fr_{j+} at the trailing edge of the jump. Here $Ga = 100$ and $r_\infty = 93.75$, corresponding to the parameters in the experiment of Duchesne et al. (2014). 143

Figure 3-17: Influence of Fr (flow rate) on the relative energy loss. Here $Ga = 100$ and $r_\infty = 93.75$, corresponding to the parameters in the experiment of Duchesne et al. (2014). 145

Figure 3-18: Influence of the supercritical approaching Froude number Fr_{j-} on (a) the relative energy loss $\Delta E_j/E_{j-}$ and (b) the conjugate depth ratio H_j/h_j 147

Figure 3-19: Influence of gravity on the vortex and jump size. Shown is the dependence of (a) the vortex length, (b) the vortex height and (c) the jump length on Fr for different Re for a disk of dimensionless radius $r_\infty = 25$ 148

Figure 3-20: Influence of viscosity on the vortex and jump size. Shown is the dependence of (a) the vortex length, (b) the vortex height and (c) the jump length on Re for different Fr for a disk of dimensionless radius $r_\infty = 25$ 149

Figure 3-21: Influence of Fr and Re on the maximum length (a) and maximum height (b) of the separation zone in a 3D plot. Another dimensionless parameter is $r_\infty = 25$. The curves

projected on the $L_{vortex}Fr$ and $H_{vortex}Fr$ planes are for $Re = 400$ (red lines), 600 (green lines), 800 (blue lines) and 1000 (cyan lines), and the curves projected on the $L_{vortex}Re$ and $H_{vortex}Re$ planes are for $Fr = 2$ (red lines), 10 (green lines), 17 (blue lines) and 25 (cyan lines). Also shown in (c) is the influence of Fr and Re on the jump length in a 3D plot. 151

Figure 3-22 Marginal separation curve in the (α, β) plane for the existence of the hydraulic jump and vortex on a flat solid disk. The log-log plot in (b) reflects the scaling laws (3.5.3) and (3.5.4) for the separation curve. The region of existence of a vortex in (c) lies above the surface. The curves projected on the $r_{\infty}Fr$ plane are for $Re = 400$ (red lines), 600 (green lines), 800 (blue lines) and 1000 (cyan lines), and the curves projected on the $r_{\infty}Re$ plane are for $Fr = 2$ (red lines), 10 (green lines), 17 (blue lines) and 25 (cyan lines). 152

Figure 4-1: Schematic illustration of the non-axisymmetric flow of a circular jet impinging on a flat stationary disk, and the hydraulic jump of type *I*. Shown are the developing boundary-layer region, the fully-developed viscous region, and the subcritical region downstream of the jump. All notations are dimensionless. 168

Figure 4-2: Schematic of the control volume across the hydraulic jump. Arrows indicate direction of velocity components. 174

Figure 4-3: Free-surface profile. Comparison between theoretical predictions and the measurements of Duchesne *et al.* (2014) for silicon oil (20 cSt). Results plotted in dimensionless form with $Re = 169$, $Fr = 16.88$, $Bo = 1.19$, $R_{\infty} = 94$ 179

Figure 4-4: Hydraulic jump on a triangular disk. The figure shows (a) polar plots of the jump radius $r_J(\theta)$, transition radius r_0 , disk radius $R_{\infty}(\theta)$ and its average $R_{\infty 0}$. The dependence on the azimuthal angle is also shown for (b) $r_J(\theta)$ and $R_{\infty}(\theta)$, and (c) $h_J(\theta)$ and $H_J(\theta)$, with corresponding axisymmetric levels. The parameters used are $Re = 169$, $Fr = 16.88$, $Bo = 1.19$, $H_{\infty 0} = 1.3$ and $R_{\infty 0} = 12$ 183

Figure 4-5: Surface film height (a), the flow field (b), the radial (c) and azimuthal (d) velocity contours at the surface for a jet on a triangular disk for $Re = 169$, $Fr = 16.88$, $Bo = 1.19$, $H_{\infty 0} = 1.3$, and $R_{\infty 0} = 12$ 185

Figure 4-6: Influence of the flow rate (Froude number) on the maximum and minimum jump radii for a triangular disk (red curves), square disk (green curves), pentagonal disk (blue curves) and circular disk (black curve). The inset shows the influence of Fr on the difference between the maximum and minimum jump radii, Δr_J . Here, $Re = 100 - 170$, $Bo = 1.19$, $H_{\infty 0} = 1.14 - 1.3$ and $R_{\infty 0} = 12$ 186

Figure 4-7: Influence of the surface tension (Weber number) on the maximum and minimum jump radii for a triangular disk (red curves), square disk (green curves), pentagonal disk (blue curves) and circular disk (black curve). Here, $Re = 169$, $Fr = 16.88$, $H_{\infty 0} = 2.41 - 1.3$ and $R_{\infty 0} = 12$. The lower inset shows the influence of We and asymptotes for large surface tension on the difference between the maximum and minimum jump radii, Δr_J ($H_{\infty 0} = 2.22 - 0.58$ and $R_{\infty 0} = 24$)..... 187

Figure 4-8: Influence of the non-circular disk size on the maximum and minimum jump radii for a triangular disk (red curves), square disk (green curves), pentagonal disk (blue curves) and circular disk (black curve). The inset shows the influence of $R_{\infty 0}$ on the difference between the maximum and minimum jump radii, Δr_J . Here, $Re = 169$, $Fr = 16.88$, $Bo = 1.19$, $H_{\infty 0} = 1.3 - 1.1$ 188

Figure 4-9: Dependence of the jump width Δr_J on the normalized jump area for various disk shapes (modes) with number of sides ranging from 3 to 13. Each set comprises symbols and fitting curve, corresponding to $Re = 170$, $Fr = 17$, $H_{\infty 0} = 1.30$ (red), $Re = 150$, $Fr = 15$, $H_{\infty 0} = 1.26$ (green), $Re = 130$, $Fr = 13$, $H_{\infty 0} = 1.22$ (blue) and $Re = 100$, $Fr = 10$, $H_{\infty 0} = 1.14$ (cyan), $Bo = 1.19$. Below the solid line the jump width is independent of the aspect ratio..... 189

Figure 4-10: Influence of the circular disk size ($4 \leq R_{\infty} \leq 7$) on a non-circular hydraulic jump induced by edge thickness azimuthal variation $H_{\infty}(\theta)$ shown in (a). The jump radius $r_J(\theta)$ is shown in (b). Corresponding polar plots of the jump radius $r_J(\theta)$ and transition radius r_0 are shown in (c). Here, $Re = 322$, $Fr = 3.3$, $Bo = 6$, $H_{\infty 0} = 1.26, 1.29, 1.32, 1.38$ and $A = 0.6$.. 192

Figure 4-11: Details of the flow for $R_\infty = 7$: radial (a) and azimuthal (b) velocity contours at the film surface, (c) flow field and (d) film thickness profiles in the corner and valley directions. Here, $Re = 322$, $Fr = 3.3$, $Bo = 6.$, $H_{\infty 0} = 1.26$ and $A = 0.6$ 194

Figure 4-12: Details of the flow for $R_\infty = 4$: (a) film surface topography, (b) flow field, (c) radial and (d) azimuthal velocity contours at the film surface. Here, $Re = 322$, $Fr = 3.3$, $Bo = 6$, $H_{\infty 0} = 1.38$ and $A = 0.6$ 195

Figure 5-1: Schematic illustration of the axisymmetric jet of a viscoplastic fluid impinging on a flat stationary circular disk and the hydraulic jump. Shown are the supercritical and subcritical regions. All notations are dimensionless. 214

Figure 5-2: Influence of the yield stress on the film thickness h and the fully-yielded layer thickness h_0 in the supercritical region ($Re = 50$). Shown are the profiles for $n < 1$ (a-c), $n = 1$ (d-f) and $n > 1$ (g-i). 222

Figure 5-3: Influence of the yield stress on the distribution of (a) the pseudo-plug layer velocity and (b) the wall shear stress for a Bingham fluid ($n = 1$). Also shown is the influence of viscosity on the distribution of (c) the wall shear stress and (d) the wall shear rate for $B = 0.5$. Here $Re = 50$ 225

Figure 5-4: The influence of the yield stress on (a) the minimum film height h_{min} and its location r_{min} , (b) the first local maximum thickness h_{0max1} and its location r_{0max1} , (c) the local minimum thickness h_{0min} and its location r_{0min} , and (d) the second local maximum thickness h_{0max2} and its location r_{0max2} of the fully-yielded layer, for $n = 0.5$ (solid lines), 1 (dash-dotted lines) and 1.8 (dashed lines). Here $Re = 50$ 226

Figure 5-5: Comparison between the exact and the small- B asymptotic profiles. Shown are the pseudo-plug layer velocity U (a), the film height h (b) and pseudo-plug layer thickness h_0 (c) for Bingham fluid $n = 1$ and $B = 0.5$. Here $Re = 50$. The solid lines are the exact numerical results, and the dashed lines are the asymptotic results. 231

Figure 5-6: The size of the impinging zone (distance between the origin and the intersection point). The black lines are the boundary-layer thickness obtained from the expression (5.3.20),

and the color lines are the result from the solution of equations (5.3.6) for the fully-yielded layer. (a) $n = 0.8$, (b) $n = 1$, and (c) $n = 1.2$ 234

Figure 5-7: Influence of the yield stress on the film thickness h and the fully-yielded layer thickness h_0 in the supercritical and subcritical regions. Shown are the profiles for $n < 1$ (a-c), $n = 1$ (d-f) and $n > 1$ (g-i). Here, $Re = 50$, $Fr = 15$, $Ca = 2$ and $R_\infty = 8$ 244

Figure 5-8 Influence of the yield stress on the pseudo-plug layer velocity U (a) and the wall shear stress τ_w (b) for a Bingham fluid. Insets show the magnification over the subcritical region. Here, $Re = 50$, $Fr = 15$, $Ca = 2$ and $R_\infty = 8$ 246

Figure 5-9: The influence of yield stress on (a) the hydraulic jump location r_j for $n = 0.5$, 1 and 1.8, and (b) the film height and fully-yielded layer thickness immediately upstream of the jump, h_j and h_{0j} , downstream of the jump, H_j and H_{0j} , and the critical film height at the jump h_{cJ} for $n = 1$. Here $Re = 50$, $Fr = 15$, $Ca = 2$, and $R_\infty = 8$ 248

Figure 5-10: The influence of gravity on (a) the hydraulic jump location rJ for $B = 0.001$, 0.05, 0.5 and 1, and (b) the film height and fully-yielded layer thickness immediately upstream of the jump, h_j and h_{0j} , downstream of the jump, H_j and H_{0j} , and the critical film height at the jump h_{cJ} for $B = 0.5$. Here $Re = 50$, $Ca = 2$, $n = 1$ and $R_\infty = 8$ 251

Figure 5-11: The influence of surface tension on (a) the hydraulic jump location rJ for $B = 0.001$, 0.05, 0.5 and 1, and (b) the film height and fully-yielded layer thickness immediately upstream of the jump, h_j and h_{0j} , downstream of the jump, H_j and H_{0j} , and the critical film height at the jump h_{cJ} for $B = 0.5$. The dashed lines are asymptotic limits obtained by excluding the surface tension effect ($Ca \rightarrow \infty$) in equations (5.4.6) and (5.4.8). Here $Re = 50$, $Fr = 15$, $n = 1$ and $R_\infty = 8$ 252

Figure 5-12: The influence of the radius of the disk R_∞ on (a) the hydraulic jump location rJ for $B = 0.001$, 0.05, 0.5 and 1, and (b) the film height and fully-yielded layer thickness immediately upstream of the jump, h_j and h_{0j} , downstream of the jump, H_j and H_{0j} , and the critical film height at the jump h_{cJ} for $B = 0.5$. Here $Re = 50$, $Fr = 15$, $Ca = 2$, and $n = 1$. Inset in (b) shows enlarged behaviour for the small range of disk radius. 254

Figure 5-13: Dependence of Fr_{j+} on yield stress, gravity, surface tension and disk size. Here $Re = 50$, $Fr = 15$, $Ca = 2$, $B = 1$, $n = 1$ and $R_\infty = 8$ unless otherwise indicated in the figure. 256

Figure 5-14: The dependence of the conjugate height ratio H_j/h_j on the local upstream Froude number Fr_{j-} . Here $Re = 601 - 1203$, $B = 0.2 - 0.1$, $Ca = 0.6 - 1.2$, $R_\infty = 30$ and $n = 1$. Inset shows the theoretical result of Zhou *et al.* (2006) in red line and the measurements of Ogihara & Miyazawa (1994) in blue \times symbols. 257

Figure 5-15: The dependence of the critical height on the flow rate or Froude number. Here $Re = 601 - 1203$, $B = 0.2 - 0.1$, $Ca = 0.6 - 1.2$, $R_\infty = 30$ and $n = 1$. Inset shows the theoretical result of Zhou *et al.* (2006) in red line and the measurements of Ogihara & Miyazawa (1994) in blue \times symbols. 258

List of Appendices

Appendix A: The thin-film equations and boundary conditions	278
---	-----

Chapter 1

1 Introduction

1.1 Background and applications

Circular hydraulic jumps are a common phenomenon in our daily lives, which can be widely observed when opening a kitchen faucet. When the water from the tap impacts the solid plate of the sink, a thin liquid film in the vicinity of the impact point is formed. As the flow spreads outward in the radial direction, the film thickness abruptly increases at a specific radial location to a significantly thicker film (see Figure 1-1). This sudden increase in liquid film thickness is known as the hydraulic jump. In addition to the increase in film thickness, this phenomenon is accompanied by a decrease in wall shear stress and heat transfer ability, as well as the formation of a vortex near the solid (Watson 1964; Craik *et al.* 1981; Liu *et al.* 1993; Askarizadeh *et al.* 2020).

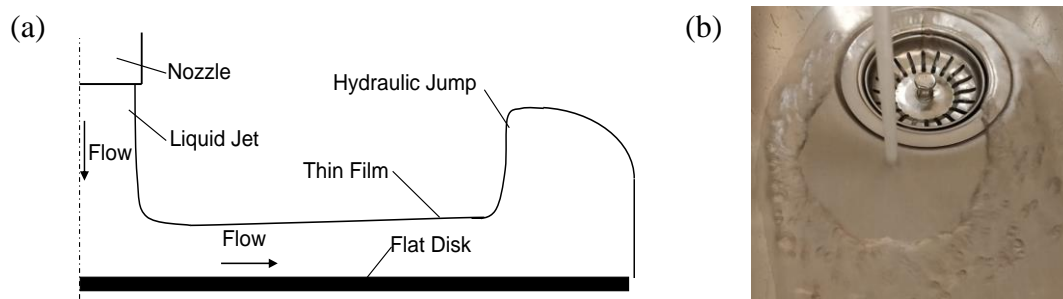


Figure 1-1: (a) Schematic illustration of an impinging jet and circular hydraulic jump, (b) a water jet and formed hydraulic jump in a kitchen sink.

The hydraulic jump is also widely observed near various hydraulic structures, including block ramps, rock sills and rock weirs (Palermo & Pagliara 2018). The hydraulic jump in these scenarios is normally called the planar hydraulic jump, which has been extensively explained in undergraduate fluid mechanics textbooks (Kundu *et al.* 2016; White 2006). Figure 1-2 illustrates a planar jump near a dam on the St. Joseph River in Niles, Michigan. In this figure, the hydraulic jump occurs, as high-speed flow discharges into a region of slower velocity. The planar hydraulic jump is widely used to dissipate kinetic energy and reduce potential damage and erosion to the bed of the hydraulic facility. Extensive studies

have been conducted to investigate factors influencing the dissipative process, such as bed roughness and channel slope (Ead & Rajaratnam 2002; Palermo & Pagliara 2018). Although the current thesis focuses on the circular jump, we will also investigate some relevant characteristics extensively studied in the planar jump.

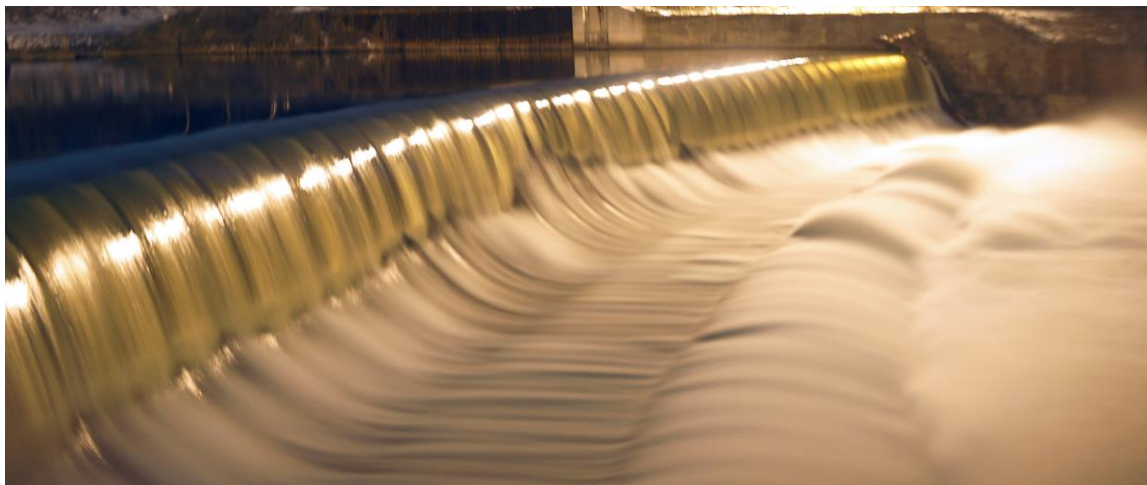


Figure 1-2: Planar hydraulic jump on the St. Joseph River in Niles, Michigan (from flickr)

Despite its simplicity and common occurrence in daily life, the investigation of impinging jet flow and the resulting hydraulic jump is of great interest and importance for both industrial and academic communities.

The most common application of impinging jet flow is surface rising and cleaning. Except for using the impinging jet to wash personal vehicles, it is also extensively employed as a component of cleaning-in-place systems. The utilization of liquid jet cleaning in the food, pharmaceutical, and chemical industries is significant, as it can effectively tackle the problem of fouling layers or residual soil layers that accumulate on surfaces during material processing. (Oevermann *et al.* 2019). Similar applications can also be found in the cleaning of air heaters in power plants. In this case, pressurized high-pressure water, chemicals, or even liquid nitrogen are utilized to remove accumulated fly ash, dust, and oil from the surface of the heat exchanger (Hovland *et al.* 2011). This cleaning process can effectively prevent the reduction of heat transfer rate within the heaters.

The impinging jet can also be used in many practical cooling applications. For instance, in power electronic modules, a jet of water or other types of coolant is directed onto the upper surface of the semiconductor package to effectively remove heat (Wadsworth & Mudawar 1990; Jörg *et al.* 2017). Efficiently dissipating the heat generated by these electronic components is crucial to prevent overheating and ensure optimal performance. Additional cooling applications can be observed in the piston chamber of car engines, heat treatment processes for steel, and hot strip rolling production lines. In these situations, effective cooling processes are employed to manage and regulate temperatures, ensuring the proper functioning of the engine, desired material properties in steel, and efficient production in rolling lines (Melaniff 2003; Linz 2011).

Impinging jet technology also finds additional applications in industrial coating (Weinstein & Ruschak 2004) and chemical reactors (Pask, Nuyken & Cai 2012). For example, in chemical reactors utilizing impinging jet, liquid impinging at the center of a rotating disk. The liquid then spreads over the surface of the disk, and the resulting liquids are collected through an outlet. The use of impinging jets with rotating disks can generate centrifugal forces, resulting in a highly sheared liquid film. This film facilitates efficient mass transfer, favouring processes such as absorption, stripping, mixing, and reaction (Pask *et al.* 2012). These capabilities make impinging jet systems valuable in enhancing the efficiency and effectiveness of various chemical processes within reactors.

The occurrence of a hydraulic jump when a jet impinges on a surface, regardless of whether the surface is horizontal, vertical, flat, or wavy, is quite common. As mentioned earlier, the fast and thin film inner the hydraulic jump offers several advantages such as high mass and heat transfer rates, as well as high shear stress. These characteristics make it favourable for numerous applications. On the other hand, downstream of the hydraulic jump, the flow becomes slower, resulting in a significant decrease in mass and heat performance (Mohajer & Li 2015). To cover larger surface areas, multiple impinging jets are often employed, so it is important to adopt an appropriate arrangement for the jets. Therefore, accurately predicting the radius of the hydraulic jump becomes crucial to ensure optimal performance in related applications.

The investigation of the hydraulic jump phenomenon holds significant interest within the academic community, in addition to the above-mentioned applications in industry. The earliest document of the hydraulic jump phenomenon can be traced back to the description by Leonardo da Vinci in the 1500s. However, it was Rayleigh (1914), who conducted the first theoretical investigation on this phenomenon. Since then, numerous studies have contributed to this simple but fascinating phenomenon.

The flow for an impinging jet and hydraulic jump can be divided into two regions, the supercritical and subcritical regions, which correspond to the flow up- and down-stream of the location of the hydraulic jump. The determination of whether the flow is supercritical or subcritical flow is based on whether the local Froude number is greater or less than 1 (Kundu *et al.* 2016). The local Froude number is defined as

$$Fr_l = \frac{\langle \bar{u} \rangle}{\sqrt{g\bar{h}}}, \quad (1.1.1)$$

in which $\langle \bar{u} \rangle$ is the average velocity of the flow, g is the acceleration due to gravity and \bar{h} is the height of the flow. The bar above the variable denotes a dimensional variable or parameter. Clearly, the super- and sub-critical flow means that the average velocity is larger and smaller than the velocity of linear surface waves $\sqrt{g\bar{h}}$, respectively (Watanabe *et al.* 2003). This transition from supercritical to subcritical flow bears a resemblance to the transition from supersonic to subsonic flow in aerodynamics. An analogous situation can be observed with a supersonic jet, where the surrounding air undergoes a transition from supersonic flow ($M = \bar{u}/\bar{u}_c > 1$, where M is Mach number, \bar{u} is the velocity of the object and \bar{u}_c is the sound speed) to subsonic flow ($M < 1$). Consequently, the investigation of circular hydraulic jumps can contribute to the advancement of research involving transition effects.

Although the appearance of the hydraulic jump is simple, the flow structure exhibits significant complexity. Based on the experimental observations of Liu & Lienhard (1993), Ellegaard *et al.* (1996), and numerical simulations of themselves, Askarizadeh *et al.* (2020)

classified hydraulic jump into five distinct types based on the configuration of the roller and separation bubble. By increasing the height of the obstacle mounted at the disk edge, different types of hydraulic jumps can be obtained. Type 0 corresponds to a circular hydraulic jump without the presence of either a vortex near the disk or a roller at the free surface (Figure 1-3a). Type Ia represents a hydraulic jump with a single vortex near the disk (Figure 1-3b), while type Ib refers to a jump with a roller formed at the free surface (Figure 1-3c). As indicated in Askarizadeh *et al.* (2020), the type Ib type was not reported in Ellegaard *et al.* (1996), or in Bush *et al.* (2006) and other related studies, as the occurrence of this type is possible during the transition from type Ia to type II, where a very weak separation bubble keeps appearing and disappearing. In fact, in the experimental work of Chang *et al.* (2001), they found that the vortex near the plate disappeared when the flow rate exceeded a critical value, resulting in a much smoother jump profile. When both a separation bubble near the disk and a roller near the free surface are observed, hydraulic jumps are called type IIa (Figure 1-3d) or type IIb (Figure 1-3e). The difference between type IIa and type IIb is the distinct shape appearance of the jump. Type IIb exhibits a tiered structure, which is referred to as a "double-jump" by Bush *et al.* (2006).

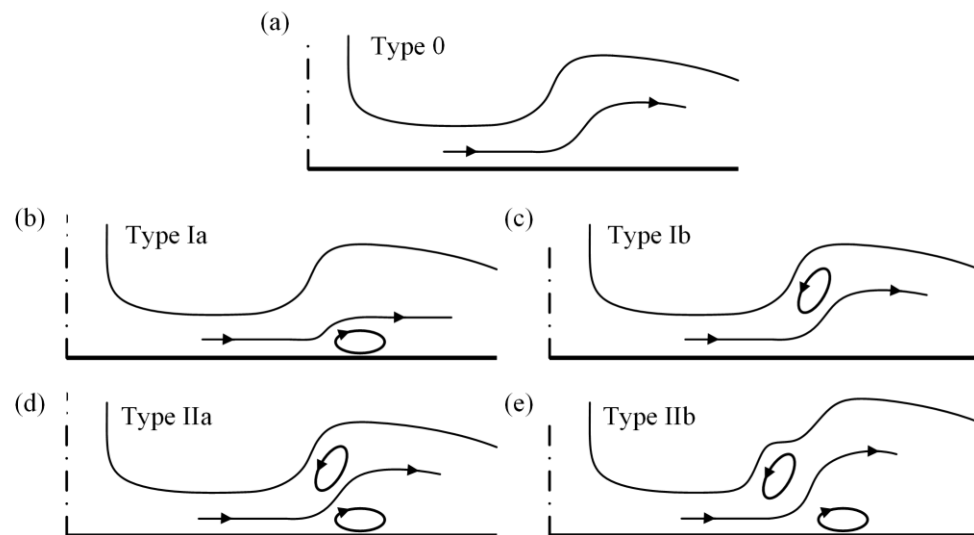


Figure 1-3: Schematic illustration of different types of hydraulic jump structures.

1.2 Methodologies

The main approach and assumptions adopted in the thesis will be presented. The boundary layer theory and thin-film approach, as well as the Kármán–Pohlhausen (K–P) approach for a Newtonian fluid will be introduced first. The Herschel-Bulkley constitutive model will be presented, and the difference in the methodologies between a Newtonian fluid and a viscoplastic fluid of the Herschel-Bulkley type will be discussed.

1.2.1 Boundary layer theory and thin-film approach for a Newtonian fluid

For laminar Newtonian flow, the boundary layer theory implies that the viscous effects play a significant role within a thin layer adjacent to the solid plate, which is known as the boundary layer. In contrast, the influence of viscosity is negligible in the bulk region away from the solid. This inviscid outer flow corresponds to the inviscid limiting solution (Schlichting & Gersten 2000). The laminar boundary layer equations for non-axisymmetric flow are written as

$$\frac{\partial \bar{u}}{\partial \bar{r}} + \frac{\bar{u}}{\bar{r}} + \frac{1}{\bar{r}} \frac{\partial \bar{v}}{\partial \theta} + \frac{\partial \bar{w}}{\partial \bar{z}} = 0, \quad (1.2.1a)$$

$$\bar{u} \frac{\partial \bar{u}}{\partial \bar{r}} + \frac{\bar{v}}{\bar{r}} \frac{\partial \bar{u}}{\partial \theta} + \bar{w} \frac{\partial \bar{u}}{\partial \bar{z}} - \frac{\bar{v}^2}{\bar{r}} = -\frac{1}{\rho} \frac{\partial \bar{p}}{\partial \bar{r}} + \nu \frac{\partial^2 \bar{u}}{\partial \bar{z}^2}, \quad (1.2.1b)$$

$$\bar{u} \frac{\partial \bar{v}}{\partial \bar{r}} + \frac{\bar{v}}{\bar{r}} \frac{\partial \bar{v}}{\partial \theta} + \bar{w} \frac{\partial \bar{v}}{\partial \bar{z}} + \frac{\bar{u}\bar{v}}{\bar{r}} = -\frac{1}{\rho \bar{r}} \frac{\partial \bar{p}}{\partial \theta} + \nu \frac{\partial^2 \bar{v}}{\partial \bar{z}^2}, \quad (1.2.1c)$$

$$-\frac{1}{\rho} \frac{\partial \bar{p}}{\partial \bar{z}} + g = 0. \quad (1.2.1d)$$

Here, the bar denotes a dimensional variable. \bar{u} , \bar{v} and \bar{w} are the velocities in \bar{r} (radial), θ (azimuthal) and \bar{z} (vertical) directions, respectively. \bar{p} is the pressure. ρ is the fluid density, and ν is the kinematic viscosity of the fluid. ρ and ν are parameters of the fluid, so they are not barred. g is the gravity acceleration.

For the axisymmetric laminar flow, $\bar{v}=0$ and $\partial/\partial\theta=0$, so the above laminar boundary layer equations become

$$\frac{\partial\bar{u}}{\partial\bar{r}} + \frac{\bar{u}}{\bar{r}} + \frac{\partial\bar{w}}{\partial\bar{z}} = 0, \quad (1.2.2a)$$

$$\bar{u} \frac{\partial\bar{u}}{\partial\bar{r}} + \bar{w} \frac{\partial\bar{u}}{\partial\bar{z}} = -\frac{1}{\rho} \frac{\partial\bar{p}}{\partial\bar{r}} + \nu \frac{\partial^2\bar{u}}{\partial\bar{z}^2}, \quad (1.2.2b)$$

$$-\frac{1}{\rho} \frac{\partial\bar{p}}{\partial\bar{z}} + g = 0. \quad (1.2.2c)$$

Figure 1-4a illustrates the schematic description of the boundary layer formed on a flat plate, showing the velocity distribution within this thin layer. It is observed that the velocity within the boundary layer increases continuously from zero at the solid surface toward the outer velocity. However, there is no distinct border between the boundary layer and the outer inviscid layer. To define the thickness of the boundary layer δ , a criterion has been established. The boundary layer thickness is artificially defined as the distance from the solid surface to the point where the velocity reaches 99% of the outer velocity or free stream velocity (Schlichting & Gersten 2000). In addition, the flow within the boundary layer can undergo separation, and experiences reverse flow, which is shown in Figure 1-4b. In this case, a significant thickening of the boundary layer occurs, as the presence of backflow in the vicinity of the plate. The occurrence of separation is determined by the condition that the velocity gradient perpendicular to the wall becomes zero at the wall $(\partial\bar{u}/\partial\bar{z})_{\bar{z}=0} = 0$ (Schlichting & Gersten 2000).

As indicated above, the general boundary layer is bound by the fluid in the inviscid layer and the solid. However, the thin-film theory specifically focuses on the dynamics of a thin liquid layer flowing over a solid surface, where a distinct liquid-air interface is present. This is known as the free-surface thin-film flow, as schematically depicted in Figure 1-4c. Within the thin-film flow, the velocity distribution exhibits characteristics akin to those observed in boundary layers. The velocity gradient and shear stress near the free surface are negligible, as the viscosity of the air is much lower compared with the viscosity of the

liquid. At the liquid-air interface, a pressure boundary condition is typically imposed, taking into account the air pressure (and surface tension when substantial surface curvature is present). In the present thesis, the theoretical analysis heavily relies on the assumptions inherent in the boundary-layer equations and the thin-film theory.

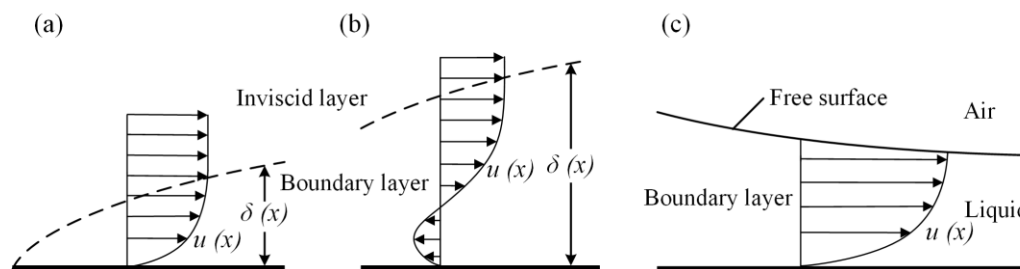


Figure 1-4: A schematic illustration of (a) the boundary layer, (b) the boundary layer separation and (c) the thin-film flow.

1.2.2 The Kármán–Pohlhausen approach for a Newtonian fluid

The Kármán–Pohlhausen (K–P) approach is a well-established and widely used method for solving boundary layer equations in fluid dynamics. The K–P approach is initially introduced by Kármán (1921) and Pohlhausen (1921), and it provides a practical and efficient way to approximate the velocity profile within the boundary layer.

One important aspect of the boundary layer equation (1.2.2) is that the partial derivatives with respect to the radial coordinate are of the first order. This is due to the fact that high velocity (Reynolds number), results in a one-way problem, implying only one boundary condition is required in the streamwise (radial) direction. In the absence of transverse (vertical) pressure gradients, an exact solution for the boundary layer equations is attainable (Watson 1964; Schlichting & Gersten 2000). However, the presence of hydrostatic pressure renders an exact solution impractical, as the problem is weakly elliptic (Bowles & Smith 1992; Higuera 1994; Bowles 1995).

Consequently, the K–P approach, known for its effectiveness and accuracy (Schlichting & Gersten 2000), is adopted. The procedures involve integrating the boundary layer equations between the solid surface and the upper edge of the boundary layer or the free surface, and approximating the velocity profile with a parabolic or cubic velocity profile which satisfies

the physic boundary condition and the conservation of mass. The approximation of the velocity profile with a parabolic or cubic velocity profile is quite accurate, which is illustrated in figure 1-5, in which the parabolic and cubic velocity profiles are compared against the exact similarity solution of Watson (1964) for a thin-film flow. The parabolic and cubic velocity profiles (normalized by the surface velocity) are

$$\frac{u}{U} = 2\eta - \eta^2, \quad \frac{u}{U} = \frac{3}{2}\eta - \frac{1}{2}\eta^3, \quad (1.2.3a, b)$$

respectively. Here, u is the radial velocity, U is the surface velocity, and $\eta = z/h$, in which h is the film height. The velocity profiles are obtained by satisfying the no-slip condition at the solid, the no-shear condition at the free surface, and $u/U = 1$ at the free surface.

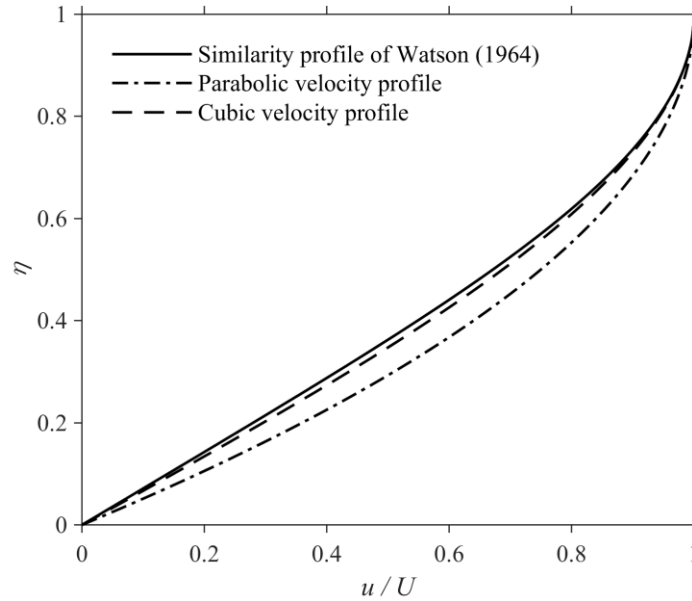


Figure 1-5: Comparison of Watson's (1964) similarity velocity profile against the parabolic and cubic velocity profiles for a thin-film flow.

A depth-averaged model can be obtained by integrating the original boundary equations between the solid plate and the upper edge of the boundary layer or the free surface. By adopting an approximation for the velocity profile (normally parabolic or cubic velocity profile) which satisfies the physic boundary condition and the conservation of mass, the

boundary-layer thickness, film thickness and wall shear stress can be obtained from the depth-average model.

In a formal numerical method, discretization (and meshing) in both the streamwise and the transverse directions are required. However, the K-P approach eliminates the need for vertical discretization by imposing a specific velocity distribution profile. This approximation for the velocity profile replaces the need for vertical meshing with a single layer of mesh cells with variable heights of each control volume. The solution is then obtained through integration in the horizontal direction, which either admits an analytical solution or can be accurately obtained with a high-order Runge-Kutta method.

1.2.3 Herschel-Bulkley constitutive model and its influence on the methodologies

Unlike Newtonian fluids, such as water and mineral oils, which follow the fundamental rheological equations described by Newton's law of viscosity and maintain a constant viscosity regardless of the applied shear rate, there are numerous fluids in our daily lives and of industrial significance that are non-Newtonian fluids. The viscoplastic fluid is one type of non-Newtonian fluid and exhibits flow properties intermediate between those of a solid and a liquid. There is a threshold stress, known as yield stress, that is required for the fluid to flow. If the applied stress is below this threshold, the fluid behaves like an ideal rigid solid. However, the fluid exhibits viscous features if the applied stress surpassed the yield stress (Bird *et al.* 1983). Viscoplastic fluid encompasses a wide range of materials including concentrated suspensions, pastes, emulsions, foams, composites, grease, polymer solutions, paints, glues and coal-oil slurries (Bird *et al.* 1983; Utracki 1988; Nguyen & Boger 1992; Ancy 2007; de Souza Mendes 2009; Mullai Venthan *et al.* 2022). Some examples that people can observe in daily life are shown in figure 1-6.

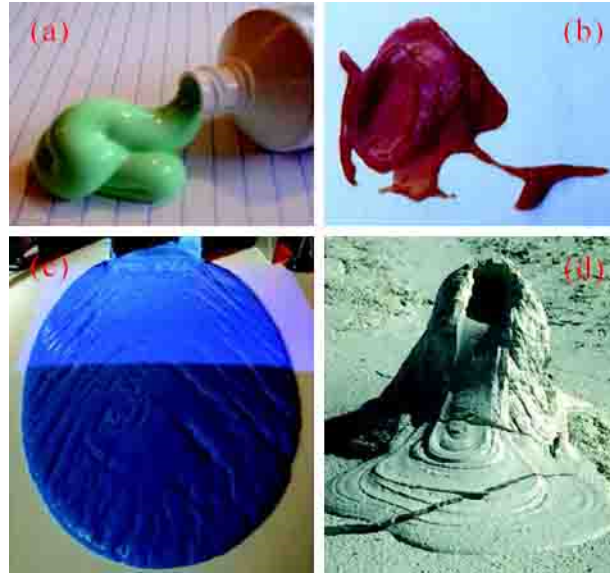


Figure 1-6: Some viscoplastic materials in different flow configurations. (a) A collapsed extrusion of toothpaste (Kamrin & Mahadevan 2012), (b) a ketchup splatter (Luu & Forterre 2009), (c) a dambreak of blue-coloured Carbopol on an incline (Cochard & Ancey 2008), and (d) a mud volcano (Photograph from the USGS).

There are several different constitutive models that can describe the behaviour of viscoplastic materials, such as the Bingham model, the Herschel-Bulkley model and the Casson model. Among them, the Herschel-Bulkley model may be the most widely used model, which is written as (Bird *et al.* 1983)

$$\tau_{ij} = \left(K\dot{\gamma}^{n-1} + \frac{\tau_0}{\dot{\gamma}} \right) \dot{\gamma}_{ij}, \quad \text{for } \tau \geq \tau_0, \quad (1.2.4a)$$

$$\dot{\gamma}_{ij} = 0, \quad \text{for } \tau < \tau_0, \quad (1.2.4b)$$

where τ_{ij} is the excess stress tensor, and $\dot{\gamma}_{ij}$ is the rate-of-strain tensor. Here,

$$\tau = \sqrt{\frac{1}{2} \tau_{jk} \tau_{jk}} \quad \text{and} \quad \dot{\gamma} = \sqrt{\frac{1}{2} \dot{\gamma}_{jk} \dot{\gamma}_{jk}}$$

are the second invariants of τ_{ij} and $\dot{\gamma}_{ij}$, respectively.

τ_0 is the yield stress, K is the consistency, and n is the power-law index. This model also includes the Bingham, power-law and Newtonian models, in the limits $n = 1$ and $B = 0$,

respectively. Also, for $n \leq 1$ the Herschel-Bulkley fluid is shear thinning, and for $n > 1$ it is shear thickening above a certain shear rate. A schematic illustration of Newtonian and viscoplastic fluids is given in figure 1-7. Some typical rheological parameters for shear-thinning and shear-thickening viscoplastic fluids, as well as the Bingham fluid, are presented in Table 1.

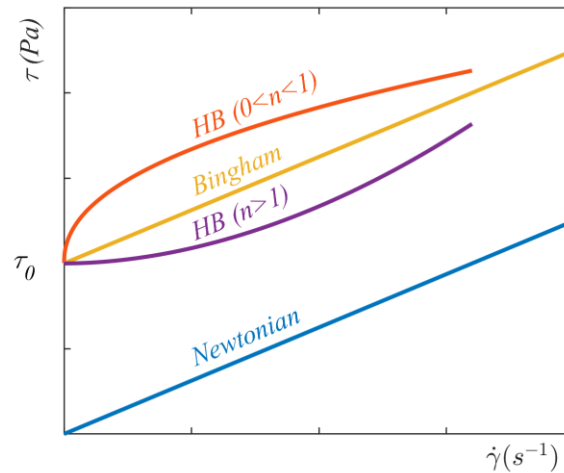


Figure 1-7: A schematic illustration of the stress-strain rate relationship for Newtonian and viscoplastic fluids.

Table 1: Typical rheological parameters for different viscoplastic fluids.

Constants	Carbopol/water solution		Silicic lava	Fresh concrete
Density, ρ ($\text{kg}\cdot\text{m}^{-3}$)	1000	1000	2600	~2400
Yield stress, τ_0 (Pa)	5.03	8.03	10^5	54.655
Consistency, K ($\text{Pa}\cdot\text{s}^n$)	2.455	7.18	10^9	64.688
Power-law index, n	0.437	0.418	1	1.193
The data for Carbopol/water solution are taken from Jalaal <i>et al.</i> (2021) and Chambon <i>et al.</i> (2014), the data for Silicic lava is taken from Griths & Fink (1993), McBirney & Murase (1984), Shaw (1969), and the data for fresh concrete are from Wang <i>et al.</i> (2022). One can also refer to Fiorot & Maciel (2019) for more viscoplastic materials.				

Due to the influence of yield stress and shear-rate-dependent viscosity, it can be observed that the stress tensor of a viscoplastic fluid of the Heschel-Bulkley type is different from that of a Newtonian fluid. Hence, the boundary layer equation would be different from (1.2.1) and (1.2.2). In this scenario, the boundary layer equations of a viscoplastic fluid for an axisymmetric flow are

$$\frac{\partial \bar{u}}{\partial \bar{r}} + \frac{\bar{u}}{\bar{r}} + \frac{\partial \bar{w}}{\partial \bar{z}} = 0, \quad (1.2.5a)$$

$$\bar{u} \frac{\partial \bar{u}}{\partial \bar{r}} + \bar{w} \frac{\partial \bar{u}}{\partial \bar{z}} = -\frac{1}{\rho} \frac{\partial \bar{p}}{\partial \bar{r}} + \frac{\partial}{\partial \bar{z}} \bar{\tau}_{rz}, \quad (1.2.5b)$$

$$-\frac{1}{\rho} \frac{\partial \bar{p}}{\partial \bar{z}} + g = 0, \quad (1.2.5c)$$

where

$$\tau_{rz} = \left(K |u_z|^n + \tau_0 \right) \text{sgn}(u_z), \quad \text{for } |\tau_{rz}| \geq \tau_0, \quad (1.2.6a)$$

$$u_z = 0, \quad \text{for } |\tau_{rz}| < \tau_0. \quad (1.2.6b)$$

Clearly, when $n = 1$ and $\tau_0 = 0$, the Newtonian limit (1.2.2) is recovered. Due to the yield stress of the fluid, the flow of a free surface flow includes a fully-yielded layer and a pseudo-plug layer. As illustrated in figure 1-8, a fake yield surface exist at $z = h_0$. A lower layer of fluid for $0 < z < h_0$ is the fully-yielded layer where the radial velocity has a parabolic-like profile. In the region $h_0 < z < h$, the radial velocity becomes plug-like and independent of z to leading order when considering the asymptotic flow field expansion in powers of the film thickness-to-length ratio (Walton & Bittlest 1991; Balmforth & Craster 1999). This difference in velocity profile is one of the fundamental differences between the flow of a Newtonian fluid and a viscoplastic fluid (see figure 1-4c for comparison).

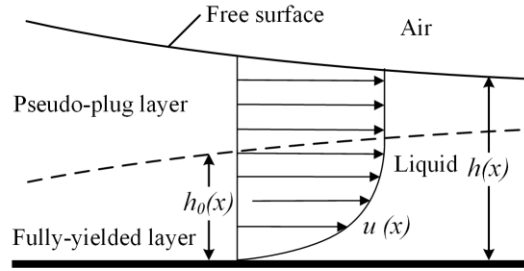


Figure 1-8: A schematic illustration of the thin-film flow for a viscoplastic fluid.

The K-P approach is also suitable for the flow of a viscoplastic fluid, and has been widely used in previous investigations (Jiang & LeBlond; Liu & Mei 1994). However, in contrast to the parabolic or cubic velocity profiles adopted in equation (1.2.3), it is customary to use to velocity profile motivated by both the equilibrium uniform flow and the lubrication approximations (Balmforth & Liu 2004). In this case, the velocity profile in the pseudo-plug layer is

$$\frac{u}{U} = 1 - (1 - \eta)^{(n+1)/n}, \quad (1.2.7)$$

which satisfies the no-slip condition at the solid, no-shear at the fake yield surface, and continuous velocity at the fake yield surface. Here, U is the velocity in the pseudo-plug layer, and $\eta = z/h_0$. Clearly, (1.2.7) collapses onto the parabolic velocity profile (1.2.3a) for a Newtonian fluid when $n = 1$.

1.3 Literature review

Extensive investigations have been dedicated to the flow of impinging jet and hydraulic jump phenomena. In this case, prior research regarding this area is discussed, aligning with the primary objectives of the present thesis.

1.3.1 The hydrodynamics of the impinging jet and circular continuous jump

As indicated earlier, the first theoretical work on a two-dimensional hydraulic jump was conducted by Rayleigh (1914) by using an inviscid assumption. Later, Birkhoff & Zarantonello (1957) examined the circular hydraulic jump formed on a flat disk when a

vertical jet impinges on this disk. Similarly, the inviscid theory was utilized in their investigation. Clearly, the inviscid theory can lead to inaccuracy, especially in situations when the influence of viscosity is important. To overcome this drawback, Watson (1964) considered the influence of viscosity on the flow upstream of the jump. Specifically, Watson (1964) analysed the flow in the developing-boundary layer near impingement with the K-P approach, and the fully-viscous layer upstream of the jump by using a similarity transformation method. Since the flow in the supercritical region is thin and largely inertia dominant, the influence of gravity was neglected in this region. The jump profile was assumed as a shock, and the location of the hydraulic jump was determined by utilizing force and momentum balance equations, assuming a known uniform film height in the subcritical region given the slow motion of the flow. Watson's thin-film approach became the basis for numerous later theoretical and experimental studies.

Watson's (1964) theory was tested against his own experiments, showing a reasonable agreement between his theory and experiments. The discrepancy between the theory and experiments was attributed to the neglect of the width of the jump. The experiments conducted by Azuma & Hoshino (1984a, b) demonstrated the validity of Watson's (1964) theory in the supercritical region. When the flow is laminar and the liquid surface remains smooth, Watson's (1964) theory accurately captured the height profile measured in Azuma & Hoshino (1984a). In addition, the measured surface velocity in the experiments of Azuma & Hoshino (1984b) also agrees closely with Watson's (1964) theory in the fully viscous region. As for predicting the jump radius, Watson's (1964) theory was also tested against experiments of Craik *et al.* (1981), Errico (1986), Stevens & Webb (1992), Bush & Aristoff (2003) and Baonga *et al.* (2006). These experimental investigations demonstrated that Watson's (1964) theory works well for a relatively large jump radius. However, Liu & Lienhard (1993) observed that Watson's predictions were least satisfactory in the limit of a relatively weak jump (of large width). In this case, the effects of surface tension become important, which motivated Bush & Aristoff (2003) to include the effects of surface tension in the force and momentum balance equation, leading to better agreement with the experiment.

Both the theory of Watson (1964) and the corrected theory by Bush & Aristoff (2003) assumed a uniform inviscid downstream flow, as the knowledge of the flow immediately downstream of the jump is required to determine the jump radius through the force and momentum balance equation. Clearly, this assumption is reasonable when an obstacle is amounted at the disk edge as have done in the experiments of Watson (1964) and Bush & Aristoff (2003), especially for a relatively high obstacle. However, a uniform flow assumption in the downstream region is inadequate, if the flow on the flat disk can drain freely at the disk edge. Especially, the flow characteristics in the subcritical region cannot be reflected through this uniform flow assumption. To capture the behaviour downstream of the jump for a free draining scenario, Duchesne *et al.* (2014) examined the downstream flow using the lubrication approach, given the flow in the subcritical region is largely inertialess and gravity driven. A good agreement between their theoretical predictions and their measurements for the height profile was obtained. Later, Wang & Khayat (2018) incorporated Watson's (1964) theory in the supercritical region and lubrication approach in the subcritical region to investigate the impinging jet flow and hydraulic jump on a rotation disk. The jump radius is still determined through the force and momentum balance equation.

Although the aforementioned theories can generate reasonable results for the flow field and jump radius, they cannot capture the flow in the vicinity of the jump accurately. Furthermore, the underlying cause of the hydraulic jump is not explored in these theories. In this case, another branch of studies can better address these issues and initially began from the theoretical work of Tani (1949). In contrast to the theoretical work of Watson (1964), Tani (1949) retained the hydrostatic pressure term in the momentum equation. By averaging the momentum equation in the vertical direction, and assuming a self-similar parabolic velocity profile, Tani (1949) derived an ordinary differential equation for the film height, indicating a single spiral critical point. The hydraulic jump is believed to occur due to separation induced by the increasing pressure gradient before reaching the infinite slope of the film height, explaining the abrupt thickening of the film (Tani 1949). This approach was adopted by Bohr *et al.* (1993) and used in both super- and sub-critical regions. By connecting the solution in both regions through a shock, they found that the jump location

is close to $r = 1$ in their notation, suggesting that the jump radius as $Q^{5/8} \nu^{-3/8} g^{-1/8}$, where Q is the flow rate, ν is the kinematic viscosity and g is the gravity acceleration. The constant of this scaling law depends on the velocity profile and is 0.73 for a self-similar parabolic velocity profile. It is obvious that this scaling law does not take the influence of disk radius into account, as it was found that the disk size only has an extremely weak influence on the jump radius (Bohr *et al.* 1993). The scaling law can generally capture the trend of the jump radius, but the discrepancy between this scaling law and experiments can arise in some situations (Duchesne *et al.* 2014). Kasimov (2008) also utilized a similar approach to that of Bohr *et al.* (1993), and incorporated the curvature of the plate at the disk edge and added the surface tension effect at the jump level. However, a boundary condition was arbitrarily imposed at a location slightly larger than the jet radius in Kasimov (2008). Wang & Khayat (2019) developed the theories of Watson (1964) and Bohr *et al.* (1993) by incorporating the gravity term in both the developing boundary layer and fully viscous layer regions. In this case, the problem can be solved from the impinging point, and no empirical initial conditions are needed. The jump location is assumed to coincide with the singularity of the resulting ordinary differential equation for film height. The result of their theoretical results yields good agreement with the experimental data for high-viscosity fluids.

Later, to capture the profile and flow feature at the jump, Bohr *et al.* (1997) and Watanabe *et al.* (2003) accounted for the additional gravity effect by adopting a non-self-similar cubic velocity profile, which includes a shape parameter and satisfies the momentum equation at the disk. The presence of the additional shape parameter in the assumed velocity profile prevents the formation of the critical point and the singularity of the averaged first-order differential equation. The resulting second-order differential equation enables them to cross the jump smoothly (in contrast to a shock-like jump profile obtained through momentum balance equation), and capture the flow features more accurately at the jump. However, two experiments point which lies immediately up- and down-stream of the jump are needed in their solution to fix the boundary conditions. Clearly, their method required some prior knowledge about the jump location. In this regard, even though their theory showed good agreement with the earlier measurements of Bohr *et al.* (1996), it remains somewhat semi-empirical. A similar approach was later adopted by Bonn, Andersen &

Bohr (2009) to study the hydraulic jump in a channel. However, results showing jump-like profiles were only presented to describe the vortex, whereas their comparison against measurements was limited to the simplified (first-order) version of the model in which the jump was treated as an abrupt shock connecting an inner and an outer solution.

As mentioned earlier, the happening of hydraulic jumps has been attributed to boundary layer separation caused by an increase in hydrostatic pressure (Tani 1949). To gain further insight into the underlying cause of the hydraulic jump, Gajjar & Smith (1983) examined the flow behaviour in a uniform velocity layer with a thin viscous sublayer at its bottom in the limit of a large Reynolds number. Their investigation revealed that the jump is the result of a viscous-inviscid interaction, and showed that it is only in a viscous sub-sublayer near the wall where the flow reacts to the reverse hydrostatic pressure gradient and separates from the wall. Bowles (1995) examined the free-interaction problem of the planar flow of a sloped liquid layer over an obstacle, in which he described the internal structure of the continuous jump as dominated by the viscous-inviscid interaction between the hydrostatic pressure gradient and the viscous effects near the solid wall (see also the earlier work of Gajjar & Smith (1983) and the dissertation of Bowles (1990)). As Bowles (1995) observes, the free interaction in the internal jump structure involves one of two types of mechanism, depending on the pressure development: “The pressure may increase, possibly leading to separation (a compressive interaction) or it may decrease, leading perhaps to a finite-distance singularity in the solution (an expansive interaction).” Higuera (1994) solved the boundary-layer equations numerically to generate the jump profile for two-dimensional flow. The boundary condition near the disk edge was fixed by matching the downstream flow with the flow at the edge of the plate.

Since the pioneering works of Watson (1964) and Tani (1949), numerous experimental, theoretical and numerical investigations have been contributed to the study of circular hydraulic jump, covering many aspects of the characteristics of hydraulic jump. The influence of flow rate has been examined extensively in previous studies. Craik *et al.* (1981) conducted experimental investigations to examine the instability of the circular hydraulic jump. In their study, a circular water jet impinges into a rectangular tank equipped with outlets at its corners. Their observations revealed that the instability

occurred when the local Reynolds number at the leading edge of the hydraulic jump exceeded a critical value. Before the onset of oscillatory instability, experimental measurements suggested that the jump radius increases with the flow rate, but agreeing poorly with the prediction of Watson's (1964) theory. Additionally, their measurements demonstrated that the length of the recirculation zone near the bottom of the tank increased with increasing flow rate, reaching a maximum at a specific flow rate. However, as the flow rate further increased, the recirculation zone diminished, and oscillatory instability showed. Similarly, Rao & Arakeri (2001) also investigated the influence of the flow rate on various characteristics of the flow and jump using a circular flat disk without any restriction at its edge. They observed that the measured jump radius also increases with the flow rate and agrees closely with the scaling law of Bohr *et al.* (1993). As for the maximum film height in the subcritical region, their measured film profile showed distinct behaviour depending on the disk size. For a larger disk size, the maximum film height exhibited a monotonic increase with the flow rate. However, for a relatively smaller disk size, it exhibited a non-monotonic trend, increasing initially within a smaller range of flow rates and then decreasing as the flow rate exceeded a certain threshold, reaching a maximum at a certain flow rate. In contrast to the observation of Craik *et al.* (1981) for flow separation, the experiments of Rao & Arakeri (2001) indicated that the separation length increases monotonically with the increase of flow rate. They attributed this observation to the influence of a fast-moving fluid flowing over the recirculation zone, thereby elongating the separation bubble. Hansen *et al.* (1997) also conducted experimental studies on the influence of flow rate by using fluids of different viscosity for a disk without any obstacle at the disk edge. In their experiments, they found that the jump radius follows a power law $r_j \sim Q^b$, where r_j is the jump radius, Q is the flow rate and b is the power law index, with $b \approx 0.77$ for water, and $b \approx 0.72$ for the oil with viscosity $\nu = 15$ cSt. In addition, they observed that the film height immediately downstream of the jump is almost constant, and only decreases abruptly at the edge of the disk. Duchesne *et al.* (2014) examined the influence of flow rate on a disk without any barrier at the disk edge. Their measurements revealed different features for the maximum film height immediately downstream of the jump from the observation of Hansen *et al.* (1997), suggesting that the maximum film height increases monotonically with the flow rate. Interestingly, they found that the local

Froude number immediately downstream of the jump is essentially a constant. Based on this observation, they proposed a scaling law which can fit their experimental data better than the scaling law of Bohr *et al.* (1993). This scaling law also takes into account the influence of disk radius, showing a weak dependence on the disk size.

The influence of viscosity on the jump radius has been examined in the experimental works of Hansen *et al.* (1997) and Duchesne *et al.* (2014), they observed that higher viscosity of the fluid leads to a smaller jump radius. In addition, Hansen *et al.* (1997) found that the hydraulic jump is more stable for a higher-viscosity fluid. A more comprehensive numerical study was conducted by Passandideh-Fard *et al.* (2011) using the volume-of-fluid method. The influence of flow rate, viscosity, gravity, and the height of the obstacle placed at the disk edge on the jump radius were explored in their simulations. In their work, the film thickness at the disk edge was controlled by placing an obstacle at the disk edge. Their numerical results suggested that the jump radius is in agreement with the scaling law of Bohr *et al.* (1993) when the viscosity of the fluid is varied. To understand the role of gravity in the formation of circular hydraulic jumps, Askarizadeh *et al.* (2019) conducted thorough numerical investigations under different conditions. Their results indicated that there are two regimes in the jump formation: gravity- and capillary-dominant flow regimes. Their results led them to conclude that the presence of gravity remains an essential factor in the formation of both developing and developed hydraulic jumps, and its influence cannot be disregarded. Furthermore, when considering varying viscosity, they observed a decrease in the jump radius with increasing viscosity, not only for developed hydraulic jumps but also for developing jumps. Fernandez-Feria *et al.* (2019) also observed a similar pattern in the simulations regarding the influence of viscosity on the jump radius. However, despite extensive examination of the influence of viscosity on the jump radius, the relationship with film profile, the jump length (the distance between the leading and the trailing edge of the jump) and the existence of vortex have not been extensively explored in these works.

Avedisian & Zhao (2000) examined the effects of the lower gravity on the jump radius and downstream flow features by conducting experiments in a drop tower with water as the working fluid. They observed that the jump was pushed towards the disk edge and the jump

profile becomes smoother (a larger jump length) as the gravity level decreased. In addition, it is easier to observe waves in the subcritical region for the lower gravity condition. The numerical simulation works of Fernandez-Feria *et al.* (2019) and Askarizadeh *et al.* (2019) also explored the influence of gravity, they found similar patterns for the jump radius, but no wave observations are reported in their studies.

1.3.2 The influence of azimuthally varying edge conditions on the hydraulic jump

Although extensive work in the literature has been devoted to understanding circular hydraulic jump, the investigation of the formation and structure of the non-circular jump is relatively recent, focusing essentially on the spontaneous destabilization of the circular jump and the onset of the stable non-circular jump.

Stationary polygonal jumps were first observed by Ellegaard *et al.* (1998) in their experiments. They utilized ethylene glycol as the working fluid and varied the film height in the subcritical region by adjusting the height of an obstacle mounted at the disk edge. They observed the type Ia jump when the film thickness in the subcritical region is small. In this case, the surface velocity flows outward everywhere, and a separation bubble forms near the solid disk under the jump. As the film thickness in the subcritical region increases, the jump becomes steeper (jump length becomes smaller). When the film height in the subcritical region exceeded a critical value, a notable transition occurred: the surface velocity immediately downstream of the jump changed from outward flow to inward flow, leading to the appearance of a polygonal hydraulic jump. They observed that the number of sides (mode number) of the polygonal jump increases with the downstream flow height first, then this number decreases by one side at a time when the downstream flow height increases further. They observed a hysteresis effect as several polygons could be stable for the same flow parameters, accompanied by a flow spiralling towards the corner. Bush *et al.* (2006) carried out a parametric study on steady polygonal jumps and the flow structure, using a similar apparatus as Ellegaard *et al.* (1998) and glycerol-water solutions and pure mineral oil as the working fluids. They reported a new class of steady two-tiered, Type IIb, asymmetric jump forms, with vortices adjoining the jump, resembling cat's eyes, three- and four-leaf clovers, bowties and butterflies. Bush *et al.* (2006) also examined the

influence of surface tension on the polygonal hydraulic jump structure. By adding a surfactant, they noticed that the polygonal jump relaxes into a circular form, and expands slightly. They compared their measurements of the jump radius with the earlier theoretical predictions of Bush & Aristoff (2003), which is a theory suitable for predicting the jump radius for circular hydraulic jump, and found that the agreement was not as close as in the case of axisymmetric flow. They attributed the discrepancy to the neglect of the influence of dynamic pressure downstream of the jump. They suggested that the symmetry-breaking mechanism behind the onset of the non-circular jump probably results from a capillary instability of the circular jump, and proposed an empirical equation for the instability wavelength of steady non-circular jumps.

Steady polygonal hydraulic jumps were theoretically examined through a phenomenological model proposed by Martens *et al.* (2012). They found that a polygonal jump emerges with a wavelength in the order of the roller width based on the Rayleigh-Plateau instability. In their model, a dimensionless equation for predicting the number of polygonal hydraulic jump corners was presented based on mass conservation and radial force balance between the hydrostatic pressure and viscous stresses on the roller surface. The surface tension effect was neglected as the free surface profile of the jump and the curvatures could not be accurately modelled. They also reported that the outer line of the vortices adjoining the jump is circular, suggesting the azimuthal flow observed downstream of the jump only exists in this circular region. The measured height profiles indicate that the downstream height at the corner is higher than at the valley, although the heights far downstream are almost the same for these two directions. They also observed that the flow upstream of the jump is purely radial and independent of azimuthal direction, and the measured height profile at the corner and valley directions for the upstream of the jump region are the same. These observations corroborate the earlier findings of Bush *et al.* (2006).

Steady polygonal hydraulic jumps were also investigated experimentally extensively by Teymourash & Mokhlesi (2015) who used a similar apparatus to that of Ellegaard *et al.* (1998) with ethylene glycol as the working fluid. They explored the region of stability for polygonal jumps and the dependence of this region on the flow parameters by varying the

obstacle height, nozzle diameter and flow rate. They reported a rotational wave encompassing the whole Type II circular jump with only one continuous surface vortex. In addition, rotational polygonal hydraulic jumps with a constant angular velocity were also observed in their experiments. The comparison between experimental data of both stable and rotational polygonal jumps and theoretical prediction by using the circular hydraulic jump theory of Bush *et al.* (2006) revealed a clear discrepancy, especially for the rotational jumps.

Of closer relevance to the present thesis are the studies on the hydraulic jump on a non-circular disk, which was examined both experimentally and numerically (Ferreira *et al.* 2002; Asadi *et al.* 2020; Nichols & Bostwick 2020; Esmaeeli & Passandideh-Fard 2020). A numerical investigation of a circular jet impinging on a square disk mounted on a square obstacle was examined by Ferreira *et al.* (2002). They implemented different upwind schemes for the convection term of the Navier-Stokes equations, and found that the shape of the hydraulic jump on the square disk was almost perfectly circular or square depending on the scheme used, implying the asymmetry of the disk may or may not affect the shape of the jump. They attributed the departure from the circular shape to the effect of grid orientation. Asadi *et al.* (2020) examined the influence of the downstream obstacle geometry and parameters such as the flow rate, the jet diameter and the downstream obstacle height on the stability range of the circular jump. Three glass obstacle shapes were used, namely, a circle, a square, and a triangle, which were placed on the target circular glass plate. Asadi *et al.* (2020) stated that the axisymmetric theory could not predict the location of the jump for cases with an obstacle, as the jump is of Type IIb.

1.3.3 The viscoplastic circular hydraulic jump

In the studies mentioned earlier, the working fluids in the experimental, numerical and theoretical works are Newtonian. However, many fluids of industrial significance are viscoplastic fluids, and the rheology of these fluids can significantly change the behaviour of related flow phenomena. The existence of the yield stress in a viscoplastic fluid can significantly change the flow structure compared to the counterpart of a Newtonian fluid. More explicitly, a viscoplastic flow exhibits a yield surface, which separates the fully yielded layer from the plug layer.

Bird *et al.* (1983) examined a unidirectional flow of a Bingham fluid between two fixed parallel plates driven by a fixed pressure gradient (Poiseuille flow). The channel had a length of L in the horizontal direction (x -axis) and a width of $2h$ in the vertical direction (z -axis), with the origin located in the middle of two plates. The flow is unidirectional in the horizontal direction, $u = u(z)$, and the constant pressure gradient is $dp/dx = (P_L - P_0)/L$, in which P_0 and P_L are the pressure at $x = 0$ and L , respectively. The continuity equation is already satisfied, and the simplified momentum equation is $dp/dx = d\tau_{xz}/dz$. Recalling the constitutive model (1.2.4), only the shear stress τ_{xz} survives in the current problem and $n = 1$ for a Bingham fluid, so $\tau_{xz} = (K|u_z| + \tau_0)\text{sgn}(u_z)$ for $\tau_{xz} \geq \tau_0$, and $u_z = 0$ for $\tau_{xz} < \tau_0$. In addition, the no-slip boundary condition must be satisfied at the surface of both plates, $u(x, z = -h) = u(x, z = h) = 0$. Because of the symmetry of the problem $u_z(x, z = 0) = 0$, it is sufficient to solve for the solution in the upper part of the channel only ($0 < z < h$). By integrating the momentum equation once between 0 and h and using the symmetric condition at $z = 0$, one finds that the yield surface, at which $\tau_{xz} = \tau_0$, is located at $z = h_0 = \tau_0 L / (P_0 - P_L)$. By integrating the momentum equation twice, using the constitutive model, and no-slip and symmetric conditions, the velocity in the yielded layer

is $u(x, h_0 \leq z \leq h) = \frac{(P_0 - P_L)h^2}{2KL} \left(1 - \frac{z^2}{h^2}\right) - \frac{\tau_0 h}{K} \left(1 - \frac{z}{h}\right)$, and the velocity in the plug layer

is $u(x, 0 \leq z \leq h_0) = \frac{(P_0 - P_L)h^2}{2KL} \left(1 - \frac{h_0^2}{h^2}\right) - \frac{\tau_0 h}{K} \left(1 - \frac{z}{h}\right)$. Figure 1-9 schematically

illustrates the velocity profile of a Bingham fluid for Poiseuille flow. Clearly, a yield surface exists for a Bingham fluid, which divides the flow into two regions: the yielded layer and the plug layer. The velocity in the plug layer is constant and independent of the horizontal variable.

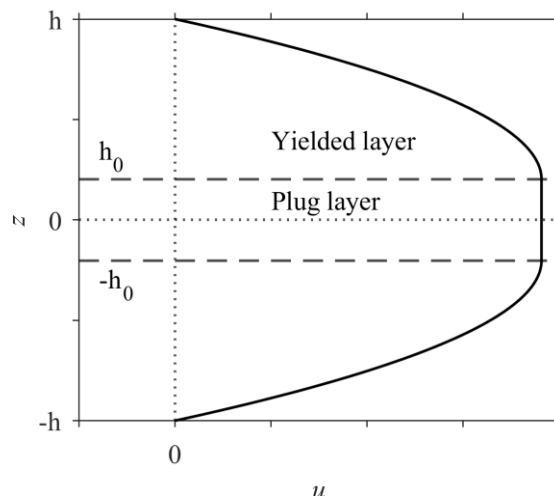


Figure 1-9: A schematic illustration of the velocity profile of Bingham fluid for a Poiseuille flow.

However, the plug flow is generally not a true plug, but a pseudo-plug flow. This character was first recognized by Walton & Bittleston (1991), who examined analytically and numerically the flow of a Bingham fluid in an eccentric annulus. By assuming the ratio of the variation of the gap between two cylinders to the mean radius is much smaller than 1 ($\varepsilon \ll 1$), they conducted an asymptotic expansion in powers of ε . Their solution suggested that the velocity in some parts of the plug layer varies around the annulus and the stress exceeds the yield stress, contrasting with the plug flow observed in the 2-D channel flow (Bird *et al.* 1983); velocity is a constant and independent of the horizontal variable. Later, Balmforth & Craster (1999) also employed an asymptotic expansion in powers of ε (where ε is the ratio of the characteristic thickness of the layer to the horizontal length scale) to investigate a flow of Bingham fluid down an inclined plate by using lubrication approach. Their solution revealed that the flow within the plug layer is weakly yielded at higher order in ε , despite appearing as a plug at the leading order solution. In this case, they identified the plug layer in this context as a pseudo-plug layer, and the yield surface which separates the fully yielded layer and pseudo-plug layer should be a fake yield surface. This feature was further examined by Liu, Balmforth & Hormozi (2019) in their theoretical and numerical studies of the inertialess viscoplastic flow of the Herschel-Bulkley type flows down an inclined surface. In their study, they improved the lubrication theory by incorporating higher-order terms in ε . This improved model agrees closely with their

numerical simulations and agrees with the experimental observation of Chambon *et al.* (2009, 2014, 2017) to some extent. Moreover, their research also indicated that the rigid plug observed in the upstream uniform region is disrupted as the flow progresses downstream due to the extensional stress across the plug, giving rise to a weakly yielded layer, referred to as a pseudo-plug layer.

To the best of the author's knowledge, the influence of the rheology on an impinging jet of viscoplastic fluid and the resulting hydraulic jump has not been investigated. However, there are numerous studies that have examined the influence of yield stress and shear-rate dependence of the viscosity on the flow behaviour. Generally, the mobility of the viscoplastic fluid can be significantly reduced when the yield stress is large. In their numerical investigation on a finite mass of viscoplastic flow of Bingham type sliding down a slope under the water and the generated surface waves, Jiang & Leblond (1993) found that the extend and the velocity of the mudslide, as well as the amplitude of the resulting surface waves, decreased significantly due to the existence of yield stress. They also reported that the velocity of the pseudo-plug layer decreases with an increasing yield stress, and the front velocity is smaller for higher yield stress. In addition, the mudslide flow on the slope finally came to a halt when the wall shear stress falls below the yield stress. Similar feature on the influence of yield stress on the spreading distance or pseudo-plug layer velocity can also be observed in the spread of flow down an inclined plane (Huang & García 1998; Balmforth *et al.* 2002; Balmforth *et al.* 2007a) and on a shallow and wide curved channel (Mei & Yuhi 2001), the spread of a droplet on a prewetted horizontal plate (Jalaal *et al.* 2021), the flow inception following the release of a volume of fluid or dam-break flow (Matson & Hogg 2007; Liu *et al.* 2016, 2018), and the squeezing of a thin film (Koblitz, Lovett & Nikiforakis 2018; Muravleva 2019), no matter the fluid is of Bingham or Heschel-Bulkley type.

In contrast to the consistent influence of yield stress mentioned above, the influence of the shear-rate dependence of the viscosity on the spreading distance and film depth is more complex and less consistent compared to that of yield stress. In their study of mud flow down a slope, Huang & García (1998) found that a more shear-thinning fluid has a shorter spread distance and a thicker flow depth away from the wave front. They also observed

that the influence of shear thinning on the spreading distance diminishes as the yield stress rises. Balmforth *et al.* (2000) also reported the influence of the power-law viscosity and yield stress on the shape of a lava dome at a certain time, which is consistent with the finding of Huang & García (1998). In contrast, Liu *et al.* (2018) reported that the power-law viscosity has little effect on the final shape of the slump. Interestingly, the influence of the power-law index may not be consistent from one region to another of the flow. For instance, for squeeze film flow between two disks, the calculations of Muravleva (2019) show that, in the core region of the flow, the fully-yielded layer thickness as well as the second stress invariant at the disks decreases with increasing power-law index. The opposite is true near the edge of the disks. The influence of the power-law rheology was found to depend significantly on the level of yield stress. Although most viscoplastic fluids exhibit a shear-thinning character, some do possess a shear-thickening viscosity, such as concentrated diblock copolymer solutions (Bauer *et al.* 1995) and cement mixtures (Heirman *et al.* 2008,2009; Yahia 2011; Estelle & Lanos 2012).

To the best of the author's knowledge, there is not much investigation focused on the impinging jet of viscoplastic fluids and hydraulic jump, except for the investigations by Ogihara & Miyazawa (1994), Shu & Zhou (2006), Zhou *et al.* (2007) and Ugarelli & Federico (2007), for yield stress flow in a rectangular channel. Ogihara & Miyazawa (1994) conducted experimental investigations in a rectangular channel to analyze the impact of yield stress on flow behaviour and the occurrence of hydraulic jumps. The working fluid in their experiment is a mixture of water and bentonite, which can be regarded as a Bingham fluid. Their experiments showed that the critical depth increased dramatically when the relative yield stress exceeds 0.1 Pa. Shu & Zhou (2006), and Zhou *et al.* (2007) examined theoretically the planar hydraulic jump on a horizontal plate for a Bingham fluid (the two studies are essentially the same). They assumed a parabolic velocity profile for both the super- and sub-critical regions, which is motivated by the lubrication approximations. By using the mass and momentum balance equation across the jump, they derive an approximate expression for the conjugate depths. However, the flow field immediately upstream of the jump, including the pseudo-plug layer velocity, the film height and the wall shear stress, were simply assumed. They determined the flow immediately downstream of the jump by using the mass and force balance across the jump.

Moreover, the flow character in both the upstream and downstream regions of the jump was not examined. Later, Ugarelli & Federico (2007) used a similar approach, adopting the Herschel-Bulkley model. They evaluated the error, mainly stemming from neglecting viscous effects, introduced by the adoption of the approximate solution by solving the equations numerically.

Similar to the work of Newtonian fluid mentioned in the previous section, a thin-film approach and K-P approach have also been widely used for steady and transient flow problems involving thin layers of viscoplastic fluids. The depth-averaged approach was proposed to study the water waves generated by an underwater Bingham viscoplastic landslide on a gentle uniform slope by Jiang & Leblond (1993). The K-P approach was also employed by Liu & Mei (1994) to investigate the flow of a mud layer down a gentle slope, in an effort to understand the periodic shocks or roll waves that are caused by unstable disturbances of small amplitude. Later, the depth-averaged approach was adopted for a viscoplastic fluid of the Herschel-Bulkley type by Huang & García (1998), who examined the dynamics of the mud-slide problem, which was simplified to a 2D, unsteady, and low-Reynolds-number laminar flow. Generally, the K-P depth-averaged method is particularly suited for fast-moving free-surface flow problems, with non-negligible inertia (Ancey 2007). For slow-moving viscoplastic flow problems, the lubrication approach is utilized, as for the spread of lava (Balmforth & Craster 1999; Balmforth *et al.* 2000), the dam-break flow (Matson & Hogg 2007; Liu *et al.* 2016, 2018), and surges down an inclined surface (Liu *et al.* 2019).

1.4 Objectives and Outline of the Thesis

1.4.1 The objectives of the thesis

As mentioned in the previous sections, the main theory utilized in the studies of the circular hydraulic jump is Watson's (1964) theory or the corrected theory by Bush & Aristoff (2003), which assumes that the jump profile is shock-like. In this case, it is impossible to examine the flow structure at the jump. The model proposed by Bohr *et al.* (1996) and Watanabe *et al.* (2003) can cross the jump smoothly, but two experiment points near the leading and trailing edge of the jump are needed to fix the boundary conditions. To

overcome the drawbacks of the previous approaches, the thesis will propose a coherent composite approach, which does not need any empirically or numerically adjusted boundary conditions, for the continuous circular hydraulic jump. The influence of flow rate, viscosity and gravity on the jump location, film height profile and the vortex structure at the jump are investigated as well.

Bohr *et al.* (1993) proposed a scaling for the hydraulic jump radius, which did not take the influence of disk size into account. In contrast, Duchesne *et al.* (2014) established their scaling law by assuming that the Froude number (immediately downstream of the jump) based on the jump location and height (Fr_j) is constant, and their scaling law involves the disk radius. Clearly, their scaling law is therefore semi-empirical since the value of Fr_j must be imposed from the experiment. In the experimental works focusing on the circular hydraulic jump, different behaviour for the dependence of the maximum film height in the subcritical region on the flow rate for different fluids and different disk size was reported (Hansen *et al.* 1997; Rao & Arakeri 2001; Duchesne *et al.* 2014; Mohajer & Li 2015). Although many studies showed that the disk size has negligible influence on the disk radius (Bohr *et al.* 1993), the influence of the size of the disk has not been examined thoroughly. Experimental and numerical investigations showed that different types of hydraulic jumps would show if the thickness of the film at the disk edge increased (Ellegaard *et al.* 1998; Bush *et al.* 2006; Teymourash *et al.* 2016; Askarizadeh *et al.* 2019), but rarely theoretical work contributed to this aspect. The thickness at the disk edge is still largely an unaddressed problem, and there are two main approaches to determine the film height or equivalent conditions at the disk edge for a free-draining situation; imposing an infinite slope (Bohr *et al.* 1993; Kasimov 2008; Dhar *et al.* 2020), or assuming the edge thickness to be essentially equal to the capillary length (Duchesne *et al.* 2014; Ipatova *et al.* 2021; Duchesne & Limat 2022). As indicated in the experimental work of Duchesne *et al.* (2014), the edge film thickness also follows a weak power law dependence on the flow rate. However, this weak power law dependence feature was not examined fully. In addition, the existence and non-existence of jump and vortex under the jump also remain an unclear problem. Therefore, with the proposed coherent composite approach, the thesis will further investigate the characteristics of the continuous circular hydraulic jump, mainly focusing

on the effect of disk size, and film thickness at the disk edge on the flow features, as well as the interplay between flow rate and disk size. The existence and non-existence of the hydraulic jump and the vortex under the jump on the flow parameters will be explored.

Many experimental and numerical works illustrated that the azimuthal flow in the subcritical region showed when the circular hydraulic jump transformed into the polygonal hydraulic jump. However, Waston's (1694) theory or the improved one by Bush & Aristoff (2003) is still utilized to compare with the measured jump radius, which showed poor agreement between the measured and predicted jump radius. To accommodate the azimuthal velocity observed in the subcritical region, a model that includes the balance of mass and momentum in both the radial and azimuthal directions will be proposed. The thesis will not explore the spontaneous non-circular hydraulic jump, but will study the influence of the geometry of the disk and varied film thickness at the disk edge on the jump radius and flow features.

The existing studies on the circular hydraulic jump are using Newtonian fluid as the working fluid, but many fluids of industrial applications are viscoplastic fluids. In addition, extensive research showed that both the yield stress and the shear-rate dependence viscosity can affect the spreading of the flow, as well as the flow structure. In the current thesis, a model that takes the rheology of the viscoplastic fluid into account will be presented. The influence of yield stress and power law index on the jump radius and the flow characteristics in both super- and sub-critical regions will be explored.

1.4.2 The outline of the thesis

In Chapter 2, to obtain a smooth jump profile without any empirically or numerically adjusted boundary conditions, a coherent composite approach will be proposed. The theory will be validated against extensive experiments and Navier–Stokes simulations. The effect of flow rate, viscosity and gravity on the flow structure will be examined. In Chapter 3, the characteristics of the continuous circular hydraulic jump will be explored. Based on the continuous model proposed in Chapter 2, we will further investigate the effects of disk size, and film height at the disk edge on the flow structure. The interplay between the flow rate and disk size will be examined further. In addition, the existence and non-existence of

vortex and jump on the flow parameters will be investigated. Furthermore, we will propose a scaling law for the jump radius, which takes the effect of the disk size into account. In Chapter 4, to explore the effect of azimuthally varying edge conditions on the hydraulic jump, a model that considered the mass and momentum balance equation in both the radial and azimuthal directions will be proposed. The effect of both the geometry of a non-circular disk and a variable film thickness at the disk edge for a circular disk on the jump radius and flow characteristics will be explored. In Chapter 5, a model for viscoplastic impinging jet flow and hydraulic jump will be presented. The constitutive model utilized is the Herschel-Bulkley model. The influence of the yield stress and shear-rate dependence viscosity on the jump radius, as well as the flow in both super- and sub-critical regions will be investigated. In Chapter 6, the overall concluding remarks and suggestions for future works will be given.

1.5 References

- ANCEY, C. 2007 Plasticity and geophysical flows: a review. *J. Non-Newtonian Fluid Mech.* **142**, 4–35.
- ASADI, A., JAFARIAN, S. M., & TEYMOURTASH, A. R. 2020 Experimental Study of Stable Circular Hydraulic Jumps. *Fluid Dyn.* **55**, 477-487.
- AVEDISIAN, C. & ZHAO, Z. 2000 The circular hydraulic jump in low gravity. *Proc. R. Soc. Lond., Ser. A* **456**, 2127-2151.
- ASKARIZADEH, H., AHMADIKIA, H., EHRENPREIS, C., KNEER, R., PISHEVAR, A. & ROHLFS, W. 2020 Heat transfer in the hydraulic jump region of circular free-surface liquid jets. *Intl J. Heat Mass Transfer* **146**, 118823.
- AZUMA, T. & HOSHINO, T. 1984a The radial flow of a thin liquid film: 2nd report, liquid film thickness. *Bulletin of JSME* **27**, 2747-2754.
- AZUMA, T. & HOSHINO, T. 1984b The radial flow of a thin liquid film: 3rd report, velocity profile. *Bulletin of JSME* **27**, 2755-2762.

BALMFORTH, N. J., BURBIDGE, A. S., CRASTER, R. V., SALZIG, J., & SHEN, A. 2000 Viscoplastic models of isothermal lava domes. *J. Fluid Mech.* **403**, 37–65.

BALMFORTH, N.J. & CRASTER, R.V. 1999 A consistent thin-layer theory for Bingham plastics. *J. Non-Newtonian Fluid Mech.* **84**, 65–81.

BALMFORTH, N.J., CRASTER, R.V., RUST, A.C. & SASSI, R. 2007a Viscoplastic flow over an inclined surface. *J. Non-Newtonian Fluid Mech.* **139**, 103–127.

BALMFORTH, N.J., CRASTER, R.V. & SASSI, R. 2002 Shallow viscoplastic flow on an inclined plane. *J. Fluid Mech.* **470**, 1–29.

BAONGA, J. B., GUALOUS, H. L. & IMBERT, M. 2006 Experimental study of hydrodynamic and heat transfer of free liquid jet impinging a flat circular heated disk. *Appl. Therm. Engng* **26**, 1125–1138.

BAUER, H., BOESE, N. & STERN, N. 1995 Viscoplastic flow and shear thickening in concentrated diblock copolymer solutions. *Colloid Polym. Sci.* **273**:480-489.

BIRD, R. B., ARMSTRONG, R. C., & HASSAGER, O. 1987 *Dynamics of polymeric liquids. Vol. 1: Fluid mechanics*. Wiley-Interscience.

BIRD, R. B., GANCE, D. & YARUSSO, B. J. 1983 The rheology and flow of viscoplastic materials. *Rev. Chem. Eng.* **1**, 1-70.

BIRKHOFF, G. & ZARANTONELLO, E. 1957 *Jets, Wakes and Cavities*. Academic.

BOHR, T., DIMON, P. & PUTZKARADZE, V. 1993 Shallow-water approach to the circular hydraulic Jump. *J. Fluid Mech.* **254**, 635-648.

BOHR, T., ELLEGAARD, C., HANSEN, A. E. & HAANING, A. 1996 Hydraulic jumps, flow separation and wave breaking: An experimental study. *Physica B* **228**, 1-10.

BOHR, T., PUTKARADZE, V. & WATANABE, S. 1997 Averaging theory for the structure of hydraulic jumps and separation in laminar free-surface flows. *Phys. Rev. Lett.* **79**, 1038-1041.

BONN, D., ANDERSEN, A. & BOHR, T. 2009 Hydraulic jumps in a channel. *J. Fluid Mech.* **618**, 71-87.

BOWLES, R. I. 1990 Applications of nonlinear viscous-inviscid interactions in liquid layer flows & transonic boundary layer transition. Ph.D. thesis, University of London.

BOWLES, R. I. 1995 Upstream influence and the form of standing hydraulic jumps in liquid-layer flows on favourable slopes. *J. Fluid Mech.* **284**, 63-96.

BUSH, J. W. M. & ARISTOFF, J. M. 2003 The influence of surface tension on the circular hydraulic jump. *J. Fluid Mech.* **489**, 229-238.

BUSH, J.W.M., ARISTOFF, J.M., & HOSOI, A.E. 2006. An experimental investigation of the stability of the circular hydraulic jump. *J. Fluid Mech.* **558**, 33-52.

CHAMBON, G., GHEMMOUR, A. & LAIGLE, D. 2009 Gravity-driven surges of a viscoplastic fluid: an experimental study, *J. Non-Newton. Fluid Mech.* **158**, 54–62.

CHAMBON, G., GHEMMOUR, A., & NAAIM, M. 2014 Experimental investigation of viscoplastic free-surface flows in a steady uniform regime. *J. Fluid Mech.* **754**, 332-364.

COCHARD, S & ANCEY, C. 2008 Experimental investigation of the spreading of viscoplastic fluids on inclined planes. *J. Non-Newton. Fluid Mech.* **158**, 73–84.

CRAIK, A., LATHAM, R., FAWKES, M., & GRIBBON, P. 1981 The circular hydraulic jump. *J. Fluid Mech.* **112**, 347-362.

DE SOUZA MENDES, P. R. 2009. Modeling the thixotropic behavior of structured fluids. *J. Non-Newtonian Fluid Mech.* **164**, 66-75.

DUCHESNE, A., LEBON, L. & LIMAT, L. 2014 Constant Froude number in a circular hydraulic jump and its implication on the jump radius selection. *Europhys. Lett.* **107**, 54002.

DUCHESNE, A. & LIMAT, L. 2022 Circular hydraulic jumps: where does surface tension matter? *J. Fluid Mech.* **937**, R2.

- EAD, S. A., & RAJARATNAM, N. 2002 Hydraulic jumps on corrugated beds. *J Hydraulic Engineering* **128**, 656–663.
- ELLEGAARD, C, HANSEN, A.E., HAANING, A., MARCUSSEN, A., BOHR, T., HANSEN, J.L. & WATANABE, S. 1998 Creating corners in kitchen sink flows. *Nature* **392**, 767-768.
- ERRICO, M. 1986 A study of the interaction of liquid jets with solid surfaces. PhD thesis, University of California, San Diego.
- ESMAEELI, A., & PASSANDIDEH-FARD, M. 2021 Characterization of Polygonal Hydraulic Jump during Liquid Jet Impingement on a Flat Substrate. *Fluid Dyn.* **56**, 552-565.
- ESTELLE, P. & LANOS, C. 2012 High torque vane rheometer for concrete: Principle and validation from rheological measurements. *Appl. Rheol.* **22**, 12881.
- FERNANDEZ-FERIA, R., SANMIGUEL-ROJAS, E. & BENILOV, E. S. 2019 On the origin and structure of a stationary circular hydraulic jump. *Phys. Fluids* **31**, 072104.
- FERREIRA, V. G., TOMÉ, M. F., MANGIAVACCHI, N., CASTELO, A., CUMINATO, J. A., FORTUNA, A. O. & MCKEE, S. 2002 High-order upwinding and the hydraulic jump. *Int. J. Numer. Meth. Fluids* **39**, 549–583.
- FIOROT, G. H., & DE FREITAS MACIEL, G. 2019 Free-surface laminar flow of a Herschel–Bulkley fluid over an inclined porous bed. *J. Non-Newton. Fluid Mech.* **272**, 104164.
- FREYDIER, P., CHAMBON, G. & NAAIM, M. 2017 Experimental characterization of velocity fields within the front of viscoplastic surges down an incline, *J. Non-Newton. Fluid Mech.* **240**, 56–69.
- GAJJAR, J., & SMITH, F. T. 1983 On hypersonic self-induced separation, hydraulic jumps and boundary layers with algebraic growth. *Mathematika*, **30**, 77-93.
- GRIFFITHS, R. W. & FINK, J. H. 1993 Effects of surface cooling on the spreading of lava flows and domes. *J. Fluid Mech.* **252**, 667-702.

- HANSEN, S. H., HORLUCK, S., ZAUNER, D., DIMON, P., ELLEGAARD, C. & CREAGH, S. C. 1997 Geometric orbits of surface waves from a circular hydraulic jump. *Phys. Rev. E* **55**, 7048-7061.
- HEIRMAN, G., HENDRICKX, R., VANDEWALLE, L., FEYS, D., VAN GEMERT, D., DE SCHUTTER, G., DESMET, B & VANTOMME, J. 2009 Integration approach of the Couette inverse problem of powder type self-compacting concrete in a wide-gap concentric cylinder rheometer. Part II. Influence of mineral additions and chemical admixtures on the shear thickening flow behaviour. *Cement Concrete Res.* **39**, 171–181.
- HEIRMAN, G., VANDEWALLE, L., VAN GEMERT, D. & WALLEVIK, O. 2008 Integration approach of the Couette inverse problem of powder type self-compacting concrete in a wide-gap concentric cylinder rheometer. *J. Non-Newtonian Fluid Mech.* **150**, 93–103.
- HIGUERA, F. J. 1994 The hydraulic jump in a viscous laminar flow. *J. Fluid Mech.* **274**, 69-92.
- HUANG, X. & GARCÍA, M. H. 1998 A Herschel–Bulkley model for mud flow down a slope. *J. Fluid Mech.* **374**, 305–333.
- HOVLAND, A., LYTER, F. G., & TRUCHOT, C. 2011 Innovative cleaning of air preheater coils with pressurized liquid nitrogen (LN₂). *ASME Power Conference* **44601**, 159-171.
- IPATOVA, A., SMIRNOV, K. & MOGILEVSKIY, E. 2021 Steady circular hydraulic jump on a rotating disk. *J. Fluid Mech.* **927**, A24.
- JALAAL, M., STOEBER, B., & BALMFORTH, N. J. 2021 Spreading of viscoplastic droplets. *J. Fluid Mech.* **914**, A21.
- JIANG, L. & LEBLOND, P. H. 1993 Numerical modeling of an underwater Bingham plastic mudslide and the waves it generates. *J. Geophys. Res.* **98**, 10 303–10 317.
- JÖRG, J., TARABORRELLI, S., SARRIEGUI, G., DE DONCKER, R. W., KNEER, R., & ROHLFS, W. 2017 Direct single impinging jet cooling of a MOSFET power electronic module. *IEEE Transactions on Power Electronics* **33**, 4224-4237.

- KAMRIN, K. & MAHADEVAN, L. 2012 Soft catenaries. *J. Fluid Mech.* **691**, 165–77.
- KÁRMÁN, T. V. 1921 Uber laminare und turbulente Reibung, *Z. angew. Math. Mech.* **1**, 233-252; *translated as* On laminar and turbulent friction, *Nut, Adv. Comm. Aero., Wash., Tech. Mem.* **1092**, 1946.
- KASIMOV, A. R. 2008 A stationary circular hydraulic jump, the limits of its existence and its gasdynamic analogue. *J. Fluid Mech.* **601**, 189–198.
- KOBLITZ, A. R., LOVETT, S. & NIKIFORAKIS, N. 2018 Viscoplastic squeeze flow between two identical infinite circular cylinders. *Phys. Rev. Fluids* **3**, 023301-023316.
- KUNDU, P.K., COHEN, I.M. & BOWLING, D.R. 2016 *Fluid Mechanics*. 6th edn. Elsevier.
- LINZ 2011 Siemens to modernize process control system in Wuhan Iron & Steel's hot rolling mill
https://www.siemens.com/press/en/pressrelease/?press=/en/pressrelease/2011/industry_solutions/iis201103939.htm
- LIU, K. & MEI, C.C. 1994 Roll waves on a layer of a muddy fluid flowing down a gentle slope—A Bingham model. *Phys. Fluids* **6**, 2577–2590.
- LIU, X. & LIENHARD, J. 1993 The hydraulic jump in circular jet impingement and in other thin liquid films. *Exp. Fluids* **15**, 108-116.
- LIU, X., GABOUR, L. A. & LIENHARD, J. 1993 Stagnation-point heat transfer during impingement of laminar liquid jets: analysis Including surface tension. *ASME J. Heat Transfer* **115**, 99–105.
- LIU, Y., BALMFORTH, N. J., HORMOZI, S. 2018 Axisymmetric viscoplastic dambreaks and the slump test, *J Non-Newtonian Fluid Mech.* **258**, 45-57.
- LIU, Y., BALMFORTH, N. J., HORMOZI, S., & HEWITT, D. R. 2016 Two-dimensional viscoplastic dambreaks. *J Non-Newtonian Fluid Mech.* **238**, 65–79.

- LIU, Y., BALMFORTH, N. J., HORMOZI, S. 2019. Viscoplastic surges down an incline. *J Non-Newtonian Fluid Mech.* **268**, 1–11.
- LUU, L.H. & FORTERRE, Y. 2009 Drop impact of yield-stress fluids. *J. Fluid Mech.* **632**,301–27.
- MARTENS, E. A., WATANABE, S. & BOHR, T. 2012 Model for polygonal hydraulic jumps. *Phys. Rev. E* **85**, 036316.
- MATSON, G. P. & HOGG, A. J. 2007 Two-dimensional dam break flows of Herschel–Bulkley fluids: The approach to the arrested state. *J Non-Newtonian Fluid Mech.* **142**, 79–94.
- MEI, C.C. & M. YUHI 2001 Slow flow of a Bingham fluid in a shallow channel of finite width. *J. Fluid Mech.* **431**, 135–159.
- MCBIRNEY, A. R. & MURASE, T. 1984 Rheological properties of magmas. *Ann. Rev. Earth Planet. Sci.* **12**, 337-357.
- MELANIFF 2003 Secrets of Dodge's new mini-muscle turbo car
http://www.melaniff.com/srt-4/hot%20rod/hot_rod_2003_09.htm
- MOHAJER, B. & LI, R. 2015 Circular hydraulic jump on finite surfaces with capillary limit. *Phys. Fluids* **27**, 117102.
- MULLAI VENTHAN, S., NISHA, M. S., SENTHIL KUMAR, P., & JAYAKARAN AMALRAJ, I. 2022 Heat transfer effect of SiC-GN hybrid nanocomposite with viscoplastic fluid in aircraft jet engine hoses. *Sustainable Energy Technologies and Assessments*, 52.
- MURAVLEVA, L. 2019 Axisymmetric squeeze flow of a Herschel–Bulkley medium. *J Non-Newtonian Fluid Mech.* **271**, 104147.
- NGUYEN, Q.D. & BOGER, D.V. 1992 Measuring the Flow Properties of Yield Stress Fluids. *Annu. Rev. Fluid Mech.* **24**, 47–88.

- NICHOLS, T. E., & BOSTWICK, J. B. 2020 Geometry of polygonal hydraulic jumps and the role of hysteresis. *Phys. Rev. Fluid* **5**, 044005.
- OEVERMANN, D., BHAGAT, R. K., FERNANDES, R. R., & WILSON, D. I. 2019 Quantitative modelling of the erosive removal of a thin soil deposit by impinging liquid jets. *Wear* **422**, 27-34.
- OGIHARA, Y. & MIYAZAWA, N. 1994 Hydraulic Characteristics of Flow over Dam and Hydraulic Jump of Bingham Fluid. *J. Hydraul. Coastal Environ. Eng. Proc. Jpn. Soc. Civil Engineers* **485**, 21–26 (in Japanese).
- PALERMO, M. & PAGLIARA, S. 2018 Semi-theoretical approach for energy dissipation estimation at hydraulic jumps in rough sloped channels. *J Hydraulic Research* **56**, 786–795.
- PASK, S.D., NUYKEN, O. & CAI, Z. 2012 The spinning disk reactor: an example of a process intensification technology for polymers and particles. *Polym. Chem.* **3**, 2698–2707.
- PASSANDIDEH-FARD, M., TEYMOURTASH, A. R., & KHAVARI, M. 2011 Numerical Study of Circular Hydraulic Jump Using Volume-of-Fluid Method. *J Fluids Engng* **133**, 11401.
- POHLHAUSEN, K. 1921 Zur näherungsweise Integration der Differentialgleichung der laminaren Grenzschicht. *Z. Angew. Math. Mech.* **1**, 252–268.
- RAO, A. & ARAKERI, J. H. 2001 Wave structure in the radial film flow with a circular hydraulic jump. *Exp. Fluids* **31**, 542-549.
- RAYLEIGH, O. M. 1914 On the theory of long waves and bores. *Proc. R. Soc. Lond. A* **90**, 324-328.
- UTRACKI, L. A. 1993 The rheology of two-phase flows. *Rheological Measurement* 479–594.
- SCHLICHTING, H. & GERSTEN, K. 2000 *Boundary-layer theory* 8th edition, Springer.
- SHAW, H. R. 1969 Rheology of basalt in the melting range. *J. Petrol.* **10**, 510-535.

- SHU J. & ZHOU J. 2006 Characteristics of a hydraulic jump in Bingham fluid. *J. Hydraul. Res.* **44**, 421-426.
- STEVENS, J. & WEBB, B. W. 1992 Measurements of the free surface flow structure under an impinging free liquid jet. *Trans. ASME J. Heat Transfer* **114**, 79–83.
- TANI, I. 1949 Water jump in the boundary layer. *J. Phys. Soc. Japan* **4**, 212–215.
- TEYMOURTASH, A. R., & MOKHLESI, M. 2015 Experimental investigation of stationary and rotational structures in non-circular hydraulic jumps. *J. Fluid Mech.* **762**, 344-360.
- UGARELLI, R. & FEDERICO, V. D. 2007 Transition from supercritical to subcritical regime in free surface flow of yield stress fluids. *Geophys. Res. Lett.* **34**, L21402.
- WADSWORTH, D. C., & MUDAWAR, I. 1990 Cooling of a multichip electronic module by means of confined two-dimensional jets of dielectric liquid. *ASME J. Heat Mass Transfer* **112**, 891-898.
- WALTON, I. C. & BITTLESTON, S. H. 1991 The axial flow of a Bingham plastic in a narrow eccentric annulus. *J. Fluid Mech.* **222**, 39–60.
- WANG, Y. & KHAYAT, R. E. 2018 Impinging jet flow and hydraulic jump on a rotating disk. *J. Fluid Mech.* **839**, 525–560.
- WANG, Y. & KHAYAT, R. E. 2019 The role of gravity in the prediction of the circular hydraulic jump radius for high-viscosity liquids. *J. Fluid Mech.* **862**, 128–161.
- WANG, Z., YAN, B., & AN, X. 2022 Rheological and flow characteristics of fresh concrete in the rotational rheometer. *Journal of Sustainable Cement-Based Materials* **12**, 487-500.
- WATANABE, S., PUTKARADZE, V. & BOHR, T. 2003 Integral methods for shallow free-surface flows with separation. *J. Fluid Mech.* **480**, 233-265.
- WATSON, E. 1964 The spread of a liquid jet over a horizontal plane. *J. Fluid Mech.* **20**, 481-499.

WEINSTEIN, S.J. & RUSCHAK, K.J. 2004 Coating flows. *Annu. Rev. Fluid Mech.* **36**, 29–53.

WHITE, F. 2006 *Fundamentals of Fluid Mechanics*. McGraw-Hill.

YAHIA, A. 2011 Removal of a viscous film from a rigid plane surface by an impinging liquid jet. *Cement Concrete Res.* **41**, 230-235.

ZHOU J., SHU J. & STANSBY, P. K. 2007 Hydraulic jump analysis for a Bingham fluid. *J. Hydraul. Res.* **45**, 455-562.

Chapter 2

2 A coherent composite approach for the continuous circular hydraulic jump and vortex structure¹

Nomenclature

a	Radius of jet, m
Fr	Froude number, $Fr = W/\sqrt{ga}$
Fr_l	Local Froude number, $Fr_l = Fr\langle u \rangle/\sqrt{\bar{h}}$
Fr_j	Froude number immediately downstream of the jump, $Fr_j = Fr/2r_j H_j^{3/2}$
g	Acceleration due to gravity, m/s^2
Ga	Galileo number, $Ga = Re^2/Fr^2$
h	Dimensionless film thickness
\bar{h}	Dimensionless rescaled height film thickness
h_0	Dimensionless film thickness at $r = r_0$
h_1	Dimensionless film thickness at $r = r_1$
h_c	Dimensionless critical height $h_c = h(r = r_c)$, when $Fr/2r_c h_c^{3/2} = 1$
h_{max}	Dimensionless (maximum) film thickness at $r = r_{max}$

¹ A version of this chapter has been published as -

Wang, W., Baayoun, A. & Khayat, R.E. 2023 A coherent composite approach for the continuous circular hydraulic jump and the vortex structure. *J. Fluid Mech.* 966, A15. <https://doi.org/10.1017/jfm.2023.374>

h_∞	Dimensionless film thickness at the disk edge
H_{J1}	Dimensionless measured jump height
H_{J2}	Dimensionless jump height based on lubrication approach
H_{vortex}	Dimensionless height of the vortex under the jump
L_{vortex}	Dimensionless length of the vortex under the jump
m	Dimensionless momentum flux, $m = \frac{Re}{r} \frac{d}{dr} \int_0^h ru^2 dz$
p	Dimensionless pressure
Q	Volume flow rate, m^3/s
r	Dimensionless radial coordinate
\bar{r}	Dimensionless rescaled radial coordinate
r_0	Dimensionless transition point of the hydrodynamic boundary layer
r_1	Dimensionless radial location of the leading edge of the hydraulic jump
r_c	Dimensionless critical radius when $Fr/2r_c h_c^{3/2} = 1$
r_s	Dimensionless radial location of singularity reached
r_m	Dimensionless radial location of maximum film thickness
r_∞	Dimensionless disk radius
r_j	Dimensionless jump radius
Re	Reynolds number, $Re = Wa/\nu$
u	Dimensionless horizontal velocity

U	Dimensionless free surface velocity
$\langle u \rangle$	Dimensionless depth average velocity
w	Dimensionless vertical velocity
W	Average jet velocity, $W = Q/\pi a^2$, m/s
z	Dimensionless vertical coordinate

Greek Symbols

δ	Dimensionless hydrodynamic boundary layer thickness
ε	Dimensionless perturbation parameter
η	Scaled vertical coordinate, $\eta = z/h$
θ	Azimuthal coordinate
ν	Kinematic viscosity, m^2/s
ρ	Density of fluid, kg/m^3
τ_w	Dimensionless wall shear stress

2.1 Introduction

When a circular liquid jet impinges vertically onto a horizontal disk, it spreads radially outwards as a thin film. At a certain radial position, the film exhibits a circular hydraulic jump or a sudden rise in the thickness (Middleman 1995). This phenomenon is of pivotal fundamental importance in free-surface flow, and it is of relevance to many practical applications (Ishigai *et al.* 1977; Kate, Das & Chakraborty 2007; Mohajer & Li 2015; Askarizadeh *et al.* 2020). The formation of the jump is associated with a flow separation and the creation of a separation bubble, or a recirculating vortex, at the bottom in conjunction with the jump (Bohr *et al.* 1996; Ellegaard *et al.* 1996), resulting from the film thickening across the jump and the simultaneous decrease in velocity. In turn, this induces a rise in pressure, which acts as an adverse wind to the flow, enabling it to separate into regions of upstream and downstream velocities of the *type I* jump (Bohr *et al.* 1998). Both the separation length and the vortex size depend on the flow conditions (Nakoryakov, Pokusaev & Troyan 1978; Craik *et al.* 1981; Rao & Arakeri 2001). The predictions of the jump radius and structure, the free-surface height and the vortex size have been of primary interest in the literature. However, the flow involving a circular hydraulic jump still lacks a coherent and systematic predictive theory for these different hydrodynamic features, even under laminar and steady-state conditions. Existing theoretical models are semi-empirical as they require some input from experiment to ensure the well-posedness of the problem. The objective of the present study is to develop a theoretical approach that addresses this issue and other drawbacks of existing models.

In the presence of gravity, the thin-film equations do not admit a similarity solution such as in the approach formulated by Watson (1964). Instead, the flow is commonly treated theoretically by reducing the boundary-layer equations using a mean-field or depth-averaging of the Kármán-Pohlhausen (KP) type (Schlichting & Gersten 2000). In the absence of surface tension, the thin-film approximation results in a hydrostatic pressure distribution that reflects the gravitational effect in the flow. By adopting a simple (often parabolic or cubic) velocity profile across the film layer, reasonably accurate quantitative predictions of the flow field and film profile can be obtained (Kurihara 1946; Tani 1949; Bohr, Dimon & Putkaradze 1993, Kasimov 2008; Wang & Khayat 2019). However, the

choice of the (radial) velocity profile constitutes a crucial step in the formulation. Almost any simple profile can lead to reasonably accurate prediction of the jump radius and height, but a more judicious choice is needed to capture more accurately the flow field. In this respect, the common practice has been to adopt a simple similarity profile, yielding a first-order equation for the film thickness, or a non-similarity profile that yields a second-order equation. We therefore refer to first- and second-order formulations when resulting in first- and second-order equations governing the film thickness, respectively. Various mechanisms can yield the second-order correction such as the inclusion of normal diffusive term (Razis, Kanellopoulos & van der Weele 2021) or gravity effect (Bohr, Putkaradze, & Watanabe 1997; Watanabe, Putkaradze & Bohr 2003) by ensuring that the velocity profile satisfies the radial momentum equation at the disk.

The first-order model is typically derived by imposing a similarity profile for the radial velocity component. As a result, a singularity in either the velocity gradient or the film surface slope emerges at a finite radius, which is often assumed to coincide with the location of the jump (Kurihara 1946; Tani 1949; Wang & Khayat 2019). This approach is particularly attractive for two main reasons. On the one hand, the problem is reduced to a one degree of freedom, thus necessitating only one boundary condition, typically imposed at some upstream location. On the other hand, the location of the jump is determined without requiring any knowledge of the subcritical flow. Once the jump is located, the subcritical flow can be determined using a lubrication approach, which was shown to give reasonable prediction ((Duchesne, Lebon & Limat 2014; Wang & Khayat 2019). Alternatively, Bohr *et al.* (1993) and Kasimov (2008) integrated the film equation radially forward upstream and backward downstream, hence generating inner and outer solutions, respectively. They assumed a simple parabolic velocity profile everywhere in the flow. In their inner solution, a boundary condition was arbitrarily imposed at a location slightly larger than the jet radius. In their outer solution, an infinite slope of either the average velocity or the film thickness was considered to coincide with the edge of the disk. Subsequently, Bohr *et al.* (1993), Kasimov (2008) and Dhar, Das & Das (2020) located the jump upon matching both solutions through a Rayleigh shock (Rayleigh 1914) that satisfies the continuity of mass and radial momentum fluxes across the shock. Later, Wang & Khayat (2019) adopted a similar solution process, but included a developing boundary-

layer region near impact, thus allowing the fixing of an upstream boundary condition at the transition location between the boundary and viscous layers. The validity of the first-order model has been tested, yielding good agreement against experiment and numerical simulation, particularly for the jump radius. However, the model suffers from significant fundamental drawbacks as it prohibits proper analysis of the jump structure: the jump can only be treated as a (discontinuous) shock, with no possibility of examining the separation downstream or the viscous-inviscid interaction leading up to jump, the ellipticity of the boundary-layer equations is lost and the upstream influence cannot be addressed (Bowles & Smith 1992; Higuera 1994; Bowles 1995). We address these issues in some detail in the present study.

In an effort to capture the smooth variation of the jump and the vortex structure, second-order corrections were introduced by Bohr *et al.* (1997) and Watanabe *et al.* (2003). They accounted for additional gravity effect by ensuring their velocity profile to satisfy the momentum equation at the disk. The presence of the resulting additional shape parameter in the cubic velocity profile prevents the formation of the critical point and the singularity of the averaged first-order model, allowing the capture of the flow separation. However, two experimental points are needed in their solution to fix the boundary conditions, and some prior knowledge of the location of the jump is required. In this regard, even though their theory showed good agreement with the earlier measurements of Bohr *et al.* (1996), it remains somewhat semi-empirical. A similar approach was later adopted by Bonn, Andersen & Bohr (2009) to study the hydraulic jump in a channel. However, results showing a jump-like profile were only presented to describe the vortex, whereas their comparison against measurements was limited to the simplified (first-order) version of the model in which the jump was treated as an abrupt shock connecting an inner and an outer solution. Fernandez-Feria, Sanmiguel-Rojas & Benilov (2019) obtained the jump profile by numerically integrating the boundary-layer equations. Their approach accommodates only an upstream boundary condition specified at some radial location close to impact. Similarly, Higuera (1994) solved the boundary-layer equations numerically to generate the jump profile for two-dimensional flow. Unlike Fernandez-Feria *et al.* (2019), he ensured the upstream influence from the downstream flow condition at the edge of the disk.

More recently, Roberts & Li (2006) derived a model based on centre-manifold theory to describe the dynamics of thin films on curved substrates. A smooth profile was generated for the circular hydraulic jump on a flat substrate, and the vortex was captured as well. However, they simply imposed the boundary conditions in a manner similar to Watanabe *et al.* (2003). Mikielewicz & Mikielewicz (2009) proposed a simple model based on the solution of Bernoulli's equation for the planar viscous fluid flow, which incorporates the dissipation losses due to the change of the film thickness as well as the presence of eddies following the jump. The model does not predict the radius of the jump as accurately as the averaged boundary-layer equations. Moreover, the model requires a prior knowledge of the size of the vortex, which, in their case, was fixed as a quarter of the subcritical depth. A more serious attempt was made by Razis *et al.* (2021) to capture the continuous jump in an inclined channel. They extended the Saint-Venant equations by including the effect of the longitudinal normal stress. They derived analytically an approximate expression for the jump length as a function of the Froude and effective Reynolds numbers, highlighting the strong interplay among inertia, gravity and viscous diffusion, as contributing to the balance of forces that shape the jump.

The aim of the present study is to present a coherent approach that predicts the different features of the *continuous* circular hydraulic jump problem. We are particularly interested in predicting the continuous jump profile so the effects of the flow conditions on the separation length and the vortex size can be explored. The rest of this paper is organized as follows. In section 2.2, we describe the general problem and physical domain. In section 2.3, we formulate the problem in terms of the general governing equations and boundary conditions in each region of the flow. The KP integral method is adopted, and the solution strategy is clearly described with a case illustration. In section 2.4, we validate our theoretical predictions against existing numerical and experimental results. Some further results and analysis are given in section 2.5, where we examine the influence of the flow rate over the same experimental range as that of Duchesne *et al.* (2014). Flow details are considered which were not reported in their experiment. Additional results on the influence of gravity and viscosity are also given. Finally, concluding remarks are given in section 2.6.

2.2 The physical domain and problem statement

Consider the steady laminar incompressible flow of a circular (axisymmetric) jet of a Newtonian fluid emerging from a nozzle of radius a , impinging at a volume flow rate Q on a flat disk of radius R_∞ lying normal to the jet direction. The flow configuration is depicted schematically in figure 1, where dimensionless variables and parameters are used. The problem is formulated in the (r, θ, z) fixed coordinates, with the origin coinciding with the disk center. The flow is assumed to be independent of θ , thus excluding polygonal flow. In this case, $u(r, z)$ and $w(r, z)$ are the corresponding dimensionless velocity components in the radial and vertical directions, respectively. The r -axis is taken along the disk radius and the z -axis is taken along the jet axis. The length and the velocity scales are conveniently taken to be the radius of the jet a , and the average jet velocity $W \equiv Q/\pi a^2$, both in the radial and vertical directions. Since the pressure is expected to be predominantly hydrostatic for a thin film, it is scaled by $\rho g a$, where g is the acceleration due to gravity. In the absence of surface tension, two main dimensionless groups emerge in this case: the Reynolds number $Re = Wa/\nu$, where ν is the kinematic viscosity, and the Froude number $Fr = W/\sqrt{ag}$. Another useful and related number is the Galileo number $Ga = Re^2/Fr^2$.

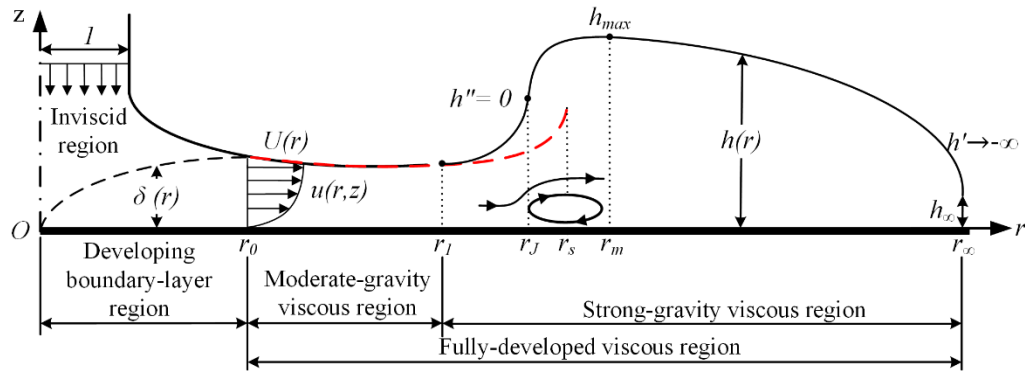


Figure 2-1: Schematic illustration of the axisymmetric jet flow impinging on a flat stationary disk and the hydraulic jump of type I with one vortex downstream. Shown are the developing boundary-layer region ($0 < r < r_0$) and the fully-developed viscous region ($r_0 < r < r_\infty$). The fully-developed viscous region comprises a region ($r_0 < r < r_1$) where gravitational effects are moderate, and a second region where

gravitational effects are strong ($r_1 < r < r_\infty$). All notations are dimensionless. In this case, the jet radius is equal to one. The film is allowed to fall freely over the edge of the disk where an infinite slope in the film thickness occurs, $h'(r = r_\infty) \rightarrow -\infty$. Shown in dashed-red curve is the schematic film-thickness profile reflecting the approach of Wang & Khayat (2019), terminating with a singularity at a finite radius denoted here by r_s . The jump location coincides with $h''(r_j) = 0$, and $h(r_m) = h_{max}$.

As shown in figure 2-1, we identify three main regions of the flow: a developing boundary-layer region ($0 < r < r_0$) where gravity is essentially dominated by inertia, a fully-developed viscous region ($r_0 < r < r_1$) with moderate gravitational effect and a fully-developed viscous region ($r_1 < r < r_\infty$) with strong gravitational effect. The jump is a smooth transition region that connects the (upstream) supercritical and the (downstream) subcritical regions. Again, the analysis of the boundary-layer region, near impact, is crucial in order to fix an upstream boundary condition for the thin-film viscous flow, relevant to the jet conditions. Throughout this study, the stagnation or impingement region is not considered, and the boundary layer is assumed to originate at the stagnation point. However, we examine in some detail the validity of this assumption (see §§2.3.1).

The boundary layer grows until it reaches the film surface at the transition location $r = r_0$. Here, the film thickness is defined as $h_0 \equiv h(r = r_0)$ which corresponds to an upstream boundary condition for the flow in the fully-developed viscous region. We denote by $\delta(r)$ the boundary-layer thickness. The leading edge of the boundary layer is taken to coincide with the disk center. We let $U(r) \equiv u(r, z = h)$ denote the velocity at the free surface. Assuming the jet and stagnation flows to be inviscid irrotational, the radial velocity outside the boundary layer is then $U(0 \leq r \leq r_0) = 1$ as the fluid there is unaffected by the viscous stresses. We recall that both velocity components have been scaled by the (inviscid) jet velocity W . The potential flow ceases to exist in the fully-developed viscous region $r_0 < r < r_\infty$, and U becomes dependent on r . We note that r_0 is the location beyond which

the viscous stresses become appreciable right up to the free surface, where the entire flow is of the boundary-layer type. We follow Rojas *et al.* (2010) and take the jump location to coincide with the vanishing of the concavity: $h''(r = r_J) = 0$. We denote by $r = r_m$ the location of the maximum film height: $h(r = r_m) = h_{\max}$. The definition of the jump radius at the location where the free surface changes concavity is reasonable as this location is very close to the start of the separation zone which is experimentally considered as the location of the jump in the literature (Bohr *et al.* 1996). Downstream of the jump, the film decreases in thickness and eventually falls freely over the edge of the disk, at $r = r_\infty$, where an infinite (downward) slope in thickness is assumed (Bohr *et al.* 1993; Kasimov 2008; Dhar *et al.* 2020). In fact, we shall see that the infinite slope is directly related to the stress singularity expected to occur at the disk edge (Higuera 1994; Scheichl, Bowles & Pasiadis 2018). More details on the condition at the disk edge and upstream influence will be given later. Finally, we shall assume throughout the present study that the locations r_J and r_m coincide with the locations of the leading and trailing edges of the jump, respectively.

Unless otherwise specified, the Reynolds number is assumed to be moderately large so that our analysis is confined to the laminar regime. Consequently, for steady axisymmetric thin-film flow, in the presence of gravity, the mass and momentum conservation equations are formulated using a thin-film or Prandtl boundary-layer approach, which amounts to assuming that the radial flow varies much slower than the vertical flow (Schlichting & Gersten 2000). We observe that the pressure for a thin film is hydrostatic as a result of its vanishing at the film surface (in the absence of surface tension) and the small thickness of the film, yielding $p(r, z) = h(r) - z$. By letting a subscript with respect to r or z denote partial differentiation, the reduced dimensionless relevant conservation equations become

$$u_r + \frac{u}{r} + w_z = 0, \quad \text{Re}(uu_r + ww_z) = -\frac{\text{Re}}{\text{Fr}^2} h' + u_{zz}, \quad (2.2.1a, b)$$

where a prime denotes total differentiation with respect to r . These are the thin-film equations commonly used to model the spreading liquid flow (Tani 1949; Bohr *et al.* 1993,

1996; Kasimov 2008; Wang & Khayat 2019). At the disk, the no-slip and no-penetration conditions are assumed to hold at any r . In this case:

$$u(r, z = 0) = w(r, z = 0) = 0. \quad (2.2.2a, b)$$

At the free surface $z = h(r)$, the kinematic and dynamic conditions for steady flow take the form

$$w(r, z = h) = u(r, z = h)h'(r), \quad u_z(r, z = h) = 0. \quad (2.2.3a, b)$$

The conservation of mass at any location upstream and downstream of the jump yields the following relation in dimensionless form:

$$\int_0^{h(r)} u(r, z) dz = \frac{1}{2r}. \quad (2.2.4)$$

Finally, a useful expression for the convective terms is obtained by first eliminating the transverse velocity component by noting from (2.2.1a) and (2.2.2b) that

$$w(r, z, t) = -\frac{1}{r} \frac{\partial}{\partial r} \left(r \int_0^z u dz \right). \text{ In this case}$$

$$uu_r + ww_z = \frac{1}{r} \left(ru^2 \right)_r - \frac{1}{r} \left(u \int_0^z (ru)_r dz \right)_z. \quad (2.2.5)$$

The flow field is sought separately in the developing boundary-layer region for $0 < r < r_0$, the fully-developed viscous region with moderate gravity for $r_0 < r < r_1$ and fully-developed viscous region with strong gravity for $r_1 < r < r_\infty$. Additional boundary conditions are needed, which are given when the flow is analysed in each region.

2.3 Formulation and solution strategy

In this section, we first present the formulation of the steady flow in the developing boundary-layer region in order to obtain the upstream boundary condition needed for the flow in the fully-developed viscous region. Next, we present the formulations of the flow in the fully-developed viscous region. In particular, effects of moderate gravity and strong gravity are discussed. We see that, depending on the level of importance of the gravitational effects, different governing equations can be used in different regions. The general strategy to obtain a unique solution of the free-surface profile and flow field, and to locate the jump, is finally described.

Aside from some specific cases, boundary-layer and thin-film flows are generally non-self-similar in character (Schlichting & Gersten 2000; Drazin & Riley 2006). Therefore, we seek an approximate solution in each flow region. An integral approach of the KP type (Schlichting & Gersten 2000) is adopted in the developing boundary-layer and fully-developed viscous regions. The KP method has been widely adopted in the literature for steady and transient jumps, not only when the thin-film equations are parabolic (Watson 1964; Bush & Aristoff 2003; Kate *et al.* 2007; Dressaire *et al.* 2010; Prince *et al.* 2012; Wang & Khayat 2018; Baayoun *et al.* 2022) but also when the equations are weakly elliptic (Tani 1949; Bohr *et al.* 1993; Bohr *et al.* 1997; Watanabe *et al.* 2003; Kasimov 2008; Fernandez *et al.* 2019; Wang & Khayat 2019; Dhar *et al.* 2020; Ipatova *et al.* 2021). The problem becomes weakly elliptic when the relatively weak effect of gravity upstream of the jump is not neglected in the analysis. In this case, the upstream influence caused by the downstream condition is small but not negligible. It is well established from the literature for impinging jet flow and hydraulic jump (Prince *et al.* 2012/2014; Wang & Khayat 2018/2019/2020; Baayoun *et al.* 2022) that a cubic similarity velocity profile taken in the supercritical region leads to close agreement with Watson's (1964) similarity solution. Consequently, in this study, we also adopt a cubic profile for the velocity, which is considered to be the leading-order solution in a comprehensive spectral approach for nonlinear flow (Khayat & Kim 2006). Other profiles such as the parabolic profile were also used in the literature (Bohr *et al.* 1993; Kasimov 2008).

2.3.1 The flow in the impingement zone and boundary-layer region ($0 < r < r_0$)

As depicted in figure 2-1, we assume that the inception of the boundary layer coincides with the stagnation point, thus assuming the impingement zone to be negligibly small, which is a common practice for an impinging jet. In fact, the velocity outside the boundary layer rises rapidly from 0 at the stagnation point to the impingement velocity in the inviscid far region. The impinging jet is predominantly inviscid close to the stagnation point, and the boundary-layer thickness remains negligibly small. Obviously, this is the case for a jet at relatively large Reynolds number. Indeed, the analysis of White (2006) shows that the boundary-layer thickness is constant near the stagnation point, and is estimated to be $O(\text{Re}^{-1/2})$. Ideally, the flow at the boundary-layer edge should correspond to the (almost parabolic) potential flow near the stagnating jet, with the boundary-layer leading edge coinciding with the stagnation point (Liu & Lienhard 1993). However, the assumption of uniform horizontal flow near the wall and outside the boundary layer is reasonable. The distance from the stagnation point for the inviscid flow to reach uniform horizontal velocity is small, of the order of the jet radius (Lienhard 2006). In the absence of gravity, the steady flow acquires a similarity character. In this case, the position or effect of the leading edge is irrelevant. This assumption was adopted initially by Watson (1964), and has been commonly used in existing theories (see e.g. Bush & Aristoff 2003; Prince *et al.* 2012, 2014; Wang & Khayat 2018, 2019, 2020).

Nevertheless, in an effort to validate the assumption of negligible impingement zone, we find it helpful to examine its extent for the free-surface jet. We therefore assume, given the strong inertia of the downward jet, that the flow above the viscous layer is purely inviscid. For a free-surface jet with no surface tension, Lienhard (2006) showed that the radial velocity component of the potential flow is given by $U(r) = cr + O(r^2)$, where $c = 0.46$.

The radial velocity component in the stagnation region is then expressed as $u(r, z) = U(r)F'(\eta)$ in terms of the similarity variables $\eta = z(c\text{Re})^{1/2}$, and

$w(r, z) = -\left(U'F + \frac{U}{r}F\right)/\sqrt{c\text{Re}}$. A prime indicates total differentiation. Substituting into

(2.2.1b) and neglecting gravity effects, the equation for F becomes (see also Maiti 1965) $F''' + 2FF'' - F'^2 + 1 = 0$, which is solved subject to $F(0) = F'(0) = 0$ and $F(\eta \rightarrow \infty) \sim 1$. The boundary-layer height in the impingement zone is then given by $\delta = \eta_\delta / \sqrt{c \text{Re}}$, where η_δ is a constant that depends on Re . The extent of the impingement zone is assessed once the flow is sought in the developing boundary-layer region.

In this region, the boundary layer grows with radial distance, eventually invading the entire film depth, reaching the free surface at the transition, $r = r_0$, where the fully-developed viscous region begins. For $0 < r < r_0$ and above the boundary layer outer edge, the free surface lies at some height $z = h(r) > \delta(r)$. The flow in the developing boundary-layer region is assumed to be sufficiently inertial for inviscid flow to prevail between the boundary-layer outer edge and the free surface (see figure 2-1). In this case, the following conditions at the outer edge of the boundary layer $z = \delta(r)$ and beyond must hold:

$$u(r < r_0, \delta \leq z < h) = 1, \quad u_z(r < r_0, z = \delta) = 0. \quad (2.3.1a, b)$$

The height of the free surface in the developing boundary-layer region is determined from mass conservation inside and outside the boundary layer. Therefore, for $r < r_0$, (2.2.4) becomes

$$\int_0^{\delta(r)} u(r, z) dz + h(r) - \delta(r) = \frac{1}{2r}. \quad (2.3.2)$$

Upon integrating (2.2.1b) across the boundary-layer thickness and considering the integral form of the convective terms in (2.2.5), we obtain the following weak form:

$$\frac{\text{Re}}{r} \frac{d}{dr} \int_0^{\delta} r u (u - 1) dz = -\frac{\text{Re}}{\text{Fr}^2} \delta h' - \tau_w. \quad (2.3.3)$$

Here we introduced the wall shear stress or skin friction $\tau_w(r) \equiv u_z(r, z=0)$. For simplicity, we choose a similarity cubic profile for the velocity, satisfying conditions (2.2.2a) and (2.3.1). Thus, we let

$$u(r \leq r_0, z) = \frac{3}{2}\eta - \frac{1}{2}\eta^3 \equiv f(\eta), \quad (2.3.4)$$

where $\eta = z/\delta$. Clearly, (2.3.4) does not satisfy the momentum equation at the disk. In this case, the effect of gravity is not accounted for in the velocity profile. This assumption should be reasonable as the effects of gravity are negligible near impingement where inertia is more dominant (Watson 1964). In this case, (2.3.4) represents a self-similar velocity profile in the boundary-layer flow.

Upon inserting (2.3.4) into (2.3.2) and (2.3.3), we obtain the following equations for the boundary-layer and free-surface heights:

$$h - \frac{3}{8}\delta = \frac{1}{2r}, \quad \frac{39}{280} \frac{\text{Re}}{r} \delta(r\delta)' = \frac{\text{Re}}{\text{Fr}^2} \delta^2 h' + \frac{3}{2}. \quad (2.3.5a, b)$$

These equations are solved numerically subject to $\delta(r=0) = 0$. The transition location is found when the boundary-layer thickness becomes equal to the film thickness. Consequently, the boundary condition for the film thickness at the transition location $h_0 \equiv h(r=r_0)$ is obtained. Clearly, the formulations presented for the flow in the developing boundary-layer region are the same as those of Wang & Khayat (2019).

Figure 2-2 illustrates the influence of inertia (Re) and gravity (Fr) on the size of the impingement zone and the boundary-layer profile dictated by (2.3.5). The intersection indicates the extent of the impingement zone, which depends on Fr (figure 2-2a) and Re (figure 2-2b). We recall that the height of the viscous layer in the impingement zone does not change with position and is independent of Fr for a Newtonian jet, and behaves like $1/\sqrt{\text{Re}}$. Figure 2a shows that the extent of the impingement zone decreases as Fr increases, remaining essentially of $O(1)$. The extent saturates asymptotically to the value 1.22 for infinite Fr, when gravity is neglected in (2.3.5). Figure 2-2b indicates that the length of the

impingement zone is essentially insensitive to the variation of the Reynolds number; only its thickness decreases with Re . Therefore, we conclude that, unless the Froude number is very low such as under strong gravity or low flow rate of the jet, the impingement-zone length is of the order of the jet radius, and can be neglected (see also Lienhard 2006).

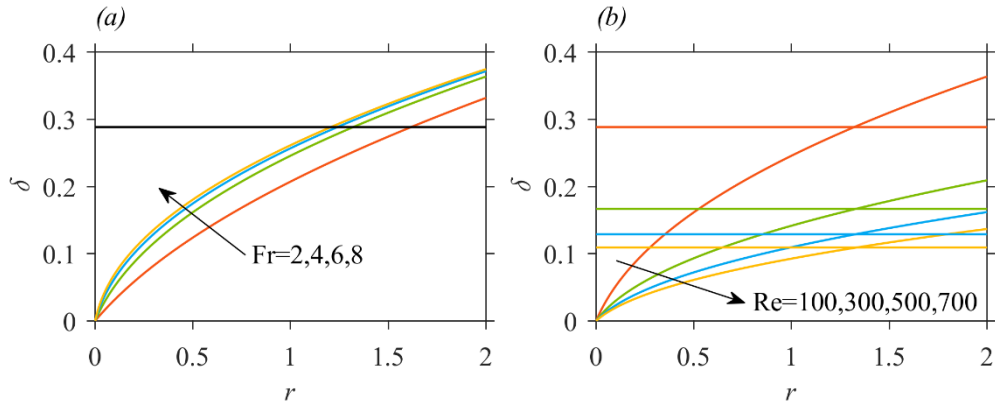


Figure 2-2: Influence of gravity and viscosity on the size of the impingement zone (distance between the origin and the point of intersection with the boundary-layer height). (a) Influence of Fr for $Re = 100$, and (b) influence of Re for $Fr = 4$. The horizontal lines are the thickness of the viscous layer in the impingement zone, and the curves are the boundary-layer profiles emanating from the origin.

2.3.2 The flow in the fully-developed viscous region ($r_0 \leq r \leq r_\infty$)

Downstream of the transition point ($r > r_0$), the potential flow ceases to exist, with the velocity at the free surface becoming dependent on r :

$$u(r > r_0, z = h) = U(r). \quad (2.3.6)$$

In this case, the weak form of the momentum equation (2.2.1b) reads:

$$\frac{Re}{r} \frac{d}{dr} \int_0^h r u^2 dz = -\frac{Re}{Fr^2} h h' - \tau_w. \quad (2.3.7)$$

If the similarity velocity profile $u(r > r_0, z) = U(r)f(\eta)$ is adopted, where $f(\eta)$ is still given in (2.3.4) with $\eta = z/h$, then, after eliminating $U = 4/5rh$ using (2.2.4), we recover, from (2.3.7), the film thickness equation of Wang & Khayat (2019):

$$\text{Re} \left(\frac{5}{4\text{Fr}^2} - \frac{68}{175} \frac{1}{r^2 h^3} \right) h' = \frac{1}{rh^2} \left(\frac{68}{175} \frac{\text{Re}}{r^2} - \frac{3}{2h} \right), \quad (2.3.8)$$

which is solved subject to $h(r = r_0) = h_0$. This equation is equivalent to that developed originally by Tani (1949). Although it (or equivalent model) has been extensively (and successfully) used in the literature (Bohr *et al.* 1993; Kasimov 2008; Wang & Khayat 2019; Fernandez-Feria *et al.* 2019; Dhar *et al.* 2020), it presents significant drawbacks when describing the jump structure and flow. Clearly, equation (2.3.8) exhibits a singularity at some finite radial position. The jump radius is typically assumed to lie between two singular points reached when (2.3.8) is integrated forward (from some initial location) and backward when integrated from the disk edge (Bohr *et al.* 1993; Kasimov 2008). Alternatively, unlike other approaches, Wang & Khayat (2019) integrated (2.3.8) starting from the transition point. They successfully identified the jump radius as coinciding with the location of the singularity, validating their approach against experiment. Fernandez-Feria *et al.* (2019) validated further this approach through comparison against their numerical solution of the boundary-layer equations. However, the flow downstream of the singularity cannot be captured by continuing the solution beyond the singularity. Consequently, equation (2.3.8) cannot be used to describe the continuous jump or to capture the vortex structure downstream of the jump. Finally, given the inherent ellipticity of the boundary-layer problem, equation (2.3.8) cannot account for any upstream influence (Bowles & Smith 1992; Higuera 1994). Next, we address these issues by considering the second-order model.

We again assume a cubic velocity profile subject to conditions (2.2.2a), (2.2.3b) and (2.3.6). In order to obtain a continuous jump profile, we take the profile to satisfy the momentum equation (2.2.1b) at the disk, namely $-\frac{\text{Re}}{\text{Fr}^2} h' + u_{zz}(r, z = 0) = 0$. In this case,

the radial velocity profile is non-self-similar, and is given as a function of the surface velocity $U(r)$ and the gravitational term $\frac{\text{Re}}{\text{Fr}^2} h^2 h'$ as

$$u(r > r_0, z) = \frac{1}{4} \left[\left(6U - \frac{\text{Re}}{\text{Fr}^2} h^2 h' \right) \eta + 2 \frac{\text{Re}}{\text{Fr}^2} h^2 h' \eta^2 - \left(2U + \frac{\text{Re}}{\text{Fr}^2} h^2 h' \right) \eta^3 \right]. \quad (2.3.9)$$

Here $\eta = z/h(r)$. We observe that the non-self-similarity is due to the presence of the gravity term. An equivalent profile to (2.3.9) was adopted by Watanabe *et al.* (2003), who introduced a shape parameter $\lambda(r)$, and the profile by Bonn *et al.* (2009) for the hydraulic jump in a channel. Clearly, if (2.3.9) is adopted, the skin friction coefficient or wall shear stress is given by $\tau_w(r) = \frac{1}{4} \left(6 \frac{U}{h} - \frac{\text{Re}}{\text{Fr}^2} h h' \right)$. The flow separation points are identified by setting $\tau_w(r) = 0$. This is the case when h' is relatively large and positive. In contrast, the flow separation cannot be captured if the similarity profile is used, as it yields

$\tau_w(r) = \frac{3}{2} \frac{U}{h} > 0$. Upon substituting (2.3.9) into (2.2.4) and (2.3.7), we obtain

$$\frac{\text{Re}}{\text{Fr}^2} h^2 h' = 30U - \frac{24}{rh}, \quad (2.3.10a)$$

$$\begin{aligned} -\frac{1}{140} \left(\frac{11}{6} \frac{\text{Re}}{\text{Fr}^2} h^2 h' + 41U \right) h U' &= \frac{3}{4 \text{Fr}^2} h h' + \frac{3}{2 \text{Re}} \frac{U}{h} \\ &+ \frac{1}{28} \left(\frac{\text{Re}}{\text{Fr}^2} U h^2 h' - \frac{27}{5} U^2 - \frac{\text{Re}^2}{60 \text{Fr}^4} h^4 h'^2 \right) \left(h' + \frac{h}{r} \right), \end{aligned} \quad (2.3.10b)$$

respectively. We observe that system (2.3.10) is equivalent to the system of equations (2.25) in Watanabe *et al.* (2003). Eliminating U , we obtain an ordinary differential equation of second order in h :

$$\begin{aligned} \frac{\text{Re}^2}{\text{Fr}^2} r^2 h^4 \left(4 \frac{\text{Re}}{\text{Fr}^2} r h^3 h' + 41 \right) h'' = 1632 \text{Re} (rh)' - 6300 r^2 \\ - 2 \frac{\text{Re}}{\text{Fr}^2} r^2 h^3 h' \left[\frac{\text{Re}^2}{\text{Fr}^2} h^3 h' (5rh' + h) + 41 \text{Re} h' + 2100r \right]. \end{aligned} \quad (2.3.11)$$

We refer to system (2.3.10) or equation (2.3.11) as the second-order model. It is not difficult to see that equation (2.3.8) can be deduced from (2.3.11) for small film thickness, slope and curvature. However, it is helpful to proceed in a more systematic manner, and derive a hierarchy of equations, reflecting the (small) level of the film thickness.

For this, we introduce more appropriate length scales for the radial position and the film thickness; recall that the jet radius has been adopted so far as the common length scale. Thus, a suitable scaling that reduces (2.3.11) to a one-parameter equation is:

$$r = \text{Re}^{2/3} \text{Fr}^2 \bar{r}, \quad h = \text{Re}^{-1/3} \bar{h}. \quad (3.12a, b)$$

When the rescaled variables (2.3.12) are used, (2.3.11) reduces to an equation involving only one parameter, namely $\varepsilon \equiv \text{Re}^{-2/3} \text{Fr}^{-4}$, which is indeed typically small in practice. For instance, for the flow of silicone oil in the experiment of Duchesne *et al.* (2014), $\text{Re} = 169.1$ and $\text{Fr} = 16.87$ so $\varepsilon = 4 \times 10^{-7}$. Therefore, we take ε as perturbation or ordering parameter to generate the following equations to first and second orders:

$$O(\varepsilon): \quad 136\varepsilon (\bar{r}\bar{h})' - 525\bar{r}^2 - 350\bar{r}^3 \bar{h}^3 \bar{h}' = 0, \quad (2.3.13a)$$

$$\begin{aligned} O(\varepsilon^2): \quad \varepsilon^{3/2} \bar{r}^2 \bar{h}^4 \left(4\sqrt{\varepsilon} \bar{r} \bar{h}^3 \bar{h}' + 41 \right) \bar{h}'' = 1632\varepsilon^2 (\bar{r}\bar{h})' - 6300\bar{r}^2 \\ - 2\bar{r}^2 \bar{h}^3 \sqrt{\varepsilon} \left[\varepsilon^{3/2} \bar{h}^3 \bar{h}'^2 (5\bar{r}\bar{h}' + \bar{h}) + \bar{h}' (41\varepsilon \bar{h}' + 2100\bar{r}) \right]. \end{aligned} \quad (2.3.13b)$$

Several observations are made here. Model (2.3.8) is recovered to $O(\varepsilon)$, with a slight difference as equation (2.3.13a) has a factor of one instead of the factor 5/4 on the left-hand side of equation (2.3.8). The original second-order equation (2.3.11) corresponds to

the $O(\varepsilon^2)$ equation (2.3.13b). The hierarchy in (2.3.13) shows how the effect of gravity, in particular, influences the type of film equation. We therefore deduce that equation (2.3.13a) or (2.3.8) is suitable for a flow under moderate gravity effect, and equation (2.3.13b) or (2.3.11) should be the choice under relatively strong gravity effect. This important observation forms the basis of our solution strategy.

2.3.3 Solution strategy

In order to obtain a unique free-surface profile that ensures a smooth continuous jump, the following steps are taken in the solution process:

- (1) System (2.3.5) is solved subject to $\delta(r=0)=0$ over the range $0 \leq r \leq r_0$ to obtain the boundary-layer and film-thickness profiles between the impingement point and the transition point $r = r_0$.
- (2) Subject to the boundary condition $h(r=r_0)=h_0$ obtained, equation (2.3.8) is integrated forward in r over the range $r_0 \leq r \leq r_s$, hence generating a film thickness profile that exhibits a singularity at some finite radius $r = r_s$. Although this location is not used in the solution process, it gives a close estimate of the jump location (Wang & Khayat 2019).
- (3) Next, we integrate the second-order equation (2.3.11) over the range $r_1 \leq r \leq r_\infty$, where $r_0 \ll r_1 < r_s$ (see figure 2-1), subject to the known values of the height $h(r=r_1)$ and slope $h'(r=r_1)$ from the solution of (2.3.8). The location of the starting point r_1 for the solution of (2.3.11) is determined by ensuring that $h'(r=r_\infty) \rightarrow -\infty$.

In sum, the composite film profile is determined by solving system (2.3.5) over the range $0 \leq r \leq r_0$, equation (2.3.8) over the range $r_0 \leq r \leq r_1$ and equation (2.3.11) over the range $r_1 \leq r \leq r_\infty$. We take the jump location $r = r_J$, to coincide with $h''(r_J)=0$. Hence, r_1 is the leading edge of the jump. Finally, it is important to point out that, given the sensitivity of the solution of equation (2.3.11) on the initial conditions and the ensuing numerical instability (Watanabe *et al.* 2003; Roberts & Li 2006), the solution must begin at a location

close to the jump, thus rendering crucial the introduction of the boundary-layer and moderate-gravity regions. This, in turn, ensures the imposition of appropriate boundary conditions: $h(r = r_1)$ and $h'(r = r_1)$.

2.3.4 Upstream influence and the free-interaction problem

Figure 2-3 illustrates the solution process of the two-point boundary-value problem, with $Re = 800$, $Fr = 5$ and $r_\infty = 25$. The flow for $0 < r < r_1$ covers the developing boundary-layer and moderate gravity regions. Equation (2.3.11) is solved subject to five different initial conditions corresponding to five locations of the leading edge and height of the jump. The figure illustrates the strong influence of the starting location $r = r_1$ and $h_1 = h(r = r_1)$ on the ensuing solution of equation (2.3.11), and how the film profile (figure 2-3a) and wall shear stress (figure 2-3b) can be obtained uniquely over the entire domain. We recall that $r_1 < r_s$, where r_s is the location of the singularity reached by solving the first-order equation (2.3.8) with initial conditions at $r_0 = 4.18$ (red curve). In particular, the figure illustrates how the jump profile is influenced by the choice of r_1 . When r_1 is close to r_s , $r_1 = 11.30$, the film profile follows closely the first-order solution but avoids the singularity exhibited by the solution of the first-order equation (2.3.8), rising slightly and dropping soon after. For a smaller r_1 , here $r_1 = 11.00$, the profile extends further in the subcritical region and becomes singular at some location upstream of the disk edge. Only one value, $r_1 = 10.79$, ensures that the tail singularity ($h' \rightarrow -\infty, \tau_w \rightarrow \infty$) occurs at $r = r_\infty$. When r_1 is taken further upstream., the profile overshoots the edge of the disk. The process illustrates clearly how the upstream influence is ensured in the present approach.

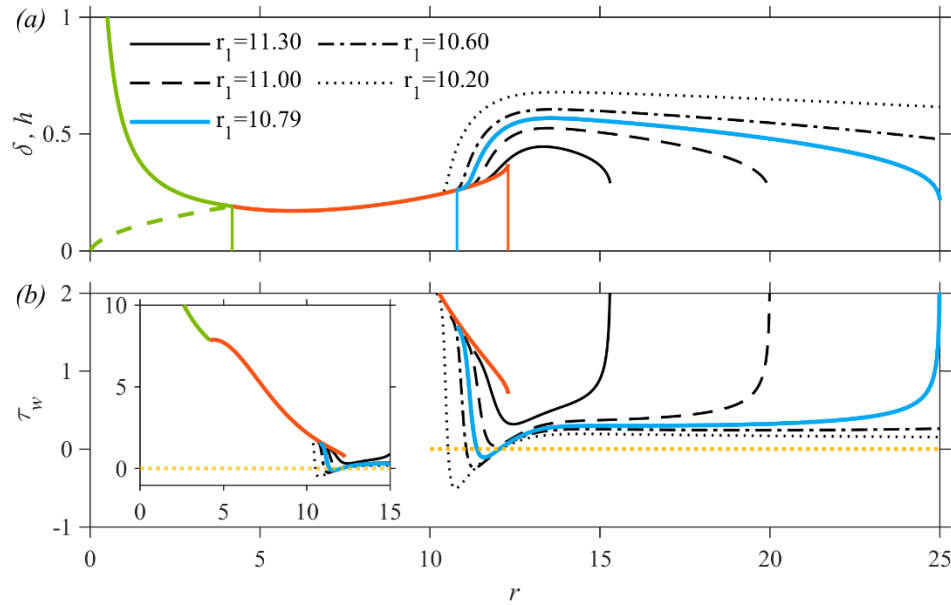


Figure 2-3: A sample case ($Re = 800$, $Fr = 5$ and $r_\infty = 25$), illustrating the shooting method and the effect of the upstream and downstream boundary conditions on the jump location (upstream influence). The distributions of film profiles (a) and the wall shear stress (b) are obtained for different initial conditions. The green solid and dashed curves correspond to the profiles of the film and boundary layer, respectively, in the developing boundary-layer region. Here, the transition location is at $r = r_0 = 4.18$. (green vertical line). The red curve corresponds to the variation of the film thickness in the moderate-gravity viscous region, obtained by solving the first-order equation (2.3.8), and exhibiting a singularity at $r = r_s = 12.3$ (red vertical line). The black and blue curves show branches of the solution for the film thickness variation in the strong-gravity viscous region obtained by solving the second-order equation (2.3.11). Depending on the value of r_1 (and consequently h_1) the solution may or may not reach the edge. The unique solution to the problem (blue curve), corresponding to an infinite slope at the edge of the disk, is obtained for $r_1 = 10.7931$ (blue vertical line).

The profiles in figure 2-3, obtained subject to different initial conditions, are reminiscent of the profiles in figure 3 of Bowles (1995), who examined the free-interaction problem of the planar flow of a sloped liquid layer over an obstacle. Bowles described the internal structure of the *continuous* jump as dominated by the viscous-inviscid interaction between

the hydrostatic pressure gradient and the viscous effects near the solid wall (see also the earlier work of Gajjar & Smith (1983) and the dissertation of Bowles 1990). As Bowles (1995) observes, the free interaction in the internal jump structure involves one of two types of mechanism, depending on the pressure development: “The pressure may increase, possibly leading to separation (a compressive interaction) or it may decrease, leading perhaps to a finite-distance singularity in the solution (an expansive interaction).” The solution branches in our figure 2-3 reflect the two possibilities, namely an expansive interaction with a singularity and no separation for $r_1 = 11.00$ and 11.30 , and a compressive interaction for $r_1 = 10.20$, 10.60 and 10.79 with separation. We recall that imposing these different initial locations is equivalent to imposing different initial film heights provided through the solution of equation (2.3.8).

Similarly, by varying the initial conditions, Bowles (1995) sought the solution for the sloped film flow by imposing a perturbation on the otherwise uniform film surface and corresponding half-Poiseuille flow far upstream. The flow was sought as a superposition of the base flow and an exponentially developing flow. The resulting (linearized) eigenvalue problem was solved numerically. Bowles found that the type of film profile obtained depends on the level of the perturbation of the uniform film. For a perturbed film with a slightly diminished thickness, the film profile was found to terminate in an expansive interaction, similar to the two profiles starting at $r_1 = 11.00$ and 11.30 in our figure 2-3, with the derivative of the layer’s depth becoming large and negative (figure 2-3a). The corresponding skin friction in figure 2-3b becomes large and positive, while the depth of the film remains finite of $O(1)$. Higuera (1994) showed that this type of singularity is algebraic rather than logarithmic as in the problem of the free interaction in hypersonic flow (Brown, Stewartson & Williams 1975; Bowles 1990). For a perturbed film with a slightly augmented height relative to the upstream uniform height, Bowles (1995) found that the film surface becomes horizontal far downstream (with no singularity). For a relatively large bed slope, a jump emerges for a positively perturbed film height. In that case, a separation occurs with compressive interaction, which is reflected in our figures 2-3a and 2-3b for $r_1 = 10.20$, 10.60 and 10.79 . Figure 2-3a indicates that if the solution starts at a relatively distant r_1 from impingement, a weak jump forms as a result of strong viscous

and weak inertial effects; the film comes to a halt. Conversely, if the initial distant r_1 is closer to impingement, fluid accumulates with a strong jump and upward slope, causing the development of an adverse pressure gradient and a separation. Consequently, we highlight an important distinction from the observations of Bowles (1995), which we demonstrate throughout the present study: the hydraulic jump can actually form without being followed by a recirculation zone. Finally, it is worth mentioning that the magnitude of the perturbations imposed by Bowles (1995) was relatively small (of the order of 10^{-6} to 10^{-2} compared to 1, the normalized film depth). This suggests that the solution is sensitive to initial conditions, which is also the case in our computations (see also Watanabe *et al.* 2003).

2.3.5 Asymptotic flows

Two well-established limit flows are worth including for reference. The first is the limit of infinite Froude number in the supercritical region. We note that the supercritical flow consists essentially of a balance between inertia and viscosity effects with negligible gravity effects. This limit was first considered by Watson (1964) and later adopted by others (see Wang & Khayat 2019 and references therein). For $Fr \rightarrow \infty$, the solution of equations (2.3.5) upstream of the transition point reduces to

$$\delta(r < r_0) = 2\sqrt{\frac{70}{39} \frac{r}{Re}}, \quad h(r < r_0) = \frac{1}{4} \left(\sqrt{\frac{210}{13} \frac{r}{Re} + \frac{2}{r}} \right), \quad (2.3.14, a, b)$$

$$U(r < r_0) = 1. \quad (2.3.14c)$$

The transition point is determined by setting $\delta(r_0) = h(r_0)$, yielding $r_0 = \left(\frac{78 Re}{875} \right)^{1/3}$, which is closely reflected in figure 2-3. Based on (2.3.14a), the boundary layer grows like \sqrt{r} , and the film height decreases predominantly like $1/r$, as is also reflected in figure 2-3. Downstream of the transition point, the flow is governed by equations (2.3.8). Setting $Fr \rightarrow \infty$, it is not difficult to show that the solution reduces to

$$h(r \geq r_0) = \frac{233}{340} \frac{1}{r} + \frac{175}{136} \frac{r^2}{\text{Re}}, \quad U(r \geq r_0) = \frac{4}{5rh}, \quad (2.3.15a, b)$$

suggesting that h decreases like $1/r$ for small r and increases like r^2 for large r , as reflected in figure 2-3. For comparison, Watson's expressions are reproduced here in dimensionless form:

$$h(r > r_0) = \frac{3c(3\sqrt{3}c - \pi)}{8\pi} \frac{1}{r} + \frac{2\pi}{3\sqrt{3}} \frac{r^2}{\text{Re}}, \quad U(r > r_0) = \frac{3\sqrt{3}c^2}{4\pi rh}, \quad (2.3.16a, b)$$

where $c = 1.402$. Comparison of the numerical coefficients between (2.3.15) and (2.3.16) reveals a surprisingly close agreement between Watson's similarity solution and that based on the cubic velocity profile (see also Prince *et al.* 2012).

The second asymptotic flow often used in the literature is the limit of negligible inertia in the subcritical region. The flow is captured using lubrication theory, which consists of integrating equation (2.2.1b) subject (2.2.2a) and (2.2.3b) to obtain the parabolic velocity profile $u = \frac{\text{Re}}{\text{Fr}^2} h' \left(\frac{z^2}{2} - hz \right)$. Upon using the mass conservation equation (2.2.4), we

obtain the equation for h . This finally yields the following profiles for the film thickness and surface velocity:

$$h = \left[h_\infty^4 + 6 \frac{\text{Fr}^2}{\text{Re}} \ln \left(\frac{r_\infty}{r} \right) \right]^{1/4}, \quad U = \frac{3}{4rh}, \quad (2.3.17a, b)$$

where we recall h_∞ to be the thickness at the edge of the disk.

2.4 Validation

In this section, we validate our approach against existing measurements and numerical simulation. Additional features are reported on the flow observed and simulated, which illustrates the capabilities of our approach to capture some of the jump and vortex structure not captured by existing models.

2.4.1 Validation against numerical models

We first validate our approach against the numerical solutions of the Navier-Stokes (NS) equations and the boundary-layer equations (2.2.1) of Fernandez-Feria *et al.* (2019), as well as the depth-averaged model of Kasimov (2008). Unlike the first-order equation (2.3.8) which requires upstream and downstream boundary conditions to generate the inner and outer solutions (Kasimov 2008; Wang & Khayat 2019), the boundary-layer equations (2.2.1) and equation (2.3.11) can accommodate two boundary conditions specified at the same or two different radial locations. However, specifying the two boundary conditions at the same location, such as near impact, may not generate an accurate profile, as seen in figure 2-4a from the boundary-layer profile. In this regard, Higuera (1994) recognized the elliptic nature of the boundary-layer equations, and the need to ensure the upstream influence of the flow near the edge; boundary conditions must be imposed upstream and downstream of the jump. We note that Kasimov (2008) imposed (arbitrarily) the surface velocity and the film thickness at a radius 20% larger than the jet radius. At this radius, Kasimov set the surface velocity equal to the jet velocity at impingement, and the film thickness was imposed by satisfying the conservation of mass. As shown in figure 2-4a, our approach yields a better agreement with the Navier-Stokes solution compared with the boundary-layer and the first-order models. Clearly, the boundary-layer solution, which is not subject to a downstream boundary condition, fails to capture the free-surface profile close to the edge of the disk. On the other hand, the condition $h'(r = r_\infty) \rightarrow -\infty$ imposed in our approach and in the first-order model of Kasimov (2008) yields a close agreement with the Navier-Stokes solution. We see that Kasimov's solution overestimates the supercritical film thickness and underestimates the jump location. This is a consequence of the over-representation of viscous friction when using the parabolic profile. Moreover, this model cannot capture the vortex below the jump due to the shock-like assumption of the jump and the simple similarity profile adopted. Our close agreement with the NS supercritical profile confirms the necessity of first determining the boundary-layer flow near impact; this yields the suitable upstream boundary condition for the solution of equation (2.3.8), and further (2.3.11), in the viscous region. Simultaneously, the treatment of the flow in the developing boundary-layer region circumvents the need to fix arbitrarily

or empirically an upstream boundary condition as in the case of Kasimov (2008) or Fernandez-Feria *et al.* (2019).

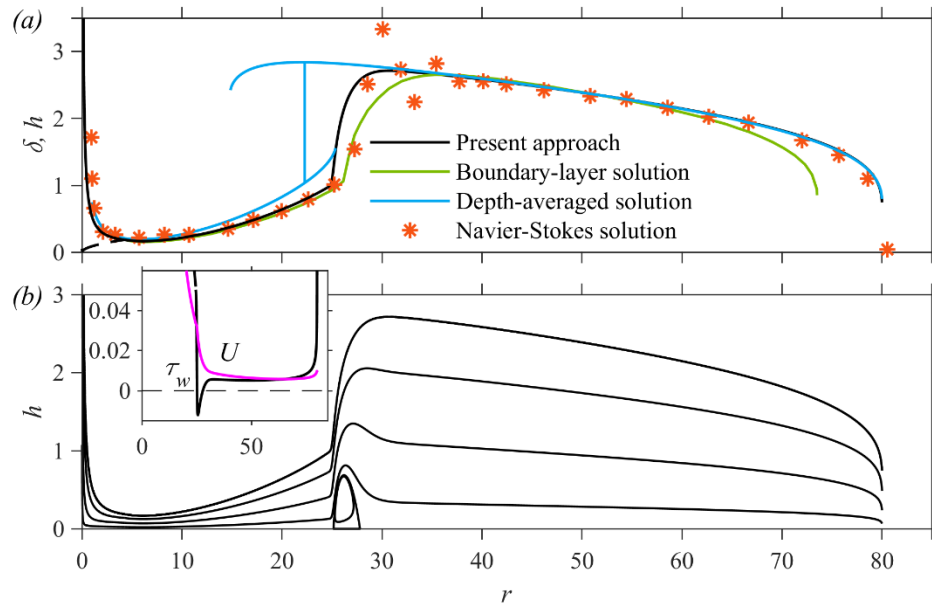


Figure 2-4: (a) Comparison of the free-surface profile based on the present approach against the boundary-layer and Navier-Stokes profiles of Fernandez-Feria *et al.* (2019), as well as the depth-averaged based profile of Kasimov (2008) for $Re = 854.29$, $Fr = 97.19$ and $r_\infty = 80$. (b) Visualization of the flow field based on the present approach (U and τ_w distributions in inset).

Figure 2-4b shows our predictions of the flow streamlines, as well as the wall shear stress and the surface velocity distributions (inset). The flow structure clearly shows a vortex at the bottom in conjunction with the jump. The shear stress decreases monotonically upstream of the jump. This monotonicity is expected given the weak gravity effect in the supercritical region; in the boundary-layer region, the wall shear stress $\tau_w = 3/2\delta$, and further downstream, the film slope is negligibly small and (2.3.9) indicates that $\tau_w \approx 3U/2h$. In the vicinity of the jump, a recirculation zone appears, corresponding to $\tau_w(r) \leq 0$. The separation and the reattachment of the flow are the consequence of the rapid change of the hydrostatic pressure induced by the rapid increase of the film thickness at the jump. We note that profile (2.3.9) indicates that τ_w vanishes when

$U = \text{Re} h^2 h' / 6\text{Fr}^2$. Consequently, (2.3.10a) reduces to $\text{Re} h^2 h' / \text{Fr}^2 = 6 / rh$, indicating that $h' > 0$. Thus, the separation and reattachment occur below the ascending film portion; the vortex is therefore confined below the jump (Higuera 1994). The vortex also takes a similar shape to that based on the boundary-layer approach of Higuera (1994), as well as the second-order models of Watanabe *et al.* (2003), Roberts & Li (2006) and Bonn *et al.* (2009). The vortex is always placed under the jump region as a result of the balance between the shear forces applied by the disk and the flow above the vortex, which are directed towards the disk edge, and the hydrostatic pressure force, directed towards the impingement zone (Higuera 1994). The surface velocity U decreases after experiencing a weak maximum (not visible here).

Figure 2-5 shows a further comparison between the present approach and the numerical solution of the boundary-layer equations of Fernandez-Feria *et al.* (2019). Shown are the radial distributions of the film profile h (figure 2-5a), the wall shear stress τ_w (figure 2-

5b), the gravity term $-\frac{\text{Re}}{\text{Fr}^2} h h'$ (figure 2-5c) and the radial momentum flux term

$m \equiv \frac{\text{Re}}{r} \frac{d}{dr} \int_0^h r u^2 dz$ (figure 2-5d) in equation (2.3.7). The comparison of the flow details

shows surprisingly close agreement given the simplicity of the present approach and its capability in reproducing the physical mechanisms at the jump. As Fernandez-Feria *et al.* (2019) observed, upstream of the jump the radial momentum flux almost balances the shear stress at the wall, the gravitational term being almost negligible in comparison with the inertial and viscous terms. Close to the jump inception, the shear stress drops suddenly (figure 2-5b), becoming negative but small in magnitude. This drop is compensated by the abrupt growth of the gravity term (figure 2-5c) to balance the momentum flux (figure 2-5d), causing the jump to form (figure 2-5a). Hence, while the shear stress is negative and small in the recirculating flow region, the momentum flux is balanced almost exclusively by gravity. Further downstream, inertia becomes negligible, leaving the viscous and gravity forces in balance. Thus, downstream of the recirculation zone, the flow reaches a lubrication limit so that the velocity profile is practically parabolic. This is the reason why the lubrication assumption in the subcritical region yields an accurate description of the

flow (Duchesne *et al.* 2014; Wang & Khayat 2018, 2019). However, and as we discuss below, the lubrication character in the bulk subcritical region does not extend all the way to the edge of the disk, where inertia, viscosity and gravity (as well as surface tension) become equally important (Higuera 1994). Fernandez-Feria *et al.* (2019) mentioned that the boundary-layer or thin-film approach equations are no longer valid (nor, of course, is the lubrication approximation) near the edge of the disk. This is, of course, true in principle as $|h'|$ becomes very large at the edge. However, as our calculations and the agreement in figure 2-4 suggest, the boundary-layer or the present thin-film approach seems to hold around the sharp corner at the edge of the disk; the coincidence of the singularity with the edge location turns out to be sufficient to account for the upstream influence analysed by Higuera (see below).

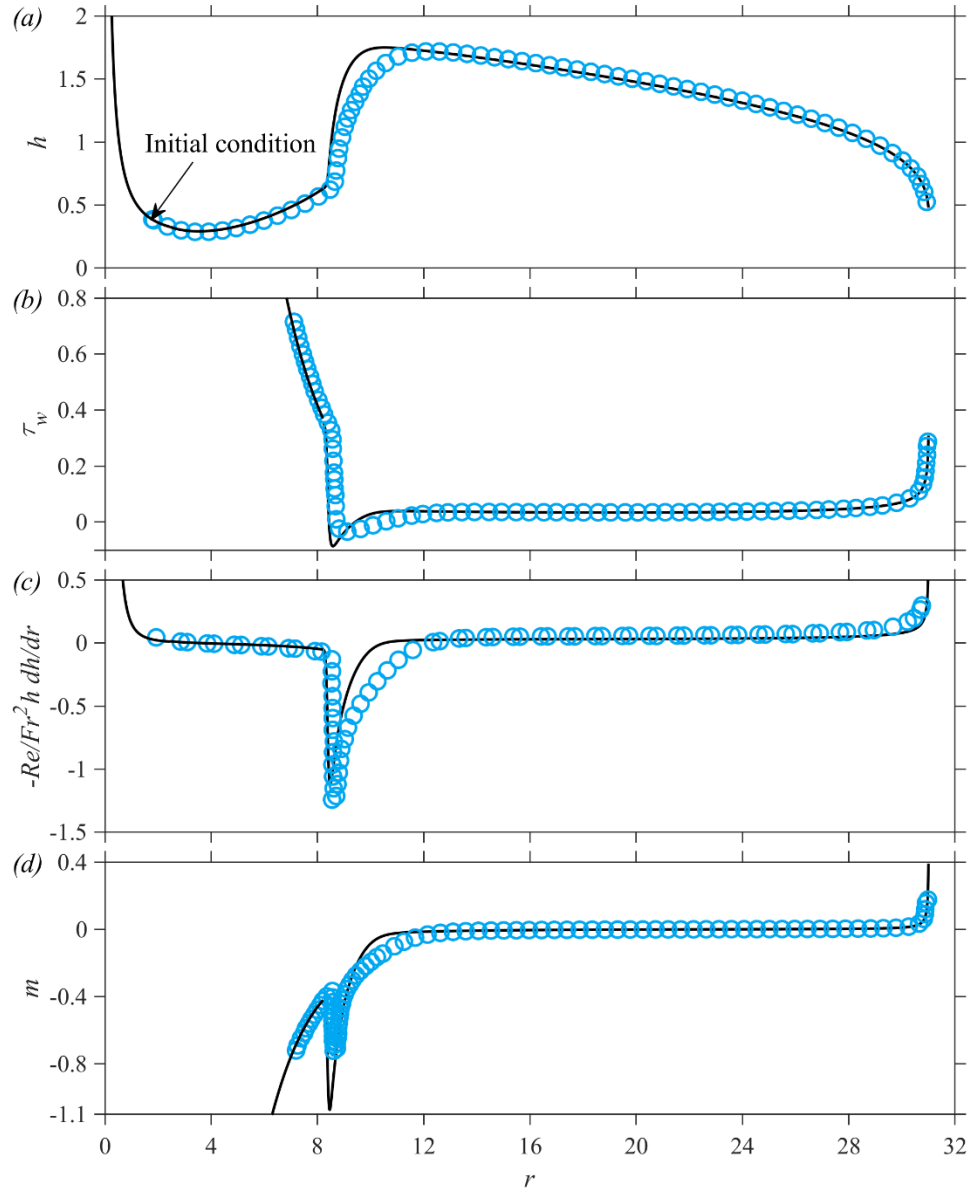


Figure 2-5: Comparison of the present approach (solid curves) against the numerical solution of the boundary-layer equations (open circles) of Fernandez-Feria *et al.* (2019) for the radial distributions of (a) the film profile, (b) the wall shear stress, (c) the gravity term and (d) the radial momentum flux term in equation (2.3.7). Here the liquid is silicone oil with $Re = 164.98$, $Fr = 16.87$ and $r_\infty = 31$.

2.4.2 Comparison against experiment

Next, we validate our approach against the measurements of Duchesne *et al.* (2014) for silicone oil (20 cSt) of density 960 kg m^{-3} and kinematic viscosity $2 \times 10^{-5} \text{ m}^2 \text{ s}^{-1}$. The liquid was injected downward from a jet of radius $a = 1.6 \text{ mm}$ onto a horizontal circular disk of radius $R_\infty = 15 \text{ cm}$. The flow conditions in dimensionless form correspond to $\text{Re} = 169.1$, $\text{Fr} = 16.87$ and $r_\infty = 93.75$. The comparison of the free-surface profiles based on our approach and experiment is shown in figure 2-6. We also included the prediction from the Navier-Stokes numerical solution of Zhou & Prosperetti (2022). As in the numerical simulation of Wang & Khayat (2021), the steady state was reached through the evolution of the transient flow. Zhou & Prosperetti (2022) reported that the computational domain was initially full of a gas medium with density and viscosity three orders of magnitude smaller than those of the liquid. The jet was injected from the inlet with a uniform velocity profile. For all wall boundaries the no-slip condition was used. At the outlet of the domain, the flow was essentially fully developed, with the static pressure fixed to a reference value. A standard outlet condition was used for the velocity; the velocity gradient normal to the boundary was set equal to zero.

The present approach agrees well with experiment, but like the numerical solution it underestimates slightly the supercritical film thickness. Measuring the film height in this thin-film region may be associated with uncertainties. In contrast, in the subcritical region, the theoretical and numerical predictions almost fit all the experimental data points, except near the disk edge. The agreement with the Navier-Stokes solution of Zhou & Prosperetti (2022) is surprisingly close. We recall that the effect of surface tension was neglected in our model but was included in the numerical simulation (see also Wang & Khayat 2021), confirming that, in this case, the effect of surface tension may only be important near the edge and at the jump. We recall that the agreement was equally close between our approach and the numerical simulation in the absence of surface tension (figure 2-4). We discuss the edge thickness in more detail later. As far as the location of the jump is concerned, we see that the experimental data suggest a slightly smaller jump radius than that predicted by our approach and the numerical simulation. However, our theoretical prediction of the free-surface profile agrees well with the numerical one in the jump region. Finally, we have also

included in figure 2-6 the subcritical profile based on the lubrication solution for reference, showing close agreement with experimental and numerical results, with some discrepancy near the jump.

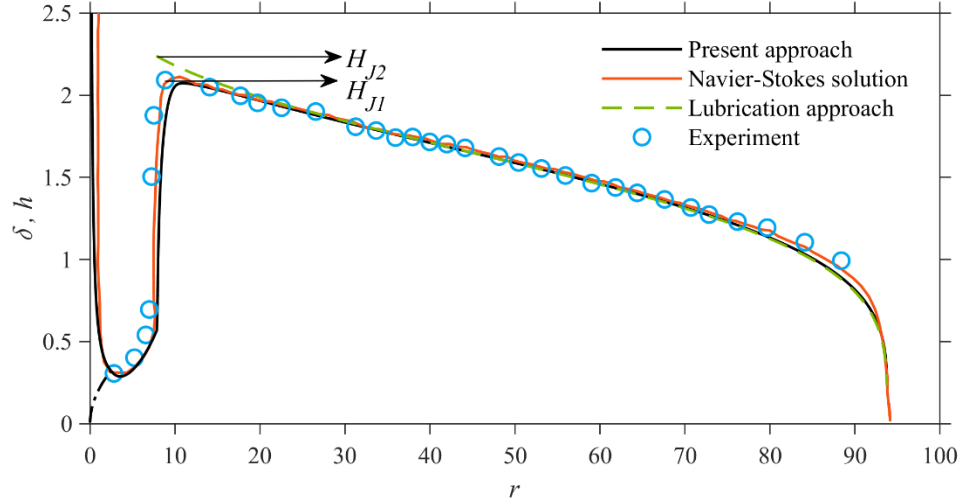


Figure 2-6: Comparison of the free-surface profiles between our present approach (black solid line) and the measurements (open blue circles) of Duchesne *et al.* (2014). The Navier-Stokes solution of Zhou & Prosperetti (2022) is also included (red solid line) as well as the lubrication solution (green dashed line). Arrows point to the jump heights $H_{J1} = h_{max}$ and H_{J2} based on the present and lubrication approaches, respectively. Here, $Re = 169.1$, $Fr = 16.87$ and $r_{\infty} = 93.75$.

Further theoretical details of the flow in figure 2-6 are given in figure 2-7, where we show our predictions of the flow streamlines (figure 2-7a), the wall shear stress (figure 2-7b) as well as the surface velocity (figure 2-7c) profiles. The flow structure in figure 2-7a clearly shows a vortex at the bottom in conjunction with the jump. The film thickness predicted using the first-order model (2.3.8) (depicted by the red curve) does not cross the jump since it terminates by a singularity. Nevertheless, the location of the singularity ($r = r_s$) is shown to be close to the end of the separation zone predicted using the second-order theory.

Figure 2-7b depicts the distribution of the wall shear stress over the entire disk. The shear stress decreases monotonically upstream of the jump. As mentioned earlier, this monotonicity is expected given the weak gravity effect in the supercritical region. In this

case, (2.3.9) indicates that $\tau_w \approx 3U/2h$, which explains the sharper drop of the stress than the velocity as h increases with r . Further downstream, near the jump, a small separation zone corresponding to $\tau_w \leq 0$ is observed over the range $7.93 < r < 9.58$. We recall from our earlier observation that separation occurs while the film slope is positive. Therefore, the vortex is confined between r_J and r_m , with $h''(r_J) = h'(r_m) = 0$. Simultaneously, U decreases, after experiencing the maximum shown in the inset of figure 2-7c. Indeed, at the separation point, we recall that $\frac{\text{Re}}{\text{Fr}^2} h^2 h' = \frac{6}{rh}$, leading to $U = \frac{1}{rh}$. In this case,

$$U' = -\frac{1}{r^2 h} - \frac{\text{Fr}^2}{\text{Re}} \frac{6}{r^2 h^5} < 0. \text{ Downstream of the separation region, the wall shear stress}$$

remains almost unchanged before exhibiting a sharp increase at the disk edge. The stress profile mimics well the flow condition at the disk edge, where a corner or stress singularity occurs (Higuera 1994; Scheichl *et al.* 2018). This, in turn, justifies taking an infinite slope at the edge of the disk. The correlation between the stress singularity and infinite slope becomes evident when we deduce the wall shear stress from profile (2.3.9) and use (2.3.10a) to eliminate U :

$$\tau_w(r = r_\infty) = \frac{1}{4} \left(6 \frac{U}{h} - \frac{\text{Re}}{\text{Fr}^2} hh' \right)_{r=r_\infty} = \frac{1}{5} \left(\frac{6}{rh^2} - \frac{\text{Re}}{\text{Fr}^2} hh' \right)_{r=r_\infty} \approx -\frac{\text{Re}}{5\text{Fr}^2} (hh')_{r=r_\infty}, \quad (2.4.1)$$

which confirms the equivalence between the stress and geometrical singularities, and justifies taking an infinite slope at the edge of the disk as a result of the stress singularity (Higuera 1994; Kasimov 2008; Dhar *et al.* 2020).

Figure 2-7c shows that the surface velocity remains equal to one in the developing boundary-layer region, then decreases, under viscous effects, almost linearly until the jump occurs. A small rise in the surface velocity is observed near the jump (see the inset of figure 2-7c, showing a small bump in U at $r \approx 7.93$). In fact, U experiences a local maximum, coinciding with the change in the concavity at the jump radius. Indeed, upon differentiating (2.3.10a) and noting the dominance of the surface slope, we see that $U' \approx \frac{1}{15} \frac{\text{Re}}{\text{Fr}^2} hh'^2$,

reflecting the increase in U at the jump location. Further downstream, U decrease

monotonically and maintains an almost constant value in the subcritical region. In fact, inertia in this region is negligible, so the flow can be predicted reasonably well using the lubrication theory (see Duchesne *et al.* 2014; Wang & Khayat 2018, 2019; Baayoun *et al.* 2022). However, as discussed by Higuera (1994), inertia becomes important again as the flow approaches the edge, resulting in a velocity increase close to the edge. Unlike the lubrication approach, our theory captures the flow complexity near the edge (see next).

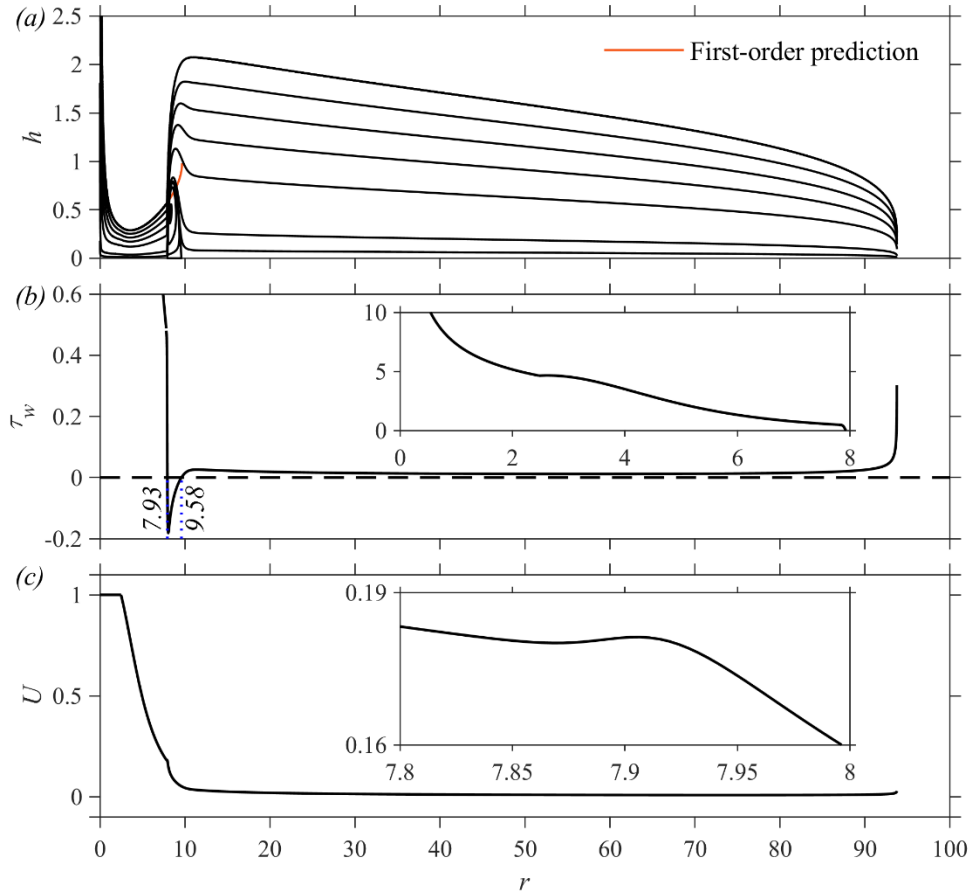


Figure 2-7: Flow details corresponding to the profile in figure 2-6 using the present approach. Shown are the flow streamlines (a), the wall shear stress distribution (b) and the surface velocity distribution (c). The results are plotted in dimensionless form with $Re = 169.10$, $Fr = 16.87$ and $r_\infty = 93.75$. In (a), the red curve represents the supercritical free surface of the film, showing a singularity, predicted using the first-order model (2.3.8).

Figure 2-8 shows the influence of Fr on the jump radius in figure 2-8a, on the maximum film height h_{\max} in figure 2-8b, and on the Froude number at the jump in figure 8c. The measurements of Duchesne *et al.* (2014) are included for comparison over the same range of Fr as the experiment. The dependence on Fr reflects the dependence on the jet flow rate, in which case the Galileo number is maintained at $Ga = Re^2 / Fr^2 = 100$. Our predictions are in good agreement with the measurements, essentially over the entire range of flow rates, reflecting a growth $r_J \sim Fr^{7/10}$ (inset in figure 2-8a). This behaviour is essentially the same as the one reported by Hansen *et al.* (1997), based on their measurements for silicone oil ($r_J \sim Fr^{0.72}$).

Figure 2-8b shows an overall good agreement for h_{\max} against the measurements of Duchesne *et al.* (2014), suggesting that $h_{\max} \sim Fr^{4/25}$ (inset in figure 2-8b). This growth is most likely accompanied by a similar or faster growth of the supercritical film thickness, eventually leading to the vanishing of the jump as gravity continues to weaken (see below). Duchesne *et al.* (2014) observed that the Froude number at the jump, $Fr_J \equiv Fr / 2r_J h_{\max}^{3/2}$, is independent of Fr . Figure 2-8c shows that this independence seems to hold when we compare our prediction against the measured Fr_J . Indeed, recalling from figures 2-8a and 2-8b that $r_J \sim Fr^{7/10}$ and $h_{\max} \sim Fr^{4/25}$, we deduce that $Fr_J \sim Fr^{0.06}$, confirming the quasi Fr independence.

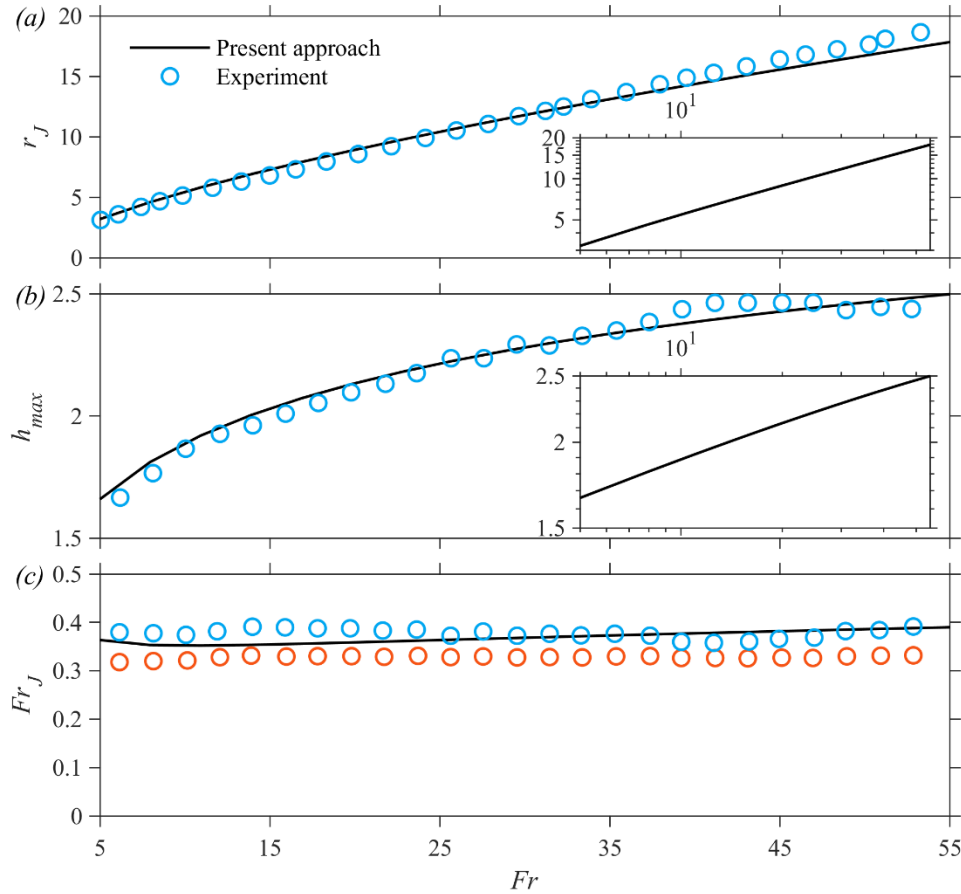


Figure 2-8: Influence of Fr (flow rate) on (a) the jump radius r_J (inset shows $r_J \approx 1.08Fr^{7/10}$), (b) the maximum film height h_{max} (inset shows $h_{max} \approx 1.32Fr^{4/25}$) and (c) the Froude number at the jump Fr_J over the experimental flow rate range of Duchesne *et al.* (2014), corresponding to $50.11 < Re < 551.25$ or $Ga = 100$. Theoretical results (black solid curves) are compared against the measurements (blue circles) of Duchesne *et al.* (2014). In (c), the open blue and red circles represent the Fr_J values based on the measured heights H_{J1} and the height H_{J2} (see figure 2-7).

Figure 2-9 shows the dependence of the jump location on the Froude number (flow rate), where comparison is carried out against the measurements of Hansen *et al.* (1997), the spectral inertial-lubrication solution of Rojas *et al.* (2010) as well as the Navier-Stokes solution of Zhou & Prosperetti (2022) for water and silicone oil. We have included our results using the same log–log ranges used by Rojas *et al.* (2010) in their figure 2 and Zhou & Prosperetti (2022) in their figure 3. Our predictions are in close agreement with both

numerical results. The agreement with the oil data is quite good. That with the water data is less so, although our results are in very close agreement with those of Rojas *et al.* (2010) and Zhou & Prosperetti (2022). We may also note that Hansen *et al.* (1997) stated that the radius of the jump was oscillating for Q greater than approximately $15 \text{ cm}^3 \text{ s}^{-1}$ ($Fr > 1.5$) so that the experimental data reported are mean values. Zhou & Prosperetti (2022) noted that the unsteadiness mentioned by Hansen *et al.* (1997) was not observed in their simulation. We also recall that Rojas *et al.* (2010) had to impose the thickness at the edge of the disk as measured by Hansen *et al.* (1997). Both the present theoretical and existing numerical predictions tend to overestimate equally the jump radius compared to the measurements for water. The discrepancy appears to be higher for low flow rates, for a given liquid. A plausible explanation for the discrepancy is the difficulty in accurately locating the jump radius in reality. The qualitative and quantitative agreement with the numerical models is especially encouraging given the simplicity of the present approach compared with the spectral approach and numerical simulation.

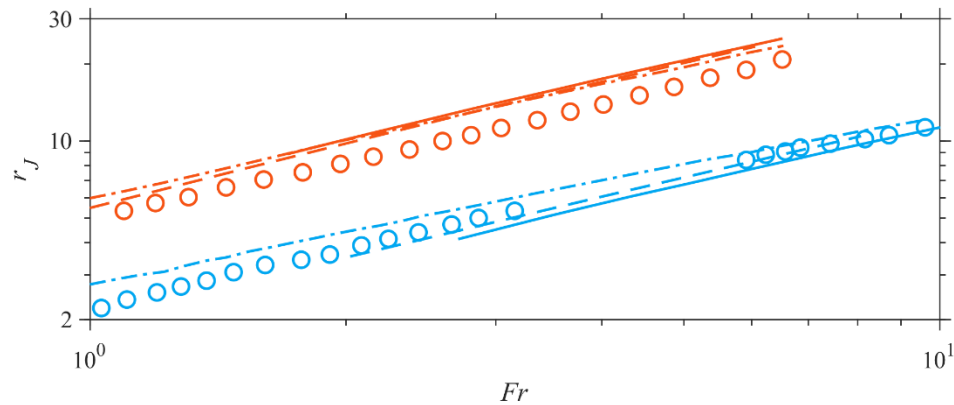


Figure 2-9: Comparison of our approach (solid lines) for the jump radius with the measurements of Hansen *et al.* (1997) (open circles). Results for water ($Ga = 627840$) are in red, those for silicone oil ($Ga = 2790$) are in blue. The dash-dotted lines are the predictions of the spectral inertial-lubrication model developed by Rojas *et al.* (2010), and the dashed lines those of the Navier–Stokes simulations of Zhou & Prosperetti (2022).

2.4.3 The nature of the subcritical flow

The present approach seems to capture well the turn-around usually observed at the edge of the disk. This is particularly obvious from our comparison with experiment and the solution of the boundary-layer and Navier-Stokes equations as shown in figures 2-4a, 2-5a and 2-6. As the work of Higuera (1994) suggests, both inertia and gravity become important at the edge. Obviously, inertia is neglected in a lubrication approach for the subcritical flow, which seems to yield an accurate description of the flow, including the vicinity of the jump, but less so near the edge, where the acceleration of the flow tends to infinity as a result of strong gravity effect (Duchesne *et al.* 2014; Wang & Khayat 2018/2019). Consequently, at the edge, the wall shear stress should exhibit a (corner) singularity, and viscous effects are confined to a thin boundary layer that develops near the wall, similar to the free-surface flow exiting a channel (Tillet 1968; Khayat 2014, 2016, 2017). Higuera (1994) carried out a matched asymptotic expansion and developed the solution in the viscous thin layer near the plate and matched it to the bulk solution in the inviscid region lying above. Higuera also estimated the order of magnitude of the region near the edge where inertial effects cease to be negligible in the subcritical region to be

$$1-x = O\left(\left(\frac{\text{Fr}^2 \text{Re}^3}{L^3}\right)^{1/3}\right). \text{ This range is recast here in terms of the jet Froude and Reynolds}$$

numbers, where L is the half-length of the plate scaled by the half-width of the jet, and $x = 1$ coincides with the plate edge. We follow Higuera (1994), and establish a similar estimate in our axisymmetric case by balancing the inertial term with the hydrostatic pressure gradient term in the momentum equation (2.2.1b), or by setting $\text{Re} U \frac{dU}{dr} \sim \frac{\text{Re}}{\text{Fr}^2} \frac{dh}{dr}$, where

U and h are the subcritical surface velocity and film thickness. On the other hand, ignoring the convective terms, and integrating (2.2.1b), we arrive at the lubrication result:

$$U = -\frac{1}{2} \frac{\text{Re}}{\text{Fr}^2} \frac{dh}{dr} h^2. \text{ Following Higuera (1994) and setting } h_\infty \approx 0, \text{ we obtain from}$$

(2.3.17a): $h = \left[\frac{6\text{Fr}^2}{\text{Re}} \ln\left(\frac{r_\infty}{r}\right) \right]^{1/4}$. Finally, the range where inertial effects become important near the edge is $1 - \frac{r}{r_\infty} = O\left(\left(\frac{\text{Fr}^2 \text{Re}^3}{r_\infty^8}\right)^{1/3}\right)$.

2.5 Further results

In this section, we examine further the influence of the flow rate on the flow and jump structure over the same range of flow rates as considered by Duchesne *et al.* (2014). We also keep the same conditions as in their experiment. In this case, $5 < \text{Fr} < 55$ and $\text{Re} = \sqrt{\text{GaFr}}$, where the Galileo number remains very close to $\text{Ga} = 100$. Although the additional theoretical details reported in this section do not have their counterpart in the experiment of Duchesne *et al.* (2014), the aim of including them here is to motivate further measurements. The influence of gravity and viscosity is also examined. We particularly focus on the film profile, the wall shear stress distribution and the flow field in the vicinity of the jump.

2.5.1 The influence of the flow rate

Further details of the influence of the flow rate on the flow are reported in figure 10, where the radial distributions of the film profile, wall shear stress and surface velocity are shown in figures 2-10a, 2-10b and 2-10c, respectively. Although similar or equivalent flow details were not reported by Duchesne *et al.* (2014), the results in figure 2-10 and this section correspond to the same range of flow rates and conditions of their experiment. Figure 2-10a shows that the boundary-layer thickness diminishes with increasing flow rate, following closely (2.3.14a), with the film thickness profile well reflected in (2.3.14b). The figure indicates that although the jump radius and height both grow with the Froude number (as shown in figure 2-8), the shape of the jump, particularly its steepness or slope, is insensitive to the Froude number. While the supercritical region extends and diminishes in thickness, the subcritical region shrinks in length with diminishing thickness growth with flow rate, evolving from an essentially linear to a logarithmic (lubrication) profile (excluding the vicinity of the edge). Figure 2-10b suggests that the recirculation zone

increases with flow rate, with the rate of drop in the wall shear stress diminishing until it eventually vanishes. Hence, the vortex beneath the jump widens but the height behaves inconsistently as the flow rate increases.

Although the surface velocity appears to decrease monotonically with radial distance (figure 2-10c), this is not the case upon local scrutiny. We have already seen in figure 2-7c that U experiences a weak maximum just where the stress drops. This is confirmed further in the first inset of figure 2-10c for $Fr = 5$ where a relatively strong maximum occurs. The second inset in figure 2-10c indicates that while the velocity increases with distance as the flow approaches the edge of the disk at relatively low Fr , it decreases with distance at relatively high Fr . Physically, this reversal in trend is the result of the enhanced accumulation of the subcritical fluid with increasing flow rate.

It is worth mentioning first that the trend reversal in figure 2-10c is not predictable for subcritical lubrication flow. Indeed, recalling (2.3.17b) above or (5.6) from Wang & Khayat (2019) for the parabolic velocity profile for lubrication flow, we see from mass

conservation that $U = \frac{3}{4rh}$ or $U' = -\frac{3}{4rh^2} \left(h' + \frac{h}{r} \right)$. When applied at the edge of the disk,

and recalling the dominant slope, this relation yields $U'_\infty \approx -\frac{3h'_\infty}{4r_\infty h_\infty^2}$, confirming that U'_∞

is always positive for a draining fluid ($h'_\infty < 0$). Rewriting equation (2.3.10b), after using (2.3.10a), as

$$-\frac{1}{35} \left(24U - \frac{11}{rh} \right) hU' = \frac{3}{4Fr^2} hh' + \frac{3}{2Re} \frac{U}{h} + \frac{12}{35} \left(U^2 - \frac{1}{r^2 h^2} \right) \left(h' + \frac{h}{r} \right), \quad (2.5.1)$$

we first observe that the coefficient of U' is always negative at the edge for any flow rate. Consequently, when applying equation (2.5.1) at the disk edge, we see that the sign of U'_∞ depends on the competition among gravity, viscosity and inertia effects, represented by the

terms $\frac{3}{4Fr^2} hh'$, $\frac{3}{2Re} \frac{U}{h}$ and $\frac{12}{35} \left(U^2 - \frac{1}{r^2 h^2} \right) \left(h' + \frac{h}{r} \right)$, respectively, on the right-hand

side of (2.5.1). As we recall from Wang & Khayat (2019), the thickness and velocity at the

edge of the disk are $h_\infty = O(\text{Fr}^{2/3})$ and $U_\infty = O(\text{Fr}^{-2/3})$, respectively. Therefore, the viscous term is $O(\text{Re}^{-1} \text{Fr}^{-4/3})$ and is negligible at the edge, so that

$$U'_\infty \sim - \left[\frac{3}{4\text{Fr}^2} h_\infty + \frac{12}{35} \left(U_\infty^2 - \frac{1}{r_\infty^2 h_\infty^2} \right) \right] h'_\infty . \quad \text{From (2.3.10a), we deduce that}$$

$U_\infty^2 - 1/r_\infty^2 h_\infty^2$ is always negative. For relatively small flow rate ($\text{Fr} < 25$ in figure 2-10c),

U'_∞ is positive, and becomes negative as Fr exceeds a critical value ($\text{Fr} > 25$).

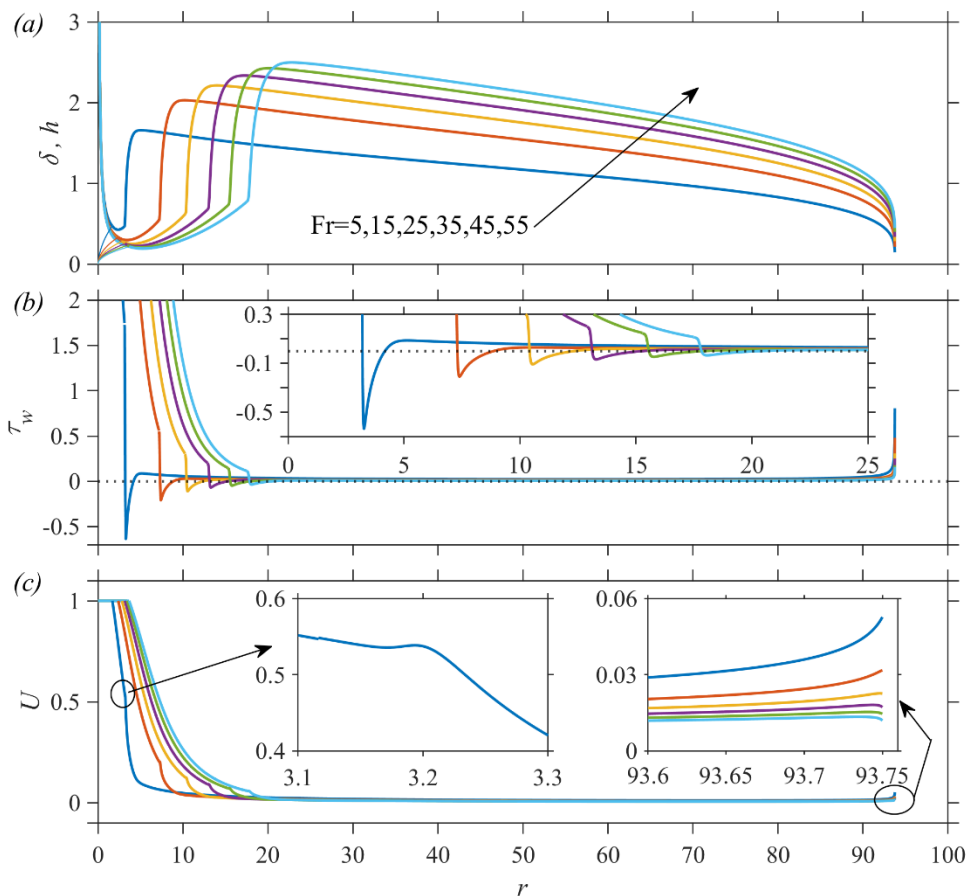


Figure 2-10: Influence of the Froude number (flow rate) on (a) the film profile, (b) wall shear stress (inset shows amplification in the downstream vicinity of the jump) and (c) surface velocity (insets show local profile for $Fr = 5$ and amplification near the disk edge). Here, $Ga = 100$ ($50.11 < Re < 551.25$) and $r_\infty = 93.75$, corresponding to the range of flow rate in the experiment of Duchesne *et al.* (2014).

One of the difficulties plaguing both theory and experiment is the identification of the jump location (Hansen *et al.* 1997; Rojas *et al.* 2013; Duchesne *et al.* 2014). Ideally, the jump location should correspond to the location where the *local* Froude number Fr_l reaches unity, changing from $Fr_l > 1$ in the supercritical region to $Fr_l < 1$ in the subcritical region. In the present work, we assumed that the jump location coincides with the vanishing of the film surface concavity: $h''(r = r_j) = 0$. We now verify the plausibility of this assumption by examining the value of Fr_l at the jump radius. We introduce the local Froude number in terms of the average velocity and film height as $Fr_l = Fr \langle u \rangle / \sqrt{h}$. Noting from (2.2.4) that $\langle u \rangle = 1/2rh$, then $Fr_l = Fr / 2rh^{3/2}$. Figure 2-11 depicts the influence of Fr (flow rate) on the distribution of Fr_l for the same range of flow rates as in the experiment of Duchesne *et al.* (2014) and the profiles in figure 2-10. We have also plotted in the inset the critical radius that satisfies $Fr / 2r_c h_c^{3/2} = 1$ as a function of Fr (flow rate), where $h_c \equiv h(r = r_c)$ is the critical height, along with the theoretical and measured jump radius from figure 2-8a. The inset shows that the r_j and r_c profiles are surprisingly close, hardly distinguishable. This excellent agreement confirms the accuracy of our assumption, $h''(r = r_j) = 0$, for identifying the location of the jump. The sharp drop of Fr_l with distance in figure 2-11 shows how quickly the effect of gravity increases in the supercritical region and across the jump, mostly relative to inertia (see figure 2-10c). Figure 2-11 also shows a sharp increase in Fr_l , reflecting a drop in gravity effects compared with inertia.

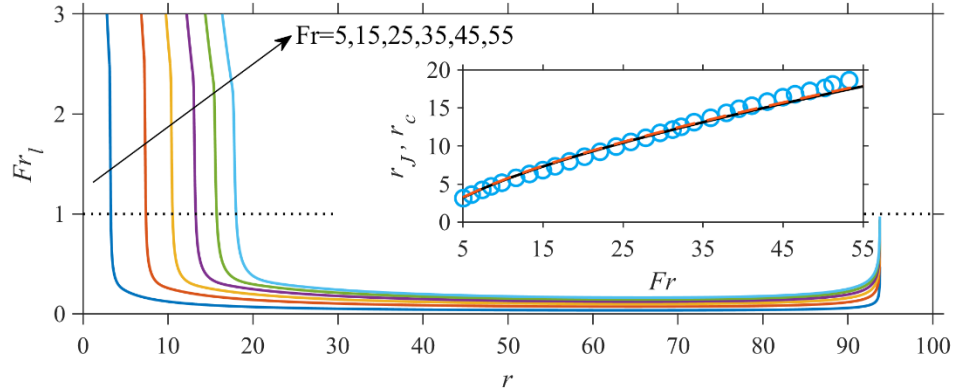


Figure 2-11: Influence of Fr (flow rate) on the local Froude number Fr_l . Inset shows the distribution of the numerically predicted jump radius (black solid curve) and the critical radius (red dashed curve), as well as the experimental data of Duchesne *et al.* (2014) (open blue circles). Here, $Ga = 100$ and $r_\infty = 93.75$, corresponding to the experiment parameters.

Figure 2-12 shows the dependence of the vortex size, namely vortex length L_{vortex} and vortex height H_{vortex} , on the flow rate or Fr , for the same range as in the experiment of Duchesne *et al.* (2014). The vortex length L_{vortex} increases monotonically with Fr , behaving roughly like $Fr^{1/2}$. Therefore, increasing the flow rate stretches the jump region in the streamwise direction (see also figures 2-10a), and thereby increasing the size of the recirculation zone (refer to the vertical dotted lines in figure 2-12b to 2-12d that delimit the jump length). However, the growth of the jump and vortex lengths is not commensurate with the growth of the vortex height, which tends to level off or saturates with increasing flow rate. The vortex immediately downstream of the jump also takes a similar shape to the one based on the boundary-layer approach of Higuera (1994), as well as the second-order models of Watanabe *et al.* (2003) and Bonn *et al.* (2009).

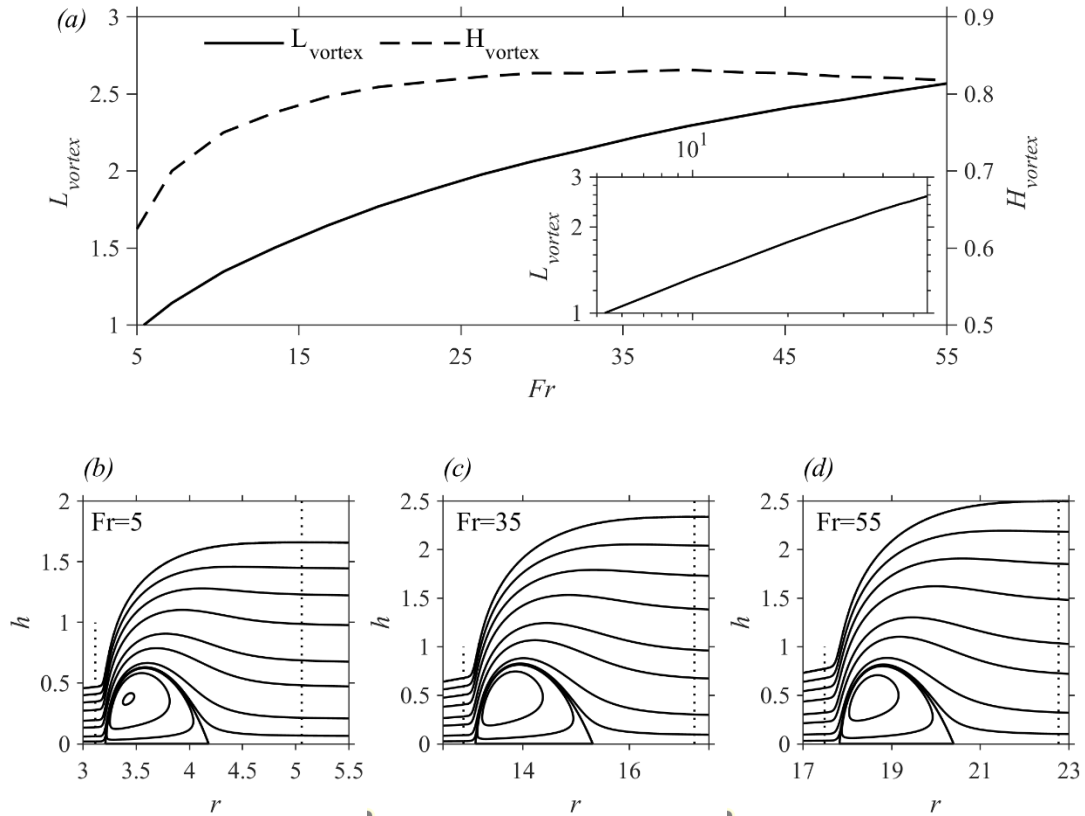


Figure 2-12: Dependence of the vortex size and structure on Fr (flow rate). (a) The vortex length and height and (b)-(d) the vortex structure for $Fr = 5-55$ (vertical dotted lines delimit the jump region/length). Here $Ga = 100$ and $r_{\infty} = 93.75$, corresponding to the parameters in the experiment of Duchesne *et al.* (2014).

2.5.2 The jump of type 0

Referring back to figure 2-10, we saw in particular from figure 2-10b that the vortex strength weakens with increasing flow rate, but the vortex does not vanish since its size remains essentially insensitive to the increase in the flow rate. Simultaneously, the jump intensity or steepness also remains, surprisingly, unaffected by the flow rate as the vortex strength diminishes. This begs the question as to whether a hydraulic jump can indeed exist for some flow conditions in the absence of recirculation. Some but little evidence of the existence of a type-0 jump can be found in the literature, particularly for a jump with an obstacle placed at the edge of the disk. Liu & Lienhard (1993) observed several forms of the circular hydraulic jump that appeared sequentially in their experiments as the downstream thickness was increased. For a small difference between the supercritical and

subcritical depth, they observed a smooth jump of gradually increasing depth without any flow reversal. Later, the numerical simulation of Passandideh-Fard *et al.* (2011) showed that a circular jump exists with no flow separation if the obstacle height is relatively small. More recently, a similar observation was made by Saberi *et al.* (2020) in their simulation for a jump on a convex target plate. Finally, Askarizadeh *et al.* (2020) observed that for small obstacles (disk height-to-diameter ratio < 0.05), the flow exhibits no vortices, and the streamlines perfectly follow the interfacial shape that represents the circular jump, which they termed as a jump of type 0. We next examine two situations by varying the effects of gravity and viscosity where separation may or may not occur.

The influence of gravity is assessed in figure 2-13 by varying Fr and keeping Re and the disk size fixed. Figure 2-13a shows that as the jump radius and height increase with Fr , the jump gets washed out of the disk for large Fr . This increasing trend of the jump radius with Fr also agrees with the simulation results of Passandideh-Fard *et al.* (2011) and the measurements of Avedisian & Zhao (2000); both groups investigated the influence of gravity on the hydraulic jump. We emphasize that although the effect of gravity is weak in the supercritical region, this effect is crucial to include in the formulation for establishing the proper upstream conditions for the flow in the viscous region. In contrast, the subcritical film thickness increases significantly with Fr , as more flow accumulates (unable to drain) under lower gravity. In fact, the influence of Fr on the film thickness in both the supercritical and subcritical regions corroborates well the profiles in figure 2 of Higuera (1994) for a planar jump. Figure 2-13b indicates that τ_w decreases sharply with Fr downstream of the recirculation, but eventually saturates for large Fr . The boundary layer and film thickness as well as the wall shear stress remain essentially uninfluenced by gravity in the supercritical region, confirming the weak influence of gravity ahead of the jump, and the earlier predictions of Wang & Khayat (2018, 2019). This is particularly evident from the inset in figure 2-13b.

In the region near the jump, where the film height undergoes a significant change, the response is not as consistent. In fact, the influence of Fr on the separation length in figure 13b is not monotonic; the vortex size increases with Fr , reaches a maximum and decreases, to eventually vanish at some critical Froude number ($Fr \approx 13$); the non-monotonic response

is also illustrated in figures 2-13d to 2-13g. Therefore, the jump can exist without a recirculation at a finite Froude number. The disappearance of the vortex suggests that there is no more flow separation, which is reflected by the wall shear stress remaining positive over the entire disk range (figure 2-13b). Recalling the discussion on the dissipation model by Mikielewicz & Mikielewicz (2009) and their figure 3, it is clear that a constant value of P , which is roughly the ratio of the downstream film height and the mean vortex radius, is unrealistic, as the vortex does not exist when Fr is sufficiently large, leading to an infinite P in this situation. It is worth noting that the hydraulic jump is not an essentially vortex or flow-separation phenomenon as indicated by Craik *et al.* (1981). The numerical simulation of Passandideh-Fard *et al.* (2011) also showed hydraulic jumps without flow separation. Here in figure 2-13a we show that the hydraulic jump still exists when the vortex disappears. In order to confirm that the profile is indeed a hydraulic jump in the absence of a vortex, we plot the value of the local Froude number in figure 2-13c, showing that the local Froude number is equal to unity where the surface concavity vanishes. The inset in figure 2-13c also confirms that the critical radius coincides with the jump radius. In reality, the disappearance of the recirculation bubble may be associated with an instability at high Fr ; the flow may become oscillatory and then turbulent downstream of the jump where the depth has increased (Craik *et al.* 1981). However, and as we confirm below, the existence of the recirculation is intimately tied to the strength of the upstream curvature of the jump and the jump steepness.

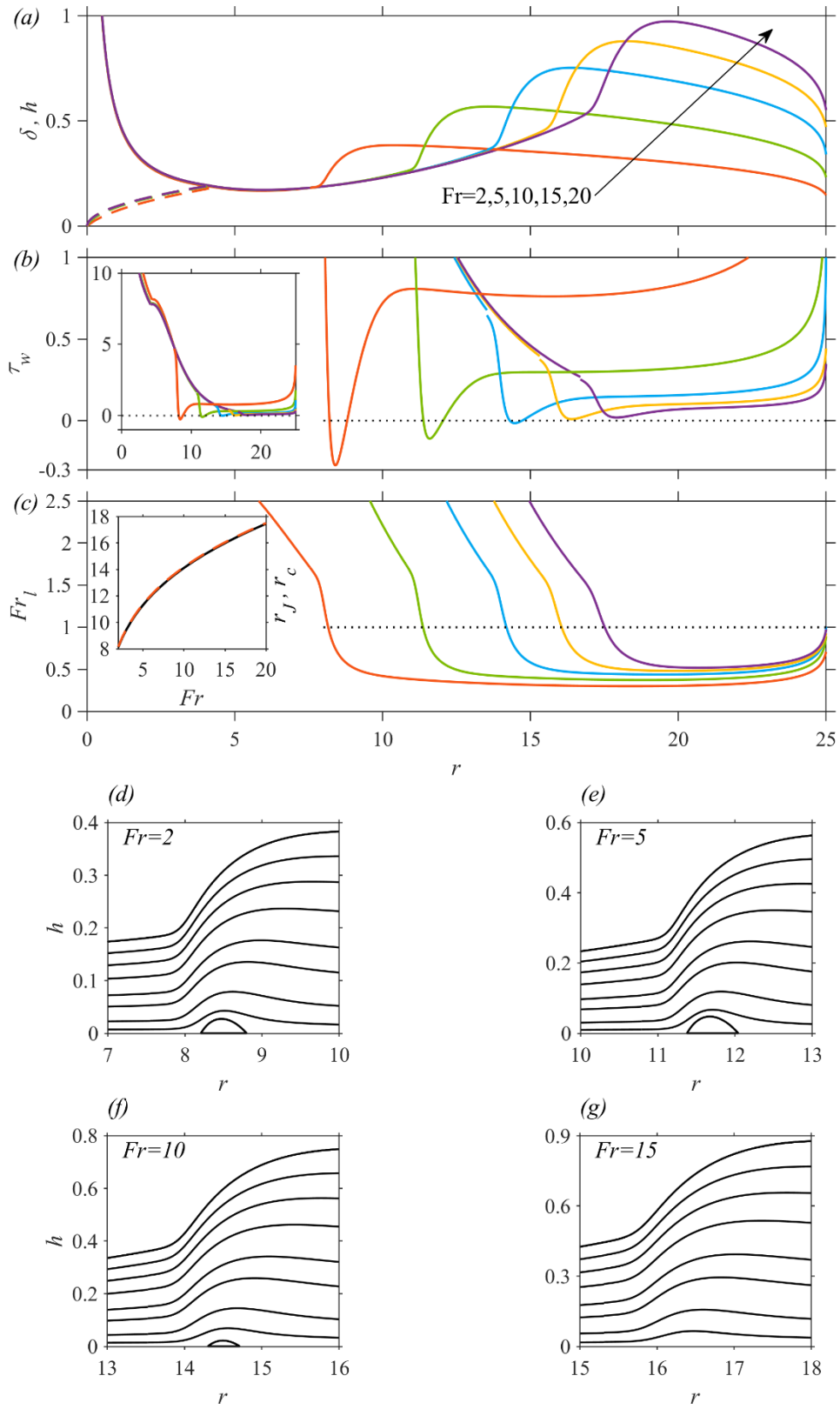


Figure 2-13: Influence of the Froude number (gravity) on (a) the free surface profile (solid curves) and the boundary-layer thickness (dashed curves), (b) the wall shear stress and (c) the local Froude number. The inset in (c) shows the distribution of the numerically predicted jump radius (black solid curve) and the critical radius (red dashed curve). (d)-(g) The streamlines for $Fr = 2, 5, 10$ and 15 . Here, $Re = 800$ and $r_\infty = 25$.

The influence of the viscosity is depicted in figure 2-14, where Re is varied and Fr is fixed. As expected, a larger Re (lower fluid viscosity) results in a thinner boundary layer and film thickness in the developing boundary-layer region (figure 2-14a). In contrast to the effect of gravity, the supercritical flow is evidently dependent on viscous effects, as depicted by the dependence of the film (figure 2-14a) and stress (figure 2-14b) profiles. As Re increases, the film profile becomes flatter, with a weakening of the supercritical minimum and subcritical maximum film thickness, as the jump is pushed towards the disk edge (figure 2-14a). The increase in the jump radius is in agreement with the simulation of Passandideh-Fard *et al.* (2011). The jump becomes essentially non-existent at a relatively large value of Re . Simultaneously, the vortex diminishes in size as Re increases, and vanishes at Re much smaller than that corresponding to the vanishing of the jump (figure 2-14b). The distribution of the local Froude number in figure 2-14c also confirms the existence of the jump for all Re values.

This clearly shows that the existence of a jump is not necessarily accompanied by the formation of a vortex (figures 2-14d to 2-14g). Finally, it is interesting to observe that the rate of increase of τ_w with Re in the supercritical region (inset of figure 2-14b) is essentially the same as near the edge of the disk. We also observe that the strength of the singularity of the stress (equivalently of the film slope) at the edge weakens considerably with Re .

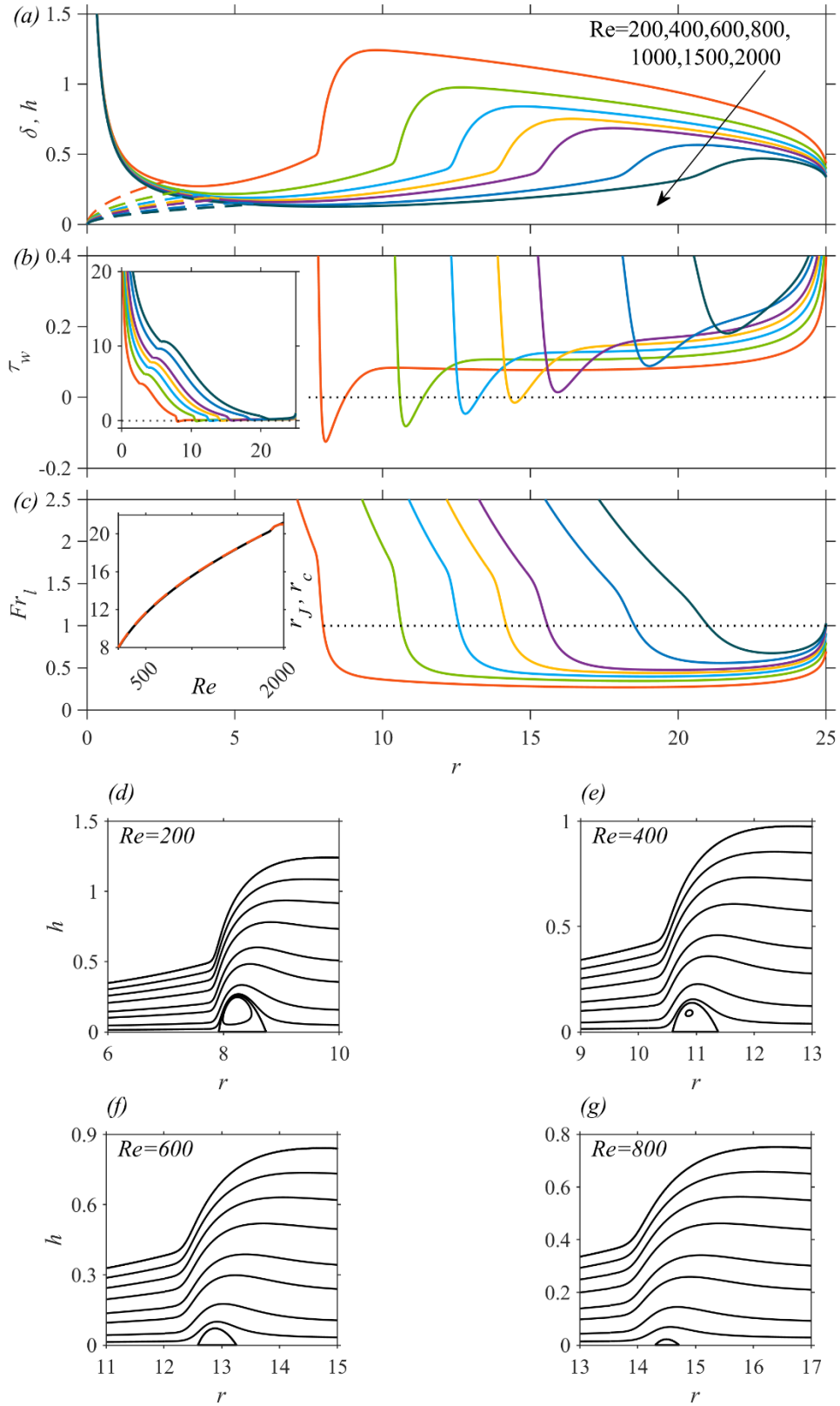


Figure 2-14: Influence of Re (viscosity) on (a) the free surface profile (solid curves) and the boundary-layer thickness (dashed curves), (b) the wall shear stress and (c) the local Froude number. The inset in (c) shows the distribution of the numerically predicted jump radius (black solid curve) and the critical radius (red dashed curve). (d)-(f) The streamlines around the jump region for $Re = 200, 400, 600$ and 800 . Here, $Fr = 10$ and $r_\infty = 25$.

2.6 Conclusion

We examined the structure of the circular hydraulic jump and the recirculation appearing for a jet impinging on a disk. We formulated a composite mean-field thin-film approach, which consists of subdividing the flow domain into three regions of increasing gravity strength: a developing boundary layer near impact, an intermediate supercritical viscous layer leading up to the edge of the jump and a region comprising the jump and subcritical flow. The flow is assumed to drain at the edge of the disk. Unlike existing formulations that capture the continuous jump profile and the recirculation zone, the present approach does not require any empirically or numerically adjustable boundary conditions. The governing boundary-layer equations for the thin film are elliptic given the presence of the hydrostatic pressure gradient in the original boundary-layer equations, thus resulting in a two-point boundary-value problem, requiring upstream and downstream boundary conditions, particularly at the edge of the disk. The ellipticity is preserved through the presence of the gravity term in the velocity profile that was taken to satisfy the momentum equation at the disk. We demonstrated that the stress or corner singularity for a film draining at the edge is equivalent to the infinite slope of the film surface, which we impose as the downstream boundary condition. We validated our approach against existing measurements and numerical data. Comparison against numerical solutions of the boundary-layer equations and Navier-Stokes equations showed excellent agreement (figures 2-4 to 2-6), as well as that against existing models of the averaged film equations (figure 2-4). Comparison against existing measurements of the film profile and jump radius also showed close agreement and/or equally accurate predictions as existing numerical solutions (figures 2-6, 2-8 and 2-9).

In an effort to stimulate further experimental work, we examined the influence of flow rate (inertia) in some detail, over the same range of experimental conditions as that of Duchesne *et al.* (2014). The results in §2.5.1 highlight the influence of the flow rate on the film profile and vortex structure (figures 2-10 and 2-12). The film profile was found to have a significant influence on the jump size and vortex structure. We also address and resolve one of the difficulties facing theory and experiment in identifying the jump location. We assumed the jump radius to coincide with the change in the film surface concavity. We showed that this assumption is accurate since the predicted jump radius is very close to the critical radius based on the local Froude number (figure 2-11).

Finally, the flow in the supercritical region remains insensitive to the change in gravity (figure 2-13) but is greatly affected by viscosity (figure 2-14). The existence of the jump is not necessarily commensurate with the presence of a recirculation zone. We identify as type 0 the class of such jumps.

2.7 References

- AVEDISIAN, C. & ZHAO, Z. 2000 The circular hydraulic jump in low gravity. *Proc. R. Soc. Lond., Ser. A* **456**, 2127-2151.
- ASKARIZADEH, H., AHMADIKIA, H., EHRENPREIS, C., KNEER, R., PISHEVAR, A. & ROHLFS, W. 2020 Heat transfer in the hydraulic jump region of circular free-surface liquid jets. *Intl J. Heat Mass Transfer* **146**, 118823.
- BAAYOUN, A., KHAYAT, R. E., & WANG, Y. 2022 The transient spread of a circular liquid jet and hydraulic jump formation. *J. Fluid Mech.* **947**, A34.
- BOHR, T., DIMON, P. & PUTZKARADZE, V. 1993 Shallow-water approach to the circular hydraulic jump. *J. Fluid Mech.* **254**, 635-648.
- BOHR, T., ELLEGAARD, C., HANSEN, A. E. & HAANING, A. 1996 Hydraulic jumps, flow separation and wave breaking: An experimental study. *Physica B* **228**, 1-10.

- BOHR, T., PUTKARADZE, V. & WATANABE, S. 1997 Averaging theory for the structure of hydraulic jumps and separation in laminar free-surface flows. *Phys. Rev. Lett.* **79**, 1038-1041.
- BOHR, T., ELLEGAARD, C., HANSEN, A. E., HAANING, A., PUTZKARADZE, V. & WATANABE, S. 1998 Separation and pattern formation in hydraulic jumps, *Physica A* **249**, 111-117.
- BONN, D., ANDERSEN, A. & BOHR, T. 2009 Hydraulic jumps in a channel. *J. Fluid Mech.* **618**, 71-87.
- BOWLES, R. I. 1990 Applications of nonlinear viscous-inviscid interactions in liquid layer flows & transonic boundary layer transition. Ph.D. thesis, University of London.
- BOWLES, R. I. 1995 Upstream influence and the form of standing hydraulic jumps in liquid-layer flows on favourable slopes. *J. Fluid Mech.* **284**, 63-96.
- BOWLES, R. I., & SMITH, F. T. 1992 The standing hydraulic jump: theory, computations and comparisons with experiments. *J. Fluid Mech.* **242**, 145-168.
- BROWN, S.N., STEWARTSON, K. & WILLIAMS, P.G. 1975 On expansive free interactions in boundary layers. *Proc. R. SOC. Edinburgh.* **74A**, 21.
- BUSH, J. W. M. & ARISTOFF, J. M. 2003 The influence of surface tension on the circular hydraulic jump. *J. Fluid Mech.* **489**, 229-238.
- CRAIK, A., LATHAM, R., FAWKES, M., & GRIBBON, P. 1981 The circular hydraulic jump. *J. Fluid Mech.* **112**, 347-362.
- DHAR, M., DAS, G. & DAS, P. K. 2020 Planar hydraulic jumps in thin film flow. *J. Fluid Mech.* **884**, A11.
- DRAZIN, P. & RILEY, N. 2006 *The Navier–Stokes Equations: A Classification of Flows and Exact Solutions*. Cambridge.
- DRESSAIRE, E., COURBIN, L., CREST, J. & STONE, H.A. 2010 Inertia dominated thin-film flows over microdecorated surfaces. *Phys. Fluids* **22**, 073602.

- DUCHESNE, A., LEBON, L. & LIMAT, L. 2014 Constant Froude number in a circular hydraulic jump and its implication on the jump radius selection. *Europhys. Lett.* **107**, 54002.
- ELLEGAARD, C., HANSEN, A., HAANING, A., HANSEN, K. & BOHR, T. 1996 Experimental results on flow separation and transitions in the circular hydraulic jump. *Phys. Scr.* **T67**, 105-110.
- FERNANDEZ-FERIA, R., SANMIGUEL-ROJAS, E. & BENILOV, E. S. 2019 On the origin and structure of a stationary circular hydraulic jump. *Phys. Fluids* **31**, 072104.
- GAJJAR, J., & SMITH, F. T. 1983 On hypersonic self-induced separation, hydraulic jumps and boundary layers with algebraic growth. *Mathematika*, **30**, 77-93.
- HANSEN, S. H., HORLUCK, S., ZAUNER, D., DIMON, P., ELLEGAARD, C. & CREAGH, S. C. 1997 Geometric orbits of surface waves from a circular hydraulic jump. *Phys. Rev. E* **55**, 7048-7061.
- HIGUERA, F. J. 1994 The hydraulic jump in a viscous laminar flow. *J. Fluid Mech.* **274**, 69-92.
- ISHIGAI, S., NAKANISHI, S., MIZUNO, M. & IMAMURA, T. 1977 Heat transfer of the impinging round water jet in the interference zone of film flow along the wall. *Bull. JSME* **20**, 85-92.
- IPATOVA, A., SMIRNOV, K. & MOGILEVSKIY, E. 2021 Steady circular hydraulic jump on a rotating disk. *J. Fluid Mech.* **927**, A24.
- KATE, R., DAS, O., & CHAKRABORTY, S. 2007 Hydraulic jumps due to oblique impingement of circular liquid jets on a flat horizontal surface. *J. Fluid Mech.* **573**, 247-263.
- KASIMOV, A. R. 2008 A stationary circular hydraulic jump, the limits of its existence and its gasdynamic analogue. *J. Fluid Mech.* **601**, 189–198.

- KHAYAT, R. E. 2014 Free-surface jet flow of a shear-thinning power-law fluid near the channel exit. *J. Fluid Mech.* **748**, 580-617.
- KHAYAT, R. E. 2016 Slipping free jet flow near channel exit at moderate Reynolds number for large slip length. *J. Fluid Mech.* **793**, 667-708.
- KHAYAT, R. E. 2017 Initial development of a free-surface wall jet at moderate Reynolds number. *J. Fluid Mech.* **826**, 235-269.
- KHAYAT, R.E. & KIM, K.T. 2006 Thin-film flow of a viscoelastic fluid on an axisymmetric substrate of arbitrary shape. *J. Fluid Mech.* **552**, 37–71.
- KURIHARA, M. 1946 On hydraulic jumps. *Report of the Research Institute for Fluid Engineering*, Kyusyu Imperial University, **3**, 11-13.
- LIENHARD, J. 2006 Heat transfer by impingement of circular free-surface liquid jets. In *18th National & 7th ISHMT-ASME Heat and Mass Transfer Conference*, pp. 1-17. IIT.
- LIU, X. & LIENHARD, J. 1993 The hydraulic jump in circular jet impingement and in other thin liquid films. *Exp. Fluids* **15**, 108-116.
- MAITI, M.K. 1965 Axially-symmetric stagnation point flow of power law fluids. *J. Appl. Maths. Phys. (ZAMP)* **16**, 594–598.
- MIDDLEMAN, S. 1995 *Modeling axisymmetric flows: dynamics of films, jets, and drops*, Academic Press.
- MIKIELEWICZ, J. & MIKIELEWICZ, D. 2009 A simple dissipation model of circular hydraulic jump. *Intl. J. Heat Mass Transfer* **52**, 17–21.
- MOHAJER, B., & LI, R. 2015 Circular hydraulic jump on finite surfaces with capillary limit. *Phys. Fluids* **27**, 117102.
- NAKORYAKOV, V. E., POKUSAEV, B. G., & TROYAN, E. N. 1978 Impingement of an axisymmetric liquid jet on a barrier. *Intl. J. Heat Mass Transfer* **21**, 1175-1184.

- PASSANDIDEH-FARD, M., TEYMOURTASH, A. R., & KHAVARI, M. 2011 Numerical Study of Circular Hydraulic Jump Using Volume-of-Fluid Method. *J Fluids Engng* **133**, 11401.
- PRINCE, J. F., MAYNES, D. & CROCKETT, J. 2012 Analysis of laminar jet impingement and hydraulic jump on a horizontal surface with slip. *Phys. Fluids* **24**, 102103.
- PRINCE, J. F., MAYNES, D. & CROCKETT, J. 2014 Jet impingement and the hydraulic jump on horizontal surfaces with anisotropic slip. *Phys. Fluids* **26**, 042104.
- RAO, A. & ARAKERI, J. H. 2001 Wave structure in the radial film flow with a circular hydraulic jump. *Exp. Fluids* **31**, 542-549.
- RAYLEIGH, O. M. 1914 On the theory of long waves and bores. *Proc. R. Soc. Lond. A* **90**, 324-328.
- RAZIS, D., KANELLOPOULOS, G., & VAN DER WEELE, K. 2021 Continuous hydraulic jumps in laminar channel flow. *J. Fluid Mech.* **915**, A8.
- ROBERTS, A. J. & LI, Z. 2006 An accurate and comprehensive model of thin fluid flows with inertia on curved substrates. *J. Fluid Mech.* **553**, 33–73.
- ROJAS, N. O., ARGENTINA, M., CERDA, E., & TIRAPEGUI, E. 2010 Inertial lubrication theory. *Phys. Rev. Lett.* **104**, 187801.
- ROJAS, N. O., ARGENTINA, M., & TIRAPEGUI, E. 2013 A progressive correction to the circular hydraulic jump scaling. *Phys. Fluids* **25**, 42105.
- SABERI, A., TEYMOURTASH, A., & MAHPEYKAR, M. R. 2020 Experimental and numerical study of circular hydraulic jumps on convex and flat target plates. *Eur. J. Mech.-B* **80**, 32-41.
- SCHEICHL, B., BOWLES, R. I., & PASIAS, G. 2018 Developed liquid film passing a trailing edge under the action of gravity and capillarity. *J. Fluid Mech.* **850**, 924–953.
- SCHLICHTING, H. & GERSTEN, K. 2000 *Boundary-layer theory* 8th edition, Springer.

- TANI, I. 1949 Water Jump in the Boundary Layer. *J. Phys. Soc. Japan.* **4**, 212-215.
- TILLET, J.P.K. 1968 On the laminar flow in a free jet of liquid at high Reynolds numbers. *J. Fluid Mech.* **32**,273.
- WANG, Y. & KHAYAT, R. E. 2018 Impinging jet flow and hydraulic jump on a rotating disk. *J. Fluid Mech.* **839**, 525-560.
- WANG, Y. & KHAYAT, R. E. 2019 The role of gravity in the prediction of the circular hydraulic jump radius for high-viscosity liquids. *J. Fluid Mech.* **862**, 128-161.
- WANG, Y. & KHAYAT, R. E. 2020 The influence of heating on liquid jet spreading and hydraulic jump. *J. Fluid Mech.* **883**, A59.
- WANG, Y. & KHAYAT, R. E. 2021 The effects of gravity and surface tension on the circular hydraulic jump for low- and high-viscosity liquids: A numerical investigation. *Phys. Fluids* **33**, 012105.
- WATANABE, S., PUTKARADZE, V. & BOHR, T. 2003 Integral methods for shallow free-surface flows with separation. *J. Fluid Mech.* **480**, 233-265.
- WATSON, E. 1964 The spread of a liquid jet over a horizontal plane. *J. Fluid Mech.* **20**, 481-499.
- WHITE, F. M. 2006 *Viscous Fluid Flow*, 3th edition, McGraw-Hill.
- ZHOU, G., & PROSPERETTI, A. 2022 Hydraulic jump on the surface of a cone. *J. Fluid Mech.* **951**, A20.

Chapter 3

3 The characteristics of the continuous circular hydraulic jump ²

Nomenclature

a	Radius of jet, m
Bo	Bond number, $Bo = \rho g a^2 / \sigma$
E_{j-}	Dimensionless energy head at the leading edge of the jump
E_{j+}	Dimensionless energy head at the trailing edge of the jump
ΔE_j	Dimensionless relative energy loss, $\Delta E_j = E_{j-} - E_{j+}$
Fr	Froude number, $Fr = W / \sqrt{ga}$
Fr_l	Local Froude number, $Fr_l = Fr \langle u \rangle / \sqrt{h}$
Fr_j	Froude number at the trailing edge of the jump, $Fr_j = Fr / 2r_j H_j^{3/2}$
Fr_{j-}	Froude number at the leading edge of the jump, $Fr_{j-} = Fr / 2r_j h_j^{3/2}$
Fr_{j+}	Froude number at the trailing edge of the jump, $Fr_{j+} = Fr / 2r_j H_j^{3/2}$
g	Acceleration due to gravity, m/s^2
Ga	Galileo number, $Ga = Re^2 / Fr^2$

² A version of this chapter has been submitted for publication as -

h	Dimensionless film thickness
h_0	Dimensionless film thickness at $r = r_0$
h_J	Dimensionless film thickness at $r = r_{J-}$
h_∞	Dimensionless film thickness at the disk edge
H_J	Dimensionless film thickness at $r = r_{J+}$
H_s	Dimensionless static thickness of the film at the disk edge
H_{vortex}	Dimensionless height of the vortex under the jump
L_{vortex}	Dimensionless length of the vortex under the jump
L_J	Dimensionless jump length, $L_J = r_{J+} - r_{J-}$
p	Dimensionless pressure
Q	Volume flow rate, m^3/s
r	Dimensionless radial coordinate
r_0	Dimensionless transition point of the hydrodynamic boundary layer
r_s	Dimensionless radial location of singularity reached
r_∞	Dimensionless disk radius
R_∞	Dimensional disk radius, m
r_J	Dimensionless jump radius
R_J	Dimensional jump radius, m
r_{J-}	Dimensionless radial location of the leading edge of the hydraulic jump

r_{j+}	Dimensionless radial location of the trailing edge of the hydraulic jump
Re	Reynolds number, $Re = Wa/\nu$
u	Dimensionless horizontal velocity
U	Dimensionless free surface velocity
$\langle u \rangle$	Dimensionless depth average velocity
w	Dimensionless vertical velocity
W	Average jet velocity, $W = Q/\pi a^2$, m/s
z	Dimensionless vertical coordinate

Greek Symbols

α	Dimensionless parameter, $\alpha = Re^{1/3} Fr^2$
β	Dimensionless parameter, $\beta = Re^{-1/3} r_\infty$
δ	Dimensionless hydrodynamic boundary layer thickness
η	Scaled vertical coordinate, $\eta = z/h$
θ	Azimuthal coordinate
θ_Y	Static contact angle
ν	Kinematic viscosity, m^2/s
ρ	Density of fluid, kg/m^3
σ	Surface tension of fluid, N/m
τ_w	Dimensionless wall shear stress

3.1 Introduction

In a recent study (Wang *et al.* 2023), we proposed a theoretical treatment to simulate the continuous circular hydraulic jump and recirculation for a jet impinging on a disk. We formulated a composite mean-field thin-film approach, which consists of subdividing the flow domain into three regions of increasing gravity strength: a developing boundary layer near impact, an intermediate supercritical viscous layer leading up to the edge of the jump, and a region comprising the jump and subcritical flow. The film was assumed to drain at the edge of the disk.

Earlier efforts to capture the smooth variation of the jump and the vortex structure are credited to Bohr *et al.* (1997) and Watanabe *et al.* (2003), who introduced second-order corrections and accounted for additional gravity effects by ensuring their velocity profile satisfies the momentum equation at the disk. The presence of the resulting additional shape parameter in the cubic velocity profile prevents the formation of the critical point and the singularity of the averaged first-order model (Wang & Khayat 2019), allowing the capture of the flow separation. However, two experimental points near the leading and trailing edges of the jump are needed in their solution to fix the boundary conditions, and some prior knowledge of the location of the jump is required. In this regard, even though their theory showed good agreement with the earlier measurements of Bohr *et al.* (1996), it remains somewhat semi-empirical. A similar approach was later adopted by Bonn *et al.* (2009) to study the hydraulic jump in a channel. Roberts & Li (2006) derived a model based on centre-manifold theory to describe the dynamics of thin films on curved substrates. A smooth profile was generated for the circular hydraulic jump on a flat substrate, and the vortex was captured as well. However, they simply imposed the boundary conditions in a manner similar to Watanabe *et al.* (2003). A more serious attempt was made by Razis *et al.* (2021) to capture the continuous jump in an inclined channel. They extended the Saint-Venant equations by including the effect of the longitudinal normal stress. They derived analytically an approximate expression for the jump length as a function of the Froude and effective Reynolds numbers, highlighting the strong interplay among inertia, gravity and viscous diffusion, as contributing to the balance of forces that shape the jump.

Unlike existing formulations that capture the continuous jump profile and the recirculation zone, our approach does not require any empirically or numerically adjustable boundary conditions. The governing boundary-layer equations for the thin film are elliptic given the presence of the hydrostatic pressure gradient in the original boundary-layer equations, thus resulting in a two-point boundary value problem, requiring upstream and downstream boundary conditions, particularly at the edge of the disk. The ellipticity is preserved through the presence of the gravity term in the velocity profile that was taken to satisfy the radial momentum equation at the disk. We demonstrated that the stress or corner singularity for a film draining at the edge is equivalent to the infinite slope of the film surface, which we imposed as the downstream boundary condition. We validated extensively our approach against existing measurements and numerical simulation. Measurement data were taken from Hansen *et al.* (1997) and Duchesne *et al.* (2014) for fluids of different viscosities and decades of flow rates. Comparisons were made for the film profile, jump location as well as the local Froude number. Comparison against the spectral inertial-lubrication model of Rojas *et al.* (2010), the numerical solution of the boundary-layer equations of Fernandez-Feria *et al.* (2019), the Navier-Stokes solution of Zhou & Prosperetti (2022), as well as existing mean-field models (Kasimov 2008; Dhar *et al.* 2020). Overall, agreement with our numerical predictions was surprisingly close; the reader is particularly referred to the validation section 4 of Wang *et al.* (2023).

The aim of the present study is to use our recent formulation and solution procedure (Wang *et al.* 2023) to examine the different features of the *type 0* and *type I* circular hydraulic jumps and elucidate the flow structure in each case. Since our numerical approach was extensively validated against experiment and numerical simulation, it will be used to establish and test new scaling arguments for the jump location, jump length, conjugate depth ratio, energy loss across the jump and film thickness at the edge of the circular disk. Using a first-order model, Bohr *et al.* (1993) located the jump by matching the up- and downstream solution branches through a Rayleigh shock (Rayleigh 1914), and proposed a scaling for the hydraulic jump radius as $R_J \sim Q^{5/8} \nu^{-3/8} g^{-1/8}$, where Q is the flow rate of the jet, ν is the kinematic viscosity of the fluid, and g is the acceleration due to gravity. More recently, Duchesne *et al.* (2014) established their scaling law by assuming that the

Froude number based on the jump location and height (Fr_J) is constant, and eliminating the jump height assuming lubrication flow to obtain an implicit relation: $R_J [\ln(R_\infty/R_J)]^{3/8} \sim Q^{5/8} \nu^{-3/8} g^{-1/8}$, involving the disk radius, R_∞ . Their scaling law is therefore semi-empirical since the value of Fr_J must be imposed from experiment. We shall revisit this issue and elucidate the conditions for the validity of existing scaling laws and demonstrate the need for a more accurate scaling law for the jump radius.

We examine another important flow characteristic: the thickness at the edge of the disk, which remains largely unaddressed in the literature, as the flow near the disk edge experiences a complex interplay of inertia, gravity and surface tension (Higuera 1994). For the situation when the flow drains freely off the disk edge, there are mainly two approaches to determine the film height or equivalent conditions at the disk edge; imposing an infinite slope (Bohr *et al.* 1993; Kasimov 2008; Dhar *et al.* 2020), or assuming the edge thickness to be essentially equal to the capillary length (Duchesne *et al.* 2014; Ipatova *et al.* 2021; Duchesne & Limat 2022). As indicated in the experimental work of Duchesne *et al.* (2014), the edge film thickness also follows a weak power law dependence on the flow rate. Although we have extensively validated our approach (Wang *et al.* 2023) for a film freely draining at the disk edge, we further verify our model against the numerical solution of the Navier-Stokes equations of Askarizadeh *et al.* (2019, 2020) when an obstacle is placed at the disk edge. We also examine the influence of the obstacle height on the jump and vortex structure. In addition, we examine the jump length and its relation to the vortex size. By balancing the drag at the disk in the jump region with fluid inertia, and assuming dominant viscous over gravity effects, Avedisian & Zhao (2000) obtained a relation between the length of the jump and its radius as $L_J R_J / h_J \sim Q / \nu$, where h_J is the film thickness at the leading edge of the jump (see also the different treatment of Razis *et al.* (2021) for the planar jump).

The rest of this paper is organized as follows. In section 3.2, we briefly review the general problem and physical domain; we review the formulation of the problem and the solution strategy in terms of the general governing equations and boundary conditions in each region of the flow. In section 3.3, we examine the influence of the disk geometry on the

jump and flow structure, namely the influence of the disk size and the height of the obstacle, which is often placed at the edge of the disk to control the subcritical film height and jump location. Further validation is conducted by comparing our approach against existing numerical simulation. Detailed scaling analyses are formulated in section 3.4 for the jump radius, jump length, energy loss, conjugate depth ratio and thickness at the edge of the disk. The scaling laws are validated against our approach and existing experimental and numerical data. In section 3.5, we conduct further parametric studies and scaling to explore the overall regions of existence for the two types (0 and 1) of jump. Finally, concluding remarks and discussion are given in section 3.6.

3.2 Review of the physical domain and problem formulation

In this section, we first present the formulation of the steady flow in the developing boundary-layer region in order to obtain the upstream boundary condition needed for the flow in the fully-developed viscous region. Next, we present the formulations of the flow in the fully-developed viscous region. In particular, effects of moderate gravity and strong gravity are discussed. We shall see that, depending on the level of importance of the gravitational effects, different governing equations can be used in this region.

3.2.1 The physical domain and problem statement

Consider the steady laminar incompressible flow of a circular (axisymmetric) jet of a Newtonian fluid emerging from a nozzle of radius a , impinging at a volume flow rate Q on a flat disk of radius R_∞ lying normal to the jet and gravity direction. The flow configuration is depicted schematically in figure 3-1, where dimensionless variables and parameters are used. The problem is formulated in the (r, θ, z) fixed coordinates, with the origin coinciding with the disk center. The flow is assumed to be independent of θ , thus excluding polygonal flow. In this case, $u(r, z)$ and $w(r, z)$ are the corresponding dimensionless velocity components in the radial and vertical directions, respectively. The r -axis is taken along the disk radius and the z -axis is taken along the jet axis. The length and the velocity scales are conveniently taken to be the radius of the jet, a , and the average

jet velocity $W \equiv Q/\pi a^2$, both in the radial and vertical directions. Since the pressure is expected to be predominantly hydrostatic for a thin film, it will be scaled by $\rho g a$, where g is the acceleration due to gravity. In the absence of surface tension, two main dimensionless groups emerge in this case: the Reynolds number $Re = Wa/\nu$, where ν is the kinematic viscosity, and the Froude number $Fr = W/\sqrt{ag}$. Another useful and related number is the Galileo number $Ga = Re^2/Fr^2$.

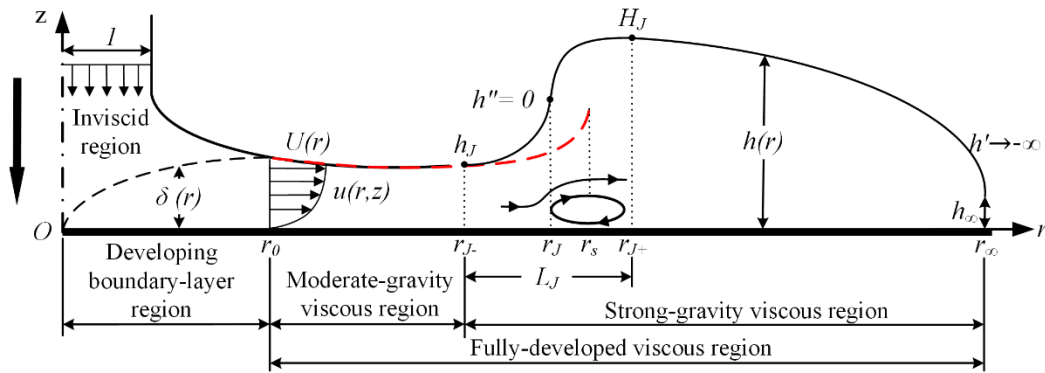


Figure 3-1: Schematic illustration of the axisymmetric jet flow impinging on a flat stationary disk and the hydraulic jump of type I with one vortex downstream. Shown are the developing boundary-layer region ($0 < r < r_0$) and the fully-developed viscous region ($r_0 < r < r_{\infty}$). The fully-developed viscous region comprises a region ($r_0 < r < r_{J-}$) where gravitational effects are moderate, and a second region where gravitational effects are strong ($r_{J-} < r < r_{\infty}$). All notations are dimensionless. In this case, the jet radius is equal to one. The film is allowed to fall freely over the edge of the disk where an infinite slope in the film thickness occurs, $h'(r = r_{\infty}) \rightarrow -\infty$. The red dashed-curve is the schematic film-thickness profile reflecting the approach of Wang & Khayat (2019), terminating with a singularity at a finite radius denoted here by r_s . The jump location coincides with $h''(r_J) = 0$, and $h(r_{J-}) = h_J$, and $h(r_{J+}) = H_J$. The downward arrow represents the gravitational acceleration.

As shown in figure 3-1, we identify three main regions of the flow: a developing boundary-layer region ($0 < r < r_0$) where gravity is essentially dominated by inertia, a fully-

developed viscous region ($r_0 < r < r_{J-}$) with moderate gravitational effect, and a fully-developed viscous region ($r_{J-} < r < r_\infty$) with strong gravitational effect. The jump is a smooth transition region that connects the (upstream) supercritical and the (downstream) subcritical regions. Again, the analysis of the boundary-layer region, near impact, is crucial in order to fix an upstream boundary condition for the thin-film viscous flow, relevant to the jet conditions. Throughout this study, the stagnation or impingement region is not considered, and the boundary layer is assumed to originate at the stagnation point (Wang *et al.* 2023).

The boundary layer grows until it reaches the film surface at the transition location $r = r_0$. Here, the film thickness is defined as $h_0 \equiv h(r = r_0)$ which corresponds to an upstream boundary condition for the flow in the fully-developed viscous region. We denote by $\delta(r)$ the boundary-layer thickness. The leading edge of the boundary layer is taken to coincide with the disk center. We let $U(r) \equiv u(r, z = h)$ denote the velocity at the free surface. Assuming the jet and stagnation flows to be inviscid irrotational, the radial velocity outside the boundary layer is then $U(0 \leq r \leq r_0) = 1$ as the fluid there is unaffected by the viscous stresses. We recall that both velocity components have been scaled by the (inviscid) jet velocity W . The potential flow ceases to exist in the fully-developed viscous region $r_0 < r < r_\infty$, and U becomes dependent on r . We note that r_0 is the location beyond which the viscous stresses become appreciable right up to the free surface, where the entire flow is of the boundary-layer type. We follow Rojas *et al.* (2010) and take the jump location r_J to coincide with the vanishing of the concavity: $h''(r = r_J) = 0$. We denote by $r = r_{J+}$ the location of the maximum film height: $h(r = r_{J+}) = H_J$. The definition of the jump radius at the location where the free surface changes concavity is reasonable as this location is very close to the start of the separation zone which is experimentally considered as the location of the jump in the literature (Bohr *et al.* 1996). Downstream of the jump, the film decreases in thickness and eventually falls freely over the edge of the disk, at $r = r_\infty$, where an infinite (downward) slope in thickness is assumed (Bohr *et al.* 1993; Kasimov 2008;

Dhar *et al.* 2020). In fact, we shall see that the infinite slope is directly related to the stress singularity expected to occur at the disk edge (Higuera 1994; Scheichl, Bowles & Pasiadis 2018). Finally, we shall assume throughout the present study that the locations r_{J-} and r_{J+} coincide with the locations of the leading and trailing edge of the jump, respectively, and we denote the film height at r_{J-} as $h(r = r_{J-}) = h_J$.

Unless otherwise specified, the Reynolds number is assumed to be moderately large so that our analysis is confined to the laminar regime. Consequently, for steady axisymmetric thin-film flow, in the presence of gravity, the mass and momentum conservation equations are formulated using a thin-film or Prandtl boundary-layer approach, which amounts to assuming that the radial flow varies much slower than the vertical flow (Schlichting & Gersten 2000). We observe that the pressure for a thin film is hydrostatic as a result of its vanishing at the film surface (in the absence of surface tension) and the small thickness of the film, yielding $p(r, z) = h(r) - z$. By letting a subscript with respect to r or z denote partial differentiation, the reduced dimensionless relevant conservation equations become

$$u_r + \frac{u}{r} + w_z = 0, \quad \text{Re}(uu_r + ww_z) = -\frac{\text{Re}}{\text{Fr}^2} h' + u_{zz}. \quad (3.2.1a, b)$$

where a prime denotes total differentiation with respect to r . These are the thin-film equations commonly used to model the spreading liquid flow (Tani 1949; Bohr *et al.* 1993/1996; Kasimov 2008; Wang & Khayat 2019). At the disk, the no-slip and no-penetration conditions are assumed to hold at any r . At the free surface $z = h(r)$, the kinematic and dynamic conditions must hold. In this case:

$$u(r, z = 0) = w(r, z = 0) = 0, \quad (3.2.2a, b)$$

$$w(r, z = h) = u(r, z = h)h'(r), \quad u_z(r, z = h) = 0. \quad (3.2.2c, d)$$

The flow field is sought separately in the developing boundary-layer region for $0 < r < r_0$, the fully-developed viscous region with moderate gravity for $r_0 < r < r_{J-}$, and fully-

developed viscous region with strong gravity for $r_{j+} < r < r_{\infty}$. Additional boundary conditions are needed, which will be given when the flow is analysed in each region.

3.2.2 The flow in the boundary layer region ($0 < r < r_0$)

In this region, the boundary layer grows with radial distance, eventually invading the entire film depth, reaching the free surface at the transition, $r = r_0$, where the fully-developed viscous region begins. For $0 < r < r_0$, the free surface lies at some height $z = h(r) > \delta(r)$ and is above the boundary-layer outer edge. The flow in the developing boundary-layer region is assumed to be sufficiently inertial for inviscid flow to prevail between the boundary-layer outer edge and the free surface (see figure 3-1). In this case, the following conditions at the outer edge of the boundary layer $z = \delta(r)$ and beyond must hold: $u(r < r_0, \delta \leq z < h) = 1$, $u_z(r < r_0, z = \delta) = 0$. Subject to these conditions, the weak form of the conservation equations for $r < r_0$, become

$$\int_0^{\delta} u dz + h - \delta = \frac{1}{2r}, \quad \frac{\text{Re}}{r} \frac{d}{dr} \int_0^{\delta} ru(u-1) dz = -\frac{\text{Re}}{\text{Fr}^2} \delta h' - \tau_w, \quad (3.2.3a, b)$$

where $\tau_w(r) \equiv u_z(r, z=0)$ is the wall shear stress or skin friction. For simplicity, we choose a similarity cubic profile for the velocity:

$$u(r \leq r_0, z) = \frac{3}{2} \eta - \frac{1}{2} \eta^3 \equiv f(\eta), \quad (3.2.4)$$

where $\eta = z/\delta$, leading to the following problem for the boundary-layer and free-surface heights:

$$h - \frac{3}{8} \delta = \frac{1}{2r}, \quad \frac{39}{280} \frac{\text{Re}}{r} \delta (r\delta)' = \frac{\text{Re}}{\text{Fr}^2} \delta^2 h' + \frac{3}{2}, \quad \delta(r=0) = 0. \quad (3.2.5a-c)$$

The transition location is found when the boundary-layer thickness becomes equal to the film thickness. Consequently, the boundary condition for the film thickness at the transition

location $h_0 \equiv h(r = r_0) = \delta(r = r_0)$ is obtained. Clearly, the formulations presented for the flow in the developing boundary-layer region are the same as those of Wang & Khayat (2019).

3.2.3 The flow in the fully-developed viscous region ($r_0 \leq r \leq r_\infty$)

Downstream of the transition point ($r > r_0$), the potential flow ceases to exist, with the velocity at the free surface becoming dependent on r : $u(r > r_0, z = h) = U(r)$. In this case, the weak form of equation (3.2.1) reads:

$$\int_0^h u dz = \frac{1}{2r}, \quad \frac{\text{Re}}{r} \frac{d}{dr} \int_0^h r u^2 dz = -\frac{\text{Re}}{\text{Fr}^2} h h' - \tau_w. \quad (3.2.6a, b)$$

If the similarity velocity profile: $u(r > r_0, z) = U(r)f(\eta)$ is adopted, where $f(\eta)$ is still given in (3.2.4) with $\eta = z/h$. The film thickness and surface velocity are governed by (Wang *et al.* 2023):

$$U = \frac{4}{5rh}, \quad \text{Re} \left(\frac{5}{4\text{Fr}^2} - \frac{68}{175} \frac{1}{r^2 h^3} \right) h' = \frac{1}{rh^2} \left(\frac{68}{175} \frac{\text{Re}}{r^2} - \frac{3}{2h} \right), \quad (3.2.7a, b)$$

$$h(r = r_0) = h_0. \quad (3.2.7c)$$

This model is equivalent to that developed originally by Tani (1949), and has been extensively (and successfully) used in the literature (Bohr *et al.* 1993; Kasimov 2008; Wang & Khayat 2019; Fernandez-Feria *et al.* 2019; Dhar *et al.* 2020). However, equation (3.2.7b) exhibits a singularity at some finite radial position, which is taken to coincide with the jump location (Wang & Khayat 2019).

In order to capture the continuous jump, we again assume a cubic velocity profile that satisfies the momentum equation (3.2.1b) at the disk or $-\frac{\text{Re}}{\text{Fr}^2} h' + u_{zz}(r, z = 0) = 0$. In this

case, the radial velocity profile is non-self similar, and is given as function of the surface velocity $U(r)$ and the gravitational term $\frac{\text{Re}}{\text{Fr}^2} h^2 h'$ as

$$u(r > r_0, z) = \frac{1}{4} \left[\left(6U - \frac{\text{Re}}{\text{Fr}^2} h^2 h' \right) \eta + 2 \frac{\text{Re}}{\text{Fr}^2} h^2 h' \eta^2 - \left(2U + \frac{\text{Re}}{\text{Fr}^2} h^2 h' \right) \eta^3 \right]. \quad (3.2.8)$$

Here $\eta = z/h$. We observe that the non-self-similarity is due to the presence of the gravity term. An equivalent profile to (3.2.8) was adopted by Watanabe *et al.* (2003), who introduced a shape parameter $\lambda(r)$, and by Bonn *et al.* (2009) for the hydraulic jump in a channel. Clearly, if (3.2.8) is adopted, the skin friction coefficient or wall shear stress is given by $\tau_w(r) = \frac{1}{4} \left(6 \frac{U}{h} - \frac{\text{Re}}{\text{Fr}^2} h h' \right)$. Substituting (3.2.8) into (3.2.6) we obtain the following second-order system in U and h :

$$\frac{\text{Re}}{\text{Fr}^2} h^2 h' = 30U - \frac{24}{rh}, \quad (3.2.9a)$$

$$\begin{aligned} & -\frac{1}{70} \left(\frac{11}{6} \frac{\text{Re}}{\text{Fr}^2} h^2 h' + 41U \right) h U' \\ & = \frac{3}{2\text{Fr}^2} h h' + \frac{3}{\text{Re}} \frac{U}{h} + \frac{1}{14} \left(\frac{\text{Re}}{\text{Fr}^2} U h^2 h' - \frac{27}{5} U^2 - \frac{\text{Re}^2}{60\text{Fr}^4} h^4 h'^2 \right) \left(h' + \frac{h}{r} \right). \end{aligned} \quad (3.2.9b)$$

Equations (3.2.9) are integrated subject to the following boundary conditions obtained from the solution of (3.2.7):

$$u_J = U(r = r_{J-}), \quad h_J = h(r = r_{J-}), \quad h'(r = r_\infty) \rightarrow -\infty. \quad (3.2.10a-c)$$

The solution strategy consists of solving problem (3.2.5) to determine the film thickness h and boundary-layer height δ over the range $0 \leq r \leq r_0$, then finding U and h in the fully viscous region $r_0 \leq r \leq r_{J-}$ by solving (3.2.7b) subject to (3.2.7c). The flow field and film profile over the remainder fully-viscous region $r_{J-} \leq r \leq r_\infty$, as well the (yet unknown)

location of the leading edge of the jump $r = r_{j-}$ are then determined by solving system (3.2.9) subject to (3.2.10). The reader is referred to Wang *et al.* (2023) for more details on the solution strategy.

We observe that system (3.2.9) is equivalent to the system of equations (3.2.25) in Watanabe *et al.* (2003). Eliminating U , we obtain an ordinary differential equation of second order in h :

$$\begin{aligned} \frac{\text{Re}^2}{\text{Fr}^2} r^2 h^4 \left(4 \frac{\text{Re}}{\text{Fr}^2} r h^3 h' + 41 \right) h'' = \text{Re} 1632 (r h)' - 6300 r^2 \\ - 2 \frac{\text{Re}}{\text{Fr}^2} r^2 h^3 h' \left[\frac{\text{Re}^2}{\text{Fr}^2} h^3 h' (5 r h' + h) + 41 \text{Re} h' + 2100 r \right]. \end{aligned} \quad (3.2.11)$$

Next, we consider two well-established limit flows for reference. The first is the limit of infinite Froude number in the supercritical region. We note that the supercritical flow consists essentially of a balance between inertia and viscosity effects with negligible gravity effects. This limit was first considered by Watson (1964) and later adopted by others (see Wang & Khayat 2019 and the references therein). For $\text{Fr} \rightarrow \infty$, the solution of problem (3.2.5) upstream of the transition point reduces to:

$$\delta(r < r_0) = 2 \sqrt{\frac{70}{39} \frac{r}{\text{Re}}}, \quad h(r < r_0) = \frac{1}{4} \left(\sqrt{\frac{210}{13} \frac{r}{\text{Re}}} + \frac{2}{r} \right), \quad (3.2.12a, b)$$

$$U(r < r_0) = 1. \quad (3.2.12c)$$

The transition point is determined by setting $\delta(r_0) = h(r_0)$, yielding $r_0 = \left(\frac{78 \text{Re}}{875} \right)^{1/3}$.

Thus, in the absence of gravity effect, the boundary layer height grows like \sqrt{r} , and the film height decreases predominantly like $1/r$. Downstream of the transition point, the flow is governed by equations (3.2.7). Setting $\text{Fr} \rightarrow \infty$, it is not difficult to show that the solution reduces to:

$$h(r \geq r_0) = \frac{233}{340} \frac{1}{r} + \frac{175}{136} \frac{r^2}{\text{Re}}, \quad U(r \geq r_0) = \frac{4}{5rh}, \quad (3.2.13a, b)$$

suggesting that h decreases like $1/r$ for small r and increases like r^2 for large r .

These expressions are surprisingly in close agreement with Watson's similarity solution and that based on the cubic velocity profile (see also Prince *et al.* 2012 and Wang *et al.* 2023). The behaviour based on (3.2.12)-(3.2.13) reflects qualitatively the profiles in the presence of gravity as illustrated in figure 3-2.

The second asymptotic flow often used in the literature is the limit of negligible inertia in the subcritical region. The flow is captured using lubrication theory, which consists of integrating equation (3.2.1b) to obtain the parabolic velocity profile $u = \frac{\text{Re}}{\text{Fr}^2} h' \left(\frac{z^2}{2} - hz \right)$,

yielding the following profiles for the film thickness and surface velocity:

$$h = \left[h_\infty^4 + 6 \frac{\text{Fr}^2}{\text{Re}} \ln \left(\frac{r_\infty}{r} \right) \right]^{1/4}, \quad U = \frac{3}{4rh}, \quad (3.2.14a, b)$$

where we recall h_∞ to be the thickness at the edge of the disk. In addition, (3.2.14a) requires imposing the value of the edge thickness h_∞ . In contrast, this value is determined accurately by our numerical approach.

3.3 The influence of the disk geometry

In this section, we examine the influence of the disk geometry, namely the disk radius and the height of the obstacle placed at the edge of the disk. In our recent paper (Wang *et al.* 2023), we have exclusively focused on the case of flows draining freely at the edge of the disk. In practice, an obstacle is placed to control the film thickness and explore its influence on the jump and flow structure.

3.3.1 The influence of the disk size

The disk size is expected to be of significant influence on the flow and jump structure. For a given flow rate, the jump location and shape are affected by the amount of fluid accumulated downstream, which is directly related to the disk size. In their solution of the Navier-Stokes equations, Fernandez-Feria *et al.* (2019) considered the flow on two disks of different diameters without accounting for the surface tension effect. Their data is reported here in our figures 3-2a and 3-2b (red symbols) from their figures 6a and 6b for two disk sizes: $r_\infty = 53.33$ and 80 (in units of a), respectively, for a flow of water-glycerol mixture at $Re = 854.29$ and $Fr = 97.19$. Comparison of our predictions in figures 3-2a and 3-2b (solid black curves) yields an overall close agreement for both disk sizes. In the absence of surface tension, the numerical profiles exhibit some waviness or ripples at the trailing edge of the jump, which is not captured by our solution or the pseudospectral solution of the full boundary-layer equations of Fernandez-Feria *et al.* (2019). The ripples are typically predicted by the Navier-Stokes solution, and are attenuated by surface tension (Fernandez-Feria *et al.* 2019; Askarizadeh *et al.* 2019; Wang & Khayat 2021). This issue will be discussed further when we examine the influence of the disk obstacle (refer to figure 3-8 below, showing the Navier-Stokes profiles of Askarizadeh *et al.* (2020) with small ripples for weak surface tension, and no ripples for moderate surface tension).

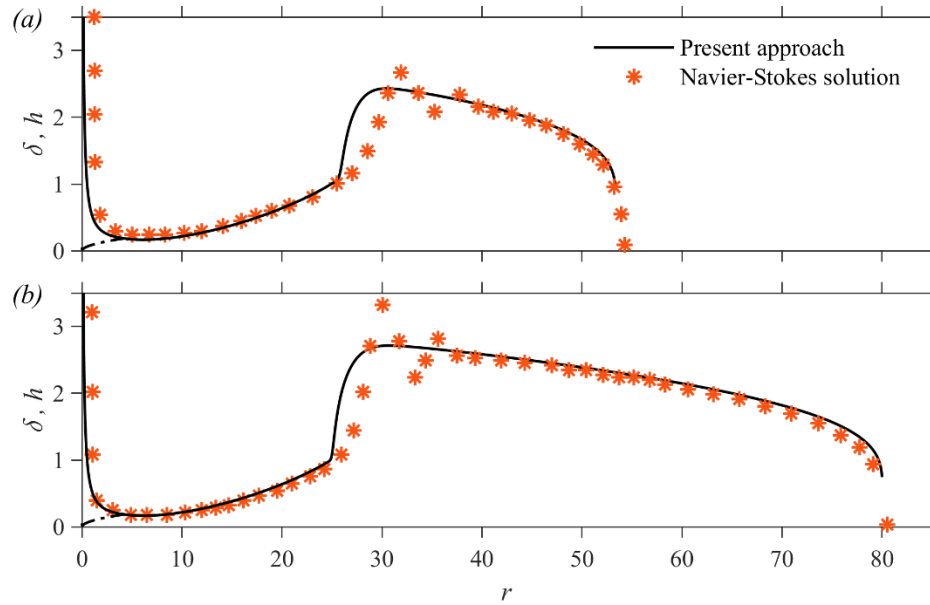


Figure 3-2: Comparison of the free-surface profile based on the present approach against the Navier-Stokes profiles of Fernandez-Feria *et al.* (2019) for $Re = 854.29$, $Fr = 97.19$ and (a) $r_\infty = 53.33$, (b) $r_\infty = 80$.

Figure 3-3 illustrates further the influence of the disk size for $Re = 854.29$ and $Fr = 97.19$. It is striking to see from figures 3-3a and 3-3b how insensitive the supercritical flow is to the variation of r_∞ , a trend well contrasted with the flow in the subcritical region, agreeing with the numerical simulation of Fernandez-Feria *et al.* (2019). The subcritical film depth increases with increasing disk size, causing τ_w to decrease. The jump moves slightly upstream as a result of the accumulated viscous drag and gravity (figures 3-3a and 3-3b). The jump response is consistent with the measurements of Rao & Arakeri (2001), the Navier-Stokes solution of Fernandez-Feria *et al.* (2019), the scaling law (3.4.6) of Duchesne *et al.* (2014) as well as our scaling law (3.4.5) (see section 3.4). Our numerical calculations (shown in the inset of figure 3-3a) suggest that $r_j \sim r_\infty^{-19/20}$, reflecting a weak dependence, which may explain the absence of the disk size dependence in the scaling law of Bohr *et al.* (1993). Both our scaling law (3.4.5) and (3.4.6) of Duchesne *et al.* (2014) propose an implicit relation for the jump radius with a logarithmic dependence on the disk size. The vortex becomes increasingly apparent as a result of the jump steepening with increasing disk size. Below a critical disk size, the recirculation vanishes (figures 3-3c to

3-3e). It is expected that no jump exists if the disk is sufficiently small (Rao & Arakeri 2001). The profiles for a small disk with no separation are reminiscent of the profiles with expansive interaction discussed by Bowles (1995) for the flow over a sloped bed. Similarly, the profiles over a larger disk with separation correspond to a compressive interaction.

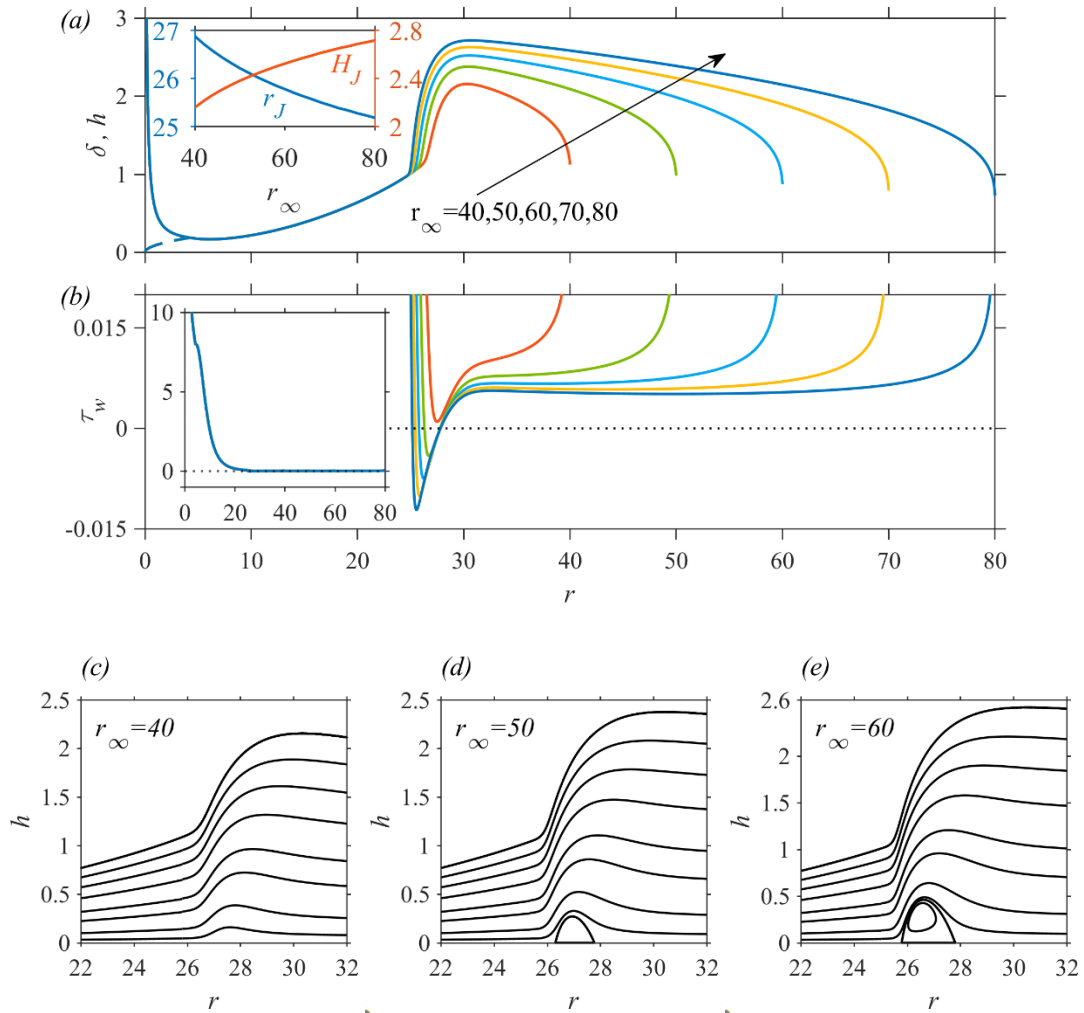


Figure 3-3: Influence of the disk radius r_∞ on (a) the free surface profile (solid curves) the boundary-layer thickness (dashed curves), and (b) the wall shear stress. Shown in (c)-(e) are the streamlines for $r_\infty = 40, 50$ and 60 . The inset in (a) shows the dependence of the jump radius and maximum film height on the disk radius. Here, $Re = 854.29$, $Fr = 97.19$ are parameters used in Fernandez-Feria *et al.* (2019).

3.3.2 The interplay between the flow rate and disk size

Although the jump position does not seem to be significantly influenced by the disk radius, the flow field and vortex structure appear to be more sensitive to the disk size (3- 2 and 3- 3). These jump features are further examined by varying the flow rate over the same experimental range as Duchesne *et al.* (2014) but for a disk almost twice and four times smaller. Figure 3-4 illustrates the influence of the flow rate on the film profile for a disk of radius $r_\infty = 93.75$ (figure 3-4a), $r_\infty = 50$ (figure 3-4b) and $r_\infty = 25$ (figure 3-4c). Figure 3-4a typically illustrates the film profiles for a film draining at the edge of the disk at different flow rates. Although similar or equivalent flow details were not reported by Duchesne *et al.* (2014), the profiles in figure 3-4a correspond to the same range of flow rates and conditions of their experiment. The figure shows that the boundary-layer thickness diminishes with increasing flow rate, following closely (3.2.12a), with the film thickness profile well reflected in (3.2.12b). The figure indicates that although the jump radius and height both grow with the Froude number, the shape of the jump, particularly its steepness or slope is insensitive to the Froude number. While the supercritical region extends in length and diminishes in thickness, the subcritical region shrinks in length with diminishing thickness growth with flow rate, evolving from an essentially linear to a logarithmic (lubrication) profile (excluding the vicinity of the edge). We shall refer extensively to this figure when examining various characteristics of the jump.

Figure 3-4c shows that the monotonic growth of the film height in figures 3-4a and 3-4b is clearly replaced by a height that increases with the flow rate, reaching an overall maximum and decreases as the flow rate is increased further. The results seem to suggest that a maximum for maximum film height will show as well when $r_\infty = 93.75$ and 50 if the flow rate increases further. Figure 3-4c also shows a significant change in the film profile in the subcritical region as well as smoothening in the jump region compared to figure 3-4a. We expect, and as we confirm below, a gradual and significant change in the flow field and vortex structure as the disk size increases.

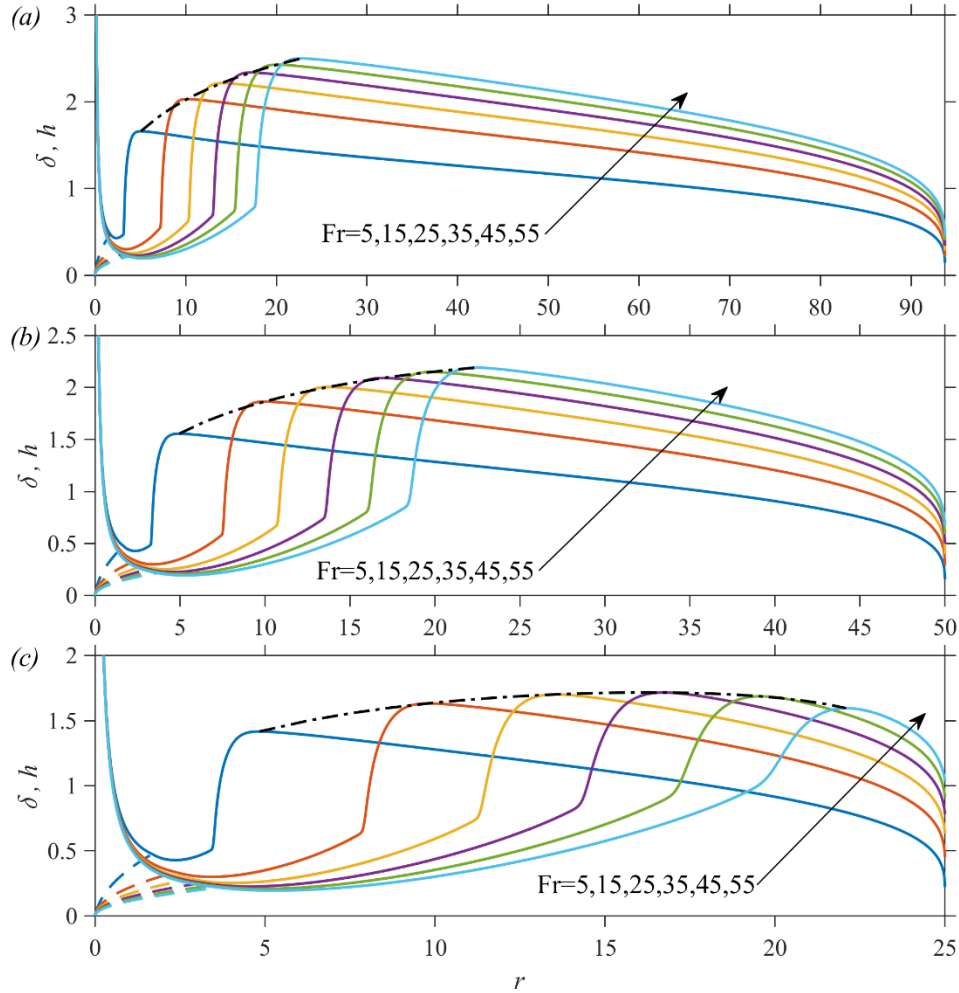
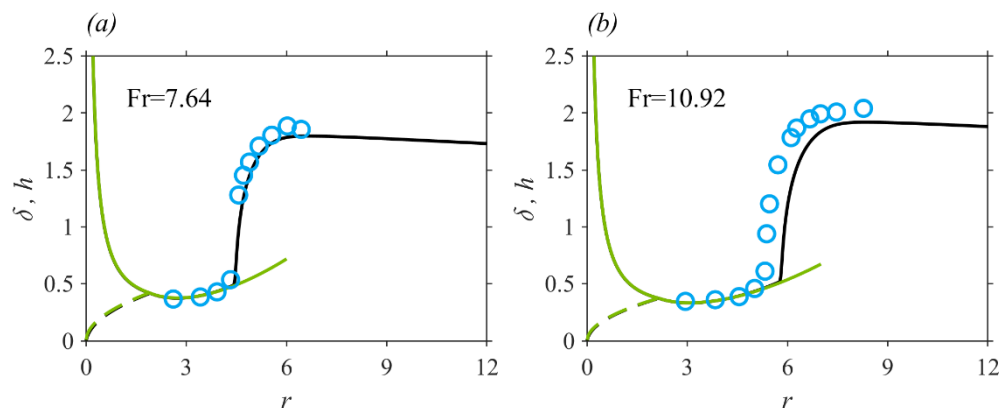


Figure 3-4: Influence of the Froude number (flow rate) on the film profile for three different disk sizes: (a) $r_\infty = 93.75$, (b) $r_\infty = 50$ and (c) $r_\infty = 25$. Here, $Ga = 100$ ($50.11 < Re < 551.25$), corresponding to the range of flow rate in the experiment of Duchesne *et al.* (2014). Dash-dotted curves in (a)-(c) represent the locus of the maximum film height.

In our earlier study (see figure 6 of Wang *et al.* 2023), we compared our theoretical prediction for the film profile over the entire domain against the measurements of Duchesne *et al.* (2014) for silicon oil (20 cSt) of density 960 kg m^{-3} and kinematic viscosity $2 \times 10^{-5} \text{ m}^2 \text{ s}^{-1}$. The liquid was injected downward from a jet of radius $a = 1.6$ mm onto a horizontal circular disk of radius $R_\infty = 15$ cm. However, although the comparison led to a close agreement against experiment, the validation was limited to a

film profile for one flow rate, namely $Q = 17 \text{ cm}^3/\text{s}$. In an effort to explore the supercritical flow, Duchesne (2014) reported measurements in his thesis for three different flow rates concentrated on the supercritical and jump regions. In his figure V.4, they considered the film profiles for $Q = 7.7, 11$ and $17 \text{ cm}^3/\text{s}$ against the predictions of Watson (1964), which showed some agreement in the supercritical region at small flow rate.

Figure 3-5 shows the comparison of the free-surface profiles based on our approach and experiment for a disk of 15 cm radius or $r_\infty = 93.75$. The flow conditions in dimensionless form correspond to $Fr = 7.64, 10.92$ and 16.87 in figures 3-5a, 3-5b and 3-5c, respectively. We also included the prediction from the Navier-Stokes numerical solution of Zhou & Prosperetti (2022) for the highest flow rate in figure 3-5c. The theoretical profiles agree well with experiment but, like the Navier-Stokes numerical solution, they underestimate slightly the supercritical film thickness at the jump, especially for the highest flow rate considered (figure 3-5c). In contrast, and as we showed previously (see figure 6 of Wang *et al.* 2023), in the subcritical region, the theoretical and numerical predictions almost fit all the experimental data points, except near the disk edge. The agreement with the Navier-Stokes solution of Zhou & Prosperetti (2022) is surprisingly close. We recall that the effect of surface tension was neglected in our model but was included in the numerical simulation (see also Wang & Khayat 2021), confirming that, in this case, the effect of surface tension may only be important near the edge and at the jump. As to the location of the jump, the experimental data suggest a slightly smaller jump radius than predicted by our approach and the numerical simulation.



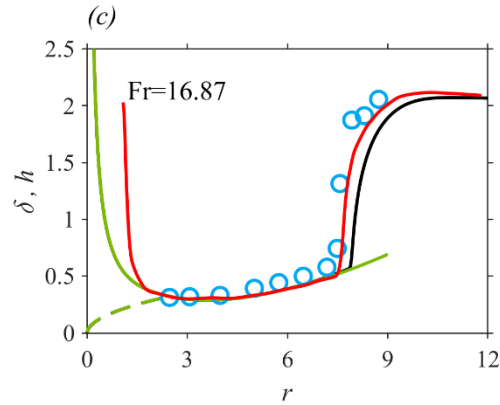


Figure 3-5: Comparison of the free-surface profile in the supercritical and jump regions based on the present approach against the measurements of Duchesne (2014) for three different flow rates. Here, $Ga = 100$ and $r_\infty = 93.75$. The green curves are based on expressions (3.2.12a,b) and (3.2.13a), the red curve in (c) is from the Navier-Stokes solution of Zhou & Prosperetti (2022), the blue circles are from Duchesne (2014), and the black curves are from the present approach.

Further details on the influence of the disk size on the jump and vortex structure are reported in figure 3-6 for the jump radius, and figure 3-7 for the jump height (figure 3-7a), length (figure 3-7b) and vortex length (figure 3-7c). The profiles are shown for three different disk sizes: $r_\infty = 93.75$, $r_\infty = 50$ and $r_\infty = 25$. Figure 3-6a confirms the overall lack of sensitivity of the jump radius to the size of the disk, simultaneously indicating a decrease in the jump radius with increasing disk size. The figure also suggests, albeit in a faint manner, the tendency of the jump radius to grow linearly with the flow rate for the smaller disk size, in agreement with the measurements of Mohajer & Li (2015), reported in their figure 4. In figures 3-6b and 3-6c, we compare our theoretical predictions against the measurements of Duchesne (2014), available only for $r_\infty = 93.75$, $r_\infty = 50$. We also added the radius distributions based on our scaling law (3.4.5) which we establish in section 3.4.1, showing a close agreement with both theory and experiment.

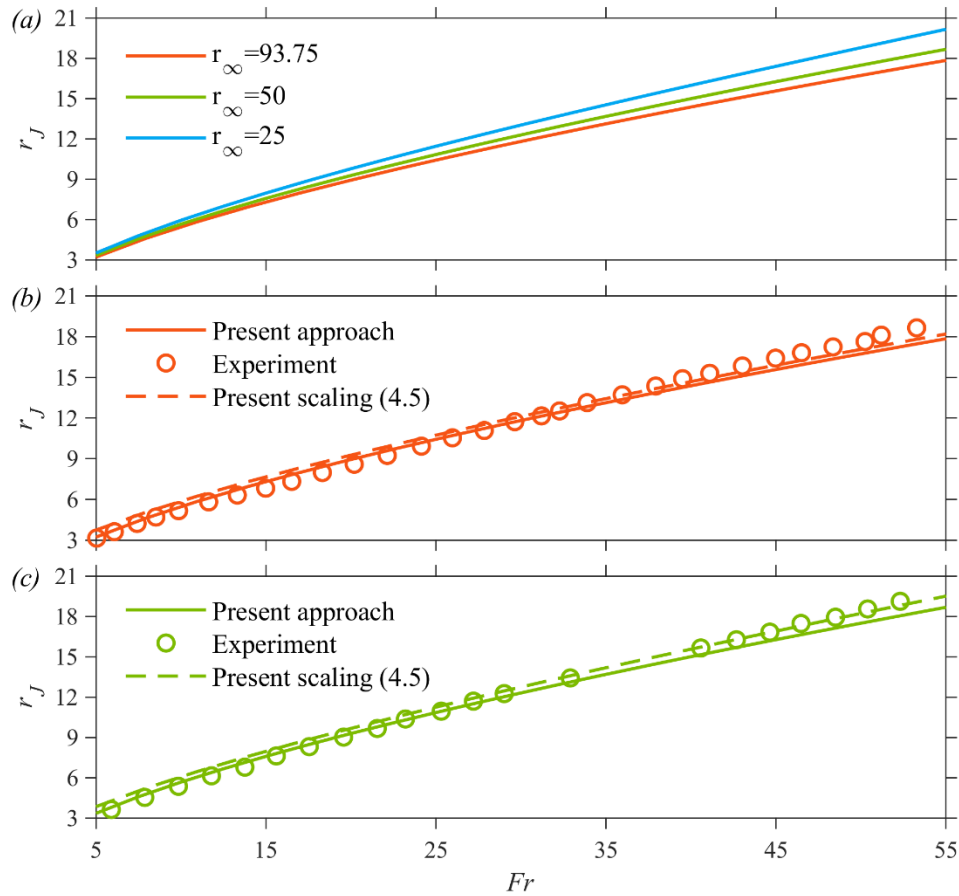


Figure 3-6: Influence of Fr (flow rate) for different disk sizes on the jump radius. Shown in (a) is the prediction based on the present approach, in (b) and (c) are the comparison between the present approach, the measurement of Duchesne (2014), and the present scaling (3.4.5) for $r_\infty = 93.75$ and 50 , respectively. Here $Ga = 100$, corresponding to the parameters in the experiment of Duchesne *et al.* (2014).

As to the jump height, figure 3-7a suggests that the height does not always increase monotonically with the flow rate. In fact, H_J reaches a maximum for a disk of radius $r_\infty = 25$. In addition, the height varies rather insignificantly with the flow rate, remaining essentially constant, again in agreement with the data in figure 4 of Mohajer & Li (2015), as well as the earlier observation of Hansen *et al.* (1997). The non-monotonicity is also reflected in the response of the jump length and vortex size in figures 3-7b and 3-7c, respectively. In fact, Craik *et al.* (1981) found that the jump length increases monotonically with the flow rate (see their figure 6). A similar trend was also observed by Rao & Arakeri

(2001) for a relatively large disk (see their figure 6), but they reported a decrease in the jump length with increasing flow rate for a small disk (see their figure 7). The monotonic increase in the vortex length was observed by Rao & Aekkeri (2001), while the non-monotonic behaviour was illustrated by Craik *et al.* (1981). Both L_J and L_{vortex} are overall smaller for a smaller disk size. The jump becomes of type 0 (no vortex) when Fr exceeds 39 for $r_\infty = 25$. In addition, as indicated by Chang *et al.* (2001), the vortex under the jump disappears when the flow rate is smaller than a critical value, meanwhile, the jump length experiences a transition and becomes much wider (see their figure 9).

Finally, Chang *et al.* (2001) reported that, as the jump radius decreases significantly, the surface tension effect becomes important. They also noted that this feature corresponds to the type II jump observed by Ellegaard *et al.* (1998), who found that a surface roller appears under the free surface, and the jump becomes much smoother. The Navier-Stokes solution of Askarizadeh *et al.* (2020) confirmed that as the surface roller appears, the vortex near the wall disappears. Clearly, this particular phenomenon is beyond the scope of our current study.

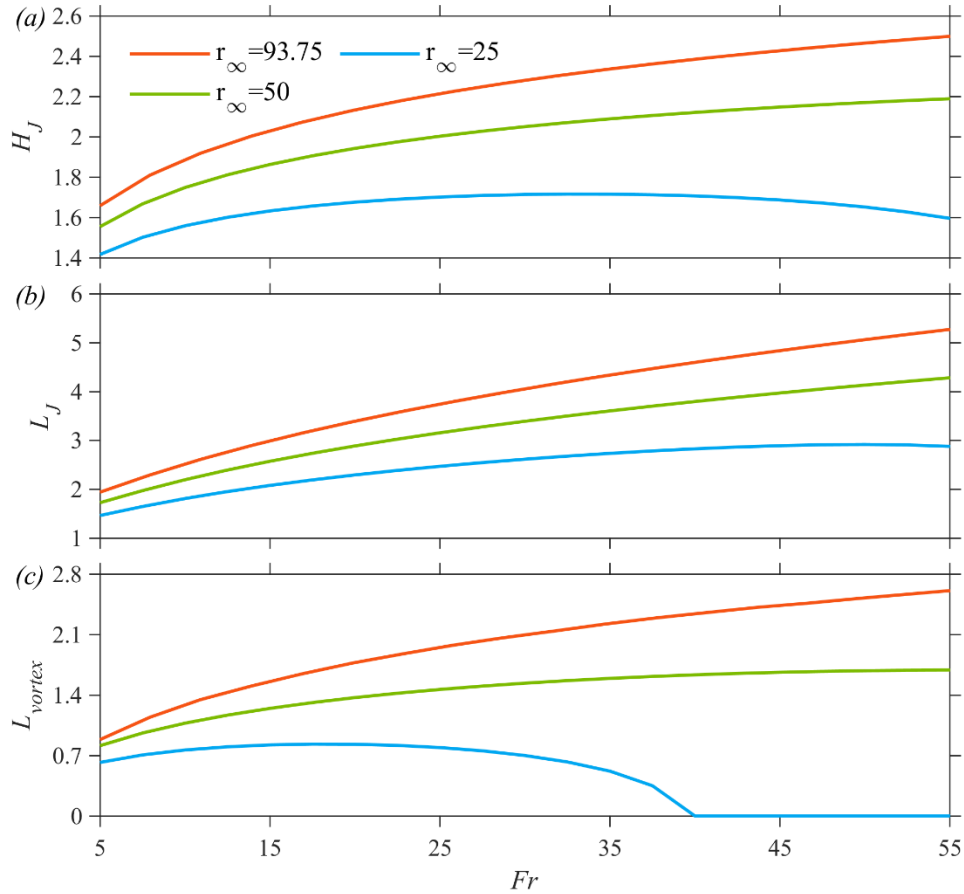


Figure 3-7: Influence of Fr (flow rate) for different disk sizes on (a) maximum film height, (b) jump length and (c) vortex length. Here $Ga = 100$, corresponding to the parameters in the experiment of Duchesne *et al.* (2014).

3.3.3 The influence of the obstacle height at the edge of the disk

Although we have extensively validated the present approach in Wang *et al.* (2023) for a film freely draining at the disk edge, we further verify our model against the numerical solution of the Navier-Stokes equations when an obstacle is placed at the disk edge. Askarizadeh *et al.* (2019) explored the origin of the hydraulic jump. They identified two different flow regimes in the jump formation: gravity- and capillary-dominant flow regimes. They found that gravity effects are important for a flow with high viscosity, density and flow rate, as well as low surface tension. Later, Askarizadeh *et al.* (2020) investigated the heat transfer in the jump region. In figure 3-8, we compare our approach against their simulated flow for a flow of density $\rho = 1100 \text{ kg/m}^3$ and kinematic viscosity

$\nu = 10$ cSt, at a flow rate $Q = 30$ ml/s. The simulated jet is injected from a nozzle of radius $a = 2.5$ mm, impinging onto a horizontal circular disk of radius $R_\infty = 40$ mm. For the flow with surface tension $\sigma = 10$ mN/m, the obstacle was 1 mm high at the disk edge (figure 3-8a), and 0.05 mm for $\sigma = 45$ mN/m (figure 3-8b), with corresponding simulation data taken from Askarizadeh *et al.* (2019) and (2020), respectively. The two figures indicate that the film thickness at the disk edge, resulting from the combined obstacle height and capillary length, is sensibly the same.

The predicted profiles based on our approach are generally in good agreement with the numerical simulation for both regimes. Recalling that surface tension effects are neglected in the present study, figures 3-8a and 3-8b suggest a minimal importance of surface tension, the discrepancy being localised at the jump level. For low surface tension (dominant gravity), our profile is slightly lower with a milder curvature than the exact numerical profile (figure 3-8a). The ripple immediately downstream of the jump is commonly predicted in numerical simulations without surface tension (Fernandez-Feria *et al.* 2019; Wang & Khayat 2021; Zhou & Prosperetti 2022). At higher surface tension, the numerical curvature is milder, and our prediction for the film height at the jump is slightly higher than the result of the numerical simulation (figure 3-8b). The agreement in the supercritical is very close, which is not surprising given the absence of strong film curvature, except for very near jet impingement. Figure 3-8c depicts the predicted flow field as well as the wall shear stress and surface velocity distributions (inset), to be contrasted against the simulated flow field reproduced in figure 3-8d from the Navier-Stokes solution of Askarizadeh *et al.* (2020). A vortex near the disk under the jump is clearly visible and is similar to the numerical prediction, especially for the height of the vortex, but the latter displays a wider vortex due to the smoother jump profile at the jump region; the maximum of film height is close to the obstacle placed at the disk edge, which may be caused by the presence of the obstacle that is not captured by our approach. We observe that the edge singularity usually reflected at the edge of a draining fluid is not present for an edge with an obstacle (see next).

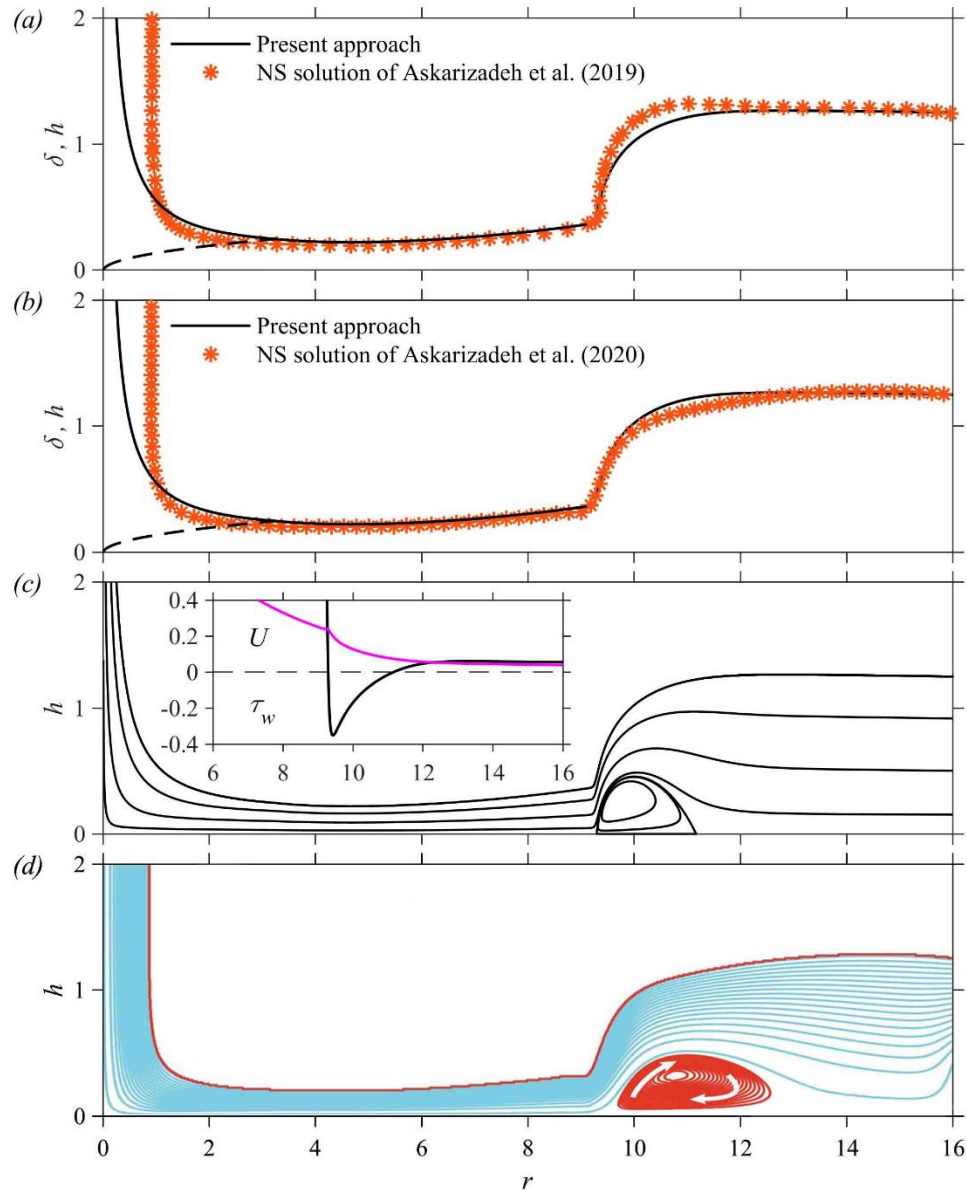


Figure 3-8: Comparison of the free-surface profiles between our approach (black solid line) and the Navier-Stokes solution of Askarizadeh *et al.* (2019) and (2020), shown in red symbols in (a) and (b), respectively, for $\sigma = 10$ and 45 mN/m, and corresponding obstacle heights of 1 and 0.05 mm. Predicted and simulated flow fields are shown in (c) and (d), respectively, with the inset in (c) depicting the surface velocity and wall shear stress distributions. In all cases, $Re = 381.97$, $Fr = 9.76$, $r_\infty = 16$.

We explore further the effect of the film thickness at the disk edge by $Re = 381.97$, $Fr = 9.76$ and $r_\infty = 16$. Similar to the experimental measurements of Bohr *et al.* (1996) and the Navier-Stokes solution of Askarizadeh *et al.* (2020), figure 3-9 indicates that the flow in the supercritical region is unaffected by the value of the film thickness at the disk edge. In contrast, the flow in the subcritical and jump regions is significantly influenced when h_∞ varies. Figure 3-9a shows that the film thickness in the subcritical region increases overall with h_∞ , pushing the jump location closer to the impinging jet, in agreement with Bohr *et al.* (1996), Passandideh-Fard *et al.* (2011) and Askarizadeh *et al.* (2019, 2020). However, as we show in the inset of figure 3-6a, both the jump radius and maximum film height saturate to a constant value in the lower range of h_∞ , which is the case when the flow drains freely at the disk edge. It also suggests that the flow at the jump is not sensitive to the edge condition for the free draining situation, as long as the film thickness at the disk edge is close to a draining fluid thickness with no obstacle. Meanwhile, the wall shear stress in the subcritical region is greatly affected; the wall shear stress decreases overall as flow is slowed down when the film thickness in the subcritical region is increased (figure 3-9b), and the strength of the separation zone increase with the increase of h_∞ as a result of the steepening of the jump (figure 3-9b to 3-9e). In fact, Askarizadeh *et al.* (2020) also showed that the heat transfer characteristics also exhibit similar features as the wall shear stress. Although we have shown that the vortex size increases with the rise of h_∞ , the behaviour of the vortex size is much more complex in reality. The surface tension becomes important when the jump radius becomes smaller, and instability will also appear as the film height rises. In this case, the size of the vortex near the wall will decrease until it disappears (Craik *et al.* 1981; Chang *et al.* 2001; Bohr *et al.* 1996; Askarizadeh *et al.* 2020), and hydraulic jump either becomes unstable (Craik *et al.* 1981) or transfer to a type Ib jump (only a surface roller shows) then type II jump (Bohr *et al.* 1996; Askarizadeh *et al.* 2020); with both a wall vortex and a surface roller. As the current study focuses on the type I jump or type Ia jump (Askarizadeh *et al.* 2020), the surface tension effect is not considered.

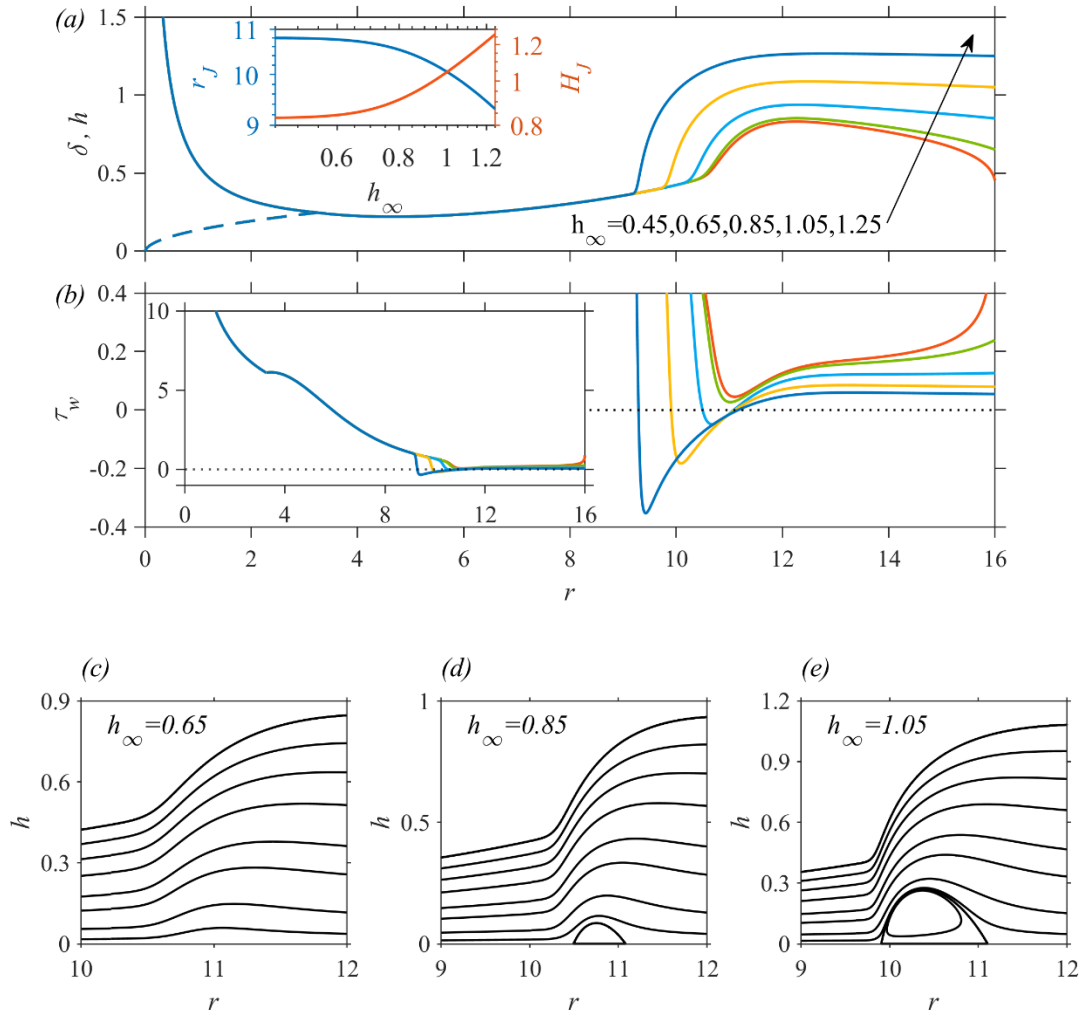


Figure 3-9: Influence of the film thickness at the disk edge on (a) the free surface profile (solid curves) and the boundary-layer thickness (dashed curves), and (b) the wall shear stress. Shown in (c)-(e) are the streamlines for $h_\infty = 0.65, 0.85$ and 1.05 . The inset in (a) shows the dependence of the jump radius and maximum film height on the film thickness at the disk edge. Here, $Re = 381.97$, $Fr = 9.76$ and $r_\infty = 16$ are parameters corresponding to the simulation of Askarizadeh *et al.* (2019, 2020).

3.4 Scaling analysis

In Wang *et al.* (2023), we have extensively validated our approach against existing measurements and numerical simulations for a flow draining freely at the disk edge. In the current study, we establish scaling laws for the jump properties, such as the jump radius

and length, vortex size, energy loss across the jump, and conjugate depth ratio, among others.

3.4.1 The scaling law for the jump radius

By considering the horizontal momentum conservation across the jump, and assuming lubrication flow downstream of the jump, Higuera (1994) derived an expression for the jump location in the plane. Following his treatment, we first consider the weak form of the radial momentum equation (3.2.6), which takes the following approximate form across a *narrow* jump:

$$\text{Re} \left[\int_0^{h_J} u^2(r_{J-}, z) dz - \int_0^{H_J} u^2(r_{J+}, z) dz \right] \approx \frac{\text{Re}}{2\text{Fr}^2} (H_J^2 - h_J^2) + L_J \tau_w(r = r_J), \quad (3.4.1)$$

where L_J is the jump length and $\tau_w(r = r_J) = u_z(r = r_J, z = 0)$ is the wall shear stress at the jump. Here, r_{J-} and r_{J+} are radial locations immediately upstream and downstream of the jump, with corresponding heights $h_J \equiv h(r = r_{J-})$ and $H_J \equiv h(r = r_{J+})$, respectively. Assuming the jump length to be relatively small ($L_J \ll r_J$), the gravity term to be negligible compared to the momentum flux in the supercritical region, and the momentum flux term to be negligible compared to the gravity term in the subcritical region, equation (3.4.1) reduces to

$$\int_0^{h_J} u^2(r_{J-}, z) dz \approx \frac{H_J^2}{2\text{Fr}^2}. \quad (3.4.2)$$

When gravity is negligible, the supercritical velocity profile (3.2.8) reduces to $u(r_{J-}, z) = u_J f(\eta)$, where we recall $u_J = U(r_{J-}) = 4/5 r_J h_J$ from (3.2.7a) and (3.2.10a),

and $f(\eta)$ from (3.2.4), with $\eta = z/h_J$, yielding $\int_0^{h_J} u^2(r_{J-}, z) dz = \frac{272}{875} \frac{1}{r_J^2 h_J}$. Thus, we

have

$$H_J \approx \frac{4}{5} \sqrt{\frac{34}{35}} \frac{\text{Fr}}{r_J \sqrt{h_J}}. \quad (3.4.3)$$

The flow downstream of the jump must be analysed in order to determine the still unknown jump radius r_J . The earlier estimates imply that the convection terms in equation (3.2.1b) are negligible in this region, and then the balance of viscous and pressure forces for lubrication flow leads to the following downstream jump height from (3.2.14a):

$$H_J = \left[h_\infty^4 + 6 \frac{\text{Fr}^2}{\text{Re}} \ln \left(\frac{r_\infty}{r_J} \right) \right]^{1/4}, \text{ where we recall } h_\infty \approx \left(\frac{27}{70} \right)^{1/3} \left(\frac{\text{Fr}}{r_\infty} \right)^{2/3} \text{ from (3.4.8) below.}$$

Finally, recalling from (3.2.13a) the supercritical thickness $h_J = \frac{233}{340} \frac{1}{r_J} + \frac{175}{136} \frac{r_J^2}{\text{Re}}$, we

obtain the desired equation for the jump radius:

$$\left(\frac{544}{875} \right)^2 \frac{\text{Fr}^4}{r_J^4} \left(\frac{233}{340} \frac{1}{r_J} + \frac{175}{136} \frac{r_J^2}{\text{Re}} \right)^{-2} = \left(\frac{27}{70} \right)^{4/3} \left(\frac{\text{Fr}}{r_\infty} \right)^{8/3} + 6 \frac{\text{Fr}^2}{\text{Re}} \ln \left(\frac{r_\infty}{r_J} \right). \quad (3.4.4)$$

This equation can be simplified for a disk of relatively large diameter so the first term on the right-hand side is negligible ($h_\infty \rightarrow 0$). In addition, the jump tends to occur

downstream of the ascending portion of the film thickness so that $h_J \approx \frac{175}{136} \frac{r_J^2}{\text{Re}}$, yielding

$$r_J \left[\ln \left(\frac{r_\infty}{r_J} \right) \right]^{1/8} = \gamma \text{Fr}^{1/4} \text{Re}^{3/8}, \quad (3.4.5)$$

where γ is a constant, that depends only on the type of velocity profile adopted in the averaging process. For a cubic profile, $\gamma = 2/3$. If the logarithmic dependence is dropped, we recover the scaling law of Bohr *et al.* (1993), who suggested the value $\gamma = 0.73$ (compared to 0.67). Relation (3.4.5) is very similar to the scaling law of Duchesne *et al.* (2014), which we recast here as

$$r_J \left[\ln \left(\frac{r_\infty}{r_J} \right) \right]^{3/8} = \gamma Fr^{1/4} Re^{3/8}, \quad (3.4.6)$$

where $\gamma = \frac{1}{2\pi} \left(\frac{\pi}{6} \right)^{3/8} Fr_J^{-1}$ is constant. We observe that Duchesne *et al.* (2014) established their scaling law by assuming that $Fr_J \equiv Fr / 2r_J H_J^{3/2}$ is constant, therefore allowing them to eliminate H_J between this relation and the lubrication result (3.2.14a)

$$H_J = \left[6 \frac{Fr^2}{Re} \ln \left(\frac{r_\infty}{r_J} \right) \right]^{1/4}$$

to obtain the expression for r_J . Their scaling law is therefore semi-empirical since the value of Fr_J must be imposed from experiment. In contrast, relation (3.4.4) and its simplified form (3.4.5), as well as that of Higuera (1994) for a planar jump, are fully theoretical.

Figure 3-10 shows the comparison between our scaling law (3.4.5) and other laws, including the measurements of Duchesne *et al.* (2014) in figure 3-10a, and those of Hansen *et al.* (1997) in figure 3-10b. As expected, the scaling law (3.4.6) of Duchesne *et al.* (2014) fits best their measurements in figure 3-10a as Fr_J was empirically adjusted. The discrepancy of the scaling of Bohr *et al.* (1993) becomes evident for $Fr > 35$, which is most likely due to the shock-like jump assumed in obtaining the scaling law. Figure 3-10b shows that our scaling law (3.4.5) is as accurate as that of Rojas *et al.* (2013). This latter relates the radius of the jump, in particular, to the height downstream of the jump (see their relation (15)). In the absence of surface tension, the relation, written here as $r_J \approx \left[(9/70) \left(Re Fr^2 / H_J^2 \right) \right]^{1/4}$, is based on their spectral approach for inertial-lubrication flow (Rojas *et al.* 2010) and the inviscid Belanger equation (White 2006).

We recall that Rojas *et al.* (2013) fixed their downstream thickness from experiment in both their numerical solution and scaling. It is important to observe that our scaling law is not expected to remain accurate for low viscosity fluids because it is based on the lubrication assumption. However, it seems to yield a reasonably accurate description if γ is

slightly readjusted from $2/3$. We have taken $\gamma = 0.45$ in figure 3-10b for water. Finally, the discrepancy at low flow rates is not surprising since it was difficult to observe the jump, so the first few data points are not reliable (Hansen *et al.* 1997). Another source for the discrepancy at low flow rates for (3.4.5) and existing scaling laws is the narrow or shock-like assumption of the hydraulic jump made when deriving the scaling.

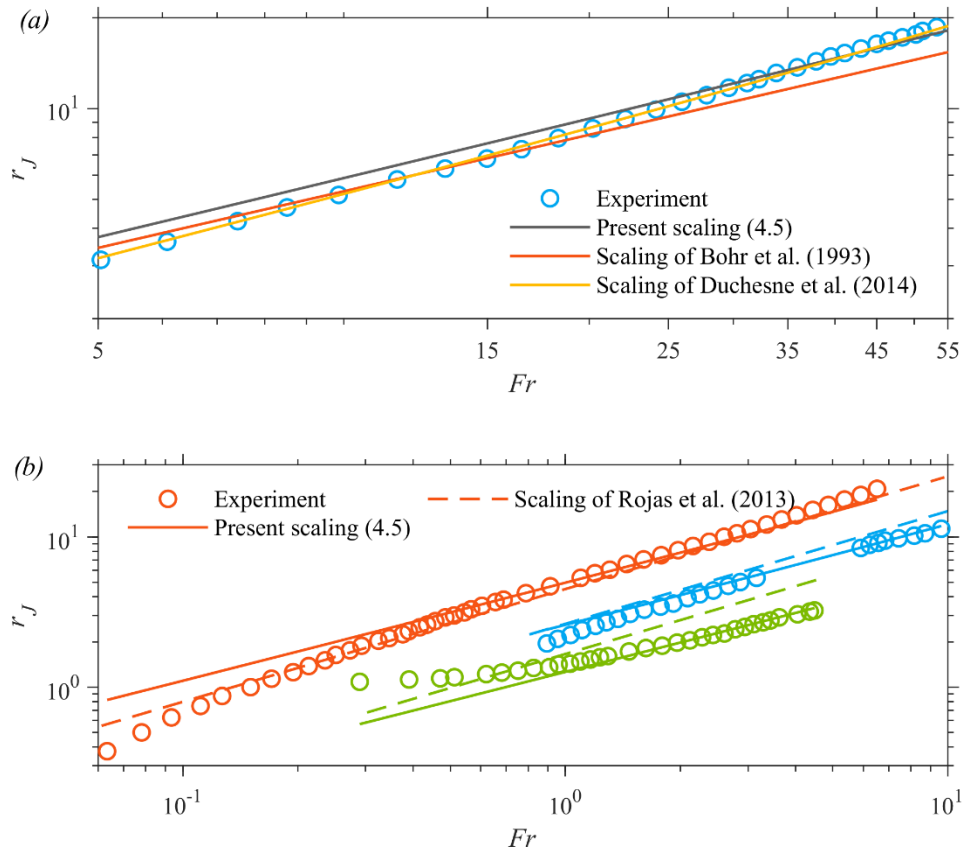


Figure 3-10: Comparison of scaling laws for the influence of the Froude number (flow rate) on the jump radius. Our scaling law (3.4.5) is compared in (a) against those of Bohr *et al.* (1993) and Duchesne *et al.* (2014), and in (b) against the scaling law of Rojas *et al.* (2013). Measurements of Duchesne *et al.* (2014) are added in (a) and those of Hansen *et al.* (1997) in (b) for reference. In (b), results for water ($\nu = 1\text{cSt}$) ($Ga = 627840$) are in red, those for silicon oil ($\nu = 15\text{cSt}$) ($Ga = 2790$) are in blue, and those for silicon oil ($\nu = 95\text{cSt}$) ($Ga = 70$) are in green.

Finally, we show how our scaling law (3.4.5) can be used to estimate the (constant) value of Fr_J . We consider the flow on a large disk so $r_\infty \gg r_J$. In this case, assuming lubrication

subcritical flow, evaluating (3.2.14a) at the jump, and keeping the dominant terms, we have

$$H_J \approx \left(6 \frac{\text{Fr}^2}{\text{Re}} \ln r_\infty \right)^{1/4}. \text{ Simultaneously, (3.4.5) reduces to } r_J \approx \gamma \text{Fr}^{1/4} \text{Re}^{3/8} (\ln r_\infty)^{-1/8}.$$

Then, recalling the definition $\text{Fr}_J = \text{Fr} / 2r_J H_J^{3/2} = \frac{1}{2 \times 6^{3/8} \gamma (\ln r_\infty)^{1/4}}$, we then have

$$\text{Fr}_J = \frac{1}{2 \times 6^{3/8} \gamma (\ln r_\infty)^{1/4}}, \quad (3.4.7)$$

which clearly demonstrates that Fr_J is independent of Fr (or Re), and depends only on the size of the disk. If γ is taken equal to 0.54 (instead of 0.67 for a cubic profile), then (3.4.7) yields to $\text{Fr}_J = 0.32$, in agreement with the data from the measurements of Duchesne *et al.* (2014) for $r_\infty = 93.75$, based on the jump height estimated from lubrication flow. It is important to recall that we arrived at (3.4.7) by assuming that the jump radius is small relative to the disk radius ($r_\infty \gg r_J$). As we shall see later, the constancy of Fr_J may not hold under some flow conditions.

3.4.2 The film thickness and velocity at the edge of the disk without an obstacle

The thickness at the edge of the disk remains largely unaddressed in the literature, as the flow near the disk edge experiences a complex interplay of inertia, gravity and surface tension (Higuera 1994; Wang *et al.* 2023). For the situation when the flow drains freely off the disk edge, there are mainly two approaches to determine the film height or equivalent conditions at the disk edge; imposing an infinite slope (Bohr *et al.* 1993; Kasimov 2008; Dhar *et al.* 2020), or assuming the edge thickness to be essentially equal to the capillary length (Duchesne *et al.* 2014; Ipatova *et al.* 2021; Duchesne & Limat 2022). As indicated in the experimental work of Duchesne *et al.* (2014), the edge film thickness also follows a weak power law dependence on the flow rate.

To explore the small variation of the film height at the disk edge, we follow Yang & Chen (1992) and Yang *et al.* (1997), and utilize the minimum mechanical (Gibbs free) energy

principle for the dynamic thickness contribution. We thus consider the minimum of the energy flux, and set $\frac{\partial}{\partial h} \int_0^h \left(\frac{1}{2} Fr^2 u^2 + h \right) u r dz = 0$ at $r = r_\infty$. This principle states that a fluid

flowing over the edge of a disk under the influence of a hydrostatic pressure gradient will adjust itself so that the mechanical energy within the fluid will be minimum with respect to the film thickness at the disk edge. Since the flow is predominantly slow and of lubrication character in the subcritical region (Duchesne *et al.* 2014), we then can use

$$u = \frac{3}{2rh^3} \left(hz - \frac{z^2}{2} \right) \quad (\text{Wang \& Khayat 2019}),$$

yielding the following estimates for the edge thickness (and average velocity $\langle u_\infty \rangle = \frac{1}{2r_\infty h_\infty}$):

$$h_\infty \approx \left(\frac{27}{70} \right)^{1/3} \left(\frac{Fr}{r_\infty} \right)^{2/3}. \quad (3.4.8)$$

Although expression (3.4.8) seems to yield overall a good agreement with numerical and experimental results, they are not expected to hold when the subcritical flow deviates from lubrication flow, especially near the disk edge where inertia (and possibly surface tension) effects become tangible. Our own numerical predictions suggest that the flow can accelerate considerably near the edge for the local Froude number Fr_l to exceed unity near the edge (see figure 11 in Wang *et al.* 2023). We recall the local Froude number in terms of the average velocity and film height as $Fr_l = Fr \langle u \rangle / \sqrt{h}$. Noting from (3.2.6a) that $\langle u \rangle = 1/2rh$, then $Fr_l = Fr / 2rh^{3/2}$. Upon setting $Fr_l = 1$ at the edge of the disk, we obtain

$$h_\infty = \left(\frac{1}{4} \right)^{1/3} \left(\frac{Fr}{r_\infty} \right)^{2/3}. \quad (3.4.9)$$

Aside from a few percentage difference in the coefficients, expressions (3.4.8) and (3.4.9) yields the same dependence of the edge thickness on the flow parameters, involving only the Froude number and disk radius. The validity of the two estimates is established by

comparison against our numerical result. Figure 3-11 shows that the numerical predictions for the edge thickness (figures 3-11a and 3-11b) and average velocity (figure 3-11c) follow closely (3.4.8) for low flow rates and (3.4.9) for high flow rates. The numerical (solid) curves in figure 3-11 fall in between the two estimates over the entire Fr range considered. It eventually merges with the (3.4.9) curve as Fr increases beyond the range shown. Recalling that we determine the edge condition by assuming an infinite slope at the disk edge, the obtained film thickness at the disk edge indeed depends on the flow conditions, which we explore further below. In other words, the flow upstream is sensitively influenced by edge conditions (Higuera 1994).

Here, for the experimental measurement of film thickness at the disk edge in Duchesne *et al.* (2014), as they found that the film thickness at the disk edge is only weakly dependent on the flow rate, we then only try to compare our predictions with the dynamic thickness at the disk edge, which is the original measured thickness minus the static thickness

$$H_s = \frac{2}{\sqrt{Bo}} \sin\left(\frac{\theta_Y}{2}\right) \quad (\text{Wang \& Khayat 2019}), \quad \text{where } Bo = \frac{\rho g a^2}{\gamma} \text{ is the Bond number, in}$$

which γ is the surface tension, $\gamma = 20\text{mN/m}$, and θ_Y is the contact angle, $\theta_Y = \pi/4$. The close agreement in figure 3-11b between our numerical profile and the measurements of Duchesne (2014) highlights the very presence of the dynamic component of the thickness at the edge of the disk.

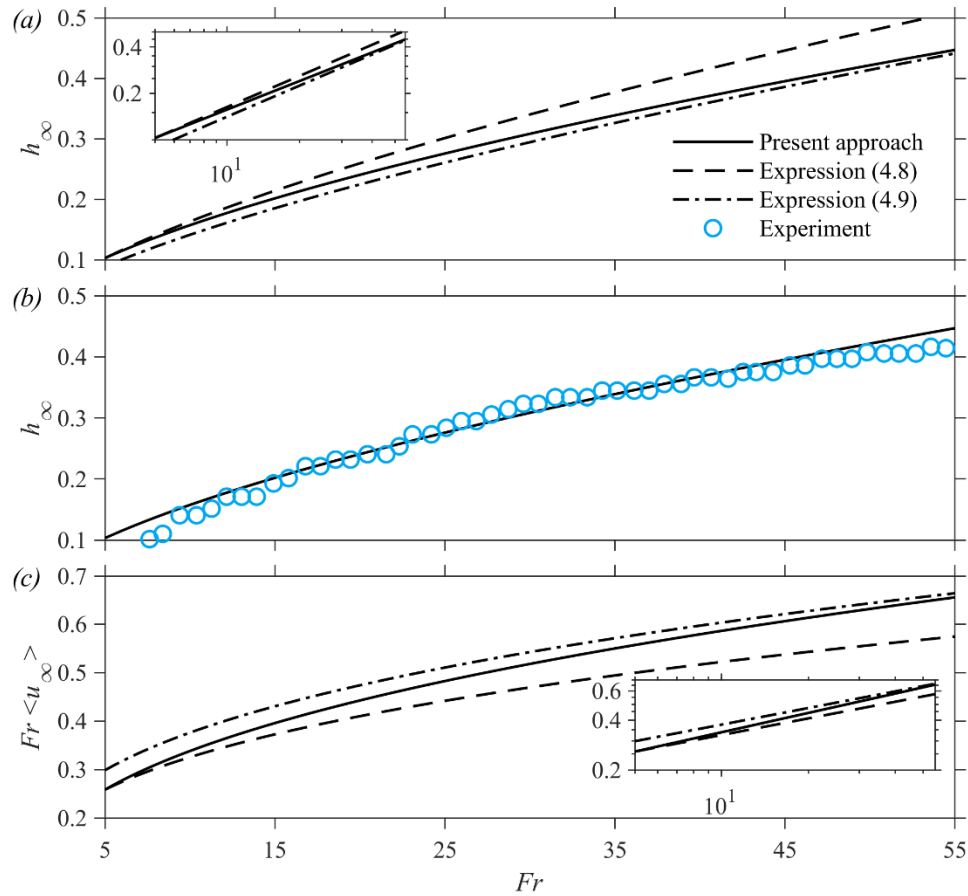


Figure 3-11: Influence of Fr (flow rate) on film thickness h_∞ and surface velocity $Fr\langle u_\infty \rangle$ at the edge of the disk. Shown in (a) and (c) are predictions based on the present approach against expressions (3.4.8) and (3.4.9), and in (b) is the comparison between the present approach and the measurements in Duchesne (2014). Here, $Ga = 100$ ($50.11 < Re < 551.25$) and $r_\infty = 93.75$, corresponding to the range of flow rates in the experiment of Duchesne *et al.* (2014).

Figure 3-12 displays the influence of the disk radius on the film thickness at the edge for two different flow rates corresponding to $Re = 854$, $Fr = 97$ (in red) and $Re = 356$, $Fr = 194$ (in blue), for $50 < r_\infty < 80$. The solid curves correspond to our numerical predictions and the dashed curves are based on expression (3.4.9), showing a close agreement. This also indicates that the local Froude number has reached unity near the edge as a result of flow acceleration. The edge thickness decreases essentially at the same rate with respect to the disk radius independently of the flow rate. The decrease of h_∞ in the figure appears to be

almost linear in both cases but it follows the $r_\infty^{-2/3}$ behaviour shown in (3.4.9). We have also added four values of the edge thickness based on the Navier-Stokes solution of Fernandez-Feria *et al.* (2019), which agree with our predictions and expression (3.4.9) to within a few percent; the two red circles correspond to the Navier-Stokes profiles in figures 3-2a and 3-2b.

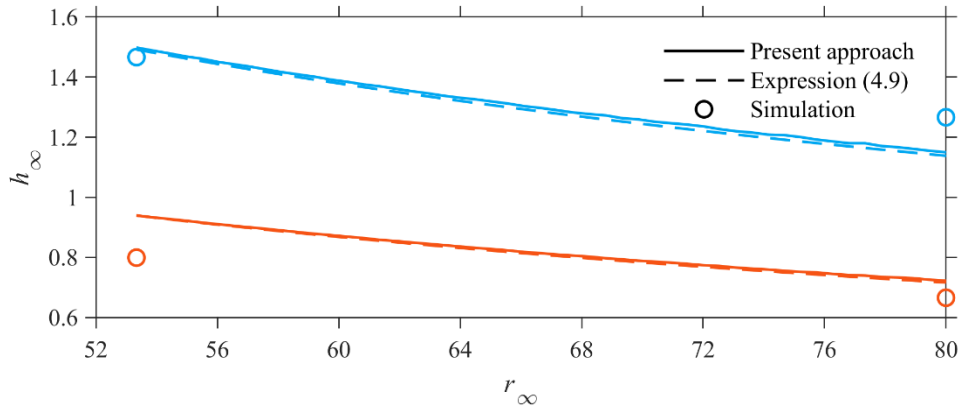


Figure 3-12: Influence of r_∞ (disk radius) on thickness h_∞ at the edge of the disk. Here, red curves and circle symbols correspond to $Re = 854$, $Fr = 97$, and blue curves and circle symbols correspond to $Re = 356$, $Fr = 194$. Simulation results come from the Navier-Stokes solutions of Fernandez-Feria *et al.* (2019).

3.4.3 The jump length and vortex size

We identify the jump length, $L_J \equiv r_{J+} - r_{J-}$, as the difference in position between the leading edge of the jump and its trailing edge (location of maximum film height). Figure 3-13 illustrates the dependence of the jump length, vortex length and height on the film thickness at the disk edge for the same parameter range used in figure 3-8. All three quantities increase when the subcritical film thickens. In particular, both the jump and vortex lengths grow at the same rate, while the vortex height grows more rapidly with the film thickness. We already reported in figure 3-7 that the jump and vortex lengths experience the same growth rate with the flow rate, especially in the lower Fr range. Whether the correlation between the jump length and vortex size exists under more general conditions is an interesting and fundamental issue, which we explore further next.

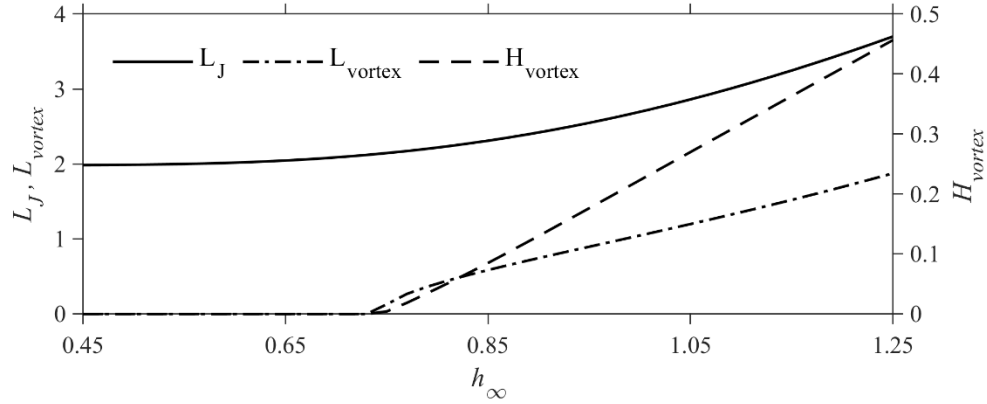


Figure 3-13: Dependence of the jump length, vortex length and vortex height on the film thickness at the disk edge. Here, $Re = 381.97$, $Fr = 9.76$ and $r_\infty = 16$ are parameters corresponding to the simulation of Askarizadeh *et al.* (2019, 2020).

By balancing the drag at the disk in the jump region with fluid inertia, and assuming dominant viscous over gravity effects, Avedisian & Zhao (2000) obtained a relation between the length of the jump and its radius as $L_J r_J / h_J \approx Re$, where h_J is the film thickness at the leading edge of the jump (see also the different treatment of Razis *et al.* (2021) for the planar jump). An approximate relation among the jump length, location and height can be derived by applying equation (3.2.11) at r_{J-} and r_{J+} . We observe that both the slope and concavity are relatively small at these two locations (Bush & Aristoff 2003), so (3.2.11) reduces to $136Reh \approx 525r$, yielding $L_J (r_{J+} - r_{J-}) / (H_J - h_J) \approx 136Re / 525$. If we take $r_J \approx (r_{J-} + r_{J+}) / 2$, we obtain a more general relation than Avedisian & Zhao (2000):

$$L_J \approx \frac{68}{525} Re \frac{H_J - h_J}{r_J}. \quad (3.4.10)$$

We can further simplify this expression to obtain a relation between the jump length and jump radius. We first note that at the leading edge of the jump, $r = r_{J-}$, where the film slope is small, equation (3.2.7b) yields $h_J \approx \left(272Fr^2 / 875r_J^2 \right)^{1/3}$. The trailing edge, $r = r_{J+}$, is part of the subcritical region where the local Froude number is sensibly constant

(Duchesne *et al.* 2014; Wang & Khayat 2019; Wang *et al.* 2023), except perhaps near the edge where the flow may accelerate. Recalling the definition of the local Froude number at the jump location, we have $H_J = (\text{Fr} / 2r_J \text{Fr}_J)^{2/3}$. In this case:

$$L_J \approx C \text{Re} \left(\frac{\text{Fr}^2}{r_J^5} \right)^{1/3}. \quad (3.4.11)$$

where $C = \frac{68}{525} \left[\left(\frac{1}{2\text{Fr}_J} \right)^{2/3} - \left(\frac{272}{875} \right)^{1/3} \right]$ is a constant that depends on Fr_J . Interestingly,

if the scaling law of Bohr *et al.* (1993) is used: $r_J \approx 0.73 \text{Re}^{3/8} \text{Fr}^{1/4}$, then we find from (3.4.11) that $L_J \approx 0.73 C \text{Re}^{3/8} \text{Fr}^{1/4}$. In other words, the jump length also scales like the jump radius. Perhaps a more accurate estimate would be to adopt the scaling law (3.4.5) or that of Duchesne *et al.* (2014), which account for the influence of the disk radius. Thus, by applying the scaling law (3.4.5) to determine the jump radius, we use (3.4.11) to obtain an estimate of the jump length in terms of the flow parameters Re , Fr and r_∞ . We suspect that the vortex length may follow closely (3.4.11) if a different constant than C is used. Although it is difficult to establish this correlation, it is worth assessing its validity numerically (see next).

Figure 3-14 shows the influence of the flow rate on the jump and vortex lengths, based on the profiles corresponding to the flow rate range of Duchesne *et al.* (2014) in figure 4a. The behaviour of the jump length L_J with respect to the flow rate agrees qualitatively with the measurements of Craik *et al.* (1981) (see their figure 6) and Rao & Arakeri (2001) (see their figure 6). Figure 3-14 shows that the dependence of the jump length on the flow rate follows closely $L_J \sim \text{Fr}^{1/2}$. This behaviour becomes closely mimicked by estimate (3.4.11) once the dependence of r_J on the flow rate is established. This can be done by adopting the scaling law (3.4.5). Alternatively, for the range of flow rates considered in figure 3-14, which is the same as the range examined by Duchesne *et al.* (2014), the data

in figure 3-10a suggest that the jump radius follows closely $r_j \approx 1.08Fr^{7/10}$, yielding the $L_J \sim Fr^{1/2}$ behaviour in figure 3-14. Incidentally, the $r_j \sim Fr^{7/10}$ behaviour is also consistent with the measurements of Hansen *et al.* (1997).

The measurements of Duchesne *et al.* (2014) suggest that $Fr_J \approx 0.37$ for the range of flow rates considered, yielding $C = 0.07$. Given the simplifying assumptions made to obtain (3.4.11), we have adjusted this value to $Fr_J \approx 0.32$ to obtain the closer agreement shown in figure 3-14. The vortex length also appears to follow closely the same dependence on the flow rate, namely $L_{\text{vortex}} \sim Fr^{1/2}$. Finally, and as we shall see below, the monotonicity depicted in figure 3-14 is lost for the variation of the jump and vortex lengths with respect to parameters other than the flow rate, and consequently (3.4.11), does not always hold.

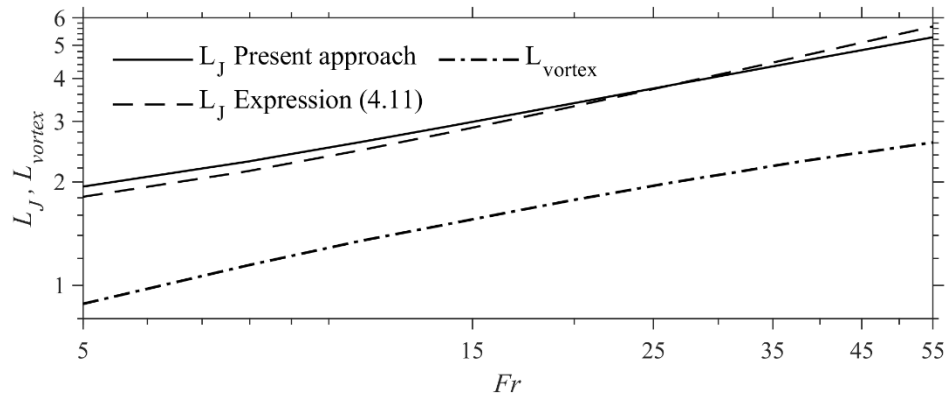


Figure 3-14: Influence of the Froude number (flow rate) on the jump and vortex lengths. Solid and dash-dotted curves based on our predictions and dashed curve based on expression (3.4.11). Here $Fr_J = 0.32$, $Ga = 100$ and $r_\infty = 93.75$, corresponding to the parameters in the experiment of Duchesne *et al.* (2014).

3.4.4 The energy loss and conjugate depth

For the flow of an impinging jet and hydraulic jump, the supercritical film thickness follows closely the analytical expression (3.2.13a) given the negligible gravity effect over a wide range of the supercritical region, up to the leading edge of the jump. Consequently,

if the jump occurs close to the jet impact point then $h_J \approx \frac{233}{340} \frac{1}{r_J}$, reflecting the dominant

radial spreading effect, and if it occurs further downstream, then $h_J \approx \frac{175}{136} \frac{r_J^2}{\text{Re}}$, implying

the dominant viscous effect (Bowles & Smith 1992). We again consider the influence of flow rate over the experimental range of Duchesne *et al.* (2014), and recall that the jump radius follows closely $r_J \approx 1.08\text{Fr}^{7/10}$. Recalling that $\text{Re} = \sqrt{\text{Ga}}\text{Fr}$ with $\text{Ga} = 100$ yields

$h_J \approx 0.64\text{Fr}^{-7/10}$ and $h_J \approx 0.15\text{Fr}^{2/5}$, close and far from impingement, respectively.

Referring to figure 3-4a, these two trends correspond roughly to the small flow rate range ($\text{Fr} < 10$) when $r_J = O(1)$, and the higher range ($\text{Fr} > 10$), respectively. The overall behaviour for the supercritical thickness at the leading edge of the jump may then be given from (3.2.13a). As to the film height immediately downstream of the jump, our numerical predictions indicate that $H_J \approx 1.3\text{Fr}^{4/25}$ (Wang *et al.* 2023). In sum, we have the following dependence on the flow rate (Froude number) based on our approach, for the film heights at the leading and trailing edge of the jump:

$$h_J \approx 0.64\text{Fr}^{-7/10} + 0.15\text{Fr}^{2/5}, \quad H_J \approx 1.3\text{Fr}^{4/25}, \quad (3.4.12a, b)$$

which, in turn, yield

$$\frac{H_J}{h_J} \approx \frac{1}{0.49\text{Fr}^{-43/50} + 0.12\text{Fr}^{6/25}}. \quad (3.4.13)$$

These expressions are used to produce the plots in figure 3-15. The behaviour (3.4.12b) of H_J , based on our approach, agrees closely with the measurements of Duchesne *et al.* (2014), as shown in figure 3-15a. Our numerical results overlap with the predictions of expression (3.4.12a) for h_J , and also agree with the available measurements of Duchesne (2014). We have also added in the inset of figure 3-15a the data from figure 7 of Craik *et al.* (1981), who investigated the stability of the hydraulic jump for a water jet impinging onto a rectangle tank with outflow at four corners. The data is included only for reference,

showing a similar trend to our approach. As indicated in the numerical simulation work of Askarizadeh *et al.* (2019), there are two different flow regimes in the jump formation, gravity- and capillary-dominant flow regimes, and the role of surface tension is significant when the flow regime is capillary dominant. Clearly, the high surface tension value of the working fluid in the experiments of Craik *et al.* (1981) results in the non-negligible effect of surface tension. More importantly, the tank container used as the impinging plate and unclear downstream flow condition for a certain h_J in Craik *et al.* (1981) make the quantitative comparison unachievable.

The estimate of H_J/h_J (3.4.13) is used to plot the conjugate depth ratio against Fr (flow rate) in figure 3-15b, which shows a close agreement with our numerical solution. More importantly, it helps elucidate the origin of the non-monotonicity in figure 3-15b, and a similar behaviour of the Froude numbers at the leading and trailing edge and energy loss across the jump, which we examine shortly. The behaviour of the conjugate depth ratio in figure 3-15b should be contrasted with that of Higuera (1994) in his figure 3. Interestingly, Higuera's figure shows a monotonically decreasing depth ratio with the Froude number, thus corresponding to the descending part of the curves in figure 3-15b. The absence of an ascending branch in Higuera's formulation is due to the nature of his supercritical profile, which increases predominantly linearly with the streamwise distance for a planar hydraulic jump in a 2D channel. Consequently, and as we can see from his figure 2, this implies monotonically increasing h_J and H_J , yielding the monotonically decreasing behaviour in his figure 3.

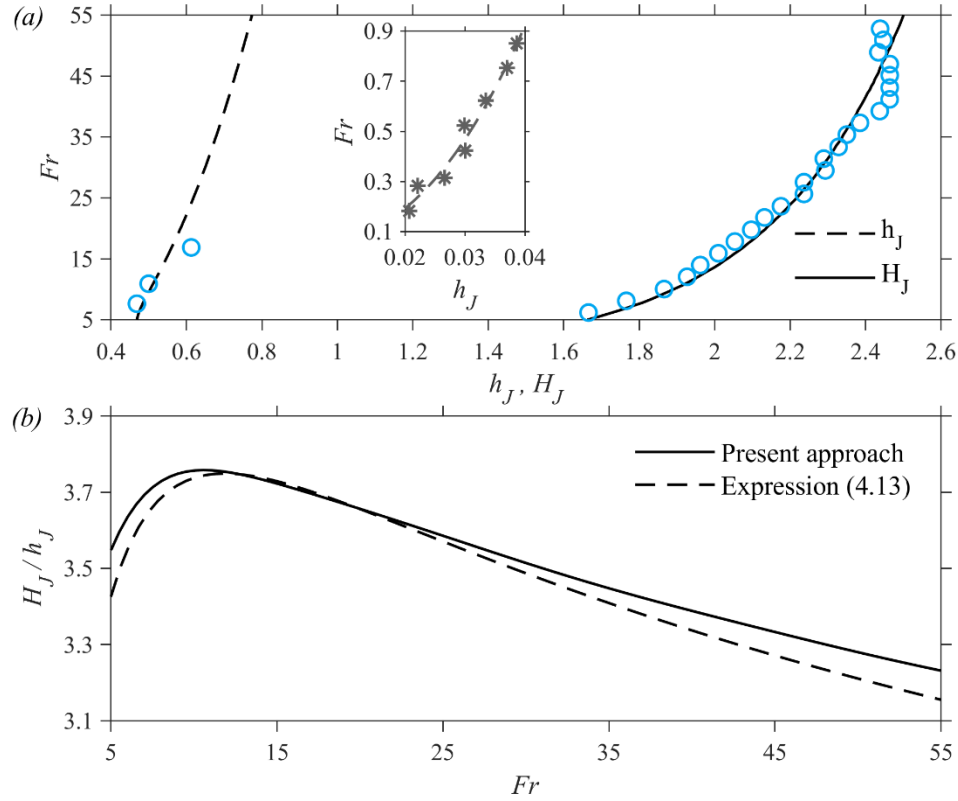


Figure 3-15: Influence of Fr (flow rate) on (a) the film depth immediately upstream and downstream of the jump, and (b) the conjugate depth ratio. Here $Ga = 100$ and $r_\infty = 93.75$, corresponding to the parameters in the experiment of Duchesne *et al.* (2014). Inset in (a) shows the experimental measurements of Craik *et al.* (1981) for $Re = 265.46 - 1238.44$, $Fr = 0.18 - 0.85$, and the grey dashed curve in the inset is included for visual guidance.

In the hydraulic jump literature, it is customary to consider the conjugate depth ratio and relative energy loss across the jump in terms of the supercritical approaching Froude

number $Fr_{J-} = \frac{Fr}{2r_J h_J^{3/2}}$ (Lawson & Phillips 1983; Palermo & Pagliara 2018). The Froude

number at the trailing edge of the jump $Fr_{J+} = \frac{Fr}{2r_J H_J^{3/2}}$ (equal to Fr_J introduced earlier) is

also of interest. To establish the expression of Fr_{J-} and Fr_{J+} , we first recall the momentum balance equation (3.4.1) for a shock-like jump, assuming $L_J \approx 0$. To further proceed, a

velocity profile in both super- and sub-critical regions is required. Liu & Lienhard (1993) assumed a uniform velocity both up- and down-stream of the jump, and obtained an expression between the depth ratio and the supercritical approaching Froude number. More accurate profiles, parabolic, cubic or a combination of them, are extensively employed to study the flow of hydraulic jump, yielding a good agreement with experiment and numerical simulation (Bohr *et al.* 1993; Kasimov 2008; Wang & Khayat 2018, 2019; Dhar *et al.* 2020). For simplicity, we adopt the cubic velocity profile (3.2.8) for both regions and neglect gravity: $u = Uf(\eta) = \frac{U}{2}(3\eta - \eta^3)$. Of course, choosing a parabolic velocity profile for both regions is also widely used in studies on hydraulic jumps (Bohr *et al.* 1993; Kasimov 2008; Dhar *et al.* 2020), and can lead to a similar result. By substituting $u = Uf(\eta)$, and recalling $U = \frac{4}{5rh}$ from (3.2.13b), the momentum balance equation (3.4.1) reduces to

$$\frac{544}{875} \left(\frac{1}{h_J H_J} \right) \approx \frac{r_J^2}{Fr^2} (H_J + h_J). \quad (3.4.14)$$

This equation can be rearranged to yield the local Froude numbers at the leading and trailing edge of the jump in terms of the conjugate depth ratio H_J/h_J :

$$Fr_{J-} = \sqrt{\frac{875}{2176} \frac{H_J}{h_J} \left(\frac{H_J}{h_J} + 1 \right)}, \quad \text{and} \quad Fr_{J+} = \sqrt{\frac{875}{2176} \frac{h_J}{H_J} \left(\frac{h_J}{H_J} + 1 \right)}. \quad (3.4.15a,b)$$

Once expression (3.4.13) of the conjugate depth ratio is used, the leading and trailing Froude numbers become functions of Fr (flow rate), and are next compared to our present approach and experiment.

We examine in figure 3-16 the dependence of Fr_{J-} (figure 3-16a) and Fr_{J+} (figure 3-16b) on Fr over the same experimental range of flow rates of Duchesne *et al.* (2014). In contrast to the monotonic behaviour of Fr_{J-} observed in the planar hydraulic jump (Higuera 1994), the Fr_{J-} of the circular hydraulic jump increases over the smaller range of flow rate ($Fr <$

10) and decreases over the larger range of flow rate ($Fr > 10$), exhibiting a maximum at $Fr \approx 10$. This behaviour of Fr_{j-} is well captured by the expression (3.4.15a) and the behaviour of the conjugate depth ratio in figure 3-15b. The discrepancy between the present approach and the prediction from the expression (3.4.15a) is expected, since the inviscid-viscous interaction comes into play at the leading edge of the jump (Bowles & Smith 1992; Higuera 1994; Bowles 1995), which is not reflected in (3.2.13a). In addition, the shock-like assumption adopted in the momentum balance equation (3.4.14) also can result in discrepancy. The almost constant Fr_{j+} reflected in the measurements of Duchesne *et al.* (2014) is also well reflected in both our numerical calculation and the expression (3.4.15b). However, the theoretical profiles in figure 3-16b suggest the presence of non-monotonic responses that are not clearly visible from experiment. Both profiles based on our current approach and expression (3.4.15b) show a decrease in Fr_{j+} for smaller Fr , consistent with experiment, reaching a minimum, and an increase over the higher Fr range, which is somewhat consistent with experiment. Perhaps more precise measurements will show a more coherent trend similar to theory. We emphasise again, that the non-monotonic response in figure 3-16 and other figures is the result of the non-monotonicity of the conjugate depth ratio with respect to the radial distance.

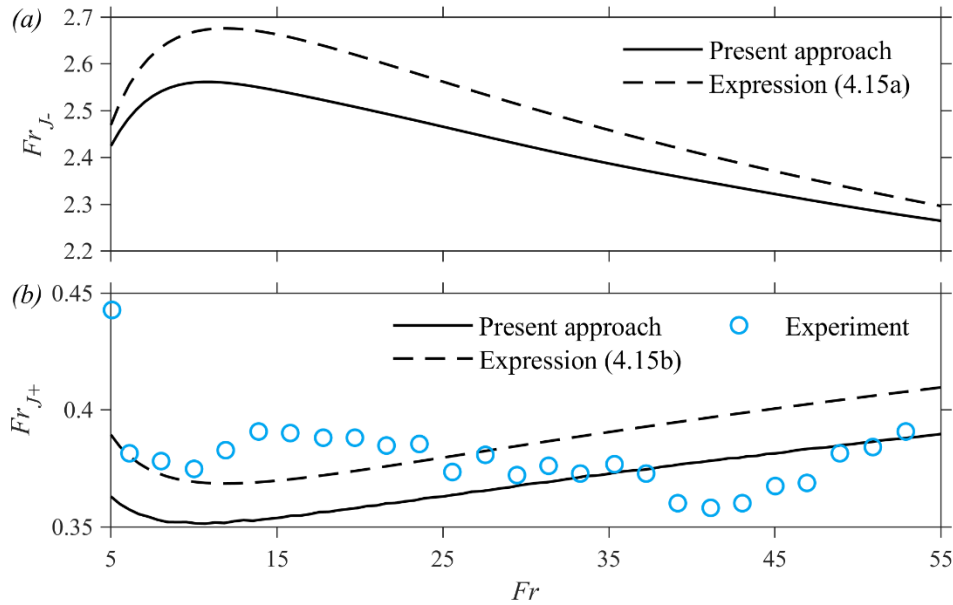


Figure 3-16: Influence of Fr (flow rate) on the Froude number (a) Fr_{J-} at the leading edge and (b) Fr_{J+} at the trailing edge of the jump. Here $Ga = 100$ and $r_{\infty} = 93.75$, corresponding to the parameters in the experiment of Duchesne *et al.* (2014).

We next follow Palermo & Pagliara (2018), and introduce the energy dissipation as the difference in the total energy heads $E_{J-} = \frac{1}{2} Fr^2 \langle u_{J-} \rangle^2 + h_J$ and

$E_{J+} = \frac{1}{2} Fr^2 \langle u_{J+} \rangle^2 + H_J$ at the leading and trailing edge of the jump, respectively, where

$\langle u \rangle = \frac{1}{h} \int_0^h u dz$ is the local average velocity. Recalling from the mass conservation equation

(3.2.6a) that $\langle u \rangle = 1/2rh$, then the energy dissipation becomes

$\Delta E_J \equiv E_{J-} - E_{J+} = \frac{1}{8} Fr^2 \left(\frac{1}{r_{J-}^2 h_J^2} - \frac{1}{r_{J+}^2 H_J^2} \right) + h_J - H_J$. It is not difficult to show, upon

recalling the definition of the jump length $L_J = r_{J+} - r_{J-}$ and the approximation

$r_J \approx (r_{J-} + r_{J+})/2$ for the jump radius, that the relative energy dissipation is

$$\frac{\Delta E_J}{E_{J-}} = \frac{Fr_{J-}^2 \left[1 - \left(1 + \frac{L_J}{r_J} \right)^{-2} \frac{h_J^2}{H_J^2} \right] + 2 \left(1 - \frac{H_J}{h_J} \right)}{Fr_{J-}^2 + 2}. \quad (3.4.17)$$

after recalling L_J from (3.4.11), Fr_{J-} from (3.4.15a) and the conjugate depth ratio H_J/h_J from (3.4.13). This expression is the same as expression (12) of Lawson & Phillips (1983), who investigated the turbulent circular hydraulic jump from a source with a circular deflection plate to control its exiting height. If we further assume that $L_J \ll r_J$, then we recover essentially expression (8) of Palermo & Pagliara (2018) for a horizontal channel, who examined the energy dissipation for a jump in a sloped channel with a rough bottom. Both research groups found that their theory agrees well with the experimental data available either from the existing literature or their own measurements. In particular, they found that the relative energy dissipation always increases monotonically with the approaching Froude number. They attributed the monotonicity to that of the conjugate depth ratio. As we shall see next, the monotonic behaviour is not preserved for the circular hydraulic jump as a result of the non-monotonic depth ratio in our current problem (see figure 3-17).

Figure 3-17 illustrates the influence of the Froude number on the relative energy dissipation $\Delta E_J/E_{J-}$ over the same range of flow rates as in the experiment of Duchesne *et al.* (2014). The relative energy dissipation $\Delta E_J/E_{J-}$ exhibits a maximum after a relatively rapid increase in the low Fr range, reaching a maximum and decrease rather slowly with increasing Fr. The non-monotonic response is at first surprising since it has not been predicted or observed in the hydraulic jump literature (see Palermo & Pagliara (2018) and the references therein). There are important differences between the flow across the present circular jump and that across the typical jump in a channel. For the present jump, both the supercritical and subcritical film thickness vary significantly with the radial position as a result of jet impingement and film drainage at the edge of the disk. We have shown how these differences can lead to the non-monotonic response for the depth ratio in figure 3-15b. Clearly, the maximum of the energy dissipation is closely tied to the maximum in the conjugate depth ratio. To confirm the trend predicted by the present approach, we have

also computed the distributions based on the simpler shock-jump model (Bohr *et al.* 1993; Wang & Khayat 2019), and also found a similar response, which is based on expression (3.4.17) and shown in figure 3-17.

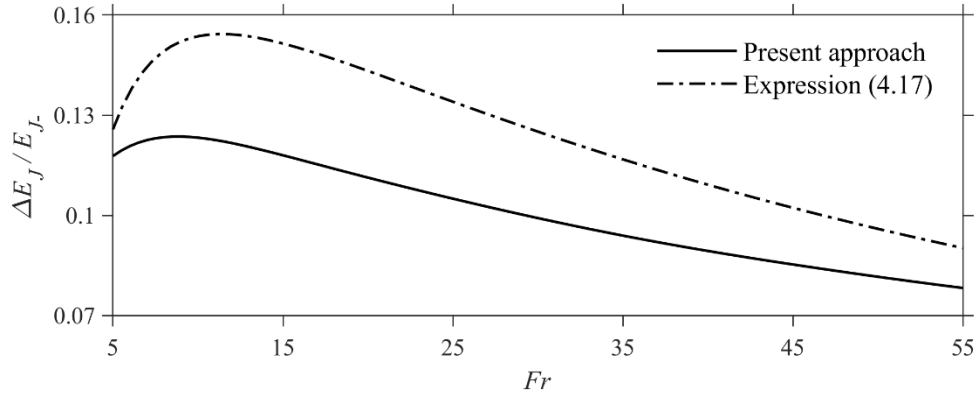


Figure 3-17: Influence of Fr (flow rate) on the relative energy loss. Here Ga = 100 and $r_\infty = 93.75$, corresponding to the parameters in the experiment of Duchesne *et al.* (2014).

As mentioned earlier, it is customary in the hydraulic jump to examine the influence of the approaching Froude number on the jump parameters (Lawson & Phillips 1983; Liu & Lienhard 1993; Higuera 1994; Palermo & Pagliara 2018). Liu & Lienhard (1993) showed that the depth ratio H_J/h_J is a monotonic function of the approaching Froude number by considering the momentum balance equation (3.4.1) and assuming a uniform velocity $u = 1/2rh$ both up- and downstream of the jump, yielding

$$\frac{H_J}{h_J} = \frac{1}{2} \left(\sqrt{1 + 8Fr_{J-}^2} - 1 \right). \quad (3.4.18a)$$

Using a cubic velocity profile in both regions, we obtained (3.4.15a), which is rewritten as

$$\frac{H_J}{h_J} \approx \frac{1}{2} \left(\sqrt{1 + 10Fr_{J-}^2} - 1 \right). \quad (3.4.18b)$$

By substituting the depth ratio (3.4.18a,b) into (3.4.17) and adopting a shock-like jump assumption $L_J = 0$, we obtain the relation between the approaching Froude number and the relative energy loss:

$$\frac{\Delta E}{E_{J-}} = \frac{8Fr_{J-}^4 + 38Fr_{J-}^2 + 8 - (10Fr_{J-}^2 + 8)\sqrt{8Fr_{J-}^2 + 1}}{\left(\sqrt{8Fr_{J-}^2 + 1} - 1\right)^2 (Fr_{J-}^2 + 2)} =, \quad (3.4.19a)$$

for a uniform velocity profile, and

$$\frac{\Delta E}{E_{J-}} \approx \frac{10Fr_{J-}^4 + 48Fr_{J-}^2 + 8 - (12Fr_{J-}^2 + 8)\sqrt{10Fr_{J-}^2 + 1}}{\left(\sqrt{10Fr_{J-}^2 + 1} - 1\right)^2 (Fr_{J-}^2 + 2)}, \quad (3.4.19b)$$

for a cubic velocity profile.

Figure 3-18 illustrates the influence of the approaching Froude number Fr_{J-} on the relative energy dissipation $\Delta E_J/E_{J-}$ (figure 3-18a) and the conjugate depth ratio H_J/h_J (figure 3-18b) based on the parameters used in the experiments of Lawson & Phillips (1983) and Liu & Lienhard (1993). The theoretical profiles correspond to estimates (3.4.18a, b) for the depth ratio and (3.4.19a, b) for the relative energy loss, which are widely used in planar and circular hydraulic jumps, and also used in figures 3-16 and 3-17. We also include the experimental measurements of depth ratio and relative energy loss of Liu & Lienhard (1993) and Lawson & Phillips (1983). Overall, the comparison is favourable, especially for the relative energy loss. As to the conjugate depth ratio, the agreement is good up to $Fr_{J-} \approx 14$. For larger values, the theoretical profiles appear to pursue their almost linear growth while the (scattered) experimental data suggest a constant or slightly decaying trend. It should be noted that parameters used both in Lawson & Phillips (1983) and Liu & Lienhard (1993) are much higher than encountered in laminar hydraulic jump studies, leading to an even turbulent hydraulic jump in Lawson & Phillips (1983).

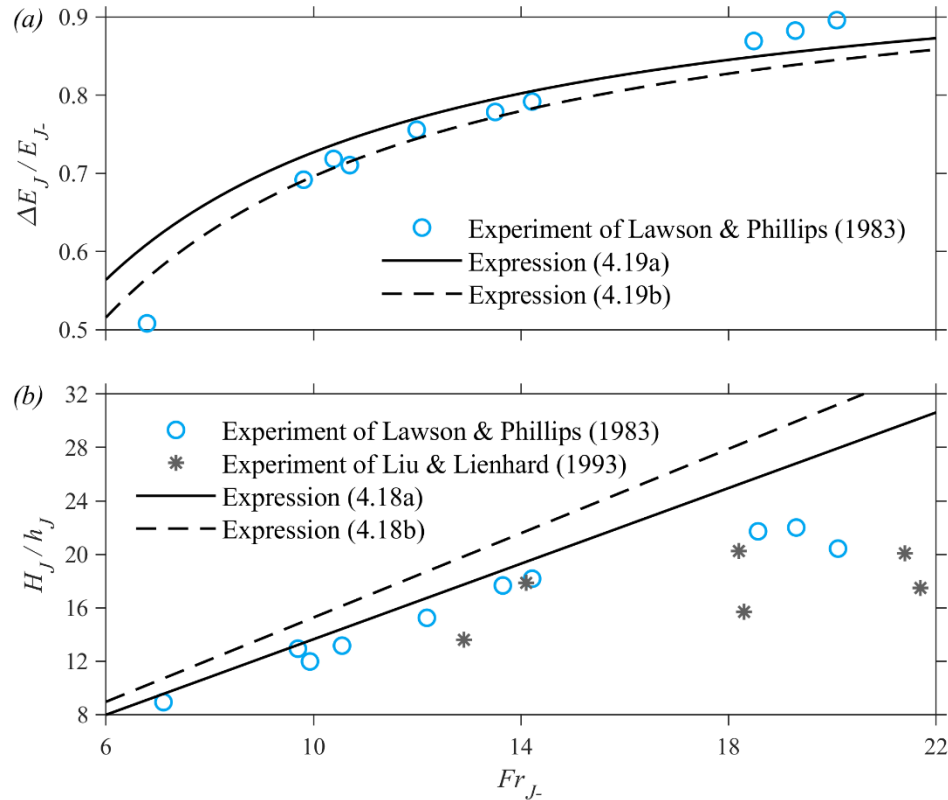


Figure 3-18: Influence of the supercritical approaching Froude number Fr_{J-} on (a) the relative energy loss $\Delta E_J/E_{J-}$ and (b) the conjugate depth ratio H_J/h_J .

3.5 Further parametric assessment

After validating our approach against experiment and numerical simulation, and reporting a detailed account of the influence of the flow rate in this and earlier studies of Wang *et al.* (2023), we observed the non-monotonic behaviour for the jump length and vortex size, so we now examine theoretically the effects of gravity (Fr) and viscosity (Re) on the flow structure. We particularly focus on the conditions of jump and vortex existence in the parameter space.

3.5.1 Influence of the gravity

The influence of gravity on the vortex size and jump length is shown in figure 3-19, where the vortex length, vortex height and jump length are plotted against Fr for different Re and a disk radius $r_\infty = 25$ in figures 3-19a, 3-19b and 3-19c, respectively. The behaviour for $Re = 800$ corresponds to the flow in figure 13 of Wang *et al.* (2023). In contrast to the

behaviour in figures 3-13 and 3-14, and similar to figures 3-7b and 3-7c for $r_\infty = 25$, the vortex and jump sizes in figure 3-19 do not behave monotonically with respect to Fr . For any Re considered in the figure, the vortex size initially increases with Fr , attaining a maximum, while the jump length decreases to a minimum coinciding with the maximum of the vortex length. The vortex decreases in size to eventually vanish while the jump continues to extend in length, but exhibits a maximum before it continues to shrink. Both the maximum in vortex length and the minimum in jump length occur at the same Froude number. The growth rate in the vortex length and the drop rate in the jump length with Fr are much weaker than the growth rate of the vortex height, but both vortex length and height vanish at the same Froude number, signalling the disappearance of the recirculation zone. It is interesting to note that the vortex length and height do not achieve the maximum values at the same Fr .

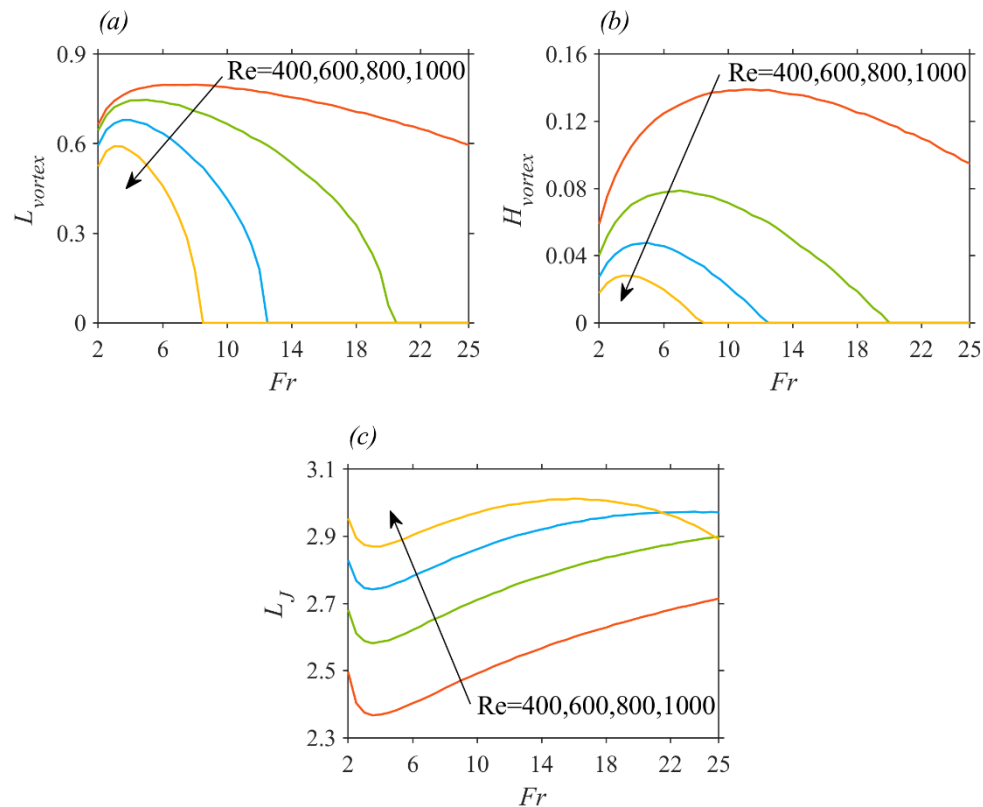


Figure 3-19: Influence of gravity on the vortex and jump size. Shown is the dependence of (a) the vortex length, (b) the vortex height and (c) the jump length on Fr for different Re for a disk of dimensionless radius $r_\infty = 25$.

3.5.2 Influence of the viscosity

Figure 3-20 shows the dependence of the vortex size (figures 3-20a and 3-20b) and the jump length (figure 3-20c) on Re for different Fr . In contrast to the effect of gravity in figure 3-19, the response with Re is essentially monotonic for the vortex size. Over the range of Re considered, we see that as viscosity decreases (Re increases), the jump lengthens and the vortex shrinks in size to eventually disappear at a rate that increases with increasing Fr . However, we observe that the jump length exhibits a maximum at any Froude number if a wider range of Re is considered; this is reflected in figure 3-20c for $Fr = 25$.

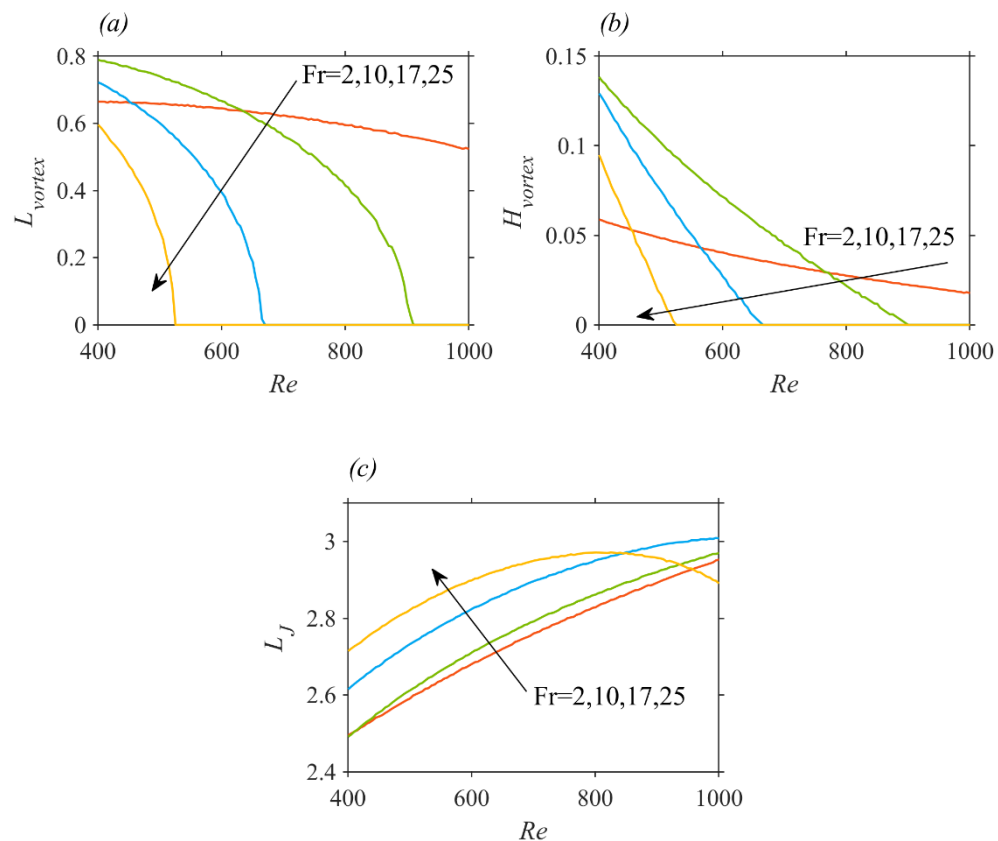


Figure 3-20: Influence of viscosity on the vortex and jump size. Shown is the dependence of (a) the vortex length, (b) the vortex height and (c) the jump length on Re for different Fr for a disk of dimensionless radius $r_\infty = 25$.

3.5.3 Existence of the jump and the recirculation zone

Although our discussion has been in terms of the three parameters Re , Fr and r_∞ , it is helpful to introduce the following transformation (Wang & Khayat 2019):

$$r \rightarrow Re^{1/3} r, \quad (z, h, \delta) \rightarrow Re^{-1/3} (z, h, \delta), \quad (3.5.1a, b)$$

$$\mathbf{u} \rightarrow \mathbf{u}, \quad \mathbf{w} \rightarrow Re^{-2/3} \mathbf{w}. \quad (3.5.c, d)$$

In this case, the problem is reduced to a two-parameter problem, involving

$$\alpha \equiv Re^{1/3} Fr^2, \quad \beta \equiv Re^{-1/3} r_\infty, \quad (3.5.2a, b)$$

as the two parameters.

The results reported above clearly indicate that a jump may form with no recirculation downstream. There are also instances where the jump itself does not appear or is so weak that is difficult to identify its location. This is clearly illustrated in figure 3-4c for $Fr = 55$ and $r_\infty = 25$ where the jump is washed down close to the edge, exhibiting a large jump length (figure 3-7b). We therefore expect the jump to simply not form for some flow parameter range (particularly for low viscosity), with the liquid flowing off the edge as a very thin film over the entire disk, resembling supercritical flow. Figure 3-21 shows three-dimensional perspectives of the simultaneous influence of Re and Fr on the vortex size and jump length, summarizing our findings. In particular, figures 3-21a and 3-21b show the region (bottom dark blue region) where the vortex has essentially disappeared, while the jump length has increased.

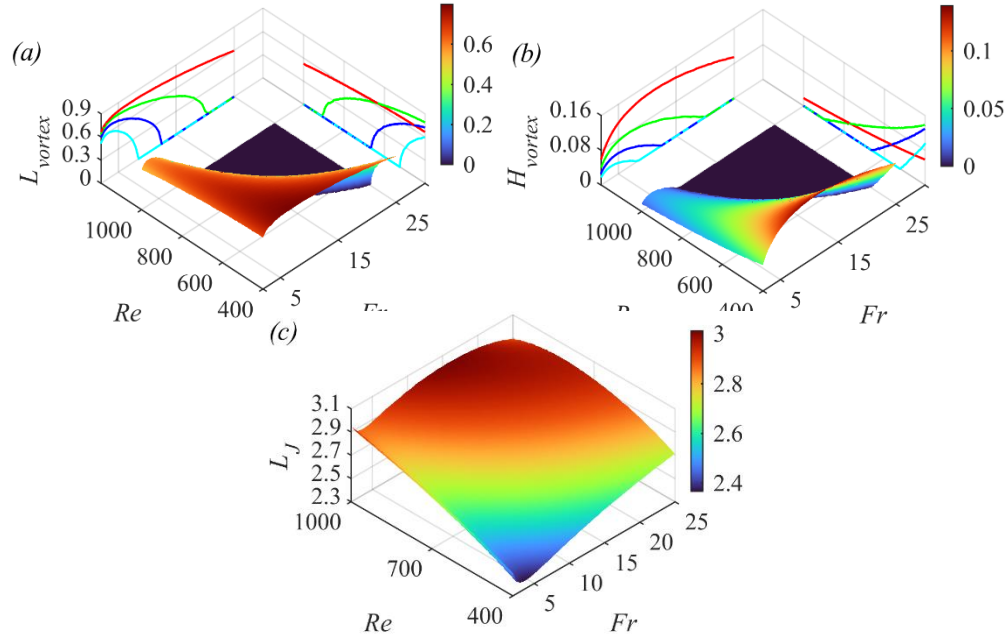


Figure 3-21: Influence of Fr and Re on the maximum length (a) and maximum height (b) of the separation zone in a 3D plot. Another dimensionless parameter is $r_\infty = 25$. The curves projected on the $L_{vortex}Fr$ and $H_{vortex}Fr$ planes are for $Re = 400$ (red lines), 600 (green lines), 800 (blue lines) and 1000 (cyan lines), and the curves projected on the $L_{vortex}Re$ and $H_{vortex}Re$ planes are for $Fr = 2$ (red lines), 10 (green lines), 17 (blue lines) and 25 (cyan lines). Also shown in (c) is the influence of Fr and Re on the jump length in a 3D plot.

We estimate the limit condition for the non-existence of the jump by recalling (3.4.5). Noting that the jump disappears (falls off the edge) when it reaches the edge of the disk, setting $r_J = r_\infty$ and keeping the dominant terms in (3.4.5) yields:

$$r_\infty \approx \left(\frac{4}{5}\right)^{3/8} \left(\frac{136}{175}\right)^{3/4} \left(\frac{70}{27}\right)^{1/4} Fr^{1/4} Re^{3/8}. \text{ The numerical coefficient is very close to}$$

unity, so that:

$$r_\infty = Fr^{1/4} Re^{3/8} \text{ or } \alpha = \beta^8, \quad (3.5.3)$$

represents the boundary in the parametric space (Fr, Re, r_∞) or plane (α, β) for the existence of the jump. We recall (3.5.2) for the expressions of α and β .

The region of existence for the recirculation zone is established numerically from the data in figures 3-19 to 3-21, which turned out to be above the surface:

$$Re^{10/3} Fr^2 = 9r_\infty^9 / 50 \text{ or } \alpha = 9\beta^9 / 50. \quad (3.5.4)$$

Figures 3-22a and 3-22b show the regions of existence of the jump and the vortex in the two-parameter plane (α, β) and corresponding three-dimensional perspective. The region of vortex existence lies above the surface in figure 3-22c. This surface therefore represents the disk radius below which no vortex exists. Gravity and viscosity enhance the formation of recirculation.

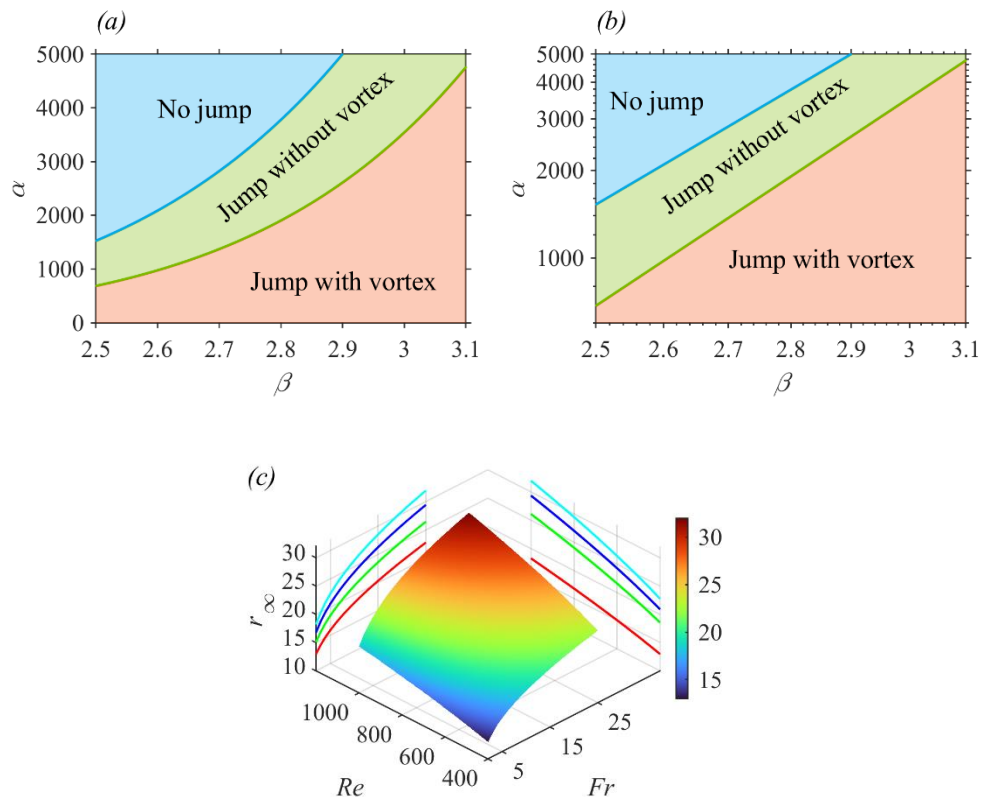


Figure 3-22 Marginal separation curve in the (α, β) plane for the existence of the hydraulic jump and vortex on a flat solid disk. The log-log plot in (b) reflects the

scaling laws (3.5.3) and (3.5.4) for the separation curve. The region of existence of a vortex in (c) lies above the surface. The curves projected on the $r_\infty Fr$ plane are for $Re = 400$ (red lines), 600 (green lines), 800 (blue lines) and 1000 (cyan lines), and the curves projected on the $r_\infty Re$ plane are for $Fr = 2$ (red lines), 10 (green lines), 17 (blue lines) and 25 (cyan lines).

3.6 Concluding remarks

In a recent study (Wang *et al.* 2023), in an effort to capture the continuous hydraulic jump and flow structure for a jet impinging on a disk, we proposed a composite mean-field thin-film approach consisting of subdividing the flow domain into three distinct connected regions of increasing gravity strength: a developing boundary layer near the impact of negligible gravity, an intermediate supercritical viscous layer of moderate gravity, and a region comprising the jump and subcritical flow of strong gravity. Unlike existing models, the approach does not require any empirically or numerically adjusted boundary conditions. We demonstrated that the stress or corner singularity for a film draining at the edge is equivalent to an infinite slope of the film surface, which we imposed as the downstream boundary condition that ensures the upstream influence. The approach was extensively validated against existing experiment and numerical simulation of the boundary-layer and Navier-Stokes equations. In section 3.2, we briefly reviewed the general problem and physical domain; as well as the formulation of the problem and the solution strategy in terms of the general governing equations and boundary conditions in each region of the flow.

In the present study, we further validated our approach, and examined the characteristics and structure of the continuous circular hydraulic jump and recirculation. In section 3.3, we examined the influence of the disk geometry on the jump and flow structure, namely the influence of the disk size and the height of the obstacle, which is often placed at the edge of the disk to control the subcritical film height and jump location. We further validated our approach against the numerical simulation of Fernandez-Feria *et al.* (2019). We found the influence of the disk size to be significant, especially in the subcritical region. Below a critical disk radius, the jump transits from type I to type 0, after which the

recirculation zone has faded. The supercritical flow and, to a lesser extent, the jump location are surprisingly insensitive to the variation of the disk size (figure 3-3). In an effort to stimulate further experimental work, we examined the influence of the disk size over the same experimental flow rate and conditions of Duchesne *et al.* (2014); see figure 3-4. Unlike the location of the jump, the jump height, jump length and vortex size are strongly affected by the disk size, all decreasing with increasing disk radius for $r_\infty = 25$ when Fr is larger than a certain value, and exhibiting a non-monotonic response (maximum) with respect to the flow rate (see figures 3-4, 3-6 and 3-7, including further validation against experiment). We also explored the influence of the obstacle height, often placed at the edge of the disk in practice. The jump is relatively steep with a strong recirculation zone for a high obstacle. As the obstacle height decreases, the jump moves downstream, and the recirculation zone shrinks to disappear below a critical obstacle height. The supercritical flow remains unaffected (figure 3-9). Upon comparing our approach against the Navier-Stokes solution of Askarizadeh *et al.* (2019), we found that our predicted film profile remains close to the simulated profiles in the presence and absence of surface tension (figure 3-8); the surface tension effect is unimportant in this case.

Detailed scaling analyses were formulated in section 3.4 for the jump radius, jump length, energy loss, conjugate depth ratio and thickness at the edge of the disk in the presence and absence of an obstacle. The scaling laws were validated against our approach and existing experimental and numerical data. By keeping the dominant terms in the momentum balance equation across the jump, we derived a new scaling law (3.4.5) based on the conservation equations across the jump and lubrication flow for the jump height:

$$r_J \left[\ln \left(\frac{r_\infty}{r_J} \right) \right]^{1/8} \approx \frac{2}{3} Fr^{1/4} Re^{3/8}. \text{ This scaling is similar to that proposed by Duchesne } et al.$$

(2014) but does not require any empirical input or adjustment. It generalizes that of Bohr *et al.* (1993) to include the effect of the disk size, and appears to hold well for flows at high and low flow rates (see figure 3-10).

The film thickness at the edge of the disk remains largely unaddressed in the literature. We showed that, in addition to the static component, the thickness being proportional to the

capillary length (Duchesne & Limat 2022), there is a dynamic component: $h_\infty \sim (\text{Fr} / r_\infty)^{2/3}$ that we established by minimizing the Gibbs free energy of the flow at the disk edge. We also showed that this behavior is also the consequence of the flow becoming supercritical near the disk edge, and was validated against the measurements of Duchesne (2014) in figure 3-11 and the Navier-Stokes solutions of Fernandez-Feria *et al.* (2019) in figure 3-12. By assuming negligible film slope and curvature at the leading edge of the jump and maximum height at the trailing edge, we showed that the jump length is related to the jump radius as $L_J \sim \text{Re}(\text{Fr}^2 / r_J^5)^{1/3}$ or (3.4.11), which reduces to $L_J \sim \text{Fr}^{1/2}$ when Fr represents the dimensionless flow rate. This behaviour is reflected in figure 3-14 in close agreement with our numerical predictions over the range of experimental flow rates of Duchesne *et al.* (2014). The figure also shows that the vortex length follows the same behaviour as the jump length. Unfortunately, we were unable to establish the behaviour of L_{vortex} using scaling arguments as we did for L_J .

In contrast to channel flow, the energy dissipation exhibits a maximum at some flow rate (or Fr), which we showed to result from the non-monotonic behaviour of the depth ratio, originating from the descending and ascending branches of the film thickness in the supercritical region for an impinging jet (figure 3-15). This connection was missed in the existing literature, particularly studies on channel flow or flows where the developing boundary-layer and viscous-film regions were not fully accounted for in the supercritical formulation for a circular jump. In the work of Higuera (1994), for instance, the conjugate depth ratio was predicted to monotonically decrease with the Froude number due to the linearly growing film profile upstream. The non-monotonicity of the conjugate depth ratio and energy loss, as well as the local Froude number, with respect to the flow rate, reflected in figures 3-15, 3-16 and 3-17, was confirmed by incorporating the supercritical film thickness behaviours close and far from impingement, as reflected by (3.4.12a). Finally, the presence of the jump is not necessarily commensurate with that of a recirculation, reflecting a jump of *type 0*; the existence of the vortex closely depends on the upstream curvature and steepness of the jump. Our calculations suggest that the surface in the parametric space separating the regions of existence/non-existence of the recirculation is

given by the universal relation $Re^{10/3} Fr^2 = 9r_\infty^9 / 50$ (figure 3-22). The jump itself can be washed down off the edge of the disk, particularly at low viscosity and small disk size (figure 3-4c).

3.7 References

- ASKARIZADEH, H., AHMADIKIA, H., EHRENPREIS, C., KNEER, R., PISHEVAR, A. & ROHLFS, W. 2019 Role of gravity and capillary waves in the origin of circular hydraulic jumps. *Phys. Rev. Fluids* **4**, 114002.
- ASKARIZADEH, H., AHMADIKIA, H., EHRENPREIS, C., KNEER, R., PISHEVAR, A. & ROHLFS, W. 2020 Heat transfer in the hydraulic jump region of circular free-surface liquid jets. *Intl. J. Heat Mass Transfer* **146**, 118823.
- AVEDISIAN, C. & ZHAO, Z. 2000 The circular hydraulic jump in low gravity. *Proc. R. Soc. Lond., Ser. A* **456**, 2127-2151.
- BAAYOUN, A., KHAYAT, R. E. & WANG, Y. 2022 The transient spread of a circular liquid jet and hydraulic jump formation. *J. Fluid Mech.* **947**, A34.
- BOHR, T., DIMON, P. & PUTZKARADZE, V. 1993 Shallow-water approach to the circular hydraulic jump. *J. Fluid Mech.* **254**, 635-648.
- BOHR, T., ELLEGAARD, C., HANSEN, A. E. & HAANING, A. 1996 Hydraulic jumps, flow separation and wave breaking: An experimental study. *Physica B* **228**, 1-10.
- BOHR, T., PUTKARADZE, V. & WATANABE, S. 1997 Averaging theory for the structure of hydraulic jumps and separation in laminar free-surface flows. *Phys. Rev. Lett.* **79**, 1038-1041.
- BONN, D., ANDERSEN, A. & BOHR, T. 2009 Hydraulic jumps in a channel. *J. Fluid Mech.* **618**, 71-87.
- BOWLES, R. I. 1995 Upstream influence and the form of standing hydraulic jumps in liquid-layer flows on favourable slopes. *J. Fluid Mech.* **284**, 63-96.

- BOWLES, R. I. & SMITH, F. T. 1992 The standing hydraulic jump: theory, computations and comparisons with experiments. *J. Fluid Mech.* **242**, 145-168.
- BUSH, J. W. M. & ARISTOFF, J. M. 2003 The influence of surface tension on the circular hydraulic jump. *J. Fluid Mech.* **489**, 229-238.
- CHANG, H. C., DEMEKHIN, E. A. & TAKHISTOV, P. V. 2001 Circular hydraulic jumps triggered by boundary layer separation. *J. Colloid Interface Sci.* **233**, 329-338.
- CRAIK, A., LATHAM, R., FAWKES, M. & GRIBBON, P. 1981 The circular hydraulic jump. *J. Fluid Mech.* **112**, 347-362.
- DHAR, M., DAS, G. & DAS, P. K. 2020 Planar hydraulic jumps in thin film flow. *J. Fluid Mech.* **884**, A11.
- DUCHESNE, A. 2014 Trois problèmes autour du ressaut hydraulique circulaire (thesis - Université Denis Diderot (Paris 7) - Sorbonne Paris Cité).
- DUCHESNE, A., LEBON, L. & LIMAT, L. 2014 Constant Froude number in a circular hydraulic jump and its implication on the jump radius selection. *Europhys. Lett.* **107**, 54002.
- DUCHESNE, A. & LIMAT, L. 2022 Circular hydraulic jumps: where does surface tension matter? *J. Fluid Mech.* **937**, R2.
- ELLEGAARD, C., HANSEN, A.E., HAANING, A., HANSEN, K., MARCUSSEN, A., BOHR, T., HANSEN, J.L. & WATANABE, S. 1998 Creating corners in kitchen sinks. *Nature* **392**, 767-768.
- FERNANDEZ-FERIA, R., SANMIGUEL-ROJAS, E. & BENILOV, E. S. 2019 On the origin and structure of a stationary circular hydraulic jump. *Phys. Fluids* **31**, 072104.
- HANSEN, S. H., HORLUCK, S., ZAUNER, D., DIMON, P., ELLEGAARD, C. & CREAGH, S. C. 1997 Geometric orbits of surface waves from a circular hydraulic jump. *Phys. Rev. E* **55**, 7048-7061.

- HIGUERA, F. J. 1994 The hydraulic jump in a viscous laminar flow. *J. Fluid Mech.* **274**, 69-92.
- IPATOVA, A., SMIRNOV, K. & MOGILEVSKIY, E. 2021 Steady circular hydraulic jump on a rotating disk. *J. Fluid Mech.* **927**, A24.
- KASIMOV, A. R. 2008 A stationary circular hydraulic jump, the limits of its existence and its gasdynamic analogue. *J. Fluid Mech.* **601**, 189–198.
- LAWSON, J.D. & PHILLIPS, B.C. 1983 Circular hydraulic jump. *J. Hydraul. Eng.* **109**, 505-518.
- LIU, X. & LIENHARD, J. 1993 The hydraulic jump in circular jet impingement and in other thin liquid films. *Exp. Fluids* **15**, 108-116.
- MOHAJER, B. & LI, R. 2015 Circular hydraulic jump on finite surfaces with capillary limit. *Phys. Fluids* **27**, 117102.
- PALERMO, M. & PAGLIARA, S. 2018 Semi-theoretical approach for energy dissipation estimation at hydraulic jumps in rough sloped channels. *J Hydraulic Research* **56**, 786–795.
- PASSANDIDEH-FARD, M., TEYMOURTASH, A. R. & KHAVARI, M. 2011 Numerical Study of Circular Hydraulic Jump Using Volume-of-Fluid Method. *J Fluids Engng* **133**, 11401.
- PRINCE, J. F., MAYNES, D. & CROCKETT, J. 2012 Analysis of laminar jet impingement and hydraulic jump on a horizontal surface with slip. *Phys. Fluids* **24**, 102103.
- RAO, A. & ARAKERI, J. H. 2001 Wave structure in the radial film flow with a circular hydraulic jump. *Exp. Fluids* **31**, 542-549.
- RAYLEIGH, O. M. 1914 On the theory of long waves and bores. *Proc. R. Soc. Lond. A* **90**, 324-328.
- RAZIS, D., KANELLOPOULOS, G. & VAN DER WEELE, K. 2021 Continuous hydraulic jumps in laminar channel flow. *J. Fluid Mech.* **915**, A8.

- ROBERTS, A. J. & LI, Z. 2006 An accurate and comprehensive model of thin fluid flows with inertia on curved substrates. *J. Fluid Mech.* **553**, 33–73.
- ROJAS, N. O., ARGENTINA, M., CERDA, E. & TIRAPEGUI, E. 2010 Inertial lubrication theory. *Phys. Rev. Lett.* **104**, 187801.
- ROJAS, N. O., ARGENTINA, M. & TIRAPEGUI, E. 2013 A progressive correction to the circular hydraulic jump scaling. *Phys. Fluids* **25**, 42105.
- SCHEICHL, B., BOWLES, R. I. & PASIAS, G. 2018 Developed liquid film passing a trailing edge under the action of gravity and capillarity. *J. Fluid Mech.* **850**, 924–953.
- SCHLICHTING, H. & GERSTEN, K. 2000 *Boundary-layer theory* 8th edition, Springer.
- TANI, I. 1949 Water Jump in the Boundary Layer. *J. Phys. Soc. Japan.* **4**, 212-215.
- WANG, W., BAAYOUN, A. & KHAYAT, R. E. 2023 A coherent composite approach for the continuous circular hydraulic jump and vortex structure. *J. Fluid Mech.* **966**, A15.
- WANG, Y. & KHAYAT, R. E. 2018 Impinging jet flow and hydraulic jump on a rotating disk. *J. Fluid Mech.* **839**, 525-560.
- WANG, Y. & KHAYAT, R. E. 2019 The role of gravity in the prediction of the circular hydraulic jump radius for high-viscosity liquids. *J. Fluid Mech.* **862**, 128-161.
- WANG, Y. & KHAYAT, R. E. 2021 The effects of gravity and surface tension on the circular hydraulic jump for low- and high-viscosity liquids: A numerical investigation. *Phys. Fluids* **33**, 012105.
- WATANABE, S., PUTKARADZE, V. & BOHR, T. 2003 Integral methods for shallow free-surface flows with separation. *J. Fluid Mech.* **480**, 233-265.
- WATSON, E. 1964 The spread of a liquid jet over a horizontal plane. *J. Fluid Mech.* **20**, 481-499.
- WHITE, F. M. 2006 *Viscous Fluid Flow*, 3th edition, McGraw-Hill.

YANG, S. & CHEN, C. 1992 Laminar film condensation on a finite-size horizontal plate with suction at the wall. *Appl. Math. Model.* **16**, 325-329.

YANG, Y., CHEN, C. & HSU, P. 1997 Laminar film condensation on a finite-size wavy disk. *Appl. Math. Model.* **21**, 139-144.

ZHOU, G. & PROSPERETTI, A. 2022 Hydraulic jump on the surface of a cone. *J. Fluid Mech.* **951**, A20.

Chapter 4

4 The influence of azimuthally varying edge conditions on the hydraulic jump³

Nomenclature

a	Radius of jet, m
A	A constant amplitude
Bo	Bond number, $Bo = \rho g a^2 / \sigma$
Fr	Froude number, $Fr = W / \sqrt{g a}$
g	Acceleration due to gravity, m/s^2
h	Dimensionless film thickness in the supercritical region
H	Dimensionless film thickness in the subcritical region
H_0	Dimensionless film thickness at disk edge for a circular disk of radius $R_{\infty 0}$
h_1	Dimensionless film height at $r = R_1$
h_2	Dimensionless film height at $r = R_2$
h_j	Dimensionless film thickness immediately upstream of the jump
H_j	Dimensionless film thickness immediately downstream of the jump
H_{∞}	Dimensionless film edge thickness for a circular disk (function of θ)

³ A version of this chapter has been published as -

Wang, W. & Khayat, R.E. 2022 The influence of azimuthally varying edge conditions on the hydraulic jump. *Acta Mech.* 233, 3679-3698. <https://doi.org/10.1007/s00707-022-03295-3>

$H_{\infty 0}$	Dimensionless constant film edge thickness
p	Dimensionless pressure
P	The perimeter of the jump
Q	Volume flow rate, m^3/s
r	Dimensionless radial coordinate
R_1	Dimensionless radial location of the inner bound on the jump
R_2	Dimensionless radial location of the outer bound on the jump
r_0	Dimensionless transition point of the hydrodynamic boundary layer
R	Dimensionless radius used for a non-circular disk, $R = R_{\infty} - R_{\infty 0}$
R_{∞}	Dimensionless disk radius
$R_{\infty 0}$	Dimensionless average radius of the disk for a non-circular disk
r_j	Dimensionless jump radius
r_{jmean}	Dimensionless mean jump radius for non-circular jump
r_{jmin}	Dimensionless minimum jump radius for non-circular jump
r_{jmax}	Dimensionless maximum jump radius for non-circular jump
Δr_j	Dimensionless jump width of
Δr	Dimensionless width of a control volum
Re	Reynolds number, $Re = Wa/\nu$
T	The departure function of θ for the edge thickness

u	Dimensionless horizontal velocity in the supercritical region
U	Dimensionless horizontal velocity in the subcritical region
u_j	Dimensionless horizontal velocity immediately upstream of the jump
U_j	Dimensionless horizontal velocity immediately downstream of the jump
v	Dimensionless azimuthal velocity in the supercritical region
V	Dimensionless azimuthal velocity in the subcritical region
V_j	Dimensionless azimuthal velocity immediately downstream of the jump
w	Dimensionless vertical velocity in the supercritical region
W	Dimensionless vertical velocity in the subcritical region
We	Weber number, $We = BoFr^2$
z	Dimensionless vertical coordinate

Greek Symbols

$\alpha_0, \alpha_k, \alpha_n, \beta_n$	Coefficients of expansion
Λ	The jump inner area
δ	Dimensionless hydrodynamic boundary layer thickness
θ	Azimuthal coordinate
θ_Y	Static contact angle
ν	Kinematic viscosity, m^2/s
ρ	Density of fluid, kg/m^3
σ	Surface tension of fluid, N/m

4.1 Introduction

Although extensive work in the literature has been devoted to the understanding and prediction of the hydraulic jump structure, forming when a circular liquid jet impinges on a solid disk, most of the work concentrated on the axisymmetric flow and the resulting circular jump. Some of the most significant practical relevance is in jet cooling (Baonga *et al.* 2006; Askarizadeh *et al.* 2020; Wang & Khayat 2020). Watson (1964) analysed the isothermal flow in the developing boundary layer near impingement, and the fully-viscous layer upstream of the jump. Watson's thin-film approach became the basis for numerous later theoretical and experimental studies. Watson's theory was tested in a number of experimental investigations, including those of Watson himself, Craik *et al.* (1981) and Baonga *et al.* (2006). Liu & Lienhard (1993) observed that Watson's predictions were least satisfactory in the limit of a relatively weak jump. The effect of surface tension was further examined by Mohajer & Li (2015). To capture the behaviour downstream of the jump, Duchesne *et al.* (2014) examined the downstream flow using the lubrication approach. Good agreement between their theoretical predictions for the height profile and their measurements is observed. Some extensions have been considered, such as the spread of an impinging non-Newtonian jet by Zhao & Khayat (2008), the formation of a hydraulic jump on an inclined plane by Kate, Das & Chakraborty (2007) and Benilov (2015), and impingement on a rotating disk by Ozar, Cetegen & Faghri (2003), Wang & Khayat (2018) and Ipatova *et al.* (2021). The influence of slip was examined by Dressaire *et al.* (2010), Prince, Maynes & Crockett (2012) and Khayat (2016). The influence of gravity on the jump radius was studied by Avedisian & Zhao (2000), Wang & Khayat (2019), Askarizadeh *et al.* (2019), Fernandez-Feria *et al.* (2019) and Dhar *et al.* (2020).

The investigation of the formation and structure of the non-circular jump is relatively recent, focusing essentially on the spontaneous destabilization of the circular jump and the onset of stable non-circular jump. Some of the experimental work was conducted by Ellegaard *et al.* (1998), Andersen *et al.* (2010) and Martens *et al.* (2012). To a lesser extent, theoretical stability analyses (Kasimov 2008), as well as a variational approach (Watanabe 2013) were also carried out. Perhaps the most compelling attempts to model steady non-circular jumps were made by Martens *et al.* (2012) and Rojas & Tirapegui (2015). In the

present study, we focus our attention on another mechanism for the generation of non-circular jumps, namely by imposing azimuthally varying conditions at the edge of the disk. This is an important problem in pattern generation, which can be pursued in practice under very controlled and systematic conditions. Although there is little direct relevance of the present problem to the spontaneous jumps, we will highlight the similarities and differences with the edge induced jumps. Stationary non-circular jumps were first observed by Ellegaard *et al.* (1998) in ethylene glycol. The increased downstream flow was varied by raising or lowering the obstacle mounted around the disk. They observed that the number of sides or wavenumber of the non-circular jump increases with the downstream flow height first, then this number decreases by one side at a time when the downstream flow height increases further. They observed a hysteresis effect as several polygons could be stable for the same flow parameters, accompanied by a flow spiralling towards the corner.

Martens *et al.* (2012) proposed a phenomenological model based on mass conservation and radial force balance between the hydrostatic pressure and viscous stresses on the roller surface. They found that a non-circular jump emerges with a wavelength in the order of the roller width based on the Rayleigh-Plateau instability. The surface tension effect was neglected as the free surface profile of the jump and the curvatures could not be accurately modelled. They observed that the flow upstream of the jump is purely radial and independent of azimuthal direction, as the measured height profile at the corner and valley directions for the upstream of the jump region are the same. These observations corroborate the earlier findings of Bush *et al.* (2006). A more rigorous approach was later proposed by Rojas & Tirapegui (2015), who derived the thin-film equations, including inertia, by averaging the conservation equations and adopting a polynomial representation of the flow field from Taylor expansion about the conditions at the disk. The resulting coupled film equations were further reduced by neglecting the azimuthal velocity component. Other studies devoted to fully non-axisymmetric flow configurations include the case of an inclined impinging jet and, more recently, the flow in the presence of non-circular obstacles placed close to the disk edge (Ferreira *et al.* 2002). Of some relevance is the asymmetric jump on an inclined plane (Watanabe *et al.* 2003; Benilov 2015), and the jet on a microindented disk Dressaire *et al.* (2010). Like Rojas & Tirapegui (2015) also neglected the azimuthal flow component for an inclined jet. Recently, this problem was further

addressed by Abdelaziz & Khayat (2022) who solved the fully coupled problem. They found that the azimuthal velocity can be negligible in the region near impingement, it becomes of the same order of magnitude further downstream in the fully-viscous region and the jump.

In the present study, we do not attempt to model the steady spontaneous non-circular jump observed in the experimental literature, typically resulting from the destabilization of the axisymmetric flow. We examine theoretically the influence of the azimuthally varying edge conditions on the structure of the induced non-circular hydraulic jump and non-axisymmetric flow field. In particular, we examine the effect of disk non-circularity and non-axisymmetric edge film thickness. In contrast to the spontaneous emergence of non-circular jump, the non-circularity of the jump is induced systematically by varying the edge conditions. The two types of edge conditions should easily be imposable in practice for a circular jet impinging on a non-circular disk and/or an azimuthally periodic obstacle to control the variation of the film thickness at the disk edge. Given the nonlinearity of the problem, the present study becomes one of pattern generation, and it is therefore important to examine the response in the jump shape induced by the periodicity of the conditions at the edge of the disk. Clearly, the mechanism behind the generation of the non-circular jump is different from that behind the spontaneous jump; while the (so far) observed spontaneous jumps are of type II, the jump generated by varying edge conditions is expected to be of type I. A major advantage of the present problem over the spontaneous jump problem is that it can be easily investigated experimentally, under very controlled conditions, thus allowing the generation of numerous non-circular jump patterns and complex flow fields. The jump is treated as a discontinuity with the subcritical flow assumed inertialess of the lubrication type. In this limit, the vortex structure downstream of the jump cannot be captured. The inclusion of inertia and the consequent higher-order polynomial representation of both the radial and azimuthal velocity components would be extremely challenging for varying edge conditions given the additional boundary conditions required to solve the film thickness equation. We refer the reader to some relevant studies conducted for the circular jump (Watanabe *et al.* 2003; Rojas *et al.* 2010, 2013) and the numerical treatment of the non-circular jumps (Rojas & Tirapegui 2015). Although rollers of type I and type II jumps were possible to predict, a thin-film approach typically involves limiting

assumptions and drawbacks, such as the need for additional experimental data and the shooting method (Watanabe *et al.* 2003), and neglecting the azimuthal component of the velocity (Rojas & Tirapegui 2015). The latter assumption becomes particularly problematic for a non-circular jump with strong peaks and valleys or severe azimuthal variation (Abdelaziz & Khayat 2022).

The paper is organized as follows. The general non-axisymmetric formulation and physical domain are described in section 4.2. The treatment of the supercritical flow is briefly given in section 4.3. The momentum balance across a non-circular jump is formulated in section 4.4. Also in this section, we include the effect of surface tension by extending the formulation to a non-circular jump. Validation and results are covered in section 4.5, where we examine the influence of the non-circular disk geometry on the jump shape and height, as well as the influence of a periodic thickness at the edge of a circular disk. Finally, concluding remarks and discussion are given in section 4.6.

4.2 Physical domain and problem statement

We consider the steady incompressible flow of a circular jet of a Newtonian liquid emerging from a nozzle of radius a , impinging at a volume flow rate Q normal to a flat disk, which may or may not be circular. The flow configuration is depicted schematically in figure 4-1, where dimensionless variables and parameters are used. The flow is assumed to be laminar upstream and downstream of the jump. We refer the reader to the book of Acheson (2005) for some of the fundamentals behind the planar hydraulic jump. The problem is formulated in the (r, θ, z) fixed coordinates, with the origin coinciding with the stagnation point of the jet. The axial symmetry is broken by the disk non-circularity or the θ -dependent distribution of the film thickness along the edge of a circular disk, thus causing the formation of a non-circular hydraulic jump. We denote by $u(r, \theta, z)$, $v(r, \theta, z)$ and $w(r, \theta, z)$ the dimensionless velocity components in the radial, azimuthal and vertical directions, respectively. The r -axis is taken along the disk radius and the z -axis is taken normal to the disk. The length and the velocity scales are conveniently taken to be the radius of the jet, a , and $W \equiv Q/\pi a^2$ in all directions. Since the pressure is expected to be

predominantly hydrostatic for a thin film, it will be scaled by $\rho g a$, g being the gravitational acceleration. Three main dimensionless groups emerge in this case: the Reynolds number $Re = Wa/\nu$, where ν is the kinematic viscosity, the Froude number $Fr = W/\sqrt{ag}$ and the Bond number $Bo = \rho g a^2/\sigma$, where σ is the surface tension.

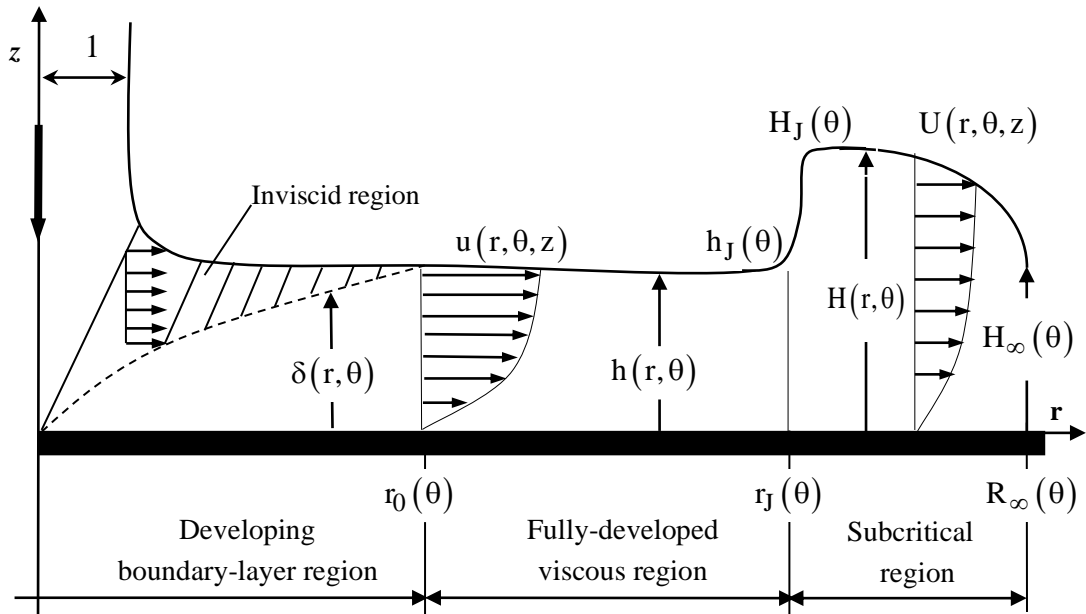


Figure 4-1: Schematic illustration of the non-axisymmetric flow of a circular jet impinging on a flat stationary disk, and the hydraulic jump of type I. Shown are the developing boundary-layer region, the fully-developed viscous region, and the subcritical region downstream of the jump. All notations are dimensionless.

Following the usual treatment (Watson 1964; Bush & Aristoff 2003; Prince *et al.* 2012; Wang & Khayat 2018, 2019), we assume the stagnation flow region to be negligible, and identify three distinct flow regions for the jet over the disk, with smooth passage from one region to the next. The region $0 < r < r_0(\theta)$ will be referred to as the *developing boundary-layer region*, with boundary-layer thickness $\delta(r, \theta)$, outside which the flow is inviscid and uniform. Here $r_0(\theta)$ is the location of the *transition point* at which the viscous stresses become appreciable right up to the free surface, where the whole flow is of the boundary-layer type. The region between the transition point and the jump, $r_0(\theta) < r < r_J(\theta)$, will be

referred to as the *fully-developed viscous* region, and is bounded by the disk and the free surface $z = h(r, \theta)$. The jump may occur upstream or downstream of the transition point. Referring to figure 4-1, we conveniently introduce the supercritical film thickness (upstream of the jump) as $h(r, \theta) = h(r < r_J, \theta)$, and the subcritical thickness (downstream of the jump) as $H(r, \theta) \equiv h(r > r_J, \theta)$. The heights immediately upstream and downstream of the jump are denoted by $h_J(\theta) \equiv h(r = r_J, \theta)$ and $H_J(\theta) \equiv H(r = r_J, \theta)$, respectively. In this study, the fluid is assumed to be drained at the edge of the disk, at $r = R_\infty(\theta)$, and the flow remains steady, with the film thickness denoted by $H_\infty(\theta) = H(r = R_\infty, \theta)$. The subcritical height $H(r, \theta)$ is generally different from the height $H_J(\theta)$.

For steady non-axisymmetric thin-film flow, the mass and momentum conservation equations are formulated using Prandtl boundary-layer approach (Schlichting & Gersten 2000). We note that the pressure is hydrostatic, and vanishes at the free surface, yielding $p(r, \theta, z) = h(r, \theta) - z$. By letting a subscript with respect to r , θ or z denote partial differentiation, and eliminating the pressure, the reduced dimensionless conservation equations become

$$u_r + \frac{u}{r} + \frac{v\theta}{r} + w_z = 0, \quad (4.2.1a)$$

$$\text{Re} \left(uu_r + \frac{v}{r} u_\theta + wu_z - \frac{v^2}{r} \right) = -\frac{\text{Re}}{\text{Fr}^2} h_r + u_{zz}, \quad (4.2.1b)$$

$$\text{Re} \left(uv_r + \frac{v}{r} v_\theta + wv_z + \frac{uv}{r} \right) = -\frac{\text{Re}}{\text{Fr}^2} \frac{h_\theta}{r} + v_{zz}. \quad (4.2.1c)$$

At the solid disk, the no-slip and no-penetration conditions are assumed to hold for any r and θ :

$$u(r, \theta, z = 0) = v(r, \theta, z = 0) = w(r, \theta, z = 0) = 0. \quad (4.2.2a-c)$$

At the free surface $z = h(r < r_J, \theta)$ or $z = H(r > r_J, \theta)$, the kinematic and dynamic conditions for steady flow take the form:

$$w(r, \theta, z = h) = u(r, \theta, z = h)h_r(r, \theta) + \frac{v(r, \theta, z = h)}{r}h_\theta(r, \theta), \quad (4.2.3)$$

$$u_z(r, \theta, z = h) = v_z(r, \theta, z = h) = 0. \quad (4.2.4a-b)$$

The effect of surface tension will be accounted for across the non-circular jump. The conservation of mass at any location upstream and downstream of the jump yields the following relation in dimensionless form:

$$\int_0^{2\pi} \int_0^{h(r, \theta)} u(r, \theta, z) dz d\theta = \frac{\pi}{r}. \quad (4.2.5)$$

The flow field is sought separately in the developing boundary-layer region, for $0 < r < r_0(\theta)$, the fully developed viscous region, for $r_0(\theta) < r < r_J(\theta)$, and the hydraulic jump region, for $r_J(\theta) < r < R_\infty(\theta)$.

4.3 The axisymmetric supercritical flow

We shall now argue that the supercritical flow remains axisymmetric for a thin film, and is therefore not affected by the loss of axial symmetry at the jump level and the subcritical flow downstream of the jump. For a circular jet, the thin-film equations (4.2.1) are solved subject to conditions on the velocity and film thickness at some small distance from the stagnation point. Consequently, for a circular jet, and close to the impingement point, we have

$$u(r \rightarrow 0, \theta, z) \sim 1, \quad v(r \rightarrow 0, \theta, z) \sim 0. \quad (4.3.1a-b)$$

An additional constraint on the film thickness is obtained from the conservation of mass (4.2.5), which, based on (4.3.1), suggests the following integral equation for $h(r, \theta)$:

$$\int_0^{2\pi} h(r, \theta) d\theta \sim \frac{\pi}{r}. \quad (4.3.2)$$

Conditions (4.3.1) and constraint (4.3.2) clearly indicate that, unless some azimuthal dependence is imposed on the film thickness or velocity near impingement, such as the case of a jet of non-circular cross section or an inclined jet (Abdelaziz & Khayat 2022), the film surface remains axisymmetric, with $h(r, \theta) \sim 1/2r$ for small r , independently of θ . Additionally, the adherence condition (4.2.2b) at the solid disk and the stress-free condition (4.2.4b) at the film surface ensure that the azimuthal velocity component vanishes everywhere, with equation (4.2.1c) identically satisfied. Consequently, the supercritical flow upstream of the (non-circular) jump remains axisymmetric. This conclusion is physically plausible given the relatively high strength of the circular impinging jet; there is simply no mechanism for the supercritical flow to lose its axial symmetry. Indeed, Martens *et al.* (2012) observed that the supercritical flow remains axisymmetric upstream of a non-circular jump, which is evident in their figure 4-3, where the film height was measured in the supercritical region of a pentagonal hydraulic jump in ethylene glycol. In particular, they found that the film height in the radial directions through a corner and a valley are the same, indicating no dependence of the height on the azimuthal angle. They measured the film heights across the corner and the valley of the jump, and found that they are identical. They noted that the supercritical film thickness is below the threshold for a transition to occur in the supercritical region when the circular type-I jump loses its stability to the non-circular type-II jump (see also Jannes *et al.* 2011). These observations were also echoed by Bush *et al.* (2006) in their experimental investigation of the stability of the hydraulic jump.

The solution procedure of the supercritical flow, in the developing boundary-layer and fully-developed viscous regions, can be found in several references, and will not be pursued here (Watson 1964; Prince *et al.* 2012; Wang & Khayat 2018, 2019).

4.4 The non-axisymmetric subcritical flow formulation

We examine the flow and the film height in the subcritical region downstream of the jump, in particular the location and height of the jump. The vertical velocity component is first eliminated by noting from (4.2.1a) that

$$w(r, \theta, z) = -\frac{1}{r} \frac{\partial}{\partial r} \left(r \int_0^z u(r, \theta, z) dz \right) - \frac{1}{r} \frac{\partial}{\partial \theta} \int_0^z v(r, \theta, z) dz. \text{ In this case:}$$

$$uu_r + \frac{v}{r} u_\theta + wu_z = \frac{1}{r} (ru^2)_r + \frac{1}{r} (uv)_\theta - \frac{\partial}{\partial z} \left[\frac{u}{r} \int_0^z ((ru)_r + v_\theta) dz \right]. \quad (4.4.1a)$$

$$uv_r + \frac{v}{r} v_\theta + wv_z = (uv)_r + 2\frac{v}{r} v_\theta + \frac{uv}{r} - \frac{\partial}{\partial z} \left[v \int_0^z \left(u_r + \frac{u}{r} + \frac{v}{r} v_\theta \right) dz \right]. \quad (4.4.1b)$$

Using these relations, the integral forms of (4.2.1a-b) become

$$\frac{\text{Re}}{r} \left(\frac{\partial}{\partial r} \int_0^h ru^2 dz + \frac{\partial}{\partial \theta} \int_0^h uv dz - \int_0^h v^2 dz \right) = -\frac{\text{Re}}{\text{Fr}^2} hh_r - u_z(r, \theta, z=0), \quad (4.4.2a)$$

$$\frac{\text{Re}}{r} \left(\frac{\partial}{\partial r} \int_0^h ruv dz + \frac{\partial}{\partial \theta} \int_0^h v^2 dz + \int_0^h uv dz \right) = -\frac{\text{Re}}{\text{Fr}^2} \frac{h}{r} h_\theta - v_z(r, \theta, z=0). \quad (4.4.2b)$$

4.4.1 Conservation of momentum across the jump

Across the jump, equations (4.4.2) are applied for a control volume of width Δr in the radial direction. Assuming finite changes with respect to r and θ , we have

$$\text{Re} \left(\Delta \int_0^h u^2 dz + \frac{1}{r} \frac{\Delta r}{\Delta \theta} \Delta \int_0^h uv dz - \frac{\Delta r}{r} \int_0^h v^2 dz \right) = -\frac{\text{Re}}{\text{Fr}^2} \frac{\Delta h^2}{2} - \Delta ru_z(r, \theta, z=0). \quad (4.4.3a)$$

$$\frac{\text{Re}}{r} \left(\Delta \int_0^h ruv dz + \frac{\Delta r}{\Delta \theta} \Delta \int_0^h v^2 dz + \Delta r \int_0^h uv dz \right) = -\frac{\text{Re}}{\text{Fr}^2} \frac{\Delta r}{\Delta \theta} \frac{\Delta h^2}{2r} - \Delta rv_z(r, \theta, z=0). \quad (4.4.3b)$$

We conveniently introduce the following change in notation for the subcritical velocity:

$$U(r, \theta, z) \equiv u(r > r_J, \theta, z), \quad V(r, \theta, z) \equiv v(r > r_J, \theta, z). \quad (4.4.4a-b)$$

Since the width of the jump Δr is assumed to be small, equations (4.4.3) reduce to

$$\frac{H_J^2 - h_J^2}{2Fr^2} = \int_0^{h_J} u_J^2(\theta, z) dz - \int_0^{H_J} U_J^2(\theta, z) dz - \frac{1}{r_J} \frac{dr_J}{d\theta} \int_0^{H_J} U_J(\theta, z) V_J(\theta, z) dz, \quad (4.4.5a)$$

$$\frac{H_J^2 - h_J^2}{2Fr^2 r_J} \frac{dr_J}{d\theta} = - \int_0^{H_J} U_J(\theta, z) V_J(\theta, z) dz - \frac{1}{r_J} \frac{dr_J}{d\theta} \int_0^{H_J} V_J^2(\theta, z) dz, \quad (4.4.5b)$$

Here $u_J(\theta, z) \equiv u(r = r_J(\theta), z)$ is the velocity just upstream of the jump. Their expression for a cubic profile is available from earlier axisymmetric formulations (Bohr *et al.* 1993; Rojas *et al.* 2013; Wang & Khayat 2019):

$$u_J(\theta, z) = \frac{2}{5h_J r_J} \left(3 \frac{z}{h_J} - \frac{z^3}{h_J^3} \right), \quad h_J(\theta) = \frac{175}{136} \frac{r_J^2}{Re} + \frac{233}{340} \frac{1}{r_J}. \quad (4.4.6a-b)$$

We note that $U_J(\theta, z) \equiv U(r = r_J, \theta, z)$ and $V_J(\theta, z) \equiv V(r = r_J, \theta, z)$ are the velocity components just downstream of the jump. We observe that the jump can occur before ($r_J < r_0$) or after ($r_J > r_0$) the transition location in the supercritical region. The jump height is completely determined as a function of the Froude and the Reynolds numbers once the subcritical velocity profiles $U_J(\theta, z)$ and $V_J(\theta, z)$ are determined.

4.4.2 Accounting for surface tension effect

Bush & Aristoff (2003) extended Watson's theory by including radial curvature force due to surface tension. Comparison with their experimental measurements show that the surface tension correction becomes particularly significant for a jump of small radius and height. It is therefore expected that surface tension effect can become significant for a non-circular jump where sharp peaks and valleys emerge as we shall see. We follow closely the

treatment of Bush & Aristoff (2003), and extend their formulation for the non-circular jump. We refer to the flow through the control volume across the jump shown in figure 4-2, which is similar to that adopted by Martens *et al.* (2012) in their theoretical model.

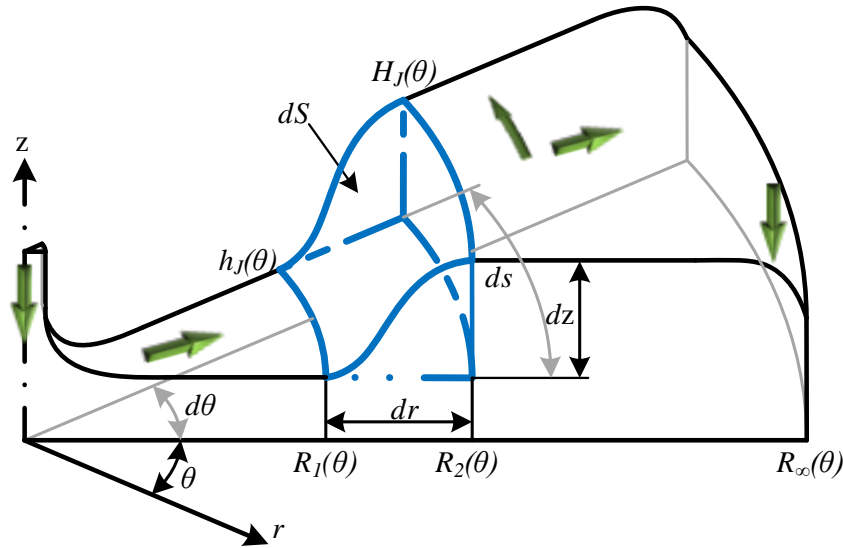


Figure 4-2: Schematic of the control volume across the hydraulic jump. Arrows indicate direction of velocity components.

We consider the radial and azimuthal components of the surface tension force associated with the azimuthal curvature of the jump. If we define the jump surface as $J(r, \theta, z) = z - h(r, \theta) = 0$, then the resulting radial curvature force over a surface element

$dS = rd\theta ds = rd\theta \sqrt{dr^2 + dz^2} = r\sqrt{1 + h_r^2} dr d\theta$ may be expressed as

$$d\mathbf{F} = \text{Bo}^{-1} d\theta \int_{R_1(\theta)}^{R_2(\theta)} (\nabla \cdot \mathbf{n}) \mathbf{n} \sqrt{1 + h_r^2} r dr, \quad (4.4.7)$$

where $R_1(\theta)$ and $R_2(\theta)$ represent the inner and outer bounds on the jump, defined as the nearest points up- and downstream of the jump. The unit normal becomes

$$\mathbf{n} = \frac{\nabla J(r, \theta, z)}{|\nabla J(r, \theta, z)|} = \frac{\mathbf{e}_z - h_r \mathbf{e}_r - r^{-1} h_\theta \mathbf{e}_\theta}{\sqrt{1 + h_r^2 + r^{-2} h_\theta^2}}, \quad \text{where } (\mathbf{e}_r, \mathbf{e}_\theta, \mathbf{e}_z) \text{ is the vector base in the}$$

cylindrical polar system. Noting that

$$\nabla \cdot \mathbf{n} = -\frac{1}{r} \frac{\partial}{\partial r} \frac{rh_r}{\sqrt{1+h_r^2+r^{-2}h_\theta^2}} - \frac{1}{r^2} \frac{\partial}{\partial \theta} \frac{h_\theta}{\sqrt{1+h_r^2+r^{-2}h_\theta^2}}, \text{ we then have}$$

$$\frac{dF_r}{d\theta} = \frac{1}{Bo} \int_{R_1}^{R_2} \left(\frac{\partial}{\partial r} \frac{rh_r}{\sqrt{1+h_r^2+r^{-2}h_\theta^2}} + \frac{1}{r} \frac{\partial}{\partial \theta} \frac{h_\theta}{\sqrt{1+h_r^2+r^{-2}h_\theta^2}} \right) \sqrt{\frac{1+h_r^2}{1+h_r^2+r^{-2}h_\theta^2}} h_r dr, \quad (4.4.8a)$$

$$\frac{dF_\theta}{d\theta} = \frac{1}{Bo} \int_{R_1}^{R_2} \left(\frac{\partial}{\partial r} \frac{rh_r}{\sqrt{1+h_r^2+r^{-2}h_\theta^2}} + \frac{1}{r} \frac{\partial}{\partial \theta} \frac{h_\theta}{\sqrt{1+h_r^2+r^{-2}h_\theta^2}} \right) \sqrt{\frac{1+h_r^2}{1+h_r^2+r^{-2}h_\theta^2}} \frac{h_\theta}{r} dr, \quad (4.4.8b)$$

We approximate the integrals by recognizing that the radial variation of the film thickness is dominant in the limit of a sharp jump; we expect the azimuthal variation of h to remain finite, thus excluding the emergence of sharp corners, so that $h_r \gg h_\theta$. Consequently, in

the limit $R_1 \rightarrow R_2$, $h_r \rightarrow \infty$, so that $\frac{rh_r}{\sqrt{1+h_r^2+r^{-2}h_\theta^2}} \sim r$, $\frac{h_\theta}{\sqrt{1+h_r^2+r^{-2}h_\theta^2}} \sim 0$ and

$\sqrt{\frac{1+h_r^2}{1+h_r^2+r^{-2}h_\theta^2}} \sim 1$. In this case, equations (4.4.8) reduce to

$$\frac{dF_r}{d\theta} \approx \frac{1}{Bo} \int_{R_1}^{R_2} h_r dr, \quad \frac{dF_\theta}{d\theta} \approx \frac{1}{Bo} \int_{R_1}^{R_2} \frac{h_\theta}{r} dr. \quad (4.4.9a-b)$$

Clearly, $\int_{R_1}^{R_2} h_r dr = h_2 - h_1$. Applying Leibniz' rule,

$$\int_{R_1}^{R_2} \frac{\partial}{\partial \theta} \left(\frac{h}{r} \right) dr = \frac{\partial}{\partial \theta} \int_{R_1}^{R_2} \frac{h}{r} dr - \frac{dR_2}{d\theta} \frac{h_2}{R_2} + \frac{dR_1}{d\theta} \frac{h_1}{R_1}. \text{ We note that the area under the jump}$$

vanishes in the limit $R_1 \rightarrow R_2$ so that $\int_{R_1}^{R_2} \frac{h}{r} dr \sim 0$. Recalling that $h_1 \equiv h_J$ and $h_2 \equiv H_J$,

expressions (4.4.8) become

$$\frac{dF_r}{d\theta} \approx \frac{H_J - h_J}{Bo}, \quad \frac{dF_\theta}{d\theta} \approx -\frac{1}{Bo} \frac{dr_J}{d\theta} \left(\frac{H_J - h_J}{r_J} \right). \quad (4.4.10a-b)$$

Clearly, the result of Bush & Aristoff (2003) is recovered in the limit of an axisymmetric jump.

4.4.3 The subcritical flow field and film height

We follow Duchesne *et al.* (2014), and adopt a lubrication flow approach. In this case, a differential equation for H can be obtained by neglecting the inertial terms in equation (4.4.1), yielding the following profile for the velocity components:

$$U(r, \theta, z) = \frac{Re}{Fr^2} H_r \left(\frac{z^2}{2} - Hz \right), \quad (4.4.11a)$$

$$V(r, \theta, z) = \frac{Re}{Fr^2 r} H_\theta \left(\frac{z^2}{2} - Hz \right), \quad (4.4.11b)$$

$$W(r, \theta, z) = -\frac{Re}{Fr^2 r} \frac{z^2}{2} \left[\left(rH_{rr} + H_r + \frac{H_{\theta\theta}}{r} \right) \left(\frac{z}{3} - H \right) - rH_r^2 - \frac{H_\theta^2}{r} \right]. \quad (4.4.11c)$$

Substituting (4.4.6) and (4.4.11a-b) in (4.4.5), and including the force components (4.4.10), finally yields

$$\left(\frac{H_J + h_J}{2Fr^2} + \frac{1}{We r_J} \right) (H_J - h_J) - \frac{272}{875 h_J r_J^2} = -\frac{2}{15} \frac{Re^2}{Fr^4} H_r H_J^5 \left(H_r + \frac{H_\theta}{r_J^2} \frac{dr_J}{d\theta} \right), \quad (4.4.12a)$$

$$\left[\left(\frac{H_J + h_J}{2Fr^2} - \frac{1}{We r_J} \right) (H_J - h_J) + \frac{2}{15} \frac{Re^2}{Fr^4} H_J^5 \frac{H_\theta^2}{r_J^2} \right] \frac{dr_J}{d\theta} = -\frac{2}{15} \frac{Re^2}{Fr^4} H_\theta H_J^5 H_r. \quad (4.4.12b)$$

We note that $H_r = \left. \frac{\partial H}{\partial r} \right|_{r=r_J}$ and $H_\theta = \left. \frac{\partial H}{\partial \theta} \right|_{r=r_J}$ are partial derivatives of the thickness

downstream of the jump evaluated at the jump radius. We next seek the evaluation of

$H(r, \theta)$. Clearly, all the terms in the square bracket in (4.4.12b) are positive except the surface tension term. This suggests that surface tension tends to weaken the variation of the jump radius in the azimuthal direction. Also, (4.4.12b) suggests that a peak or a valley is bound to form whenever H_r or H_θ vanish.

The equation for $H(r, \theta)$ is obtained from mass conservation. We first integrate the continuity equation (4.2.1a) across the film, and use the kinematic condition (4.2.3) to eliminate w , to arrive at

$$\frac{\partial}{\partial r} \int_0^{H(r, \theta)} rU(r, \theta, z) dz + \frac{\partial}{\partial \theta} \int_0^{H(r, \theta)} V(r, \theta, z) dz = 0. \quad (4.4.13)$$

Substituting (4.4.11a-b) and integrating lead to the following Laplace's equation for $H(r, \theta)$, along with the most general conditions at the disk edge:

$$\frac{\partial}{\partial r} \left(r \frac{\partial H^4}{\partial r} \right) + \frac{1}{r} \frac{\partial^2 H^4}{\partial \theta^2} = 0, \quad H(r = R_\infty(\theta), \theta) = H_\infty(\theta), \quad (4.4.14a, b)$$

$$r_J(\theta) \leq r \leq R_\infty(\theta). \quad (4.4.14c)$$

In addition, periodicity is also imposed, namely $H_\infty(\theta = 0) = H_\infty(\theta = 2\pi)$ and $R_\infty(\theta = 0) = R_\infty(\theta = 2\pi)$. We observe that the edge conditions are written in its most general form to accommodate specification of the thickness at a circular or non-circular disk. We note that another way of obtaining the H equation (4.4.14a) is to evaluate (4.4.11c) at the free surface $z = H$ and use the kinematic condition (4.2.3). An additional constraint on H is deduced from mass conservation when substituting (4.4.11a) into (4.2.5), yielding

$$\frac{d}{dr} \int_0^{2\pi} H^4 d\theta = -12 \frac{Fr^2}{Re} \frac{\pi}{r}. \quad (4.4.15)$$

The formulation must collapse onto the axisymmetric theory when $H_\infty(\theta)$ and $R_\infty(\theta)$ are both constant.

4.5 Results and discussion

The numerical results are reported for two flow configurations for a non-circular hydraulic jump: the flow on a non-circular disk with constant film thickness at the disk edge, and the flow on a circular disk with azimuthally periodic film thickness imposed at the disk edge. We begin by validating the theoretical approach.

4.5.1 Validation

In order to validate the formulation, particularly justifying the assumption of lubrication flow in the subcritical region, we resort to comparison with experimental data for the circular jump since no data exists for us to assess the non-axisymmetric formulation. For the flow on a circular disk of radius R_∞ , and an imposed constant edge thickness $H_\infty = H(r = R_\infty)$, equation (4.4.12a) and the solution of (4.4.15) reduce to (Bohr *et al.* 1993; Rojas *et al.* 2013; Wang & Khayat 2019)

$$\left(\frac{H_J + h_J}{2Fr^2} + \frac{1}{We_{r_J}} \right) (H_J - h_J) - \left(\frac{272}{175h_J} - \frac{3}{2H_J} \right) \frac{1}{5r_J^2} = 0, \quad (4.5.1a)$$

$$H(r) = \left[H_\infty^4 + 6 \frac{Fr^2}{Re} \ln \left(\frac{R_\infty}{r} \right) \right]^{1/4}. \quad (4.5.1b)$$

In this case, (4.4.12b) is identically satisfied. When evaluating (4.5.1b) at the jump location $r = r_J$, and substituting for H_J into (4.5.1a), and substituting h_J from (4.4.6b), we obtain a nonlinear algebraic equation for r_J . Comparison between our predictions and the measurements of Duchesne *et al.* (2014) is reported in figure 4-3 for the film thickness distribution with distance in the super- and subcritical regions for silicon oil (20 cSt). The data are reproduced here in dimensionless form from their figure 2, corresponding to $Re =$

169, $Fr = 16.88$, $Bo = 1.19$ and a normalized disk radius $R_\infty = 94$. The value of the thickness at the edge of the disk is determined from

$$H_\infty = \frac{2}{\sqrt{Bo}} \sin\left(\frac{\theta_Y}{2}\right) + \left(\frac{3}{40}\right)^{1/3} \left(\frac{Fr}{R_\infty}\right)^{2/3}, \quad (4.5.2)$$

which comprises a static contribution in terms of the contact angle and a dynamic contribution based on the minimization of free energy at the disk edge (Wang & Khayat 2018, 2019). In this case, the contact angle is taken as $\theta_Y = 50^\circ$. Figure 4-3 shows that the theoretical predictions, based on (4.5.1)-(4.5.2), are generally in close agreement with the experiment of Duchesne *et al.* (2014), slightly underestimating (overestimating) the measured thickness in the supercritical (subcritical) regions. The location of the jump is predicted accurately while the jump height is slightly higher than experiment.

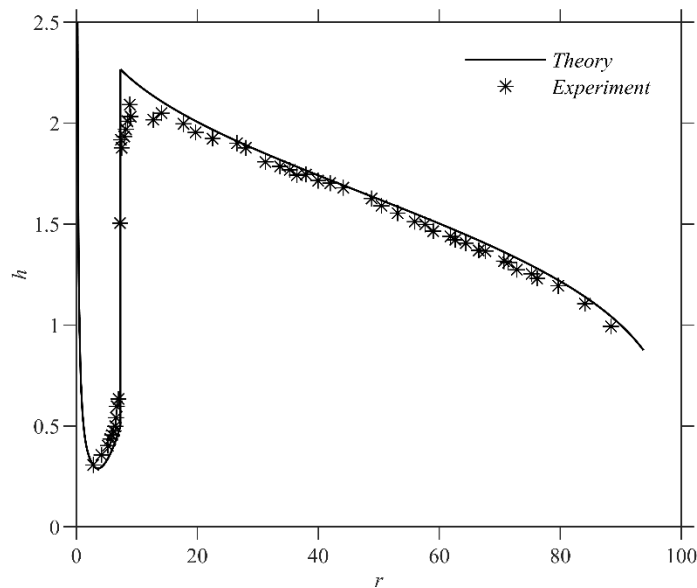


Figure 4-3: Free-surface profile. Comparison between theoretical predictions and the measurements of Duchesne *et al.* (2014) for silicon oil (20 cSt). Results plotted in dimensionless form with $Re = 169$, $Fr = 16.88$, $Bo = 1.19$, $R_\infty = 94$.

We next report results for non-axisymmetric flows. In an effort to keep the results practically and physically realistic, we have limited the parameter range close to experiment of Duchesne *et al.* (2014),

4.5.2 The non-circular jump on a non-circular disk

We consider the flow for a non-circular disk of radius $R_\infty(\theta) = R_{\infty 0} + R(\theta)$ and impose a constant thickness $H_{\infty 0}$ at the edge of the disk. In this case, the problem (4.4.14) reduces to

$$\frac{\partial}{\partial r} \left(r \frac{\partial H^4}{\partial r} \right) + \frac{1}{r} \frac{\partial^2 H^4}{\partial \theta^2} = 0, \quad H(r = R_\infty(\theta), \theta) = H_{\infty 0}, \quad (4.5.3a, b)$$

$$R_\infty(\theta = 0) = R_\infty(\theta = 2\pi). \quad (4.5.3c)$$

We shall examine three typical edge shapes, namely the triangular, square and pentagonal disk geometry. In general, the forms are given by

$$R_\infty(\theta) = \frac{L}{2 \tan(\pi/p) \cos \theta}, \quad 0 \leq \theta \leq \pi/p, \quad (4.5.4)$$

where p is the number of sides or wavenumber, and L is the side length. In this case,

$$R_{\infty 0} = \frac{p}{\pi} \int_0^{\pi/p} R_\infty(\theta) d\theta = \frac{p}{2\pi} \frac{L}{\tan(\pi/p)} \ln \left(\sec \frac{\pi}{p} + \tan \frac{\pi}{p} \right)$$

is the average radius, which is

directly related to p and L . The deviation from the average radius is conveniently expressed

as

$$R_\infty(\theta) = \sum_{k=1}^{\infty} a_k \cos(kp\theta), \quad \text{where}$$

$$a_{k \geq 1} = \frac{2p}{\pi} \int_0^{\pi/p} R_\infty(\theta) \cos(kp\theta) d\theta = \frac{p}{\pi} \frac{L}{\tan(\pi/p)} \int_0^{\pi/p} \frac{\cos(kp\theta)}{\cos \theta} d\theta.$$

Problem (4.5.3) admits a series solution of the form:

$$H^4(r, \theta) = H_0^4(r) + \alpha_0 + \sum_{n=1}^{\infty} r^n (\alpha_n \cos n\theta + \beta_n \sin n\theta), \quad (4.5.5)$$

where $H_0^4(r) = H_{\infty 0}^4 + 6 \frac{Fr^2}{Re} \ln\left(\frac{R_{\infty 0}}{r}\right)$ is the (axisymmetric) thickness distribution (4.5.1b) for a circular disk of radius $R_{\infty 0}$. We note that expansion (4.5.5) satisfies readily (4.4.15). Although (4.5.5) satisfies the Laplace's equation in (4.5.3a), it does not satisfy the boundary condition at the disk edge. Therefore, the expansion coefficients in (4.5.5) are determined by first applying (4.5.4) at the non-circular edge:

$$H_0^4(R_{\infty}) + \alpha_0 + \sum_{n=1}^{\infty} R_{\infty}^n (\alpha_n \cos n\theta + \beta_n \sin n\theta) = H_{\infty 0}^4. \quad (4.5.7)$$

Noting that $H_0^4(R_{\infty}) = H_{\infty 0}^4 + 6 \frac{Fr^2}{Re} \ln\left(\frac{R_{\infty 0}}{R_{\infty}}\right)$, we next project (4.5.7) onto each mode to obtain the following set of algebraic equations for the expansion coefficients:

$$2\pi\alpha_0 + \sum_{n=1}^{\infty} \int_0^{2\pi} R_{\infty}^n (\alpha_n \cos n\theta + \beta_n \sin n\theta) d\theta = 6 \frac{Fr^2}{Re} \int_0^{2\pi} \ln\left(\frac{R_{\infty}}{R_{\infty 0}}\right) d\theta, \quad (4.5.8a)$$

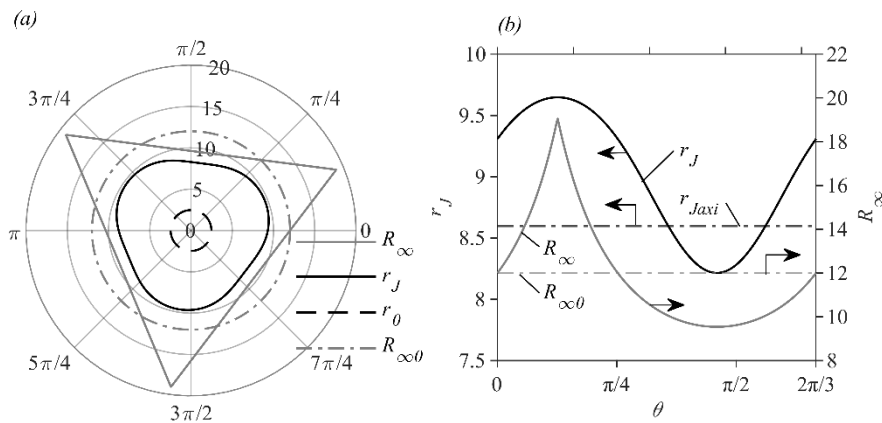
$$\sum_{n=1}^{\infty} \int_0^{2\pi} R_{\infty}^n (\alpha_n \cos n\theta + \beta_n \sin n\theta) \cos m\theta d\theta = 6 \frac{Fr^2}{Re} \int_0^{2\pi} \cos m\theta \ln R_{\infty} d\theta, \quad (4.5.8b)$$

$$\sum_{n=1}^{\infty} \int_0^{2\pi} R_{\infty}^n (\alpha_n \cos n\theta + \beta_n \sin n\theta) \sin m\theta d\theta = 6 \frac{Fr^2}{Re} \int_0^{2\pi} \sin m\theta \ln R_{\infty} d\theta, \quad (4.5.8c)$$

If N modes are considered, then there are $2N + 1$ unknown coefficients to evaluate. The linear algebraic system as well as the integrals are treated numerically using MATLAB.

We begin by considering the influence of the disk geometry on the shape, location and height of the hydraulic jump. Figures 4-4 illustrates the response for a silicon oil jet impinging on a triangular disk, under similar flow conditions as in the experiment of Duchesne *et al.* (2014); refer also to in figure 4-3. Figure 4-4a shows polar plots of the

jump radius $r_J(\theta)$, transition radius r_0 , disk radius $R_\infty(\theta)$ and its average radius $R_{\infty 0}$. Figures 4-4b and c show the dependence of $R_\infty(\theta)$, $r_J(\theta)$, $h_J(\theta)$ and $H_J(\theta)$ on the polar angle θ , and corresponding axisymmetric levels, including the averaged jump radius and heights. Generally, regardless of the disk geometry, we find little deviation of the jump from circular, except perhaps for the triangular disk where the jump shows some flattening along the sides of the disk, along with additional modulation, which is also reflected in the asymmetric pattern in figure 4-4a, but is particularly evident in figure 4-4c for the jump height. The axisymmetric radius $r_{J\text{axi}}$ is close to $r_{J\text{min}}$, and is not equal to $r_{J\text{mean}}$. A similar response is predicted for $h_{J\text{axi}}$. As to $H_{J\text{axi}}$, it remains sensibly higher than $H_J(\theta)$ (for any disk geometry). We also observe (not shown) that while the upstream height $h_J(\theta)$ depends sensibly on the disk geometry, the downstream height $H_J(\theta)$ seems uninfluenced. Finally, the relatively little influence of the non-circular disk geometry on the non-circularity of the jump is typical. However, the loss of axial symmetry is quite tangible throughout the subcritical flow region as we demonstrate next.



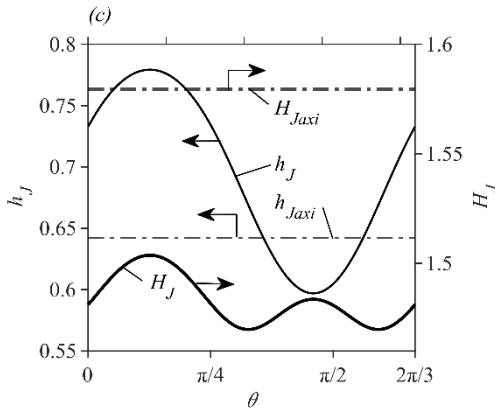
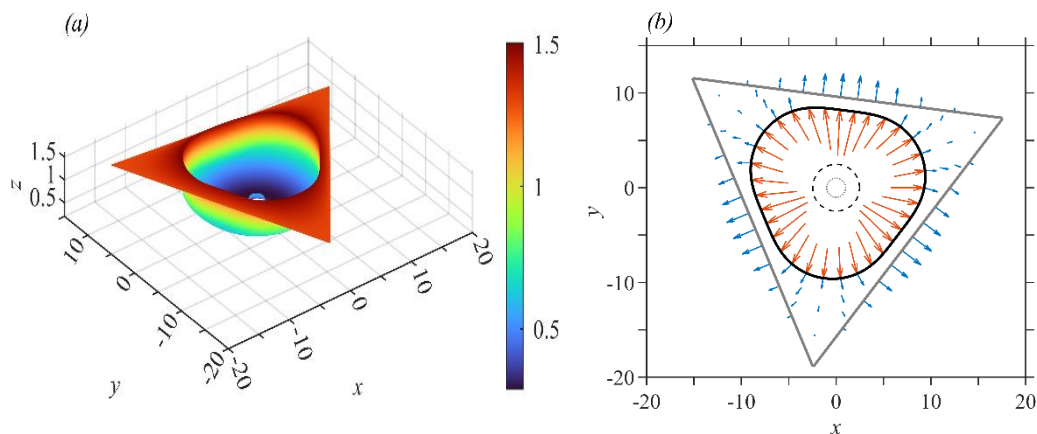


Figure 4-4: Hydraulic jump on a triangular disk. The figure shows (a) polar plots of the jump radius $r_J(\theta)$, transition radius r_0 , disk radius $R_\infty(\theta)$ and its average $R_{\infty 0}$. The dependence on the azimuthal angle is also shown for (b) $r_J(\theta)$ and $R_\infty(\theta)$, and (c) $h_J(\theta)$ and $H_J(\theta)$, with corresponding axisymmetric levels. The parameters used are $Re = 169$, $Fr = 16.88$, $Bo = 1.19$, $H_{\infty 0} = 1.3$ and $R_{\infty 0} = 12$.

Figure 4-5 depicts the flow details for the triangular disk. A 3D perspective of the film surface topography is shown in figure 4-5a. The location of the jump is fairly identifiable as it is surrounded by the brown region of the subcritical flow. A couple of surprising aspects typically found for any geometry are worth noting. The film thickness in the subcritical region is essentially independent of geometry. Another aspect is the weak azimuthal dependence of the height everywhere in the subcritical region, even for the current triangular disk. One would expect a non-axisymmetric distribution near the disk corners. However, the uniform distribution of the film height has been observed experimentally for non-circular jumps. Martens *et al.* (2012) measured the height profiles of the observed pentagonal hydraulic jump in ethylene glycol. They found that the height remains essentially the same at a distance downstream of the jump (see their figure 3). Closer to the jump they found that the height H_J is slightly larger downstream of the jump corner than the jump valley, corroborating the plots in figure 4-3.

More details of the flow field are shown in figures 4-5b to 4-5d where the radial and azimuthal velocity contours are reported, as well as the flow field. Although the jump shape is close to circular, figure 4-5b shows that the subcritical flow field is strongly non-

axisymmetric, and is, generally, significantly influenced by the disk geometry. The radial and azimuthal velocity components are of the same order of magnitude in subcritical region, particularly along the sides. The flow is strongest across the side and weakest through the corner where the fluid traverses the longest distance before reaching the disk edge, thus experiencing the dominant viscous resistance, weakening considerably at the corner. The azimuthal flow vanishes in the corner and mid-side directions due to symmetry. This is somewhat similar to the flow field at the surface of the spontaneous triangular jump of Martens *et al.* (2012), which is illustrated in their figure 4. In that case, the azimuthal flow is essentially confined behind the valley regions where the rollers are present, leaving the flow to expel radially between successive valley regions or corner. Figure 4-5c indicates that the strength of the radial flow is at least one order of magnitude higher upstream of the jump compared to the strength downstream. Figures 4-5c and 4-5d confirm that the subcritical radial and azimuthal flow strengths are of the same order of magnitude, which is surprising given the highly circular character of the jump. Given the relative uniformity of the supercritical film thickness and the constant thickness imposed along the edge, and as a result of mass conservation, the flow tends to remain radial across the mid side, and azimuthal between the corner and the mid side.



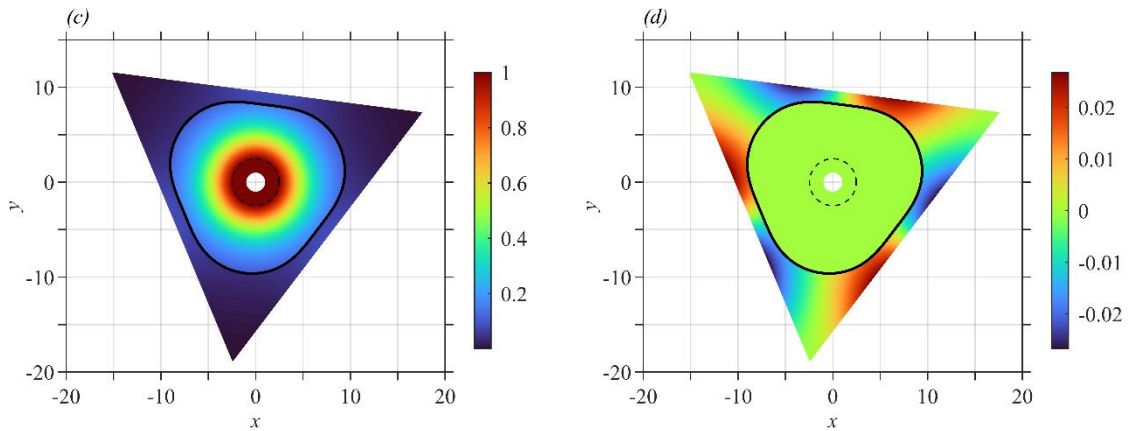


Figure 4-5: Surface film height (a), the flow field (b), the radial (c) and azimuthal (d) velocity contours at the surface for a jet on a triangular disk for $Re = 169$, $Fr = 16.88$, $Bo = 1.19$, $H_{\infty 0} = 1.3$, and $R_{\infty 0} = 12$.

We see here that the jump shape departs significantly from circularity when it is large relative to the disk (for instance, at large flow rate). The important question is then: what are the flow conditions most favourable to jump non-circularity? We address this question by next considering the parametric influence on the characteristics of the jump shape. In particular, we examine the effects of flow rate, surface tension and disk size (average radius) for triangular, square and pentagonal disks.

Figures 4-6, 4-7 and 4-8 illustrate the influence of the Froude number, Weber number and disk size on the shape and size of the jump. The dependence of both the maximum and minimum radii is shown. The circular jump radius, corresponding to a disk of radius $R_{\infty 0}$, is also included for reference. The influence of the flow rate in figure 4-6 is generated by changing the Froude and Reynolds number, keeping the Bond number fixed, thus making the influence of Fr equivalent to that of the flow rate. For small flow rate ($Fr < 10$), the jump is small and remains essentially circular as it is relatively unaffected by the disk geometry, for any pattern. At larger flow rate, the jump radius displays non-circularity as reflected by the widening between the minimum and maximum radii. This is particularly obvious for the triangular geometry. Interestingly, and in contrast to the case of spontaneous non-circular jumps, the axisymmetric radius is generally not equal to the average radius, for any geometry. The growth in the difference $\Delta r_J \equiv r_{J \max} - r_{J \min}$

depends strongly on the disk geometry and the Froude number as shown in the inset of figure 4-6. Although the growth for the triangular disk with respect to Fr is the most obvious, it is in fact the slowest. The general dependence is found to follow a power law, roughly like $\Delta r_J \approx 5p^{12} Fr^{(7+3p)/4}$ for any disk geometry, where we recall p is the number of sides.

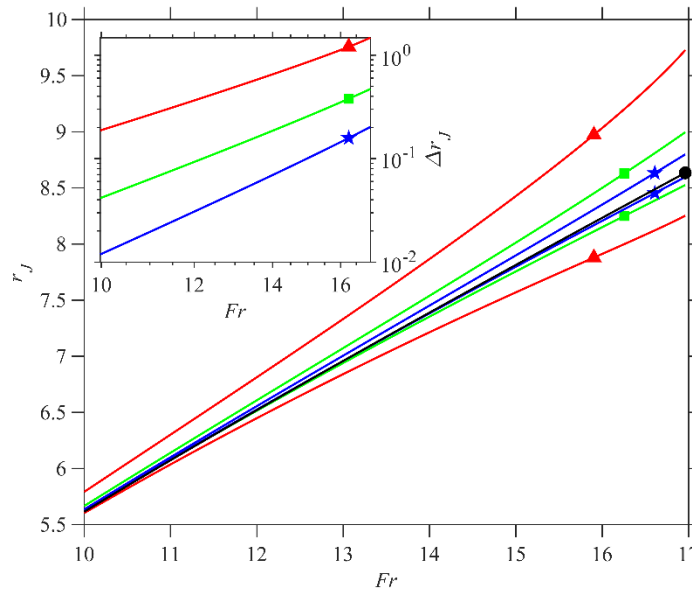


Figure 4-6: Influence of the flow rate (Froude number) on the maximum and minimum jump radii for a triangular disk (red curves), square disk (green curves), pentagonal disk (blue curves) and circular disk (black curve). The inset shows the influence of Fr on the difference between the maximum and minimum jump radii, Δr_J . Here, $Re = 100 - 170$, $Bo = 1.19$, $H_{\infty 0} = 1.14 - 1.3$ and $R_{\infty 0} = 12$.

The dependence on the Weber number (for fixed Re and Fr) in figure 4-7 indicates that surface tension tends to prohibit the growth of the jump, as in the axisymmetric case (Aristoff & Bush 2003). For liquids with low surface tension, the non-circularity of the jump becomes apparent as the difference between the maximum and minimum radius increases with We . The increase in the mean radius was also observed by Bush *et al.* (2006) in their experimental investigation of the stability of the circular jump, and is consistent with their earlier theoretical predictions for the influence of the curvature force (Bush & Aristoff 2003). This growth, however, is not indefinite; an asymptotic limit is reached at

infinite We as indicated by the horizontal asymptotes in the inset of figure 4-7. The predicted influence of surface tension is opposite to that reported by Bush *et al.* (2006) for glycerine-water mixture, who observed that, for a given Reynolds number, the circular jump tends to remain stable at high Weber number, as indicated in their figure 8a. Obviously, the mechanism of spontaneous non-circular jump formation is not the same as the one induced by disk geometry. They also found that the triangular jump is easiest to observe at relatively low surface tension. Our results also indicate that the non-circularity of the jump on a triangular disk is fastest growing with Weber number. The general dependence is found to follow roughly $\Delta r_J \approx \frac{1}{4} p^{-4} We - \frac{1}{10} p^{1/5}$, for the small to mid range of We , for any disk geometry. The lower inset in figure 4-7 shows the behaviour for large We , including the asymptotic levels.

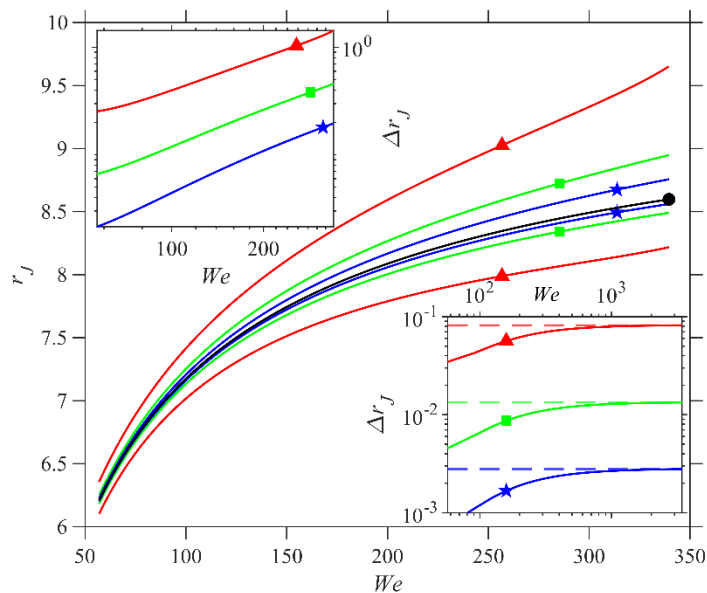


Figure 4-7: Influence of the surface tension (Weber number) on the maximum and minimum jump radii for a triangular disk (red curves), square disk (green curves), pentagonal disk (blue curves) and circular disk (black curve). Here, $Re = 169$, $Fr = 16.88$, $H_{\infty 0} = 2.41 - 1.3$ and $R_{\infty 0} = 12$. The lower inset shows the influence of We and asymptotes for large surface tension on the difference between the maximum and minimum jump radii, Δr_J ($H_{\infty 0} = 2.22 - 0.58$ and $R_{\infty 0} = 24$)

The influence of the disk size is reported in figure 4-8, where the jump minimum and maximum radii are plotted against $R_{\infty 0}$. One expects a jump on a larger disk to be more circular than on a smaller disk (considering all remaining parameters are the same). This response is indeed reflected in figure 4-8. Interestingly, the curves also show that $\Delta r_j \approx \frac{10}{3} p^9 R_{\infty 0}^{-p-1}$, suggesting that the jump on a higher-sided disk becomes circular more rapidly as the disk size increases.

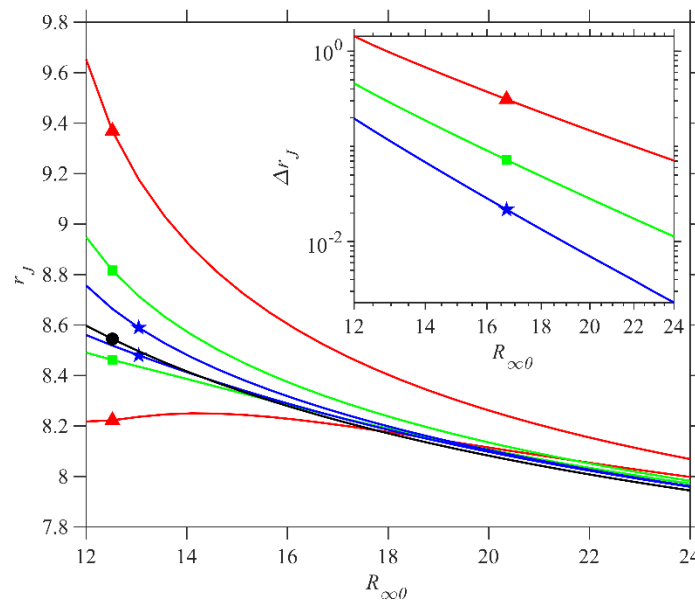


Figure 4-8: Influence of the non-circular disk size on the maximum and minimum jump radii for a triangular disk (red curves), square disk (green curves), pentagonal disk (blue curves) and circular disk (black curve). The inset shows the influence of $R_{\infty 0}$ on the difference between the maximum and minimum jump radii, Δr_j . Here, $Re = 169$, $Fr = 16.88$, $Bo = 1.19$, $H_{\infty 0} = 1.3 - 1.1$.

Finally, a general perspective of the character of the non-circular jump is shown in figure 4-9, illustrating the relation between the jump width Δr_j and the aspect ratio Λ/PH , Λ is the jump inner area, P is the perimeter and H is the downstream height (averaged in the azimuthal direction). Each set of data correspond to a given Froude number (or flow rate) for non-circular jumps corresponding to a disk geometry ranging from the triangular to the 13-sided planforms. We see that the jump width generally increases sharply with the aspect

ratio, particularly for multiple-sided disk planforms. For a given Froude number, the jump width remains independent of the aspect ratio for multi-sided disks ($p > 8$), displaying essentially the limit of a circular disk. Obviously, the limit $\Delta r_J \rightarrow 0$ corresponds to a circular jump with an aspect ratio that increases with flow rate. For $p > 8$, The jump width increases sensibly with the aspect, at a rate that increases with Fr. This behaviour roughly linear, of the form $\Delta r_J \approx \frac{2}{25} Fr^{3/2} \frac{\Lambda}{PH} - \frac{1}{40} Fr^{9/4}$. We note that the zero axisymmetric jump width is recovered in the limit of small Froude number.

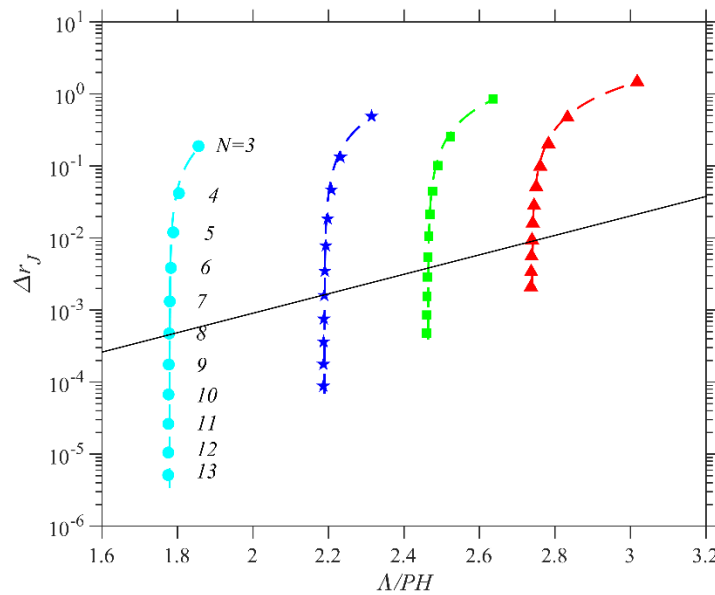


Figure 4-9: Dependence of the jump width Δr_J on the normalized jump area for various disk shapes (modes) with number of sides ranging from 3 to 13. Each set comprises symbols and fitting curve, corresponding to $Re = 170$, $Fr = 17$, $H_{\infty 0} = 1.30$ (red), $Re = 150$, $Fr = 15$, $H_{\infty 0} = 1.26$ (green), $Re = 130$, $Fr = 13$, $H_{\infty 0} = 1.22$ (blue) and $Re = 100$, $Fr = 10$, $H_{\infty 0} = 1.14$ (cyan), $Bo = 1.19$. Below the solid line the jump width is independent of the aspect ratio.

4.5.3 The non-circular jump on a circular disk, Imposed edge film thickness

For a circular disk, $R_{\infty} = R_{\infty 0}$ is constant. We therefore impose the edge thickness as $H(r = R_{\infty}, \theta) = H_{\infty}(\theta)$. In this case, the problem (4.4.14) formally becomes

$$\frac{\partial}{\partial r} \left(r \frac{\partial H^4}{\partial r} \right) + \frac{1}{r} \frac{\partial^2 H^4}{\partial \theta^2} = 0, \quad H(r = R_\infty, \theta) = H_\infty(\theta), \quad R_J(\theta) \leq r \leq R_\infty, \quad (4.5.9)$$

where the edge thickness is generally imposed as $H_\infty^4(\theta) = H_{\infty 0}^4 + AT(\theta)$, where $H_{\infty 0}$ is the constant edge thickness corresponding to axisymmetric flow, given in (4.5.2), A is a constant (amplitude) and $T(\theta)$ is the departure function of θ . We seek the solution of problem (4.5.9) as a combination of an axisymmetric component $H_0^4(r)$, satisfying $H_0(r = R_\infty) = H_{\infty 0}$, and a non-axisymmetric component:

$$H^4(r, \theta) = H_0^4(r) + \alpha_0 + \sum_{n=1}^{\infty} \frac{r^n}{R_\infty^n} (\alpha_n \cos n\theta + \beta_n \sin n\theta), \quad (4.5.10)$$

which satisfies (4.4.15). Here takes the same form as (4.5.1b):

$$H_0^4(r) = H_{\infty 0}^4 + 6 \frac{Fr^2}{Re} \ln \left(\frac{R_\infty}{r} \right). \text{ Applying (4.5.10) at the disk edge, we have}$$

$$H_\infty^4(\theta) = H_{\infty 0}^4 + \alpha_0 + \sum_{n=1}^{\infty} (\alpha_n \cos n\theta + \beta_n \sin n\theta) = H_{\infty 0}^4 + AT(\theta). \quad (4.5.11)$$

Consequently, the expansion coefficients are readily determined through

$$\alpha_0 = \frac{A}{2\pi} \int_0^{2\pi} T(\theta) d\theta, \quad \alpha_n = \frac{A}{\pi} \int_0^{2\pi} T(\theta) \cos n\theta d\theta, \quad \beta_n = \frac{A}{\pi} \int_0^{2\pi} T(\theta) \sin n\theta d\theta. \quad (4.5.12a-c)$$

Unlike the case of a non-circular disk, where the coefficients are obtained as a numerical solution of the algebraic system (4.5.8), involving numerically evaluated integrals, the coefficients in (4.5.12) are straightforward to evaluate analytically or numerically, depending on $T(\theta)$. The film thickness and its derivatives are then evaluated at the jump radius from (4.5.10), and substituted in equations (4.4.12), which are solved numerically to determine the jump radius and height.

We saw, in the case of a non-circular disk, the peaks and the valley of the jump are in phase with the maximum and minimum of the imposed edge radius, with the same wavenumber (see figure 4-4). This is not always the case for a variable edge thickness. As an illustration, consider the influence of the edge film thickness on the shape of the jump and flow field for the simplest wave form of $H_\infty(\theta)$, corresponding to $T(\theta) = \sin \theta$. Figure 4-10 depicts the response for different disk sizes, corresponding to $4 \leq R_\infty \leq 7$. All other parameters remain fixed to $Re = 322$, $Fr = 3.3$, $Bo = 6$ and wave amplitude $A = 0.6$. The H_∞ profiles in figure 4-10a show that the edge thickness decreases as the disk radius increases as a result of the $R_\infty^{-2/3}$ behaviour of the dynamic contribution in (4.5.2) for $H_{\infty 0}$. For the largest disk size considered ($R_\infty = 7$), figures 4-10b and 4-10c suggest that the jump shape is triangular, although the shape appears to be circular. When the disk size is mildly decreased ($R_\infty = 6$), the jump begins to exhibit an overall triangular shape with smooth corners and displays a concavity at the valley. For an even smaller disk size ($R_\infty = 5$), the jump acquires well defined six sides with emerging new peaks and valleys, well visible for the lowest disk size considered ($R_\infty = 4$). We have added the transition $r = r_0$ for reference, which indicates that the jump occurs in the fully-viscous region for $R_\infty = 5-7$ and inside the developing boundary-layer region for $R_\infty = 4$. We observe that little variation in the edge thickness causes a relatively large loss of circularity in the jump. Next, we present the flow details for a large and a small disk radius.

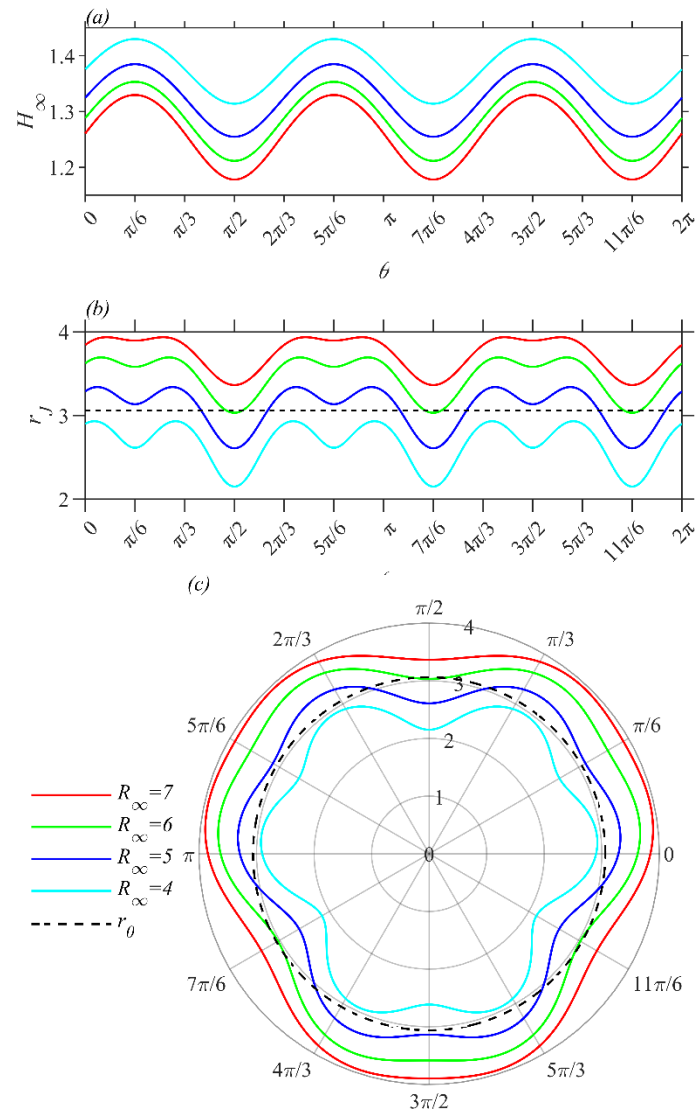
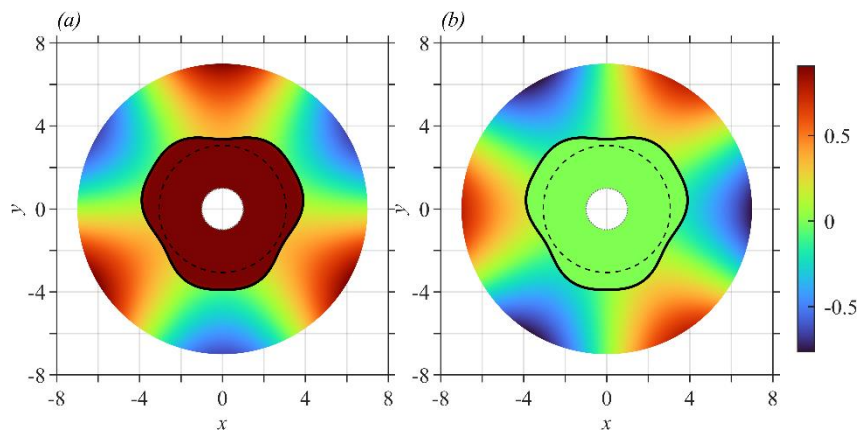


Figure 4-10: Influence of the circular disk size ($4 \leq R_\infty \leq 7$) on a non-circular hydraulic jump induced by edge thickness azimuthal variation $H_\infty(\theta)$ shown in (a). The jump radius $r_J(\theta)$ is shown in (b). Corresponding polar plots of the jump radius $r_J(\theta)$ and transition radius r_0 are shown in (c). Here, $Re = 322$, $Fr = 3.3$, $Bo = 6$, $H_{\infty 0} = 1.26, 1.29, 1.32, 1.38$ and $A = 0.6$.

The flow details for a relatively large disk size are shown in figure 4-11, for $R_\infty = 7$. Although the supercritical flow strength remains unaffected by the loss of axial symmetry just upstream of the jump, the subcritical flow diminishes in strength overall as shown in

figure 4-11a to 4-11c. Both the subcritical radial and azimuthal velocity components remain of the same order-of-magnitude. In this case, the jump occurs downstream of the transition point (dashed circle). The supercritical thickness decreases monotonically with distance (figure 4-11d), resulting in a thickness larger at a valley than a corner. This behaviour is reminiscent of the measured profiles of Martens *et al.* (2012); see their figure 4. In this case, the film is not allowed to thicken before reaching the jump as in the axisymmetric case. The jump height is approximately the same just downstream of a peak and a valley, but behave oppositely further downstream. The increase in film thickness explains the radial flow reversal shown in figure 4-11c. It is important to mention that the flow fields in the present type I jump and type II jump (Marten *et al.* 2012) are different despite the similarity in the triangular jump shape. The flow reversal in the r - z plane is not predicted in the present formulation.



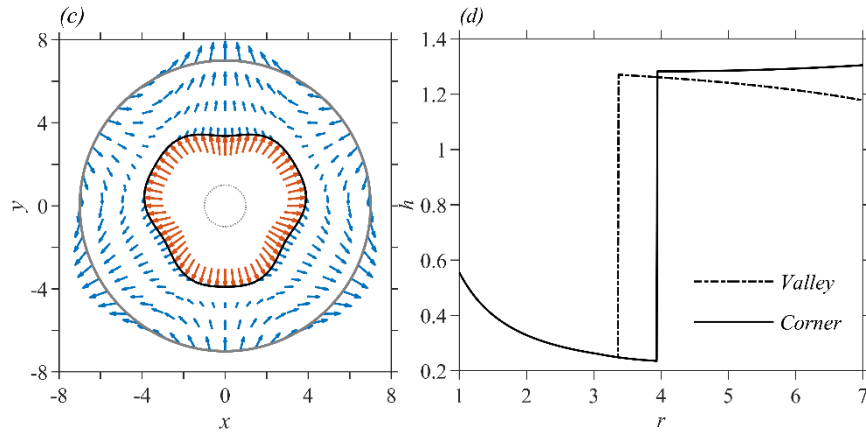


Figure 4-11: Details of the flow for $R_\infty = 7$: radial (a) and azimuthal (b) velocity contours at the film surface, (c) flow field and (d) film thickness profiles in the corner and valley directions. Here, $Re = 322$, $Fr = 3.3$, $Bo = 6.$, $H_{\infty 0} = 1.26$ and $A = 0.6$.

Finally, additional details on the jump shape and flow field are shown in figures 4-12 for a smaller disk, of radius $R_\infty = 4$. A three-dimensional perspective of the flow geometry is given in figure 4-12a. In particular, we see that the film height is essentially uniform downstream of the jump, confirming that a small imposed azimuthal change in the film thickness at the disk edge yields a significant azimuthal variation in the shape of the jump and the subcritical flow field. The surface shape is reminiscent of the clover-shaped hydraulic jump visualized by Bush *et al.* (2006). Although the predicted jump is of type I and the visualized jump is of two-tiered type IIb, the two shapes present some similarity. They both exhibit the same number of corners, primary and secondary valleys. The projections of the radial (figure 4-12c) and azimuthal (figure 4-12d) velocity contours indicate that the azimuthal flow is of the same strength as the radial flow for a disk of small size ($R_\infty = 4$). More importantly, the radial flow appears to reverse direction across from the secondary valley (figure 4-12b), becoming weaker with increasing size, eventually vanishing altogether. We have not observed this flow for the non-circular disk, regardless how sharp the disk corners are. Obviously, a negative radial velocity emerges wherever the film thickness increases with radial distance: $H_r > 0$ in (4.4.12a).

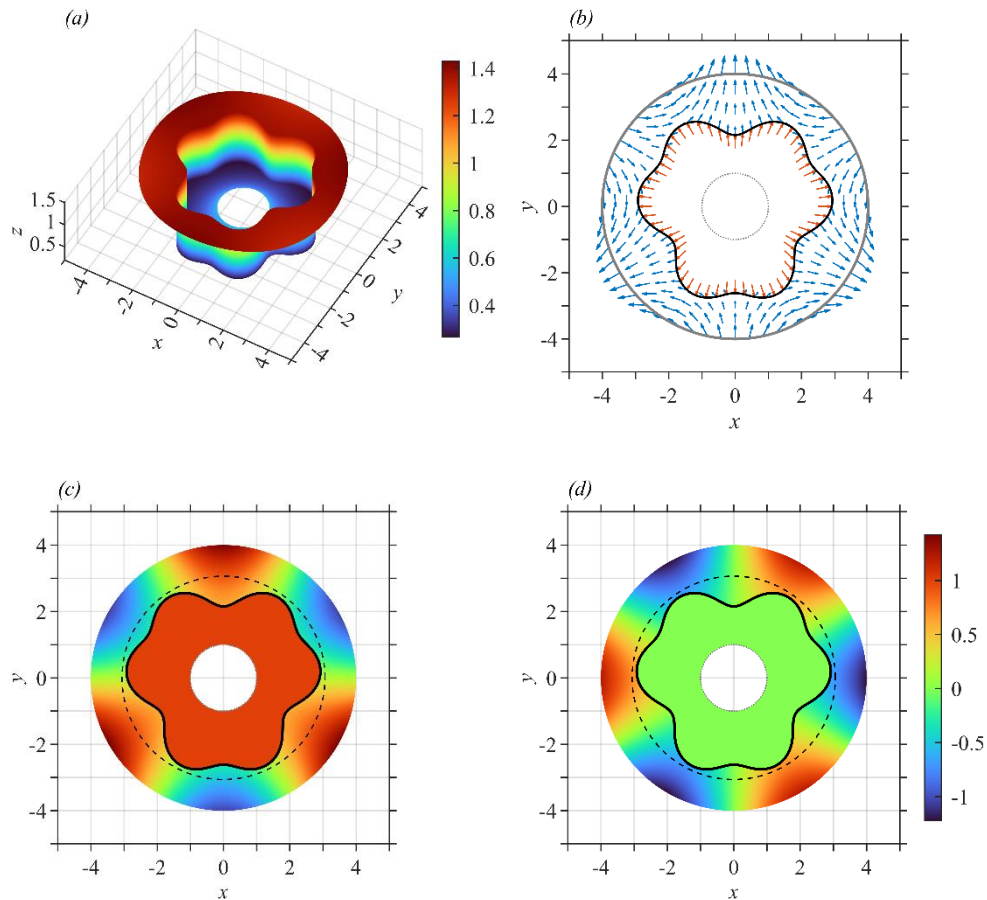


Figure 4-12: Details of the flow for $R_\infty = 4$: (a) film surface topography, (b) flow field, (c) radial and (d) azimuthal velocity contours at the film surface. Here, $Re = 322$, $Fr = 3.3$, $Bo = 6$, $H_{\infty 0} = 1.38$ and $A = 0.6$.

4.6 Concluding remarks and discussion

In this study, we examine theoretically the influence of the azimuthally varying conditions at the edge of the target disk on the shape and height of the resulting non-circular jump and flow field. Two types of edge conditions are considered: the non-circular edge and periodic edge thickness. Our aim is not to model or simulate the spontaneous non-circular jumps observed in the literature, typically resulting from the destabilization of the circular jump. Our aim, given the nonlinearity of the problem, is to establish the intricate relation between periodic edge conditions and the non-circular jump.

We show that the supercritical flow remains axisymmetric for a thin film, regardless of the subcritical flow, given the relatively high strength of the impacting jet. We thus confirm the observations and measurements upstream of the non-circular jump reported in the literature. The loss of axial symmetry occurs at the jump level, where the balance of momentum across the jump is established in both the radial and azimuthal directions. We account for surface tension effect across the jump by extending the axisymmetric formulation of Bush & Aristoff (2003) for a non-circular jump. The subcritical flow is assumed to be of the lubrication type, and the subcritical film thickness distribution is shown to obey the Laplace's equation in the polar plane.

Since the flow is entirely controllable, we show how the flow parameters can be varied systematically to study their influence on the jump shape. It is important to mention that the present approach is based on well-established assumptions and methodology for axisymmetric flow, and extended here to cover non-axisymmetric flow. The present study illustrates how the axial symmetry of the type I jump can be broken by the edge conditions, which has not been treated so far since the usually observed spontaneous jumps are of the type II. Finally, varying edge conditions and flow parameters should also enable future experiments to be conducted in a controlled and methodological manner.

For a non-circular disk and constant film thickness at the edge, we find that the disk geometry has little influence on the shape of the jump, except if the jump occurs close to the disk edge as it departs from the circular form (figure 4-4). However, the subcritical flow field is highly non-axisymmetric even for an apparently circular jump (figure 4-5). The mean radius and height of the jump do not usually correspond to the axisymmetric jump on a circular disk of equivalent radius (figure 4-4). This is particularly the case as the wavenumber (number of sides) of the disk increases (hexagonal as opposed to triangular). Surface tension is shown to prohibit flow asymmetry and jump non-circularity (figure 4-7), a behaviour opposite to the case of the spontaneous non-circular jump (Bush *et al.* 2006). It is important to observe that the mechanisms behind the loss of axial symmetry are not the same in the two cases. For a jet impinging on a circular disk with an azimuthally periodic film thickness at the edge, we find that a small azimuthal variation in the film thickness leads to a significant loss of axial symmetry. The nonlinearities in the balance

equations across the jump cause an increase in the peaks and valleys as the disk radius decreases. This is illustrated in figure 4-12 for an imposed sinusoidal thickness, yielding a jump similar to the three-leaf clover jump reminiscent of the spontaneous non-circular jump observed by Bush *et al.* (2006).

Finally, we emphasize that the aim of the present study is to demonstrate how various jump patterns can be generated by varying edge conditions in a controlled and systematic manner, which can easily be realized in practice. Although some apparent features may be reminiscent of the spontaneous jumps observed in the literature, the current formulation cannot predict the structure of such jumps, which are usually of type II, exhibiting a single step (type IIa) or a double step (type IIb), always accompanied by a vortex roller downstream of the jump. Unlike the flow reversal in the polar plane reported in figures 4-11 and 4-12, the flow reversal in a type II jump occurs in a circular reservoir, under the vortex (in the r - z plane). The liquid spreads radially downstream of the vortex (Martens *et al.* 2012), also in contrast with the present predictions.

We envisage, in the future, to extend the current formulation to capture the vortex flow in the vertical plane, induced by edge variation. The challenges will undoubtedly be daunting. One of the major obstacles is relaxing the assumption of the discontinuous (shock-like) jump, and replacing it by a continuous radial variation of the film height. Although this has been done for a circular jump (Watanabe *et al.* 2013), the practical implementation of a similar formulation for a non-circular jump is far from obvious. The presence of higher-order derivatives of the film thickness in the radial direction requires additional boundary conditions, which are typically imposed from experiment near impingement and at the circular disk edge. Consequently, some kind of a shooting method is needed, which is straightforward for axisymmetric flow, but inenvisageable for azimuthally varying flow due to the coupling between the radial and azimuthal flow components. In an effort to make the problem manageable, Rojas *et al.* (2015) simply neglected the azimuthal velocity component, an assumption which may hold for a non-circular jump that is mildly non-circular. The flow fields in figures 4-11 and 4-12 indicate that the radial and azimuthal velocity components are of the same strength, even for the milder triangular jump in figure 4-11. Another potential difficulty in employing the fully coupled thin-film equations with

inertia is the resulting nonlinear equation for the film thickness in the subcritical region, which must be solved numerically in the $r-\theta$ plane. In contrast, the present Laplace's equation (4.4.15a) admits a (Fourier) series solution, fully compliant with the imposed periodic conditions at the edge.

4.7 References

ABDELAZIZ, A. & KHAYAT, R. E. 2022 On the non-circular hydraulic jump for an impinging inclined jet. *Phys. Fluids* **34**, 023603.

ACHESON, D. J. 2005 *Elementary Fluid Dynamics* (Oxford University Press).

ANDERSEN, A., BOHR, T. & SCHNIPPER, T. 2010 Separation vortices and pattern formation. *Theor. Comput. Fluid Dyn.* **24**, 329–334.

ASKARIZADEH, H., AHMADIKIA, H., EHRENPREIS, C., KNEER, R., PISHEVAR, A. & ROHLFS, W. 2019 Role of gravity and capillary waves in the origin of circular hydraulic jumps. *Phys. Rev. Fluids* **4**, 114002.

ASKARIZADEH, H., AHMADIKIA, H., EHRENPREIS, C., KNEER, R., PISHEVAR, A. & ROHLFS, W. 2020 Heat transfer in the hydraulic jump region of circular free-surface liquid jets. *Intl J. Heat Mass Transfer* **146**, 118823.

AVEDISIAN, C. T. & ZHAO, Z. 2000 The circular hydraulic jump in low gravity. *Proc. R. Soc. Lond. A* **456**, 2127–2151.

BAONGA, J. B., GUALOUS, H. L. & IMBERT, M. 2006 Experimental study of hydrodynamic and heat transfer of free liquid jet impinging a flat circular heated disk. *Appl. Therm. Engng.* **26**, 1125–1138.

BENILOV, E. S. 2015 Hydraulic jumps in a shallow flow down a slightly inclined substrate. *J. Fluid Mech.* **782**, 5–24.

BOHR, T., DIMON, P. & PUTKARADZE, V. 1993 Shallow-water approach to the circular hydraulic jump. *J. Fluid Mech.* **254**, 635–648.

- BOHR, T., ELLEGAARD, C., HANSEN, A. E. & HAANING, A. 1996 Hydraulic jumps, flow separation and wave breaking: An experimental study. *Physica B* **228**, 1–10.
- CRAIK, A., LATHAM, R., FAWKES, M. & GIBBON, P. 1981 The circular hydraulic jump. *J. Fluid Mech.* **112**, 347–362.
- DHAR, M., DAS, G. & DAS, P. K. 2020 Planar hydraulic jumps in thin film flow. *J. Fluid Mech.* **884**, A11.
- DRESSAIRE, E., COURBIN, L., CREST, J. & STONE, H. A. 2010 Inertia dominated thin-film flows over microdecorated surfaces. *Phys. Fluids* **22**, 073602.
- DUCHESNE, A., LEBON, L. & LIMAT, L. 2014 Constant Froude number in a circular hydraulic jump and its implication on the jump radius selection. *Europhys. Lett.* **107**, 54002.
- ELLEGAARD, C., HANSEN, A. E., HAANING, A., HANSEN, K., MARCUSSEN, A., BOHR, T., HANSEN, J. L. & WATANABE, S. 1998 Creating corners in kitchen sinks. *Nature* **392**, 767–768.
- FERREIRA, V. G., TOMÉ, M. F., MANGIAVACCHI, N., CASTELO, A., CUMINATO, J. A., FORTUNA, A. O. & MCKEE, S. 2002 High-order upwinding and the hydraulic jump. *Int. J. Numer. Meth. Fluids* **39**, 549–583.
- FERNANDEZ-FERIA, R., SANMIGUEL-ROJAS, E. & BENILOV, E. S. 2019 On the origin and structure of a stationary circular hydraulic jump. *Phys. Fluids* **31**, 072104.
- IPATOVA, A., SMIRNOV, K.V. & MOGILEVSKIY, E.I. 2021. Steady circular hydraulic jump on a rotating disk. *J. Fluid Mech.* **927**, A24.
- JANNES, G., PIQUET, R., MAISSA, P., MATHIS, C. & ROUSSEAU, G. 2011 Experimental demonstration of the supersonic-subsonic bifurcation in the circular jump: A hydrodynamic white hole. *Phys. Rev. E* **83**, 056312.

- KASIMOV, A. R. 2008 A stationary circular hydraulic jump, the limits of its existence and its gasdynamic analogue. *J. Fluid Mech.* **601**, 189–198.
- LIU, X., GABOUR, L. A. & LIENHARD, J. H. 1993 Stagnation-point heat transfer during impingement of laminar liquid jets: analysis including surface tension. *Trans. ASME J. Heat Transfer* **115**, 99–105.
- LIU, X. & LIENHARD, J. H. 1993 The hydraulic jump in circular jet impingement and in other thin liquid films. *Exp. Fluids* **15**, 108–116.
- MARTENS, E. A., WATANABE, S. & BOHR, T. 2012 Model for polygonal hydraulic jumps. *Phys. Rev. E* **85**, 036316.
- MOHAJER, B. & LI, R. 2015 Circular hydraulic jump on finite surfaces with capillary limit. *Phys. Fluids* **27**, 117102
- OZAR, B., CETEGEN, B. M. & FAGHRI, A. 2003 Experiments on the flow of a thin liquid film over a horizontal stationary and rotating disk surface. *Exp. Fluids* **34**, 556–565.
- PRINCE, J. F., MAYNES, D. & CROCKETT, J. 2012 Analysis of laminar jet impingement and hydraulic jump on a horizontal surface with slip. *Phys. Fluids* **24**, 102103.
- ROJAS, N., ARGENTINA, M. & TIRAPEGUI, E. 2010 Inertial lubrication theory. *Phys. Rev. Letts.* **25**, 042105.
- ROJAS, N., ARGENTINA, M. & TIRAPEGUI, E. 2013 A progressive correction to the circular hydraulic jump scaling. *Phys. Fluids* **104**, 187801.
- ROJAS, N. & TIRAPEGUI, E. 2015 Harmonic solutions for polygonal hydraulic jumps in thin fluid films. *J. Fluid Mech.* **780**, 99–119.
- SCHLICHTING, H. & GERSTEN, K. 2000 *Boundary-Layer Theory*. 8th edn. Springer.
- WANG, Y. & KHAYAT, R. E. 2018 Impinging jet flow and hydraulic jump on a rotating disk. *J. Fluid Mech.* **839**, 525–560.

WANG, Y. & KHAYAT, R. E. 2019 The role of gravity in the prediction of the circular hydraulic jump radius for high-viscosity liquids. *J. Fluid Mech.* **862**, 128–161.

WATANABE, S., PUTKARADZE, V. & BOHR, T. 2003 Integral methods for shallow free-surface flows with separation. *J. Fluid Mech.* **480**, 233–265.

WATANABE, S. 2013 A constrained variational model for radial symmetry breaking. *Math. J. Ibaraki Univ.* **45**, 15–31.

WATSON, E. J. 1964 The radial spread of a liquid jet over a horizontal plane. *J. Fluid Mech.* **20**, 481–499.

ZHAO, J. & KHAYAT, R. E. 2008 Spread of a non-Newtonian liquid jet over a horizontal plate. *J. Fluid Mech.* **613**, 411–443.

Chapter 5

5 The viscoplastic circular hydraulic jump⁴

Nomenclature

a	Radius of jet, m
B	Bingham number, $B = \tau_0 a / \rho \nu W$
Bo	Bond number, $Bo = Ca Re / Fr^2$
Ca	Capillary number, $Ca = \rho \nu W / \sigma$
Fr	Froude number, $Fr = W / \sqrt{ga}$
Fr_{j-}	Froude number immediately upstream of the jump
Fr_{j+}	Froude number immediately downstream of the jump
g	Acceleration due to gravity, m/s^2
h	Dimensionless film thickness in the supercritical region
h_0	Dimensionless fully-yielded layer thickness in the supercritical region
h_{01}	First-order departure for the dimensionless fully-yielded layer thickness
h_{0min}	Dimensionless fully-yielded layer thickness at $r = r_{0min}$
h_{0max1}	Dimensionless fully-yielded layer thickness at $r = r_{0max1}$

⁴ A version of this chapter has been published as -

h_{0max2}	Dimensionless fully-yielded layer thickness at $r = r_{0max2}$
h_1	First-order departure for the dimensionless film thickness
h_{cJ}	Critical film height at the jump
H	Dimensionless film thickness in the subcritical region
H_0	Dimensionless fully-yielded layer thickness in the subcritical region
H_N	Dimensionless film thickness for a Newtonian fluid
h_J	Dimensionless film thickness immediately upstream of the jump
h_{0J}	Dimensionless fully-yielded layer thickness right upstream of the jump
H_J	Dimensionless film thickness immediately downstream of the jump
H_{0J}	Dimensionless fully-yielded layer thickness right downstream of the jump
H_∞	Dimensionless film thickness at the disk edge
$H_{0\infty}$	Dimensionless fully-yielded layer thickness at the disk edge
K	Consistency index, $Pa \cdot s^n$
L_J	Dimensionless jump length, $L_J = r_{J+} - r_{J-}$
n	Power-law index
p	Dimensionless pressure
Q	Volume flow rate, m^3/s
r	Dimensionless radial coordinate
r_0	Dimensionless transition point of the hydrodynamic boundary layer

r_{min}	Dimensionless radial location for the local minimum h_0
r_{0max1}	Dimensionless radial location for the first local maximum h_0
r_{0max2}	Dimensionless radial location for the second local maximum h_0
R_∞	Dimensional disk radius
r_J	Dimensionless jump radius
r_{J-}	Dimensionless radial location immediately upstream of the jump
r_{J+}	Dimensionless radial location immediately downstream of the jump
Re	Reynolds number, $Re = Wa/\nu$
u	Dimensionless horizontal velocity in the fully-yielded layer
U	Dimensionless velocity in the pseudo-plug layer
U_{J-}	Dimensionless pseudo-plug layer velocity at $r = r_{J-}$
U_{J+}	Dimensionless pseudo-plug layer velocity at $r = r_{J+}$
U_N	Dimensionless free surface velocity for a Newtonian fluid
$\langle u_{J-} \rangle$	Dimensionless depth average velocity at $r = r_{J-}$
$\langle u_{J+} \rangle$	Dimensionless depth average velocity at $r = r_{J+}$
w	Dimensionless vertical velocity
W	Average jet velocity, $W = Q/\pi a^2$, m/s
z	Dimensionless vertical coordinate

Greek Symbols

χ_1, χ_2, χ_3	Integrals
$\dot{\gamma}$	The second invariant of $\dot{\gamma}_{ij}$, s^{-1}
$\dot{\gamma}_{ij}$	The rate-of-stress tensor, s^{-1}
δ	Dimensionless boundary layer thickness for a Newtonian fluid
ε	Dimensionless perturbation parameter
η	Scaled vertical coordinate, $\eta = z/h_0$
θ	Azimuthal coordinate
ν	Effective kinematic viscosity $\nu = K\rho^{-1}(W/a)^{n-1}$, m^2/s
ρ	Density of fluid, kg/m^3
σ	Surface tension of fluid, N/m
τ_0	The yield stress, Pa
τ_w	Dimensionless wall shear stress
τ	The second invariant of τ_{ij}
τ_{ij}	The excess stress tensor

5.1 Introduction

The thin-film flow over a solid is significant in numerous industrial applications, such as cleaning, cooling, coating, and etching (Hsu *et al.* 2011; Walker *et al.* 2012; Reay 2013; Barnes 1999; Kaneko *et al.* 2007). In reality, many fluids of industrial significance are non-Newtonian, exhibiting flow properties intermediate between those of a solid and a liquid. A threshold stress, known as yield stress, is required for the fluid to flow. For an applied stress below the yield stress, the fluid exhibits ideal rigid solid behaviour, and does not deform. However, as the applied stress exceeds this threshold value, the fluid exhibits a viscous character (Bird *et al.* 1983). This important class of fluids, referred to as viscoplastic fluids, encompasses a wide range of materials including concentrated suspensions, pastes, emulsions, foams, composites, grease, polymer solutions, paints, glues and coal-oil slurries (Bird *et al.* 1983; Utracki 1988; Nguyen & Boger 1992; Ancy 2007; de Souza Mendes 2009; Mullai Venthan *et al.* 2022). For an overview of viscoplastic flow modelling, stability analysis, thin-film and lubrication flows, constitutive models, and applications, we refer the reader to the review by Balmforth *et al.* (2014). The rheology of the fluid can significantly change the behaviour of related flow phenomena. Both the yield stress and the shear-rate dependence of the viscosity can change the spread distance, film height, surface velocity of the film and other flow behaviour for the spread of a viscoplastic fluid (Jiang & Leblond 1993; Huang & García 1998; Balmforth *et al.* 2000; Liu *et al.* 2016, 2018, 2019; Jalaal *et al.* 2021). Given the significant impact of the fluid rheology on the flow, we examine the spread of a viscoplastic jet and the structure of the emerging hydraulic jump as the jet impinges on a circular disk. We anticipate that a viscoplastic jet exhibits fundamentally different features not observed for a Newtonian jet.

More explicitly, a viscoplastic flow exhibits a yield surface under and above which are the fully-yielded (shear layer) and plug layers, respectively. However, the plug flow (a region with no velocity gradients and infinite viscosity) is generally not a true plug, but a pseudo-plug flow (a region of predominantly elongational character), as earlier identified in a bounded annular flow by Walton & Bittleston (1991), and the yield surface has been referred to as a fake yield surface (Balmforth & Craster 1999; Liu *et al.* 2019). As the pseudo-plug layer exists for any film flow, that raises the question as to its shape and

thickness in the supercritical and subcritical regions of an impinging jet, and, particularly across the jump. More precisely, a jump in the film surface is expected to occur as in a Newtonian fluid. In this case, what is the profile of the (fake) yield surface, a jump or a drop? Another crucial issue that we shall scrutinize is the nature of the transition from the developing boundary layer (near impingement) to the fully-viscous layer (the thin-film region where the viscous stress become appreciable right up to the free surface), which has been extensively investigated for a Newtonian fluid (refer to the earlier work of Watson 1964, the more recent studies of Wang & Khayat 2018/2019 and the references therein). In other words, what happens to the transition when the Newtonian boundary layer is replaced by the viscoplastic fully-yielded layer?

The mobility of the viscoplastic fluid can be significantly reduced when the yield stress is large. In their numerical simulation of wave generation due to underwater plastic mudslide flow, Jiang & Leblond (1993) reported that the velocity of the pseudo-plug layer decreases with increasing yield stress, and the front velocity is smaller for a higher yield stress as well. A similar behaviour for the phase velocity of the stationary wave front was later predicted by Mei & Yuhi (2001) when they examined a Bingham fluid down a shallow channel of finite width. In fact, the flow of a viscoplastic fluid comes to a halt when the stress falls below the yield stress, as in the spread of flow down an inclined plane (Jiang & Leblond 1993; Huang & García 1998; Balmforth *et al.* 2002; Balmforth *et al.* 2007a) and on a shallow and wide curved channel (Mei & Yuhi 2001), the spread of a droplet on a prewetted horizontal plate (Jalaal *et al.* 2021), the flow inception following the release of a volume of fluid or dam-break flow (Matson & Hogg 2007; Liu *et al.* 2016, 2018), and the squeezing of a thin film (Koblitz, Lovett & Nikiforakis 2018; Muravleva 2019).

We expect the shear-rate dependence of the viscosity to influence the spreading distance and film depth as well, affecting, in turn, the location and height of the jump. The influence of the power-law rheology can be less consistent than that of the yield stress. In their study of mud flow down a slope, Huang & García (1998) found that a more shear-thinning fluid has a shorter spread distance and a thicker flow depth away from the wave front. They also observed that the influence of shear thinning on the spreading distance diminishes as the yield stress rises. Balmforth *et al.* (2000) also reported the influence of the power-law

viscosity and yield stress on the shape of a lava dome at a certain time, which is consistent with the finding of Huang & García (1998). In contrast, Liu *et al.* (2018) reported that the power-law viscosity has little effect on the final shape of the slump. Interestingly, the influence of the power-law index may not be consistent from one region to another of the flow. For instance, for squeeze film flow between two disks, the calculations of Muravleva (2019) show that, in the core region of the flow, the fully-yielded layer thickness as well as the second stress invariant at the disks decrease with increasing power-law index. The opposite is true near the edge of the disks. The influence of the power-law rheology was found to depend significantly on the level of yield stress. We shall explore the interplay between the effect of yield stress and the effects of shear-thinning. We note that, although most viscoplastic fluids exhibit a shear-thinning character, some do possess a shear-thickening viscosity, such as concentrated diblock copolymer solutions (Bauer *et al.* 1995) and cement mixtures (Heirman *et al.* 2008/2009; Yahia 2011; Estelle & Lanos 2012).

The spread of an impinging Newtonian jet and the emergence of a hydraulic jump over a smooth solid surface has been examined extensively. Given the close relevance to the methodology and analysis employed in this study, it is helpful to briefly review the Newtonian literature. Early predictions for the planar jump based on inviscid theory were reported by Rayleigh (1914), but did not yield a good agreement with the experiment. Although Tani (1949) later considered viscous effects, the dominant influence of viscosity was addressed much later. Watson (1964) analysed the flow in the developing-boundary layer near impingement, and the fully-viscous layer upstream of the jump. Watson's thin-film approach became the basis for numerous later theoretical and experimental studies. Watson's theory was tested in a number of experimental investigations, including those of Watson himself, Craik *et al.* (1981), Stevens & Webb (1992), Bush & Aristoff (2003) and Baonga *et al.* (2006). Liu & Lienhard (1993) observed that Watson's predictions were least satisfactory in the limit of a relatively weak jump (of large width). Watson neglected surface tension effects, which were later included by Bush & Aristoff (2003) for a small circular jump radius, leading to better agreement with the experiment. To capture the behaviour downstream of the jump, Duchesne *et al.* (2014) examined the downstream flow using the lubrication approach. A good agreement between their theoretical predictions for the height profile and their measurements was obtained. Some extensions have been

considered, such as the spread of an impinging power-law jet by Zhao & Khayat (2008), the formation of a hydraulic jump on an inclined plane by Kate *et al.* (2007) and Benilov (2015), and impingement on a rotating disk by Ozar *et al.* (2003), Wang & Khayat (2018) and Ipatova *et al.* (2021). The influence of slip was examined by Dressaire *et al.* (2010), Prince *et al.* (2012) and Khayat (2016). The influence of gravity on the jump radius was studied by Avedisian & Zhao (2000) and Wang & Khayat (2019). Finally, it is worth mentioning that the role of surface tension has generated recent debate since the controversial claims of Bhagat *et al.* (2018) and Bhagat & Linden (2020) that surface tension is at the origin of the circular jump. The claims were later challenged (Duchesne *et al.* 2019; Wang & Khayat 2021 Duchesne & Limat 2022) given the overwhelming evidence in early and recent studies of the importance of gravity in jet impingement and hydraulic jump formation (see also the recent account of Yamamura *et al.* 2022).

Here we examine the spread of an impinging jet and the hydraulic jump of a viscoplastic liquid, as there are very few investigations of this flow problem. Despite the significant progress in understanding the general free surface flows of yield fluids, studies dealing with the characteristics of the hydraulic jump or the transition from the supercritical to the subcritical regimes are relatively scarce. Notable exceptions are the papers by Ogihara & Miyazawa (1994), Shu & Zhou (2006), Zhou *et al.* (2007) and Ugarelli & Federico (2007), for yield stress flow in a rectangular channel. Experiments were conducted by Ogihara & Miyazawa (1994) on a hydraulic jump in a Bingham fluid using a mixture of water and bentonite. They observed that the critical depth increased dramatically when the relative yield stress exceeds 0.1. Shu & Zhou (2006) and Zhou *et al.* (2007) examined the planar hydraulic jump on a horizontal plate for a Bingham fluid (the two studies are essentially the same). They derive an approximate expression for the conjugate depths. However, the flow field immediately upstream of the jump, including the pseudo-plug layer velocity, the film height and the wall shear stress, were simply assumed. They determined the flow immediately downstream of the jump by using the mass and force balance across the jump. Moreover, the flow character in both the upstream and downstream regions of the jump was not examined. Later, Ugarelli & Federico (2007) used a similar approach, adopting the Herschel-Bulkley model. They evaluated the error, mainly stemming from neglecting viscous effects, introduced by the adoption of the approximate solution by solving the

equations numerically. Clearly, the influence of the rheology of a viscoplastic fluid on the thin film flow of an impinging jet and subsequent hydraulic jump has not been investigated.

As mentioned earlier, a thin-film approach is used to describe the spread of the impinging jet and the resulting hydraulic jump. More specifically, the depth-averaged approach of the Kármán–Pohlhausen (KP) type (Schlichtling & Gersten 2000) is used in the supercritical region (where the average velocity is larger than the velocity of the surface wave), and the lubrication approach is employed in the subcritical region (where the average velocity is smaller than the velocity of the surface wave), typically as in Newtonian formulations (Duchesne *et al.* 2014; Wang & Khayat 2019). In fact, these approaches have also been widely used for steady and transient flow problems involving thin layers of viscoplastic fluids. The depth-averaged approach was proposed to study the water waves generated by an underwater Bingham viscoplastic landslide on a gentle uniform slope by Jiang & Leblond (1993). The KP approach was also employed by Liu & Mei (1994) to investigate the flow of a mud layer down a gentle slope, in an effort to understand the periodic shocks or roll waves that are caused by unstable disturbances of small amplitude. Later, the depth-averaged approach was adopted for a viscoplastic fluid of the Heschel-Bulkley type by Huang & García (1998), who examined the dynamics of the mud-slide problem, which was simplified to a 2D, unsteady, and low-Reynolds-number laminar flow. Generally, the KP depth-averaged method is particularly suited for fast-moving free-surface flow problems, with non-negligible inertia (Ancey 2007). For slow-moving viscoplastic flow problems, the lubrication approach is utilized, as for the spread of lava (Balmforth & Craster 1999; Balmforth *et al.* 2000), the dam-break flow (Matson & Hogg 2007; Liu *et al.* 2016, 2018), and surges down an inclined surface (Liu *et al.* 2019).

In the present work, we explore the spread of a thin film of viscoplastic fluid flowing on a solid disk as a result of an impinging jet. The paper is organized as follows. The general axisymmetric formulation and physical domain are described in section 5.2. The treatment of the supercritical flow is given in section 5.3. The formulation of the subcritical flow and momentum balance across the jump are presented in section 5.4. The influence of the yield stress and viscosity, and other parameters on the hydraulic jump are covered in section 5.5. Finally, concluding remarks and discussion are given in section 5.6.

5.2 Physical domain and problem statement

Consider the axisymmetric steady laminar incompressible flow of a circular jet of a viscoplastic fluid of the Herschel-Bulkley type, emerging from a nozzle of radius a , and impinging vertically on a horizontal circular disk at a volume flow rate Q . The general constitutive Herschel-Bulkley model is written as (Bird *et al.* 1983):

$$\tau_{ij} = \left(K\dot{\gamma}^{n-1} + \frac{\tau_0}{\dot{\gamma}} \right) \dot{\gamma}_{ij}, \quad \text{for } \tau \geq \tau_0, \quad (5.2.1a)$$

$$\dot{\gamma}_{ij} = 0, \quad \text{for } \tau < \tau_0, \quad (5.2.1b)$$

where τ_{ij} is the excess stress tensor, and $\dot{\gamma}_{ij}$ is the rate-of-strain tensor. Here,

$$\tau = \sqrt{\frac{1}{2} \tau_{jk} \tau_{jk}} \quad \text{and} \quad \dot{\gamma} = \sqrt{\frac{1}{2} \dot{\gamma}_{jk} \dot{\gamma}_{kj}}$$

are the second invariants of τ_{ij} and $\dot{\gamma}_{ij}$, respectively.

We denote the yield stress by τ_0 , the consistency by K , and the power-law index by n . This model also includes the Bingham, power-law and Newtonian models, in the limits $n = 1$ and $B = 0$, respectively. Also, for $n \leq 1$ the Herschel-Bulkley fluid is shear thinning, and for $n > 1$ it is shear thickening above a certain shear rate.

As indicated by Bird, Armstrong & Hassager (1987), the incompressible generalized Newtonian fluid model should be used only for shearing flows, or at least flows that are very nearly shearing. Bird *et al.* (1983) also indicate that the Bingham model can yield correct predictions for steady shear flows. Clearly, the Herschel-Bulkley model is also a generalized Newtonian fluid model, and should therefore be restricted to shearing dominated flows. However, extensive theoretical studies adopted the Herschel-Bulkley model to examine flows that are not purely shear flows, yielding a good agreement with experimental measurements (Balmforth *et al.* 2000; Liu *et al.* 2018). In our present problem, we have shown in the appendix that the contribution of the elongation terms is negligible for a thin film, and the flow is a shear-dominated flow in both the supercritical and subcritical regions. At the jump, the thin-film assumption is expected to break down. However, we treat the jump as a shock, and apply the conservation of mass and momentum

across the jump. In this case, the treatment is confined to the supercritical and subcritical regions, which are treated as thin films. Consequently, the Herschel-Bulkley model should be valid over the entire domain. We also observe that the von Mises criterion appears to be appropriate for yield-stress fluids. Measurements of yield stress for squeeze flow seem to correspond to equivalent measurements under shear for some materials in accord with the von Mises condition (Engmann et al. 2005; Rabideau et al. 2009). Of course, given the wide range of types of viscoplastic materials, one cannot rule out exceptions to this rule. For further details, the reader is referred to the review of Balmforth *et al.* (2014).

The problem is formulated in the dimensionless (r, z) coordinates, with the origin coinciding with the stagnation point of the jet. Gravity is in the negative z direction. In this case, we denote by $u(r, z)$ and $w(r, z)$ the corresponding dimensionless velocity components in the radial and vertical directions, respectively. The r -axis is taken along the disk radius and the z -axis is normal to the disk. The jet radius a is taken as the length scale, and the average jet velocity $W \equiv Q/\pi a^2$ as the velocity scale. The shear stress is normalized with respect to $\rho v W/a$, where $v = K\rho^{-1} (W/a)^{n-1}$ is an effective kinematic viscosity scale. Since the pressure is expected to be predominantly hydrostatic for a boundary layer or a thin film, it will be scaled by $\rho g a$, g being the gravitational acceleration and ρ the density of the fluid. Four main dimensionless groups emerge in this case: the Reynolds number $Re = Wa/v = \rho a^n W^{2-n}/K$, the Froude number $Fr = W/\sqrt{ag}$, the Bingham number $B = \tau_0 a/\rho v W$ and the capillary number $Ca = \rho v W/\sigma$ (equivalently, the Bond number $Bo = Ca Re/Fr^2$), where σ is the surface tension. Since Re must be a monotonically increasing function of W , the form of Re found here suggests that the validity of the boundary-layer or thin-film approach is restricted to the range $n < 2$ (Acrivos *et al.* 1960). In other words, a boundary-layer flow is expected to form when W is large. However, if $n > 2$, $Re \rightarrow 0$ for large W , and the boundary-layer approximation breaks down. Therefore, we shall limit our results to the range $n < 2$.

5.2.1 The physical domain

The flow configuration is depicted schematically in figure 5-1, identifying the supercritical and subcritical regions upstream and downstream of the jump, respectively. The dimensionless disk radius is denoted by R_∞ . The stagnation region is neglected, which is an assumption widely adopted in the Newtonian case (Watson 1964; Bush & Aristoff 2003; Prince *et al.* 2012; Wang & Khayat 2019). We will revisit this assumption for a viscoplastic fluid in subsection 5.3.4. We take the Bingham number to be of order one or smaller, so the yield and viscous stresses are of similar strengths. We assume the jet to be sufficiently inertial, so the jet should be largely inviscid on impact, and a potential flow arises over the stagnation zone. As the fully-yielded layer develops near the wall, it displaces the outer potential flow away from the wall.

After being diverted into the horizontal outflows, the velocity in this situation has little shear, and so should be largely controlled by the yield stress, with viscous effects appearing over a growing shear layer as pictured in figure 5-1. As mentioned earlier, unlike a Newtonian jet, the diverted flow is not a true plug flow, but a pseudo-plug flow which was earlier identified in a bounded annular flow by Walton & Bittleston (1991), and the yield surface is a fake yield surface (Balmforth & Craster 1999; Liu *et al.* 2019).

The analysis for a viscoplastic fluid is similar to that for a Newtonian fluid. The influence of the yield stress and non-linear viscosity on the vertical profile of the radial velocity, and the emergence of the pseudo-plug layer, constitute the fundamental difference between the two formulations (Liu & Mei 1989; Balmforth *et al.* 2007a). As illustrated in figure 5-1, a lower layer of the fluid for $0 < z < h_0$ is fully-yielded where the radial velocity has a parabolic-like profile. In the region $h_0 < z < h$, the radial velocity becomes plug-like and independent of z to leading order when considering the asymptotic flow field expansion in powers of the film thickness-to-length ratio. However, the fluid in the pseudo-plug region is not entirely unyielded. In fact, inclusion of higher-order terms in the shallow-water expansion suggests that the normal stresses are of the same order as the shear stress, making the overall stress slightly above the yield stress to permit the radial expansion (Balmforth & Craster 1999; Balmforth & Liu 2004; Liu *et al.* 2019). A similar phenomenon is

encountered for a power-law fluid, where the shear and elongation rates become comparable at the edge of the boundary layer (Denier & Dabrowski 2004) and near the surface of a thin film (Zhao & Khayat 2008).

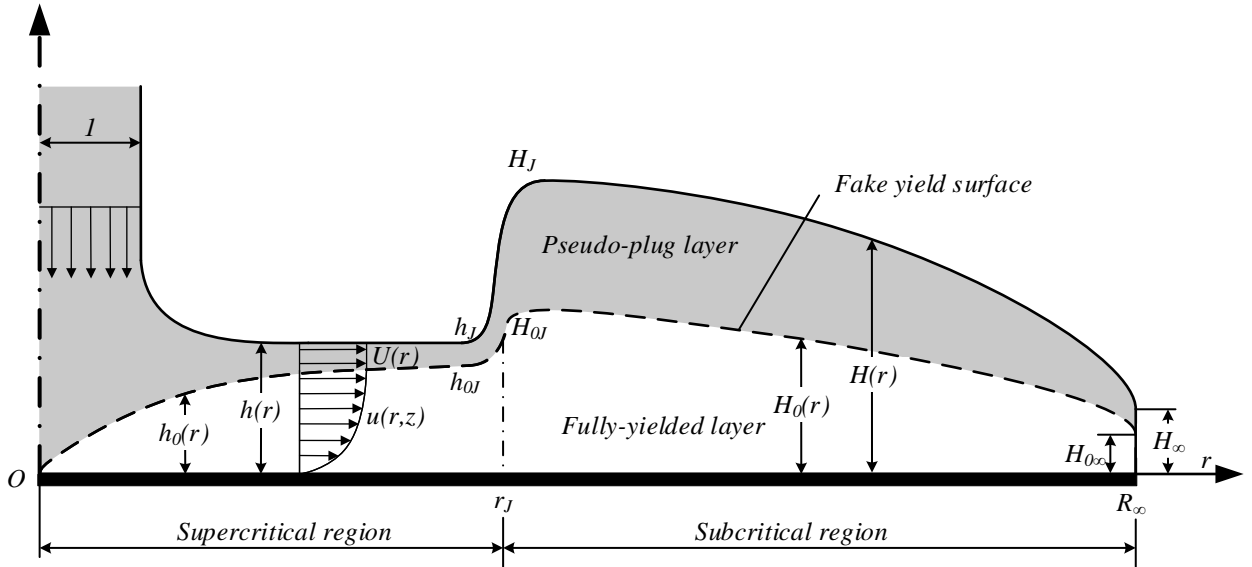


Figure 5-1: Schematic illustration of the axisymmetric jet of a viscoplastic fluid impinging on a flat stationary circular disk and the hydraulic jump. Shown are the supercritical and subcritical regions. All notations are dimensionless.

5.2.2 Governing equations and boundary conditions

For steady axisymmetric thin-film Newtonian flow, the mass and momentum conservation equations are formulated using Prandtl's boundary-layer approach in terms of a perturbation or ordering parameter $\varepsilon \ll 1$, which is the ratio of the transverse to the streamwise length scales or the film thickness to its length (Schlichting & Gersten 2000). The treatment is similar for a yield-stress fluid; we refer the reader to equations (2.3), (2.15) and (2.16) of Balmforth *et al.* (2000). Nevertheless, we detail the proper scaling of the conservation equations and boundary conditions in the appendix, adding the effect of surface tension.

Various levels of approximation can be envisaged, depending on the values of Re , Fr and Ca . If inertia and gravity are of equal strengths, then for impinging jet flow we generally

have $\text{Re} = \mathcal{O}(\varepsilon^{-1})$ or larger and $\text{Fr} = \mathcal{O}(1)$ or smaller. Even the jet flow of a relatively strongly viscous fluid like silicon oil occurs at $\text{Re} = 169$ and $\text{Fr} = 14.9$ (Duchesne *et al.* 2014; Wang & Khayat 2019), yielding a Bond number $\text{Bo} = 1.2$. In this case, recalling from (A10a) that $\tau_{rz}(r, z = h) = \mathcal{O}(\varepsilon^2)$, then (A10b) indicates that surface tension effects are important only if $\text{Bo} = \mathcal{O}(\varepsilon^2)$ or smaller. Therefore, surface tension effects are negligible, so $p(r, z = h) = \mathcal{O}(\varepsilon^2)$. These observations are expected to hold for an impinging viscoplastic jet, with surface tension typically smaller than that of water (Jalaal *et al.* 2015). Consequently, neglecting terms of $\mathcal{O}(\varepsilon^2)$, the dimensionless conservation equations reduce to:

$$u_r + \frac{u}{r} + w_z = 0, \quad (5.2.2a)$$

$$\text{Re}(uu_r + ww_z) = -\frac{\text{Re}}{\text{Fr}^2}h' + \tau_z. \quad (5.2.2b)$$

We follow the usual treatment of viscoplastic films (Balmforth *et al.* 2000; Balmforth & Liu 2004; Liu *et al.* 2016; Muravleva 2019)), and neglect surface tension effects, so the pressure is hydrostatic and vanishes at the free surface, yielding $p(r, z) = h(r) - z$. It was eliminated from equation (5.2.2b). It is important to mention that surface tensions are not necessarily precluded in viscoplastic flows. They become important in elongation rather than shear-dominated viscoplastic flows, such as surface-tension-driven viscoplastic fingering (de Bruyn *et al.* 2002) and the pinch-off, bending, and buckling of free viscoplastic sheets and filaments (Balmforth *et al.* 2010; Balmforth & Hewitt 2013; German & Bertola 2010a, b; Kamrin & Mahadevan 2012; Rahmani *et al.* 2011). We refer the reader to the review of Balmforth *et al.* (2014) for further discussion. For simplicity, we have denoted by τ the r - z component of the excess stress. We also let a subscript r or z denote partial differentiation, and a prime denote total differentiation (with respect to r). The non-dimensional Herschel-Bulkley constitutive model is deduced from (5.2.1) to read:

$$\tau = \left(|u_z|^n + B \right) \text{sgn}(u_z), \quad \text{for } |\tau| \geq B, \quad (5.2.3a)$$

$$u_z = 0, \quad \text{for } |\tau| < B. \quad (5.2.3b)$$

We note that the viscoplastic fluid is shear thinning for any n , except for $n > 1$ when the shear rate is relatively large. At the disk, the no-slip and no-penetration boundary conditions are assumed to hold for any r :

$$u(r, z = 0) = w(r, z = 0) = 0. \quad (5.2.4a, b)$$

At the free surface $z = h(r)$, the kinematic and dynamic conditions for steady flow take the form:

$$w(r, z = h) = u(r, z = h)h', \quad \tau(r, z = h) = 0. \quad (5.2.5a, b)$$

It is worth noting that the vanishing of the shear stress at the free surface is also the result of the small film thickness, slope and curvature. In this regard, we observe that the statement of Bhagat & Linden (2020) at the end of their appendix B is misleading: “The analysis implies that only for a completely flat film (that the vanishing of the shear rate) can be trivially satisfied. In all other cases the tangential stress is non-zero.” In fact, a simple rescaling of their expression (B5) shows that the shear rate is of $O(\epsilon^3)$. A vanishing shear stress at the film surface is commonly assumed in the Newtonian literature (see, e.g., Bohr *et al.* 1993; Oron *et al.* 1997; Ruyer-Quil & Manneville 1998, 2000; Watanabe *et al.* 2003; Zhou & Prosperetti 2022), as well as for a viscoplastic film (see conditions (3.6) in Balmforth *et al.* 2000; subsection 2.2 in Balmforth & Liu 2004).

On the other hand, the question remains as to whether the vanishing of the shear stress at the surface and the thin-film assumption are valid along the jump where the thin-film assumption can conceivably break down. In the present study, as in the majority of the studies on the hydraulic jump, we assumed a shock-like jump and used the balance of mass and momentum across the shock to obtain the jump radius. In other words, we do not cross the jump smoothly, so the thin-film assumption remains valid up to the jump on both the

supercritical and subcritical sides. In fact, previous studies (Watanabe 2003, Bonn *et al.* 2009) showed that the thin-film approach can still be used for a smooth jump and leads to good agreement against experiment.

In general, one can assume that there is a fake yield surface at $z = h_0(r)$ with $0 < h_0 < h$, below which is the fully-yielded layer for $0 < z < h_0$ and above which is the pseudo-plug layer for $h_0 < z < h$. At the outer edge of the fully-yielded layer and beyond (i.e., at the fake yield surface and in the pseudo-plug layer), the following conditions must hold:

$$u(r, h_0 \leq z \leq h) = U(r), \quad u_z(r, h_0 \leq z \leq h) = 0, \quad (5.2.6a, b)$$

where $U(r)$ is the surface velocity which prevails over the entire pseudo-plug layer.

Upon integrating equation (5.2.2a) over the entire film thickness, and recalling (5.2.6a), then conservation of mass yields the following relation in the dimensionless form:

$$\int_0^{h_0} u(r, z) dz + U(h - h_0) = \frac{1}{2r}. \quad (5.2.7)$$

Recalling (5.2.3a), (5.2.5b) and (5.2.6b), the momentum equation (5.2.2b) in the pseudo-plug layer can be simplified by integrating it between the fake yield surface and the film height. Consequently, the momentum equations in the pseudo-plug and fully-yielded layers become

$$\text{Re } UU' = -\frac{B}{h - h_0} - \frac{\text{Re}}{\text{Fr}^2} h', \quad h_0 < z < h, \quad (5.2.8a)$$

$$\text{Re}(uu_r + wu_z) = \tau_z - \frac{\text{Re}}{\text{Fr}^2} h', \quad 0 < z < h_0. \quad (5.2.8b)$$

In principle, these equations apply over the entire flow domain. However, some simplifying assumptions will be made as we treat the supercritical and subcritical regions separately.

5.3 The influence of the yield stress on the supercritical flow

In this section, we present the formulation of the problem in the supercritical region. A vertically averaged model for a viscoplastic fluid is adopted to obtain the weak form of the conservation equations. Gravity is assumed to be negligible given the dominant strength of the jet inertia. The asymptotic limits of small yield stress are derived for a Bingham fluid. The limit of a Newtonian flow is also discussed for reference.

5.3.1 The depth-averaged formulation and velocity profile

We start by examining the flow in the supercritical region, which includes both the fully-yielded and pseudo-plug layers. We observe that the pressure for a thin film is essentially hydrostatic as a result of its vanishing at the film surface and the small thickness of the film. In addition, upstream of the jump, the variation of the film thickness with radius is expected to be smooth and gradual. In this case, the radial variation of the hydrostatic pressure is also small. According to the calculations of Prince *et al.* (2012), the hydrostatic pressure exerts less than 0.4% cumulative influence on the dynamics of the thin film, and is thus negligible upstream of the hydraulic jump. This is generally assumed in models of hydraulic jump flow, in which the hydrostatic pressure is only included downstream of the jump where the film is relatively thicker (Watson 1964; Bush & Aristoff 2003; Dressaire *et al.* 2010; Prince *et al.* 2012). In this case, in the absence of gravity ($Fr \rightarrow \infty$), equations (5.2.8) reduce to

$$\text{Re } UU' = -\frac{B}{h-h_0}, \quad h_0 < z < h, \quad (5.3.1a)$$

$$\text{Re}(uu_r + wu_z) = nu_z^{n-1}u_{zz}, \quad 0 < z < h_0. \quad (5.3.1b)$$

We have chosen $\text{sgn}(u_z) = 1$ in equation (5.2.3a) to hold over the entire flow domain. Separation is not expected to occur in the supercritical region. As to the subcritical region, we recall that our present study is based on the assumption that the jump is a shock. In this

case, the recirculation zone cannot be captured. Therefore, we assume the radial velocity in the fully-yielded layer to be of the form (Liu & Mei 1994)

$$u(r < r_j, 0 < z < h_0) = U(r)f(\eta), \quad \eta = z/h_0, \quad (5.3.2)$$

where $f(\eta)$ is a monotonic function that will be specified shortly. Using (5.3.2), the mass conservation equation (5.2.7) yields the following relation ($r < r_j$):

$$h = (1 - \chi_1)h_0 + \frac{1}{2rU}, \quad (5.3.3)$$

where $\chi_1 = \int_0^1 f(\eta) d\eta$. The vertical velocity component is eliminated by noting from

$$(5.2.2a) \quad \text{that} \quad w(r, z) = -\frac{1}{r} \left[r \int_0^z u(r, z) dz \right]_r, \quad \text{resulting in}$$

$$uu_r + wu_z = \frac{1}{r} (ru^2)_r - \left[\frac{u}{r} \int_0^z (ru)_r dz \right]_z. \quad \text{Consequently, upon integrating (5.3.1b) over the}$$

fully-yielded layer, we obtain the integral form of the momentum equation upstream of the jump in the fully-yielded layer:

$$\frac{1}{r} \frac{d}{dr} \int_0^{h_0} (ru^2) dz - \frac{U}{r} \frac{d}{dr} \int_0^{h_0} (ru) dz = -\frac{1}{\text{Re}} u_z^n(r, z=0). \quad (5.3.4)$$

Upon substituting the velocity profile (5.3.2) into (5.3.4), we have

$$\chi_2 (rh_0 U^2)' - \chi_1 U (rh_0 U)' = -\frac{\chi_3^n}{\text{Re}} \frac{rU^n}{h_0^n}, \quad (5.3.5)$$

where $\chi_2 = \int_0^1 f^2(\eta) d\eta$ and $\chi_3 = f'(0)$. The problem upstream of the jump is now governed by equations (5.3.1a), (5.3.3) and (5.3.5), with the three unknowns being U , h and h_0 . We note that these three equations are similar to equations (3.4-3.6) in Huang & García (1998) for a stable Heschel-Bulkley flow in the plane in the limit of no gravity, and

collapse onto equations (25-27) in Liu & Mei (1994) and (6.2-6.4) in Balmforth & Liu (2004) for a stable Bingham flow in the plane in the limit of no gravity upon setting $n=1$ and choosing a parabolic velocity profile.

The film height h can be eliminated by using (5.3.3), thus reducing the problem to a second-order system governing U and h_0 :

$$(2\chi_1 r h_0 U - 1)U' = \frac{2B}{\text{Re}} r, \quad (5.3.6a)$$

$$(2\chi_2 - \chi_1) r h_0 U' + (\chi_2 - \chi_1) r U h_0' = (\chi_1 - \chi_2) h_0 U - \frac{\chi_3^n}{\text{Re}} \frac{r U^{n-1}}{h_0^n}. \quad (5.3.6b)$$

In this case, h is obtained from (5.3.3). Equations (5.3.6a, b) are solved numerically subject to $U(r=0)=1$ and $h_0(r=0)=0$. It is helpful to verify whether the system (5.3.6) becomes singular at some locations. A singularity is possible only if $2\chi_1 r h_0 U - 1 = 0$, which, from (5.3.3), implies that $h = h_0$. However, the pseudo-plug layer must always exist (Balmforth & Craster 1999). We can thus conclude that system (5.3.6) has no singularity except for when $r = U = h_0 = 0$, which happens at the origin or when the flow comes to a halt (refer to Wang & Khayat 2019 for further discussion on the emergence of the singularity in the presence of gravity for a Newtonian fluid).

We assume that the radial velocity component $u(r, z)$ in the fully-yielded layer satisfies the no-slip condition at the surface of the disk, and the vanishing of the shear rate and continuity of the velocity at the fake yield surface. In this case, the profile $f(\eta)$ in (5.3.2), must satisfy $f(0)=0$ from (5.2.4a), $f(1)=1$ from (5.2.6a), $f'(1)=0$ from (5.2.6b). In this study, we follow Ng & Mei (1994), Huang & García (1998) and Hogg & Pritchard (2004) and take

$$f(\eta) = 1 - (1 - \eta)^{(n+1)/n}, \quad 0 < \eta < 1. \quad (5.3.7)$$

In this case, the χ integrals defined above become

$$\chi_1 = \frac{n+1}{2n+1}, \quad \chi_2 = \frac{2(n+1)^2}{(2n+1)(3n+2)}, \quad \chi_3 = \frac{n+1}{n}. \quad (5.3.8a-c)$$

For a Bingham fluid, $\chi_1 = 2/3$, $\chi_2 = 8/15$ and $\chi_3 = 2$.

Although the similarity profile (5.3.7) results from the solution of the lubrication flow of a viscoplastic fluid, it is imposed here in the presence of inertia. This is commonly done for Newtonian flow for which the parabolic profile is recovered from (5.3.7) when $n = 1$. The profile (5.3.7) is obviously one of many that can be used. Generally, low-order self-similar profiles have extensively been adopted for the film spread and hydraulic jump. They lead to an accurate description of the overall flow, are simple when treating nonlinear flows, and are compatible with the exact profile for the lubrication flow in the subcritical region. The parabolic profile was earlier used by Bohr *et al.* (1993) and later by Kasimov (2008). The cubic profile was adopted by Prince *et al.* for a flow on a disk with isotropic (2012) and anisotropic (2014) slip, by Wang & Khayat (2018) and Ipatova *et al.* (2020) for the flow on a rotating disk, and Wang & Khayat (2019) on a stationary disk, including heat transfer (Wang & Khayat 2020) and transient flow (Baayoun *et al.* 2022).

The plausibility of profile (5.3.7) for viscoplastic flow is motivated by both the equilibrium uniform flow and the lubrication approximations (Balmforth & Liu 2004). However, despite their successful use in vertically averaged thin-film models, parabolic or simple similarity profiles may not be a good choice as they yield inaccurate critical conditions for the instability of Newtonian (Ruyer-Quil & Manneville 2000) and viscoplastic (Balmforth & Liu 2004) flows. In addition, self-similar profiles do not satisfy the momentum equation at the surface of the disk. As a result, they are unable to describe the vortex structure downstream of the jump (Watanabe *et al.* 2003; Roberts & Li 2009). On the other hand, their use has been tested and proven effective in the majority of depth-averaging nonlinear models. Recently, Li *et al.* (2021) carried out the numerical simulation based on the lattice Boltzmann method of the fully developed flow of a Herschel-Bulkley fluid in straight and curved pipes. They found that the velocity profile obtained from their numerical simulation agreed well with the profile (5.3.7). Finally, the earlier experimental measurements of Chambon *et al.* (2014) in an inclined conveyor-belt channel also suggest that the velocity

profile obtained from the lubrication approximation is valid for a Herschel-Bulkley type fluid.

5.3.2 The influence of the viscosity and yield stress

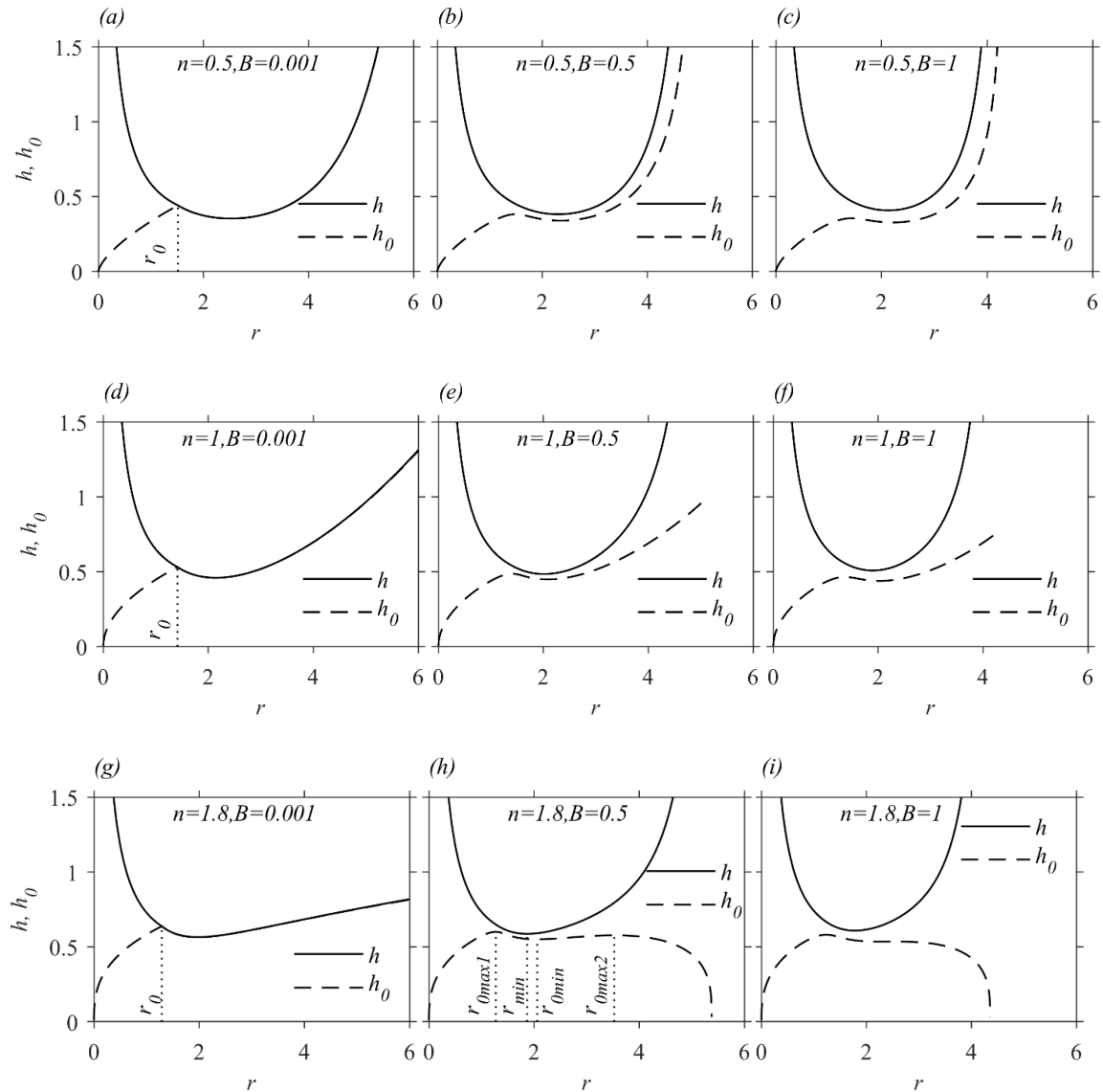


Figure 5-2: Influence of the yield stress on the film thickness h and the fully-yielded layer thickness h_0 in the supercritical region ($Re = 50$). Shown are the profiles for $n < 1$ (a-c), $n = 1$ (d-f) and $n > 1$ (g-i).

Figure 5-2 illustrates the influence of the yield stress on the film and fully-yielded layer heights in the supercritical region for $n < 1$ (figures 5-2a to 5-2c), $n = 1$ or a Bingham fluid

(figures 5-2d to 5-2f) and $n > 1$ (figures 5-2g to 5-2i). The results for $B = 0.001$ correspond essentially to a power-law fluid (Watson 1964; Zhao & Khayat 2008; Wang & Khayat 2019). In this case, and regardless of the level of viscosity, the fully-yielded layer is a boundary layer that grows with distance until it intersects the free surface at the transition location $r = r_0$ (figures 5-2a, 5-2d, 5-2g). For $B > 0.001$, while the film thickness exhibits the typical behaviour predicted for a Newtonian jet (almost parabolic with a minimum at some radial distance), the fully-yielded layer thickness exhibits a more complex behaviour, which is strongly dependent on the fluid type. The film becomes thicker as B increases, as is generally the case for a thin viscoplastic film (Mei & Yuhi 2001; Balmforth *et al.* 2000, 2002; Balmforth *et al.* 2007b, Matson & Hogg 2007; Liu *et al.* 2016, 2018). In contrast, the fully-yielded layer thickness exhibits increasingly pronounced local maximum and minimum at $r_{0\max}$ and $r_{0\min}$, respectively ($B = 0.5$ and 1).

The overall fully-yielded layer thickness decreases with increasing B (Jiang & Leblond 1993; Balmforth *et al.* 2007a, b; Balmforth *et al.* 2000, 2002), following closely the growth of the free surface height for $n < 1$ (figures 5-2a to 5-2c). For a Bingham fluid (figures 5-2d to 5-2f), h_0 grows at a slower rate than h . For $n > 1$ (figures 5-2g to 5-2i), the pseudo-plug layer becomes even thicker, abruptly invading the entire film at some point downstream. However, as we shall argue later, this abrupt response may not be observed in reality since a hydraulic jump may form upstream of this abrupt point. Moreover, the thin-film model may cease to be valid in the presence of a steep curvature (Balmforth *et al.* 2007b; Matson & Hogg 2007; Liu *et al.* 2016, 2018, 2019). Finally, and importantly, the absence of a transition point for a yield-stress fluid allows a formulation that is uniformly valid over the entire supercritical region. In contrast, for power-law and Newtonian fluids, the supercritical region is subdivided into a developing boundary-layer and fully-viscous sub-regions, and the flow is matched at the transition point (Watson 1964; Wang & Khayat 2019; Zhao & Khayat 2008). In other words, the fully-viscous flow formulation is uniformly valid and applies over the entire supercritical region for a viscoplastic fluid, no matter how small the yield-stress is.

Figure 5-3 illustrates the influence of the yield stress on the distribution of the pseudo-plug layer velocity (figure 5-3a) and wall shear stress (figure 5-3b) for a Bingham fluid, as well

as the influence of non-linear viscosity on the wall shear stress (figure 5-3c) and shear rate (figure 5-3d). Very similar profiles of U are obtained for any n (not shown). The curve for $B = 0.001$ depicts the discontinuity in dU/dr at the transition point, typically predicted for power-law and Newtonian flows. In this case, the velocity near the impingement region remains close to 1, which then starts to decrease suddenly at the transition point. This singularity is smoothed over for $B > 0.001$; in this case, dU/dr is continuous, decreasing monotonically with distance. The pseudo-plug layer velocity decreases faster as B increases.

The wall shear stress or skin friction $\tau_w(r) = \tau(r, z = 0)$ is given by

$$\tau_w(r) = \chi_3^n \frac{U^n}{h_0^n} + B. \quad (5.3.9)$$

Figure 5-3b indicates that the wall shear stress overall increases with the yield stress. This larger shear stress is the result of a thinner fully-yielded layer caused by a higher yield stress as shown in figure 5-2. Again, yield stress tends to smooth the discontinuity exhibited by a power-law or Newtonian fluid. In fact, for large r , $U/h_0 \sim 0$ and $\tau_w \sim B$ in (5.3.9); the flow comes to a halt while the film thickens. In this limit, the thin film approach breaks down, and the elongational flow terms become important. Comparing the development of the wall shear stress for different n in figure 5-3c, we observe that the fluid with a larger n has a higher τ_w near impingement and a lower τ_w away from impingement. A similar trend was observed for squeeze flow (see figure 6 of Muravleva 2019). Finally, figure 5-3d shows the influence of viscosity on the shear rate along the wall, which is predominantly large over a wide distance, essentially over the entire supercritical region. It is smaller than unity further downstream, which explains the reversal in the trend for the shear stress depicted in figure 5-3c.

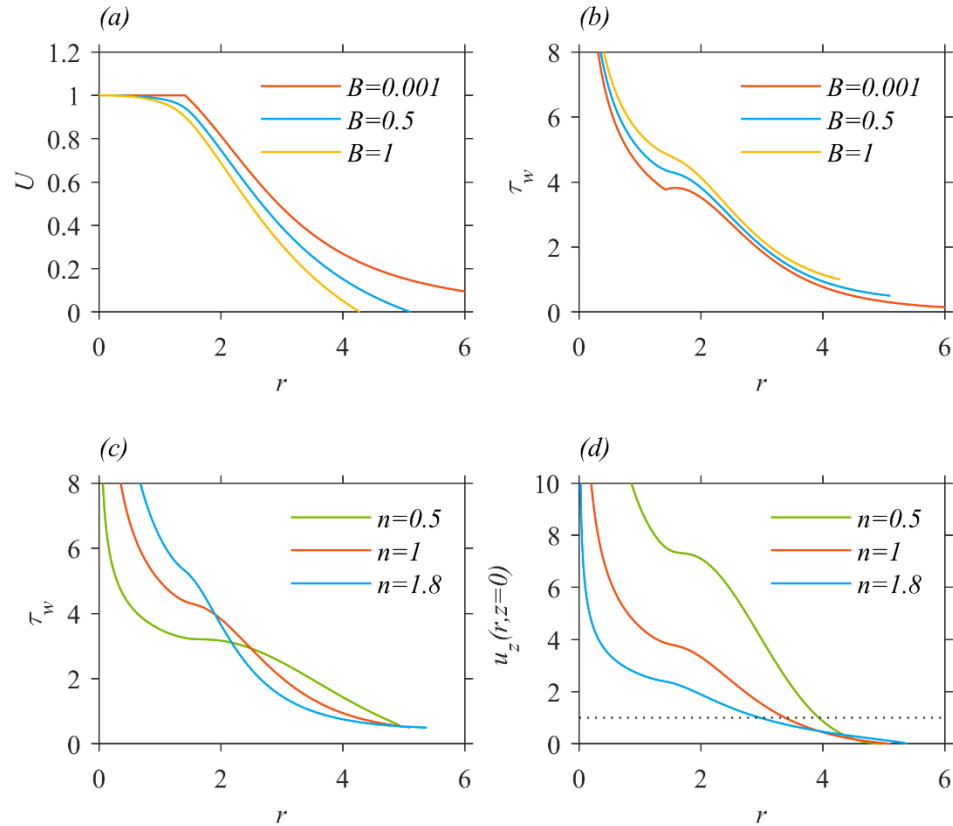


Figure 5-3: Influence of the yield stress on the distribution of (a) the pseudo-plug layer velocity and (b) the wall shear stress for a Bingham fluid ($n = 1$). Also shown is the influence of viscosity on the distribution of (c) the wall shear stress and (d) the wall shear rate for $B = 0.5$. Here $Re = 50$.

Further insight into the film structure is gained by examining figure 5-4, where we depict the influence of the yield stress on the minimum film height h_{\min} and its radial location r_{\min} (figure 5-4a), the first local maximum in the fully-yielded layer thickness $h_{0\max 1}$ and its location $r_{0\max 1}$ (figure 5-4b), the local minimum in the fully-yielded layer thickness $h_{0\min}$ and its location $r_{0\min}$ (figure 5-4c), and the second local maximum in the fully yielded-layer thickness $h_{0\max 2}$ and its location $r_{0\max 2}$ (figure 5-4d) for any viscoplastic fluids. The power-law fluid results are recovered in the limit $B \rightarrow 0$. As shown in figure 5-4a, the minimum film height increases almost at the same rate with increasing B for the three different types of fluid, and its location occurs closer to the impingement point for higher B (see also figure 5-2). On the other hand, increasing B results in a thinner

fully-yielded layer, with a drop in h_{0max1} , h_{0min} and h_{0max2} , occurring closer to the impingement point, as shown in figures 5-4b to 5-2d.

Generally, the character of the fully-yielded layer thickness and its dependence on the yield stress depend strongly on the value of n . Although the behaviour of the heights of the local minimum and maxima is always monotonically decreasing with respect to B , their locations are not, as is particularly obvious from figures 5-4b and 5-4c. Finally, the yielded layer height for $n > 1$ tends to flatten for high yield stress, as suggested from figures 5-4c and 5-4d for $B > 1$.

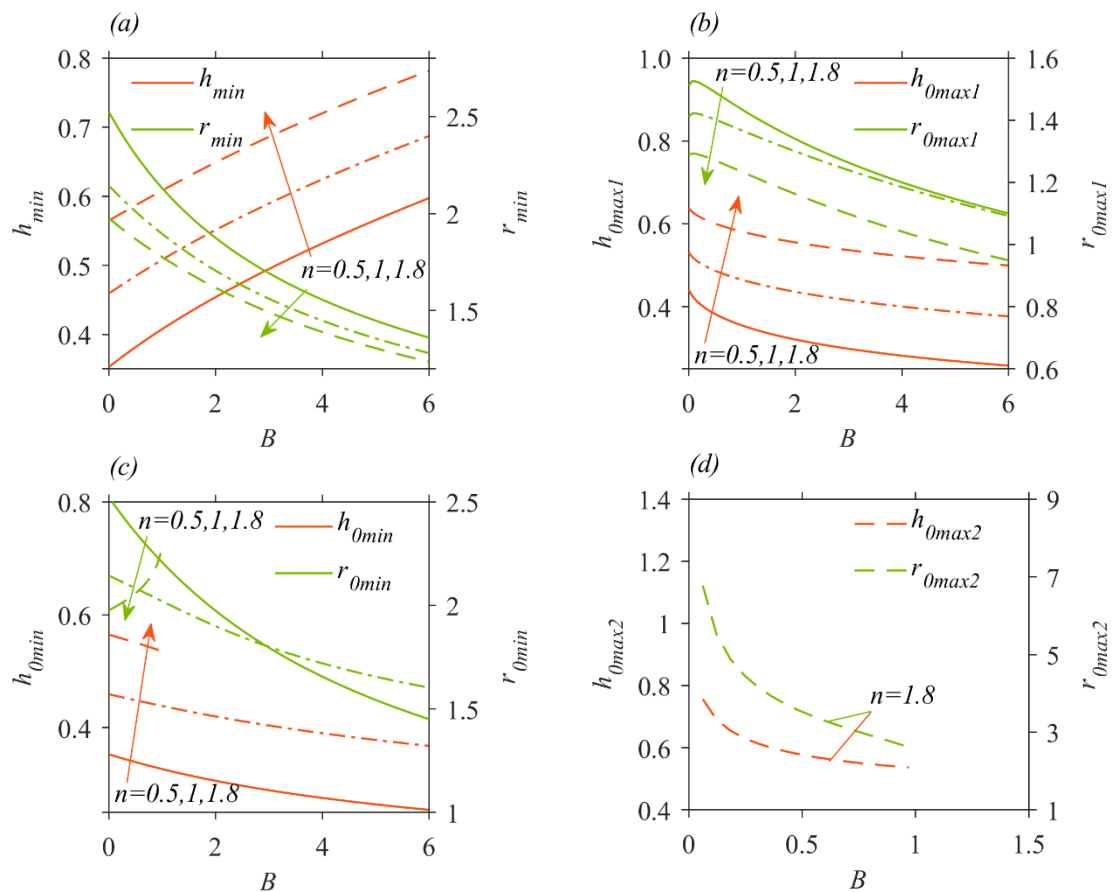


Figure 5-4: The influence of the yield stress on (a) the minimum film height h_{min} and its location r_{min} , (b) the first local maximum thickness h_{0max1} and its location r_{0max1} , (c) the local minimum thickness h_{0min} and its location r_{0min} , and (d) the second local maximum thickness h_{0max2} and its location r_{0max2} of the fully-yielded layer, for $n = 0.5$ (solid lines), 1 (dash-dotted lines) and 1.8 (dashed lines). Here $Re = 50$.

5.3.3 The limit of Newtonian supercritical flow and small B correction

By inspecting (5.3.1a), we suspect that the Newtonian limit may not necessarily be reachable as $B \rightarrow 0$ since $h_0 \rightarrow h$, suggesting a singularity in this limit. The Newtonian limit is often assumed to exist, at least as a reference (Balmforth *et al.* 2000). We explore this issue by briefly reviewing the Newtonian limit first, and then assuming it to be the leading-order solution as we try to capture the flow for small B . In order to keep the analysis manageable, we restrict it to a Bingham fluid.

5.3.3.1 The Newtonian limit

As mentioned earlier, one of the striking differences between the viscoplastic and Newtonian formulations is the absence of a developing boundary-layer region in the former case. We recall that for a Newtonian impinging jet, the problem is formulated by assuming the presence of a developing boundary-layer near impingement, and a fully-developed viscous region further downstream (Watson 1964; Wang & Khayat 2019). The two meet at the transition point $r = r_0$ as figure 5-2d indicates. Importantly, different Karman-Pohlhausen formulations are applied separately for $r < r_0$ and $r > r_0$. This is not the case for a viscoplastic fluid, and only one uniformly valid formulation is needed, yielding equations (5.3.3) and (5.3.6), valid over the entire supercritical region, and used to determine the three unknowns U , h and h_0 . We show here that the viscoplastic formulation does reduce to a uniformly valid Newtonian formulation when we set $B = 0$ and $n = 1$. In this limit, two solution branches emerge from equation (5.3.6a), namely $U' = 0$ and $2\chi_1 r h_0 U = 1$, corresponding, respectively, to the pre- ($r < r_0$) and post-transition ($r > r_0$) ranges in the supercritical region. We note that equations (5.3.6b) and (5.3.3) remain valid in both ranges. For the first solution branch, we note that since $U(r=0) = 1$, then $U(r < r_0) = 1$. Consequently, we recover the Newtonian flow in the developing boundary-layer region ($r < r_0$):

$$U_N(r) = 1, \quad \delta(r) = \sqrt{\frac{2\chi_3}{3(\chi_1 - \chi_2)} \frac{r}{\text{Re}}}, \quad (5.3.10a, b)$$

$$h_N(r) = (1 - \chi_1) \sqrt{\frac{2\chi_3}{3(\chi_1 - \chi_2)} \frac{r}{\text{Re}}} + \frac{1}{2r}. \quad (5.3.10c)$$

Here we identify h_0 as the boundary-layer thickness δ . The transition point

$$r_0 = \left[\frac{3(\chi_1 - \chi_2)\text{Re}}{8\chi_1^2\chi_3} \right]^{1/3}$$

is reflected in figure 5-2d. Based on (5.3.10), the boundary layer

grows like \sqrt{r} , and the film height decreases predominantly like $1/r$, as is also reflected in figure 5-2d.

The second solution branch in the fully-developed viscous region ($r > r_0$) yields

$$h_N(r) = \frac{2\chi_1\chi_3}{3\chi_2} \frac{r^2}{\text{Re}} + \frac{3\chi_2 - \chi_1}{4\chi_1\chi_2} \frac{1}{r}, \quad U_N(r) = \frac{1}{2\chi_1 r h_N}, \quad (5.3.11a, b)$$

suggesting that U decreases like $1/r$ as reflected in figure 5-3a. In sum, the behaviour indicated in (5.3.10) and (5.3.11) corresponds to the ranges $r < r_0$ and $r > r_0$, respectively, and corroborates the numerical predictions in figures 5-2 and 5-3 for $B = 0.001$ and $n = 1$.

Next, we examine the behaviour for small B , and whether the Newtonian flow can indeed be recovered in the limit $B \rightarrow 0$ for a Bingham fluid. For this, we need to examine the flow separately for $r < r_0$ and $r > r_0$, taking the Newtonian limit as the leading-order solution. We attempt regular power-series expansions, but include only the first-order departure.

5.3.3.2 The small B correction for $r < r_0$

For $r < r_0$, we write

$$h = h_N + Bh_1, \quad h_0 = \delta + Bh_{01}, \quad U = 1 + BU_1, \quad (5.3.12a-c)$$

where δ and h_N are given in (5.3.10). Substituting (5.3.12) into (5.3.3) and (5.3.6), we obtain the following equations for the first-order departures:

$$h_1 = (1 - \chi_1)h_{01} - \frac{U_1}{2r}, \quad U_1' = -\frac{1}{\text{Re}(h_N - \delta)}, \quad (5.3.13a, b)$$

$$(2\chi_2 - \chi_1)r\delta U_1' + (\chi_2 - \chi_1)\left[(r\delta)' U_1 + (rh_{01})'\right] = \frac{\chi_3}{\text{Re}} \frac{rh_{01}}{\delta^2}. \quad (5.3.13c)$$

Equation (5.3.13b) indicates that the problem becomes singular at the transition radius $r = r_0$ where $h_N = \delta$. Expansion (5.3.12) is therefore valid in the bulk range $0 < r \ll r_0$. The bulk solution is obtained for small r subject to homogeneous conditions at $r = 0$, with $h_N - \delta \approx \frac{1}{2r}$. In this case, it is not difficult to show that for small r ,

$$U \approx 1 - \frac{B}{\text{Re}} r^2, \quad h \approx h_N + \frac{2 - \chi_1}{2} \frac{B}{\text{Re}} r, \quad (5.3.14a, b)$$

$$h_0 \approx \delta - \frac{11\chi_2 - 7\chi_1}{10(\chi_1 - \chi_2)^{3/2}} \sqrt{\frac{2\chi_3}{3}} \frac{r^5}{\text{Re}^3} B, \quad (5.3.14c)$$

where we recall that h_N and δ are given in (5.3.10). We see that both U and h_0 decrease with B , while the film thickness increases as a result of increasing yield stress. U acquires a parabolic character.

5.3.3.3 The small B correction for $r > r_0$

For $r > r_0$, we write

$$h = h_N + Bh_1, \quad h_0 = h_N + Bh_{01}, \quad U = U_N + BU_1, \quad (5.3.15a-c)$$

where U_N and h_N are recalled from (5.3.11). Substituting (5.3.15) into (5.3.3) and (5.3.6), we obtain the following equations for the first-order departures:

$$h_1 - h_{01} = -\frac{1}{\operatorname{Re} U_N U'_N}, \quad h_1 = (1 - \chi_1) h_{01} - \frac{U_1}{2r U_N^2}, \quad (5.3.16a, b)$$

$$(2\chi_2 - \chi_1)r(h_N U'_1 + U'_N h_{01}) + (\chi_2 - \chi_1)[r U_N h'_{01} + (r h'_N + h_N)U_1 + U_N h_{01}] = \frac{\chi_3}{\operatorname{Re} h_N^2} \frac{r h_{01}}{r^2} . \quad (5.3.16c)$$

This problem is also singular since both U'_N and h'_N are discontinuous at the transition location $r = r_0$. In this case, we examine the solution for large r , and note that

$$h_N \approx \frac{2\chi_1 \chi_3}{3\chi_2} \frac{r^2}{\operatorname{Re}} \quad \text{and} \quad U_N \approx \frac{3\chi_2}{4\chi_1^2 \chi_3} \frac{\operatorname{Re}}{r^3} .$$

Upon eliminating h_1 , the equations for h_{01} and

U_1 reduce to:

$$\chi_1 h_{01} + \frac{U_1}{2r U_N^2} \approx \frac{1}{\operatorname{Re} U_N U'_N}, \quad (5.3.17a)$$

$$(2\chi_2 - \chi_1)r h_N U'_1 + (\chi_2 - \chi_1)r U_N h'_{01} \approx 3(\chi_1 - \chi_2)h_N U_1 + (5\chi_2 - 2\chi_1)U_N h_{01} + \frac{\chi_3}{\operatorname{Re} h_N^2} \frac{r h_{01}}{r^2} . \quad (5.3.17b)$$

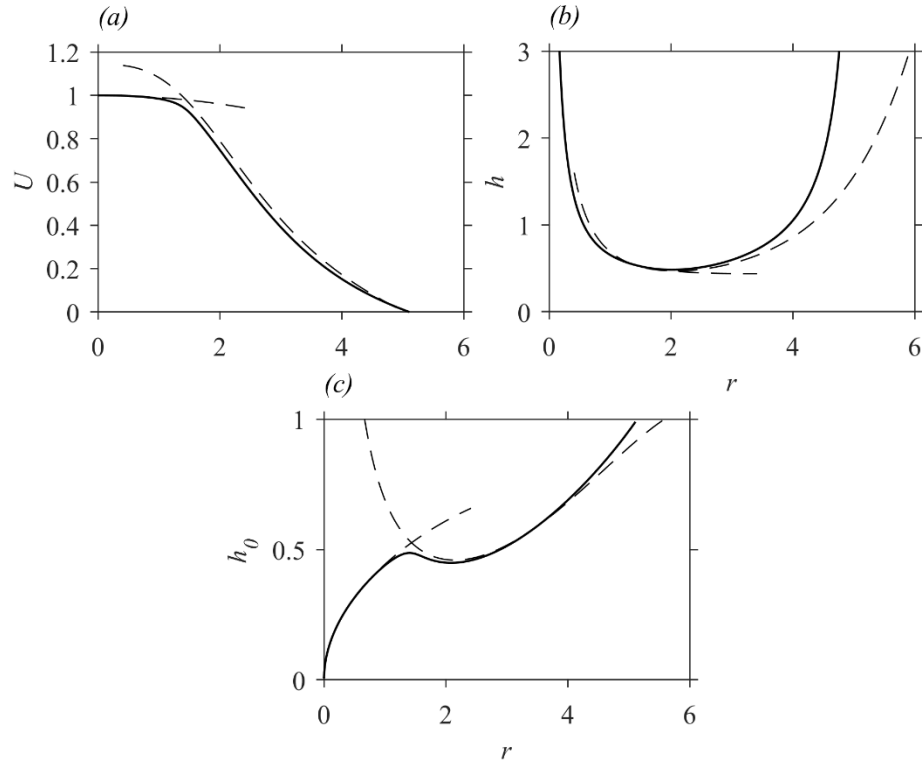


Figure 5-5: Comparison between the exact and the small- B asymptotic profiles. Shown are the pseudo-plug layer velocity U (a), the film height h (b) and pseudo-plug layer thickness h_0 (c) for Bingham fluid $n = 1$ and $B = 0.5$. Here $Re = 50$. The solid lines are the exact numerical results, and the dashed lines are the asymptotic results.

These equations admit the exact solution $U_1 = -\frac{5\chi_1 + \chi_2}{12 Re \chi_2} r^2$ and

$$h_{01} = \frac{2\chi_1^3 \chi_3^2 (5\chi_1 - 7\chi_2)}{27 Re^3 \chi_2^3} r^7. \text{ In this case,}$$

$$h = h_N + \frac{B}{Re^3} \frac{2\chi_1^3 \chi_3^2 (8\chi_1 \chi_2 + 5\chi_1 - 7\chi_2)}{27 \chi_2^3} r^7, \quad (5.3.18a)$$

$$h_0 = h_N - \frac{B}{Re^3} \frac{2\chi_1^3 \chi_3^2 (7\chi_2 - 5\chi_1)}{27 \chi_2^3} r^7, \quad U = U_N - \frac{B}{Re} \frac{5\chi_1 + \chi_2}{12 \chi_2} r^2, \quad (5.3.18b, c)$$

where we recall U_N and h_N from (5.3.11).

Figure 5-5 illustrates the small B behaviour against the numerical profiles for $B = 0.5$ ($n = 1$). The singularity is clearly depicted by the asymptotic profiles (5.3.13) and (5.3.17). We observe good agreement with the exact solution for small r . The discrepancy for large r , which is particularly visible in figures 5-5b and 5-5c, is due to our neglecting terms of higher order in B in (5.3.12) and (5.3.15). Therefore, the problem becomes singular in the limit $B = 0$, and expansions (5.3.12) and (5.3.15) are valid only far from the origin. The composite solution can be obtained using matched asymptotic expansion between the region including the origin and the bulk region. This issue will not be explored here.

5.3.4 The impingement zone

Finally, as depicted in figure 5-1, we assume that the inception of the yielded layer coincides with the stagnation point, thus assuming the impingement zone to be negligibly small. This is common practice for a Newtonian jet. In fact, the velocity outside the boundary layer rises rapidly from 0 at the stagnation point to the impingement velocity in the inviscid far region. The impinging jet is predominantly inviscid close to the stagnation point, and the boundary-layer thickness remains negligibly small. Obviously, this is the case for a jet at a relatively large Reynolds number. Indeed, the analysis by White (2006) shows that the boundary layer thickness is constant near the stagnation point, and is estimated to be $O(\text{Re}^{-1/2})$. Ideally, the flow at the boundary-layer edge should correspond to the (almost parabolic) potential flow near the stagnating jet, with the boundary-layer leading edge coinciding with the stagnation point (Liu & Lienhard 1993). However, the assumption of uniform horizontal flow near the wall and outside the boundary layer is reasonable. The distance from the stagnation point for the inviscid flow to reach uniform horizontal velocity is small, on the order of the jet radius (Lienhard 2006). In the absence of gravity, the steady flow acquires a similarity character. In this case, the position or effect of the leading edge is irrelevant. This assumption was adopted initially by Watson (1964), and is commonly used in existing theories (see, for instance, Higuera 1994; Bush & Aristoff 2003; Prince *et al.* 2012; Wang & Khayat 2018, 2019, 2020).

In contrast to a Newtonian jet, the impingement zone thickness for a power-law fluid varies with r (Maiti 1965; Koneru & Manohar 1968). In an effort to examine the impingement

zone for the impinging free-surface jet, we briefly revisit first the development of Maiti (1965) using our notations, but we limit the analysis to a power-law fluid, and account only qualitatively for the yield stress effect; a rigorous treatment of the impingement zone is quite involved and is beyond the scope of our study. We therefore assume, given the strong inertia of the downward jet, that the flow above the yielded region is purely inviscid and not pseudo-plug.

For a free-surface jet with no surface tension, Lienhard (2006) showed that the radial velocity component of the potential flow is given by $U(r) = cr + O(r^2)$, where $c = 0.46$.

The radial velocity component in the stagnation region is then expressed as $u(r, z) = U(r)F'(\eta)$ in terms of the similarity variables $\eta = z \left(c^{2-n} \frac{\text{Re}}{n} \right)^{1/1+n} r^{(1-n)/(1+n)}$, where F is governed by (Maiti 1965)

$$(F'')^{n-1} F''' + \frac{3n+1}{n+1} FF'' - F'^2 + 1 = 0, \quad (5.3.19a)$$

$$F(0) = F'(0) = 0, \quad F(\eta \rightarrow \infty) \sim 1. \quad (5.3.19b-d)$$

Although Maiti (1965) provided a power-series solution for this problem, we solve (5.3.19) numerically as a boundary-value problem. The boundary layer height in the impingement zone becomes

$$\delta(r) = \eta_\delta \left(c^{n-2} \frac{n}{\text{Re}} \right)^{1/1+n} r^{(n-1)/(1+n)}, \quad (5.3.20)$$

where η_δ is a constant that depends on n . Figure 5-6 illustrates the interplay between the viscosity and yield stress in the impingement zone for a viscoplastic fluid with $n < 1$ (figure 5-6a), $n = 1$ (figure 5-6b) and $n > 1$ (figure 5-6c). The intersection between δ and h_0 indicates the extent of the impingement zone, which depends on n and B . For $n < 1$, δ exhibits a singularity at the stagnation point and decreases at a diminishing rate with the radial distance. The boundary layer height is independent of r for a Newtonian jet, and

behaves like $1/\sqrt{\text{Re}}$. For $n > 1$, δ rises with an infinite slope from zero at the stagnation point and tends to level off at large r . The impingement zone length depends weakly on B for $n < 1$ (figure 5-6a), and is essentially insensitive to the level of the yield stress for $n \geq 1$ (figures 5-6b and 5-6c). This dependence is expected to be even weaker when yield-stress effects are accounted for. In this case, we expect the fully-yielded layer thickness in the stagnation zone for a viscoplastic fluid to be smaller than for the power-law fluid. Figure 5-6 suggests that the length of the impingement zone (distance between the origin and the intersection point) is slightly larger than 1 for $n < 1$ (figure 5-6a), slightly smaller than 1 for Newtonian and Bingham fluids (figure 5-6b), and much smaller than 1 for $n > 1$ (figure 5-6c). In sum, and similar to a Newtonian jet (Lienhard 2006), the impingement zone length for a viscoplastic jet is of the order of jet radius.

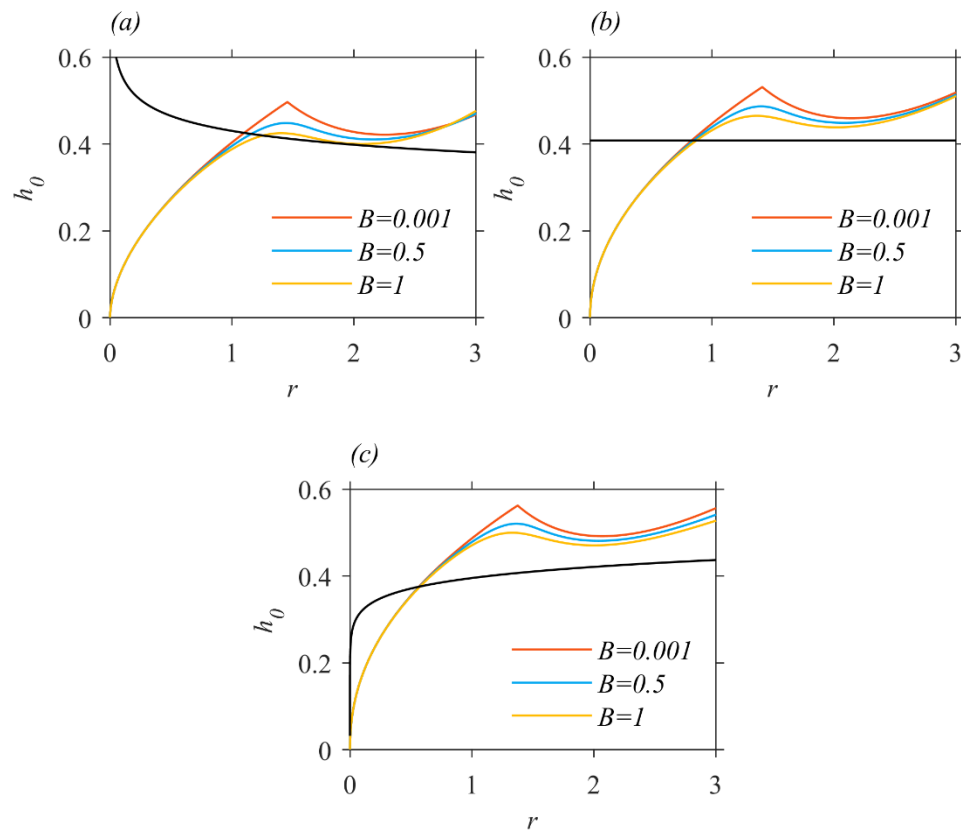


Figure 5-6: The size of the impinging zone (distance between the origin and the intersection point). The black lines are the boundary-layer thickness obtained from the expression (5.3.20), and the color lines are the result from the solution of equations (5.3.6) for the fully-yielded layer. (a) $n = 0.8$, (b) $n = 1$, and (c) $n = 1.2$.

5.4 Formulation of the subcritical viscoplastic flow and the hydraulic jump

In the subcritical region, the film is relatively thick, and the flow is slow. In this case, the effect of gravity is no longer negligible. We adopt a lubrication flow approach in this region, as it has been extensively used in studies of the hydraulic jump for a Newtonian fluid (Duchesne *et al.* 2014; Wang & Khayat 2018, 2019, 2020). This approach has been used in various viscoplastic flow problems as well (Liu & Mei 1989; Balmforth & Craster 1999; Balmforth *et al.* 2007a, b; Matson & Hogg 2007; Liu *et al.* 2016, 2018, 2019). In addition to the general formulation, we will discuss the determination of the film thickness at the edge of the disk and the jump length.

5.4.1 The flow in the subcritical region

By neglecting the effect of inertia, equations (5.2.8a) and (5.2.8b) reduce to:

$$\frac{\text{Re}}{\text{Fr}^2} H' = -\frac{B}{H-H_0}, \quad H_0 < z < H, \quad (5.4.1)$$

$$\frac{\text{Re}}{\text{Fr}^2} H' = nu_z^{n-1} u_{zz}, \quad 0 < z < H_0. \quad (5.4.2)$$

Here, we use H and H_0 for the film height and fully-yielded layer thickness in the subcritical region to differentiate them from h and h_0 in the supercritical region. Integrating equation (5.4.2) twice and using conditions (5.2.4a) and (5.2.6b), we can obtain the velocity profile in the fully-yielded layer as

$$u(r > r_J, 0 < z < H_0) = \frac{n}{n+1} \left(\frac{B}{H-H_0} \right)^{1/n} H_0^{\frac{n+1}{n}} \left[1 - \left(1 - \frac{z}{H_0} \right)^{\frac{n+1}{n}} \right]. \quad (5.4.3)$$

The velocity in the pseudo-plug layer is obtained by setting $z = H_0$:

$$U(r > r_J) = \frac{n}{n+1} \left(\frac{B}{H-H_0} \right)^{1/n} H_0^{\frac{n+1}{n}}. \quad (5.4.4)$$

We note that the model employed here is the gravity-driven shallow viscoplastic model (Liu & Mei 1989; Balmforth & Craster 1999; Balmforth *et al.* 2007a/b; Matson & Hogg 2007; Liu *et al.* 2016, 2018, 2019). Expression (5.4.4) suggests that the subcritical surface velocity decreases as a result of the decreases in the yielded-layer height and relative increase in the pseudo-layer height.

Upon substituting (5.4.3) and (5.4.4) into (5.2.7), the conservation of mass yields

$$\frac{n}{n+1} \left(\frac{B}{H-H_0} \right)^{1/n} H_0^{\frac{n+1}{n}} \left(H - \frac{n}{2n+1} H_0 \right) = \frac{1}{2r}. \quad (5.4.5)$$

Evidently, $H(r)$ and $H_0(r)$, and therefore $U(r)$, depend on position r , highlighting how the flow in $H_0 < z < H$ is only a pseudo-plug, which is an extensional flow in the radial direction (Muravleva 2019).

H and H_0 are governed by equations (5.4.1) and (5.4.5), which can be solved as a differential-algebraic system. A more convenient alternative is to differentiate (5.4.5) to obtain a second-order system of ODEs. In this case, two boundary conditions are needed, for H and H_0 .

5.4.2 Estimating the edge thickness and yielded layer height

We, therefore, choose to impose the film thickness $H_\infty \equiv H(r = R_\infty)$ at the edge of the disk. The height $H_{0\infty} \equiv H_0(r = R_\infty)$ of the fully-yielded layer at the edge is then obtained from (5.4.5). The present approach and existing literature do not capture well the flow usually observed at the edge of the disk. For a Newtonian film, Watson (1964) simply assumed a constant film height downstream of the jump, but this assumption makes no sense here if we consider a free-dropping condition at the disk edge, and a complex upstream influence of the actual conditions in the subcritical region should be taken into account. The specification of H_∞ remains largely unaddressed in the literature given the simultaneous influence of inertia, gravity and surface tension near the edge (Higuera 1994).

Direct measurements by Duchesne *et al.* (2014) of the edge thickness, give a nearly constant (independent of the jet flow rate) value when using silicone oil as the working fluid. This constant thickness, for a liquid of surface tension σ , is very close to the capillary length $\sqrt{\sigma/\rho g}$ of the fluid, which results from the balance of forces between the hydrostatic pressure and the surface tension (Young-Laplace law) at the disk perimeter. This value is also consistent with the measurements of Dressaire *et al.* (2010) for water and high flow rate. Consequently, we assume that the film thickness at the edge of the disk is essentially equal to the capillary length. The dimensionless form of the film thickness at the disk edge is therefore

$$H_\infty = c_1 \frac{\text{Fr}}{\sqrt{\text{ReCa}}}, \quad (5.4.6)$$

where c_1 is a constant dependent on the wetting properties of the edge of the disk. Its value should not exceed $\sqrt{2}$ (Landau & Lifshitz 1987). Expression (5.4.6) has been extensively used for the Newtonian problem (Duchesne *et al.* 2014; Wang & Khayat 2018/2019, Ipatova *et al.* 2021; Duchesne & Limat 2022), yielding a good agreement with experiment, particularly for the jump location and film profile. We observe that (5.4.6) should hold for both Newtonian and viscoplastic fluids; in the latter case, the fully-yielded layer thickness at the disk edge is deduced from (5.4.5).

On the other hand, and as the work of Higuera (1994) suggests, both inertia and gravity can become important near the edge. The acceleration of the flow increases significantly due to the strong effect of gravity around the edge. Consequently, at the edge, the wall shear stress should exhibit a singularity, and viscous effects are confined to a thin boundary layer that develops near the wall. In this case, we estimate the edge thickness by balancing the inertial and the hydrostatic pressure forces in the radial momentum equation, which gives $\text{Re}UU' \sim \frac{\text{Re}}{\text{Fr}^2} H'$, where U and H are the subcritical pseudo-plug velocity and film

thickness. Equivalently, we set $U^2 \sim 2 \frac{H}{\text{Fr}^2}$. To keep the treatment tractable, we limit the

argument to a Bingham fluid. In this case, (5.4.4) and (5.4.5) reduce to:

$$U = \frac{1}{2} \left(\frac{B}{H - H_0} \right) H_0^2, \quad H = H_0 + \frac{2}{3} \frac{BrH_0^3}{1 - BrH_0^2}, \quad (5.4.7a, b)$$

respectively. Substituting for U and H , assuming both H and H_0 to be small near the edge of the disk, and keeping dominant terms, we see that

$$H_\infty \approx H_{0\infty} = c_2 \left(\frac{Fr}{R_\infty} \right)^{2/3} \left(1 - c_3 B \left(\frac{Fr^4}{R_\infty} \right)^{1/3} \right), \text{ where } c_2 \text{ and } c_3 \text{ are positive constants.}$$

Wang & Khayat (2019) obtained an exact expression in the Newtonian limit based on the minimization of the free energy at the edge of the disk, yielding $c_2 = \left(\frac{3}{40} \right)^{1/3}$. In addition,

one can ask: at what distance from the disk edge does inertia become important? For the planar flow of a Newtonian fluid over a plate, Higuera (1994) estimated the order of magnitude of the region near the edge where inertia effects cease to be negligible in the

subcritical region, to be $1 - x = O \left(\frac{Fr^2 Re^3}{L^3} \right)^{1/3}$. This range is recast here in terms of the

jet Froude and Reynolds numbers, where L is the half-length of the plate scaled by the half-width of the jet, and $x = 1$ coincides with the edge of the plate. A similar formula for the

axisymmetric flow of a Newtonian fluid: $1 - \frac{r}{R_\infty} = O \left(\frac{Fr^2 Re^3}{R_\infty^8} \right)^{1/3}$, where we recall R_∞

to be the dimensionless disk radius. Similarly, for a Bingham fluid, keeping terms of order

B , and recalling the leading-order term $H \approx \left[\frac{6Fr^2}{Re} \ln \left(\frac{R_\infty}{r} \right) \right]^{1/4}$ for a Newtonian fluid

(Duchesne 2014), we arrive at the following correction for the distance upstream of the edge where inertial effects become important for a weakly viscoplastic fluid:

$$1 - \frac{r}{R_\infty} = O \left[\left(\frac{Fr^2 Re^3}{R_\infty^8} \right)^{1/3} \left(1 - \frac{8}{3} BR_\infty H_\infty^2 \right) \right]. \text{ Consequently, this distance diminishes as}$$

the yield stress and disk radius increase.

Clearly, an accurate estimate of the edge thickness remains an open issue. The measurements of Duchesne *et al.* (2014) give a thickness very close to (5.4.6) with $c_1 = 1$, for both partially and fully wetted disks. This means that inertia effects are not as important as surface tension. This corroborates the findings of Wang & Khayat (2019) in their comparison between theory and experiment for the location and height of the jump. Given these observations and since the present estimates above point to an even more diminished effect of inertia due to the yield stress, and therefore the dominance of surface tension near the edge, we adopt expression (5.4.6), setting $c_1 = 1$, in the calculations reported below.

5.4.3 Conservation of mass and momentum across the jump

To determine the location of the hydraulic jump, the momentum balance is applied across the jump. The balance equation takes the same form as in the Newtonian case. Adding the radial contribution of surface tension (Bush & Aristoff 2003; Duchesne *et al.* 2014; Wang & Khayat 2019), we have

$$\text{Re} \left[\int_0^{h_J} u^2(r_{J-}, z) dz - \int_0^{H_J} u^2(r_{J+}, z) dz \right] = \frac{\text{Re}}{2\text{Fr}^2} (H_J^2 - h_J^2) + \frac{1}{\text{Ca}} \frac{H_J - h_J}{r_J}. \quad (5.4.8)$$

Here, we conveniently let r_{J-} and r_{J+} denote the radial position immediately up- and downstream of the jump, respectively. We also recall that $h_J \equiv h(r = r_{J-})$ and $H_J \equiv H(r = r_{J+})$ are the film height immediately upstream and downstream of the jump, with corresponding pseudo-plug layer velocities denoted U_{J-} and U_{J+} . It should be noted that the influence of the yield stress enters into the balance equation through the parameters in the supercritical and subcritical regions. It does not show explicitly in equation (5.4.8). This is a consequence of the abrupt jump assumption, resulting in the vanishing of the shear stress term. We note that the gravity term immediately upstream of the jump is kept in (5.4.8). Although this term is generally negligible for a Newtonian or power-law jump (Zhao & Khayat 2008), it is expected to be more significant for a smaller jump height, as in the viscoplastic case. We also note that equation (5.4.8) is similar to equation (69) in Liu & Mei (1994) for a stable Bingham flow shock. Finally, we observe that although the

surface tension effect is generally less important for viscoplastic fluids relative to Newtonian fluids, it is expected to be somewhat significant since the jump occurs closer to impingement as a result of the yield stress, leading to a smaller jump radius (see section 5.5). Following Duchesne *et al.* (2014), we can estimate the jump radius when the surface tension effect is significant. By equating the surface tension term with the gravity term in equation (5.4.8), we obtain a relation between the jump radius and average height

$$r_J \sim \frac{Fr^2}{ReCa} \frac{2}{H_J + h_J}. \text{ This relation shows that thicker jumps occur closer to impingement,}$$

and the product of jump radius and height is equal to the capillary length.

Upon carrying out the integrals over the fully-yielded and pseudo-plug layers, and using the velocity profiles (5.3.2), (5.4.3) and (5.4.4), equation (5.4.8) reduces to

$$Re \left(U_{J-}^2 [h_J + (\chi_2 - 1)h_{0J}] - U_{J+}^2 [H_J + (\chi_2 - 1)H_{0J}] \right) = \frac{Re}{2Fr^2} (H_J^2 - h_J^2) + \frac{1}{Ca} \frac{H_J - h_J}{r_J}. \quad (5.4.9)$$

We note that $U_{J+} = \frac{n}{n+1} \left(\frac{B}{H_J - H_{0J}} \right)^{1/n} H_{0J}^{\frac{n+1}{n}}$ is readily available from (5.4.4). Along

with equations (5.4.1) and (5.4.5) for the fully-yielded and pseudo-plug layer heights, equation (5.4.9) is used to determine the jump location.

5.4.4 The jump length for a Bingham fluid

Finally, another quantity of interest is the jump length (or width). Although we assumed a shock-like jump in our work, it is still possible to estimate the length of the jump. We follow closely the treatment of Avedisian & Zhao (2000), and apply the momentum balance across the jump of finite length L_J . By balancing the drag at the disk in the jump region with the fluid inertia, and assuming the dominance of viscous over gravity effects, Avedisian & Zhao (2000) obtained a relation between the length of the jump and its radius as $L_J r_J / h_J \approx 2 Re$ (in our notations) for a Newtonian fluid, where h_J is the film thickness just upstream of the jump (see also the different treatment of Razis *et al.* (2021) for a planar

jump). In order to keep the treatment tractable, we limit the analysis to a Bingham fluid without surface tension effects. In this case, equation (5.4.9) is modified to read

$$\operatorname{Re}\left(U_{J-}^2[h_J + (\chi_2 - 1)h_{0J}] - U_{J+}^2[H_J + (\chi_2 - 1)H_{0J}]\right) = \frac{\operatorname{Re}}{2\operatorname{Fr}^2}(H_J^2 - h_J^2) + L_J\tau_w(r = r_J), \quad (5.4.10)$$

where we recall that $U_{J-} = \frac{1}{2r_J[h_J - (1 - \chi_1)h_{0J}]}$ and $U_{J+} = \frac{1}{2}\left(\frac{B}{H_J - H_{0J}}\right)H_{0J}^2$ from

(5.3.3) and (5.4.7), respectively. From (5.3.9) the wall stress on one side of the jump is

$$\tau_w(r_{J-}) = 2\frac{U_{J-}}{h_{0J}} + B, \quad \text{while from (5.4.3) the stress on the other side is}$$

$$\tau_w(r_{J+}) = 2\frac{U_{J+}}{H_{0J}} + B. \quad \text{Its mean value at the jump is then } \tau_w(r = r_J) = \frac{U_{J-}}{h_{0J}} + \frac{U_{J+}}{H_{0J}} + B.$$

The jump length can then be found explicitly from (5.4.10) in terms of the heights of the super- and subcritical films, and the yielded layer thickness at the jump as

$$L_J = \frac{\frac{\operatorname{Re}}{2}\left(\frac{h_J - (1 - \chi_2)h_{0J}}{r_J^2[h_J - (1 - \chi_1)h_{0J}]^2} - \left(\frac{BH_{0J}^2}{H_J - H_{0J}}\right)^2 [H_J + (\chi_2 - 1)H_{0J}]\right) - \frac{\operatorname{Re}}{\operatorname{Fr}^2}(H_J^2 - h_J^2)}{\frac{1}{r_J h_{0J}[h_J - (1 - \chi_1)h_{0J}]} + \frac{BH_{0J}}{H_J - H_{0J}} + B}, \quad (5.4.11)$$

after using $\frac{B}{H_J - H_{0J}} = \frac{3}{2}\frac{1 - Br_J H_{0J}^2}{r_J H_{0J}^3}$ from (5.4.7b).

For a Newtonian film, $B = 0$, $h_{0J} = h_J$ and $H_{0J} = H_J$, so that (5.4.11) reduces to

$$L_J = \frac{\frac{\operatorname{Re}}{2r_J^2}\left(\frac{\chi_2}{\chi_1^2 h_J} - \frac{9\chi_2}{4H_J}\right) - \frac{\operatorname{Re}}{\operatorname{Fr}^2}(H_J^2 - h_J^2)}{\frac{1}{r_J}\left(\frac{1}{\chi_1 h_J^2} + \frac{3}{2H_J^2}\right)} \approx \left(\frac{\chi_2}{2\chi_1^2 r_J^2 h_J} - \frac{H_J^2}{\operatorname{Fr}^2}\right) \chi_1 \operatorname{Re} r_J h_J^2. \quad (5.4.12)$$

The approximation holds when $h_J \ll H_J$.

If we further neglect gravity, then $L_J \approx \frac{\chi_2}{2\chi_1} \frac{Re h_J}{r_J} = \frac{2}{5} \frac{Re h_J}{r_J}$, which is slightly different

from $L_J \approx 2 \frac{Re h_J}{r_J}$ of Avedisian & Zhao (2000). The difference in the numerical factors

results from the way we treated the integrals in (5.4.8). Finally, an explicit relation between

the jump length and radius can be obtained by substituting $h_J \approx \frac{2\chi_1\chi_3}{3\chi_2} \frac{r_J^2}{Re}$ (which applies

near the jump) from (5.3.11a), and $H_J \approx \left[\frac{6Fr^2}{Re} \ln \left(\frac{R_\infty}{r_J} \right) \right]^{\frac{1}{4}}$ into (5.4.12) to obtain

$$L_J \approx \left(\frac{3\chi_2^2 Re^2}{4\chi_1^3 \chi_3 r_J^4} - \sqrt{\frac{6Re}{Fr^2} \ln \left(\frac{R_\infty}{r_J} \right)} \right) \chi_1 \left(\frac{2\chi_1\chi_3}{3\chi_2} \right)^2 \frac{r_J^5}{Re^2}, \quad (5.4.13)$$

which suggests, given the dominance of the $O\left(Re^2\right)$ term, that $L_J \sim r_J$. This means that

the jump length is of the same order of magnitude as the jump radius. It is important to recall that this result is based on our including the stress term at the disk in equation (5.4.10), which does not correspond strictly to a shock.

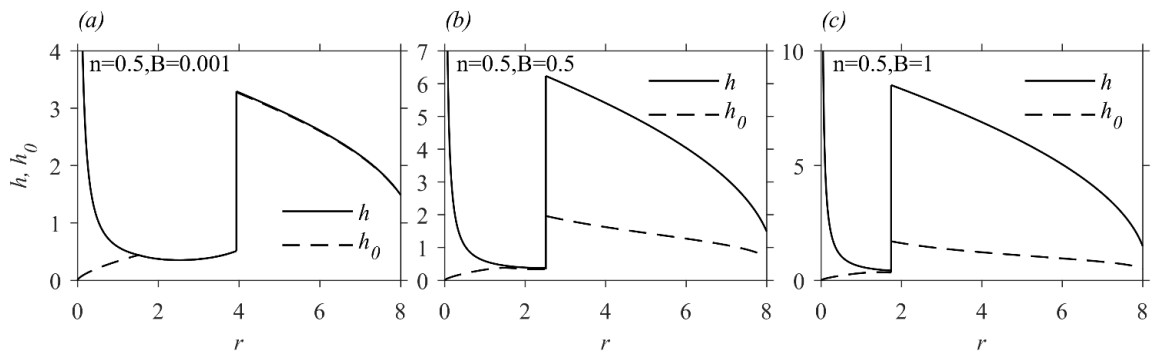
5.5 The influence of the yield stress and viscosity on the hydraulic jump

In this section, we report on the influence of the yield stress and viscosity on the entire flow, the supercritical and subcritical regions as well as the hydraulic jump. We will also report on the interplay among yield stress, viscosity, gravity, surface tension and disk size.

5.5.1 The film and yielded layer profiles

The overall effect of the yield stress and viscosity is illustrated in figure 5-7, which depicts the film height and shear layer thickness over the entire disk. Again, the result for $B = 0.001$ exhibits essentially the flow of a power-law fluid. In this limit, in the supercritical

region, the fully-yielded layer coincides with the boundary layer, and the fully-yielded layer invades essentially the entire film thickness after the transition point. This is also the case in the subcritical region where the pseudo-plug layer is almost non-existent (figures 5-7a, 5-7d and 5-7g). With an increase in fluid yield stress, the jump occurs further upstream (closer to impingement), the jump is higher, and the fully-yielded layer thickness decreases, especially in the subcritical region; overall, the pseudo-plug layer thickens. The subcritical profile in figure 5-7f is reminiscent of the “almost plastic” flow predicted by Balmforth & Liu (2004) for $B \rightarrow 1$, when the pseudo-plug fills almost the entire layer, reflecting how the fluid becomes dominated by the yield stress. Balmforth & Liu (2004) also observed that the problem can be reduced more directly in a manner similar to Oldroyd’s (1947) “plastic boundary-layer theory.” In contrast, both the film height and the fully-yielded layer thickness in the supercritical region remain relatively unaffected by fluid yield stress in comparison with the subcritical region. An interesting phenomenon is observed in figures 5-7h and 5-7i; the level of the fake yield surface immediately downstream of the jump becomes smaller than the surface level immediately upstream of the jump. It is clear that this feature can be achieved by either increasing the yield stress (see figures 5-7g to 5-7i) or increasing the power law index (see figures 5-7c, 5-7f and 5-7i). In fact, we will see this behaviour as well when reducing the disk size.



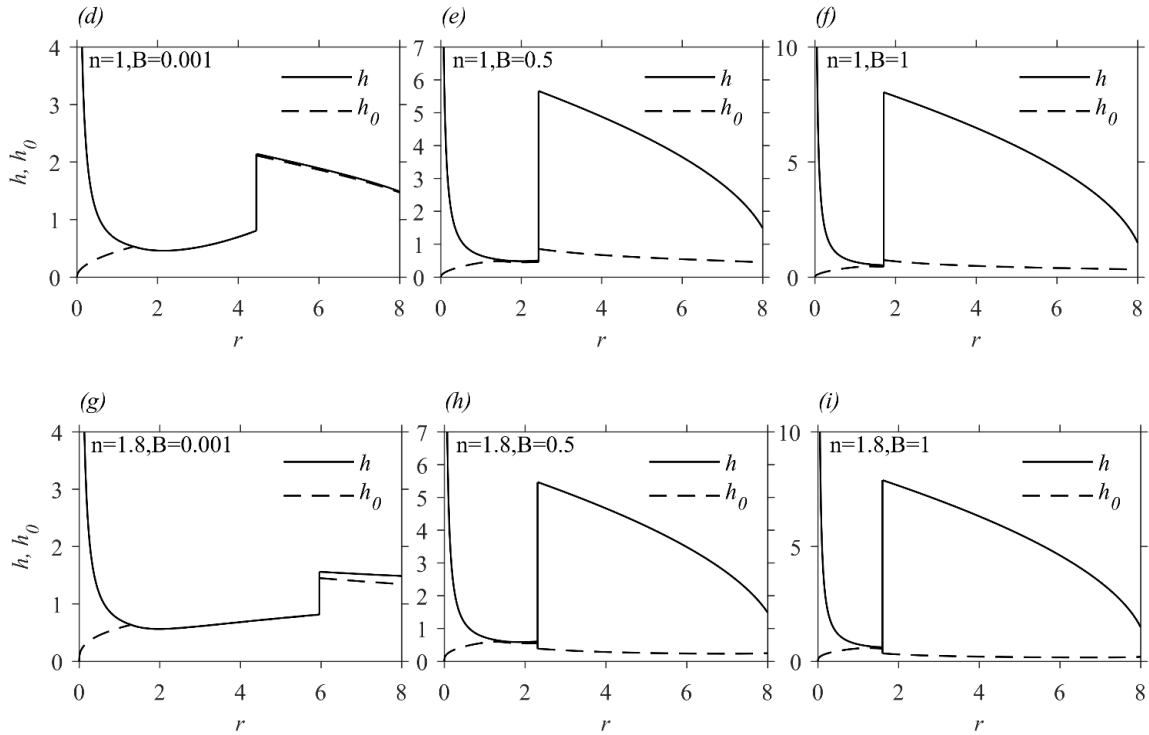


Figure 5-7: Influence of the yield stress on the film thickness h and the fully-yielded layer thickness h_0 in the supercritical and subcritical regions. Shown are the profiles for $n < 1$ (a-c), $n = 1$ (d-f) and $n > 1$ (g-i). Here, $Re = 50$, $Fr = 15$, $Ca = 2$ and $R_\infty = 8$.

Unlike the influence of the yield stress on the jump location, the influence of the power-law rheology on the jump location is only felt when B is small. However, visible differences can be seen in the influence of n on downstream heights; both the film height and fully-yielded layer thickness decrease with the increase of n in the subcritical region. The influence of the power-law index on the fully-yielded layer thickness is similar to the observation in Muravleva (2019), where the fully-yielded layer thickness shrinks with the growth of the power-law index for the central part where the pseudo-plug layer velocity is small, although this feature is contrary when B is relatively large. As for the thinner film height for a larger n value, it is similar to the observation in Huang & García (1998), who reported a thinner film depth away from the wave front for a large power-law index when fixing yield stress. We also note that the dependence of h_0 on n in the subcritical region is different from the behaviour of h_0 in the supercritical region, where h_0 increase with the increase of n . This behaviour is also observed in Muravleva (2019), as the fully-yielded

layer thickness decreases and increases with increasing of n in the central (small pseudo-plug layer velocity) and outer (large pseudo-plug layer velocity) regions, respectively. Interestingly, the influence of the power-law rheology is only manifest when B is small. For larger yield stress, the fluid behaves increasingly as a Bingham fluid as far as the jump radius and height are concerned; only the fully-yielded layer thickness remains sensitive to the power-law rheology.

Figure 5-8 illustrates the influence of the yield stress on the pseudo-plug layer velocity (figure 5-8a) and wall shear stress (figure 5-8b) distributions in both the supercritical and subcritical regions for a Bingham fluid. The velocity and stress decrease with the radial distance in the supercritical region, drop sharply across the jump as a result of the film thickening, and then remain relatively flat further downstream. The velocity and stress increase sharply at the disk edge as the flow accelerates under gravity, especially for the more viscoplastic fluid. In reality, we expect the flow to be singular at the disk edge. As the jump radius becomes smaller with the increase in B , the difference between the subcritical and supercritical pseudo-plug layer velocity and wall shear stress increases significantly, and a smaller pseudo-plug layer velocity is observed in the subcritical region. Interestingly, in contrast to the film height, we see that the velocity is far more influenced by yield stress in the supercritical region.

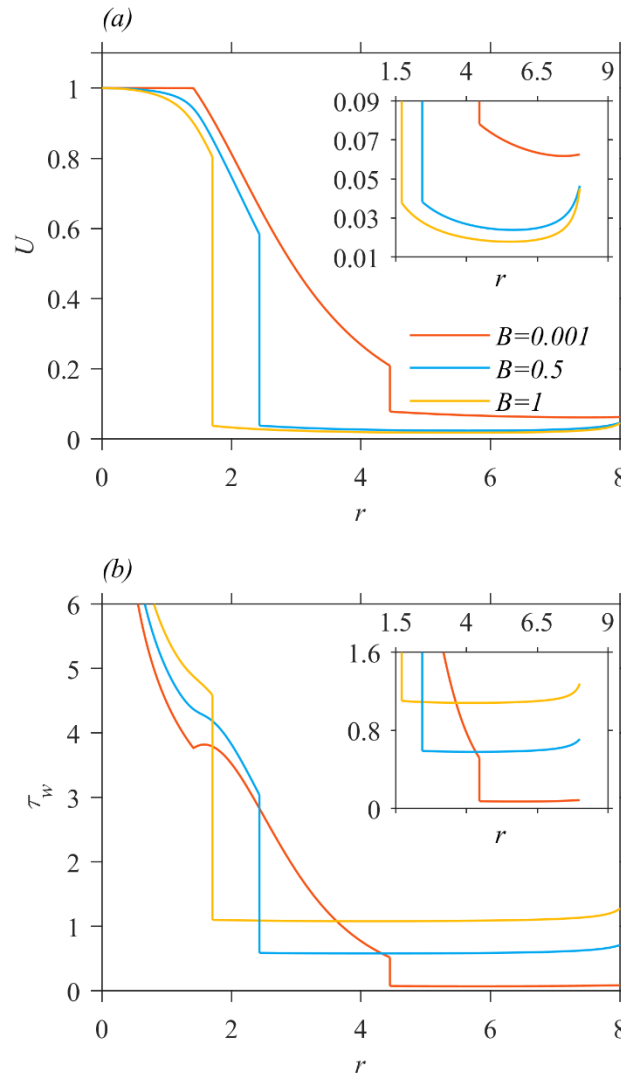


Figure 5-8 Influence of the yield stress on the pseudo-plug layer velocity U (a) and the wall shear stress τ_w (b) for a Bingham fluid. Insets show the magnification over the subcritical region. Here, $Re = 50$, $Fr = 15$, $Ca = 2$ and $R_\infty = 8$.

5.5.2 The jump radius and height

Further details on the influence of the yield stress on the hydraulic jump location for the three types of fluid and heights for a Bingham fluid are given in figure 5-9. The radius of the jump decreases monotonically with B for all fluid types. The value of n seems to have a small effect on the radius of the jump, especially for large B (figure 5-9a). The decrease in jump radius is expected, as the yield stress reduces the spread of the flow. A similar effect has also been observed in previous studies on the spreading of viscoplastic fluid

films and drops (Jiang & Leblond 1993; Huang & García 1998; Balmforth *et al.* 2000, 2002; Balmforth *et al.* 2007a; Jalaal *et al.* 2021) and viscoplastic dambreaks (Mei & Yuhi 2001; Balmforth *et al.* 2007b; Matson & Hogg 2007; Liu *et al.* 2016, 2018). The increase in jump size with increasing n found for small B is reminiscent of the findings of Huang & García (1998) and Balmforth *et al.* (2000), who reported that, for the mud flows down a slope or the spreading of isothermal lava domes, a smaller value of n results in a shorter spreading distance.

In addition, the results of Huang & García (1998) also show that the influence of the power-law index n on the spreading distance diminishes with rising yield stress, so a weaker dependence of spreading distance on n is expected when the yield stress increases. Liu *et al.* (2016, 2018) reported that the final state of a dam-break flow is controlled by the yield stress, and is either independent of or weakly dependent on the nonlinear viscosity, which seems to be consistent with the behaviour observed in figure 5-9a. Moreover, if B is sufficiently large, the jump radius becomes smaller than 1, meaning that the jump occurs in the impingement zone. In fact, Higuera (1994) found that the jump may crash onto the inlet when the Froude number is sufficiently small. This situation gives rise to another flow regime, which is not considered here.

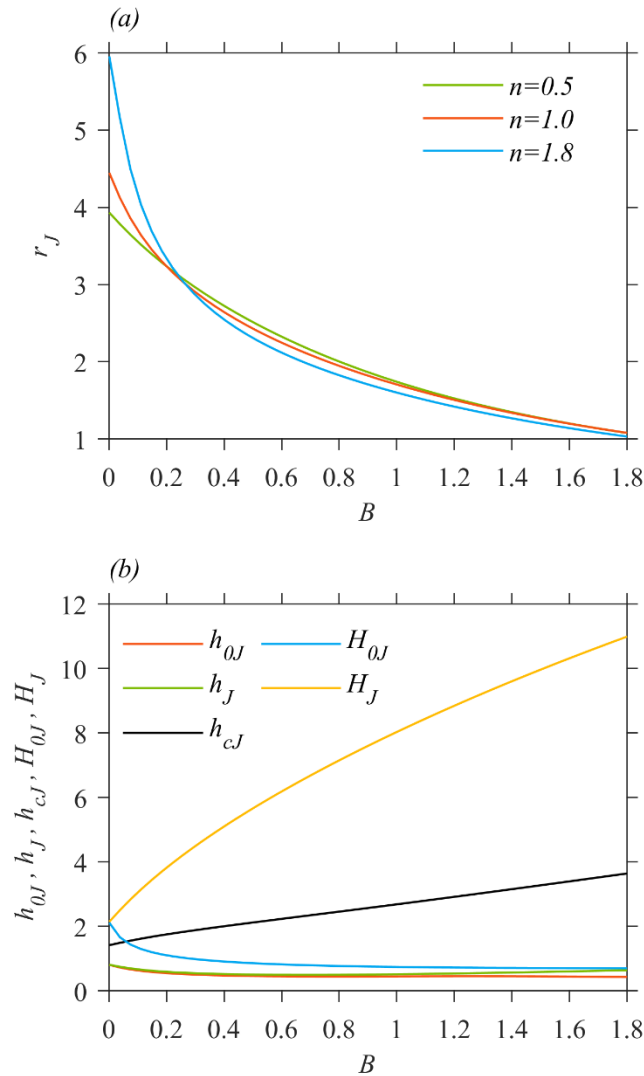


Figure 5-9: The influence of yield stress on (a) the hydraulic jump location r_J for $n = 0.5, 1$ and 1.8 , and (b) the film height and fully-yielded layer thickness immediately upstream of the jump, h_J and h_{0J} , downstream of the jump, H_J and H_{0J} , and the critical film height at the jump h_{cJ} for $n = 1$. Here $Re = 50$, $Fr = 15$, $Ca = 2$, and $R_\infty = 8$.

Figure 5-9b illustrates the influence of the yield stress on the film height and shear layer thickness immediately upstream (h_J and h_{0J}) and downstream (H_J and H_{0J}) of the jump, and on the critical film height at the jump h_{cJ} , for the Bingham fluid. H_J grows significantly with increasing B , whereas h_{0J} , h_J and H_{0J} decrease weakly with B for B

> 0.2 . We also include in figure 5-9b the critical film height at the jump, h_{cJ} , which separates the supercritical and subcritical regions (Liu & Lienhard 1993; Liu & Mei 1994; Watanabe *et al.* 2003). We determine h_{cJ} by following the treatment of Watanabe *et al.* (2003). It is not difficult to show, in the absence of surface tension, and approximating the velocities immediately up- and downstream of the jump with the average velocities, that the jump height ratio H_J/h_J can be obtained from (5.4.8) in terms of the local upstream and downstream Froude numbers $Fr_{J-} = \sqrt{Fr^2 \langle u_{J-} \rangle^2 / h_J}$ and $Fr_{J+} = \sqrt{Fr^2 \langle u_{J+} \rangle^2 / H_J}$ as

$$\frac{H_J}{h_J} = \frac{\sqrt{1 + 8Fr_{J-}^2} - 1}{2} = \frac{2}{\sqrt{1 + 8Fr_{J+}^2} - 1}, \quad (5.5.1)$$

where $\langle u_{J-} \rangle$ and $\langle u_{J+} \rangle$ are the mean radial velocities across the film immediately up- and downstream of the jump. Upon setting $H_J/h_J = 1$ in (5.5.1), and noting that $\langle u_{J-} \rangle h_J = \langle u_{J+} \rangle H_J = \frac{1}{2r_J}$ from (5.2.7), we obtain the critical height at the jump:

$$h_{cJ} = \left(\frac{Fr}{2r_J} \right)^{2/3}. \quad (5.5.2)$$

Noting that $Fr_{J-} = (h_{cJ}/h_J)^{3/2}$ and $Fr_{J+} = (h_{cJ}/H_J)^{3/2}$, we see, as in the Newtonian case (Watanabe *et al.* 2003), that $h_J < h_{cJ} < H_J$ and $Fr_{J-} > 1 > Fr_{J+}$, confirming that the jump connects a supercritical flow with $Fr_{J-} > 1$ on the shallower side ($h_J < h_{cJ}$) to a subcritical flow with $Fr_{J+} < 1$ on the deeper side ($H_J > h_{cJ}$). We note that the expression for h_{cJ} in (5.5.2) depends on the yield stress through the jump radius. In fact, as the jump radius decreases with increasing yield stress, the critical height increases (see figure 5-9b). Finally, although we assumed gravity to be negligible in the supercritical region, we obtained expressions (5.5.1) and (5.5.2) assuming that the effect of gravity becomes important at the leading edge of the jump.

5.5.3 Further parametric study

We now illustrate the influence of gravity on the jump location and corresponding heights only for a Bingham fluid in figure 5-10, as the trends for $n < 1$ and $n > 1$ Herschel-Bulkley fluids are similar. It is clear that the profile of the jump location of a Bingham fluid remains similar regardless of the yield stress; the jump size increases with increasing Fr until it reaches a maximum value, then decreases almost linearly (figure 5-10a). We note that this trend of r_j is different from that measured by Avedisian & Zhao (2000) for water, who reported that the jump radius grows as gravity drops. This discrepancy is expected since the film thickness at the disk edge was fixed for different levels of gravity in the experiment of Avedisian & Zhao (2000), whereas, in the present case, H_∞ rises with the diminishing of gravity (increasing of Fr) as (5.4.6) suggests. Higuera (1994) also showed that the jump radius grows with the reduction of gravity in a range of small Froude number in agreement with our results, but he did not investigate the large Fr range. In contrast to the non-monotonic response of the jump radius, the film height immediately downstream of the jump increases almost linearly with increasing Fr , whereas the fully-yielded layer thickness immediately up- and downstream of the jump and the film height immediately upstream of the jump almost remain constant in the whole range of Fr , and so are not influenced by gravity (figure 5-10b).

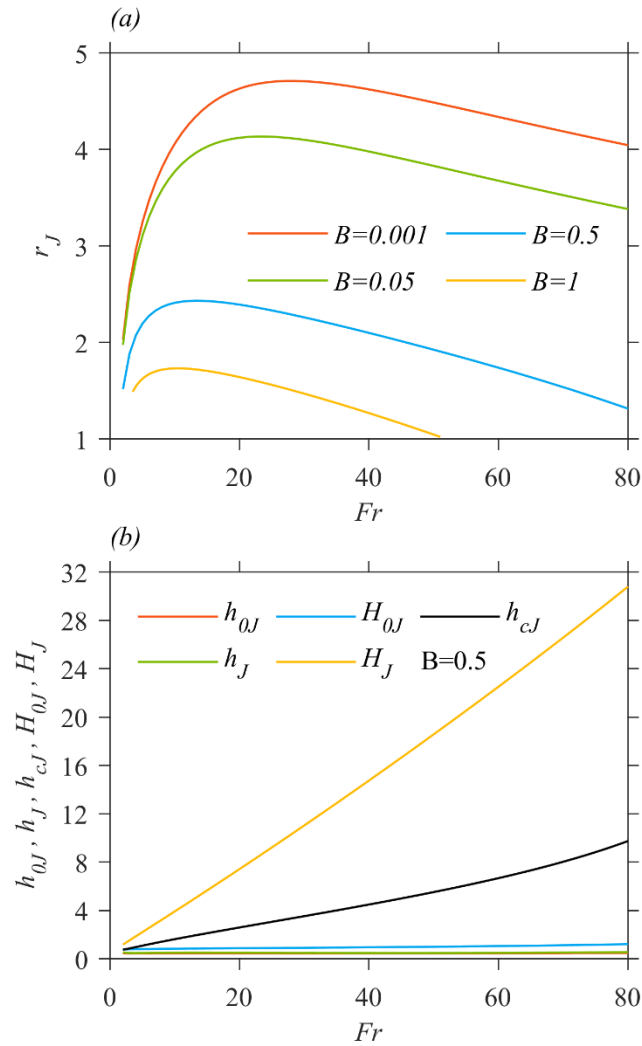


Figure 5-10: The influence of gravity on (a) the hydraulic jump location r_j for $B = 0.001, 0.05, 0.5$ and 1 , and (b) the film height and fully-yielded layer thickness immediately upstream of the jump, h_j and h_{0j} , downstream of the jump, H_j and H_{0j} , and the critical film height at the jump h_{cJ} for $B = 0.5$. Here $Re = 50$, $Ca = 2$, $n = 1$ and $R_\infty = 8$.

The interplay between surface tension and yield stress for a Bingham fluid is illustrated in figure 5-11, where the jump radius (figure 5-11a) and heights (figure 5-11b) are plotted against Ca . Figure 5-11a indicates that surface tension tends to inhibit the growth of the jump for any value of B . In particular, this corroborates the theoretical predictions of Aristoff & Bush (2003) and the experimental work of Bush *et al.* (2006) for a Newtonian jet. Generally, the influence of Ca on the radius of the jump is significant only when $Ca <$

3; beyond this value, r_J grows slowly with Ca , approaching the asymptotic limit obtained by excluding the surface tension effect in equations (5.4.6) and (5.4.8). A similar response is observed for the heights at the jump, which are almost independent of surface tension for large Ca (figure 5-11b).

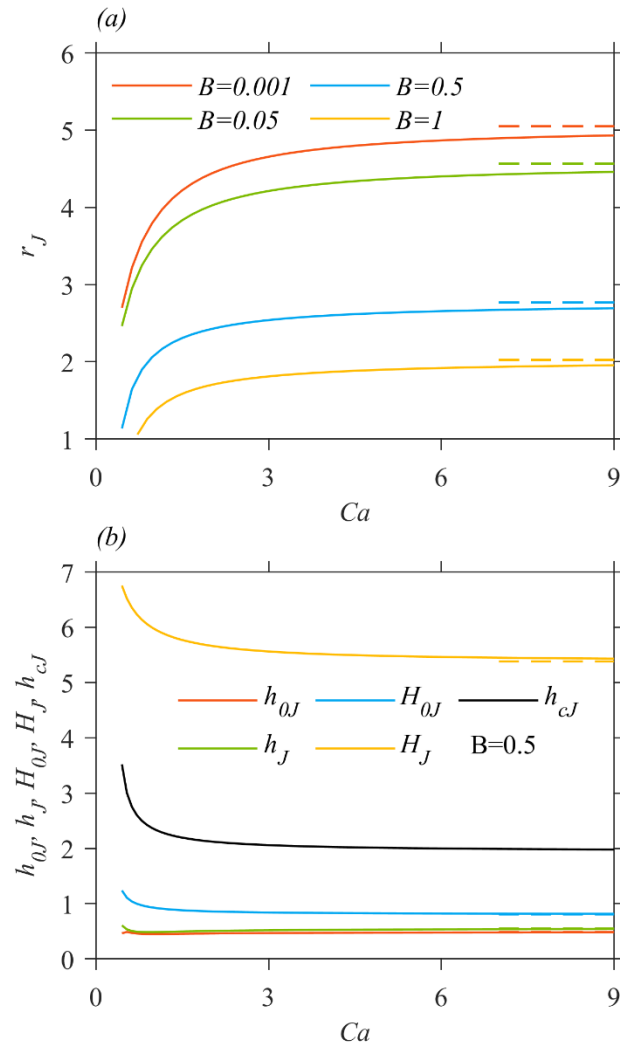


Figure 5-11: The influence of surface tension on (a) the hydraulic jump location r_J for $B = 0.001, 0.05, 0.5$ and 1 , and (b) the film height and fully-yielded layer thickness immediately upstream of the jump, h_J and h_{0J} , downstream of the jump, H_J and H_{0J} , and the critical film height at the jump h_{cJ} for $B = 0.5$. The dashed lines are asymptotic limits obtained by excluding the surface tension effect ($Ca \rightarrow \infty$) in equations (5.4.6) and (5.4.8). Here $Re = 50$, $Fr = 15$, $n = 1$ and $R_\infty = 8$.

The influence of the size of the disk on the hydraulic jump location and heights is given in figure 5-12. The jump radius decreases monotonically with the disk size, as for a Newtonian fluid (Kasimov 2008), but the influence of R_∞ for a fluid with higher yield stress is more pronounced (figure 5-12a). In addition, the jump can be washed out past the edge of the disk if the disk radius is not large enough, and this critical disk radius decreases with increasing yield stress (figure 5-12a). Figure 5-12b shows the influence of the radius of the disk on the film height and fully-yielded layer thickness immediately upstream of the jump, h_J and h_{0J} , downstream of the jump, H_J and H_{0J} , and the critical film height at the jump h_{cJ} for $B = 0.5$. The jump height H_J increases substantially with the disk radius, whereas h_{0J} , h_J and H_{0J} generally exhibit little change over the range of the disk radius considered here. The interesting behaviour of h_{0J} , h_J and H_{0J} for small R_∞ is shown in more detail in the inset; the yield surface on the upstream side of the jump surpasses the yield surface height downstream when the disk size is small enough.

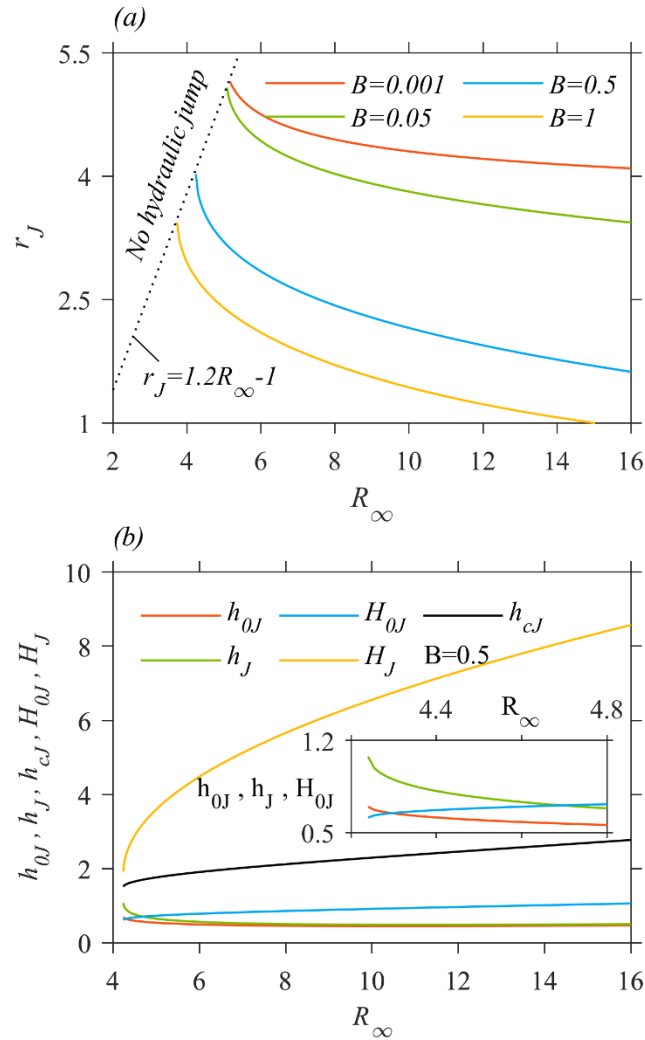


Figure 5-12: The influence of the radius of the disk R_∞ on (a) the hydraulic jump location r_J for $B = 0.001, 0.05, 0.5$ and 1 , and (b) the film height and fully-yielded layer thickness immediately upstream of the jump, h_J and h_{0J} , downstream of the jump, H_J and H_{0J} , and the critical film height at the jump h_{cJ} for $B = 0.5$. Here $Re = 50$, $Fr = 15$, $Ca = 2$, and $n = 1$. Inset in (b) shows enlarged behaviour for the small range of disk radius.

Next, we explore whether the local downstream Froude number Fr_{J+} for the viscoplastic fluid remains constant. In the measurements of Duchesne *et al.* (2014) for silicon oil, they found that this local Froude number is independent of the flow rate, kinematic viscosity and surface tension. Later, Mohajer & Li (2015) also found that the local Froude number is independent of the flow rate and disk size, but depends on surface tension. They

attributed this discrepancy to the difference in the edge flow conditions between their work and the work of Duchesne *et al.* (2014). Wang & Khayat (2019) gave an analytical and numerical perspective for this constant local Froude number. Recently, Dhar *et al.* (2020) reported that the Froude number immediately downstream of the jump varies mildly for a planar hydraulic jump when the Reynolds number, channel length and channel inclination are varied. Using the data from our results above, we explore whether Fr_{J+} is independent of the yield stress, gravity, surface tension and disk size. For this, we normalize the range of parameters B , Fr , Ca and R_∞ in figures 5-9 to 5-12 over the interval 0 to 1; each parameter P is now normalized according to $P_{Nor} = (P - P_{min}) / (P_{max} - P_{min})$. We note that the local downstream Froude number Fr_{J+} falls between 0.15-0.19 for large ranges when varying B , Fr , Ca and R_∞ , which seems to suggest that Fr_{J+} is almost a constant for the viscoplastic fluid, although this Froude number still has a weak dependence on these parameters. As we can see in figure 5-13, Fr_{J+} is strongly dependent on B , Fr , Ca and R_∞ when these parameters are small. The reason for the strong correlation between Fr_{J+} and B or R_∞ for the small range may be because the jump is close to the disk edge (see figures 5-9 and 5-12 for reference). In fact, the disk size is much larger than the jump radius in the experiments of Duchesne *et al.* (2014).

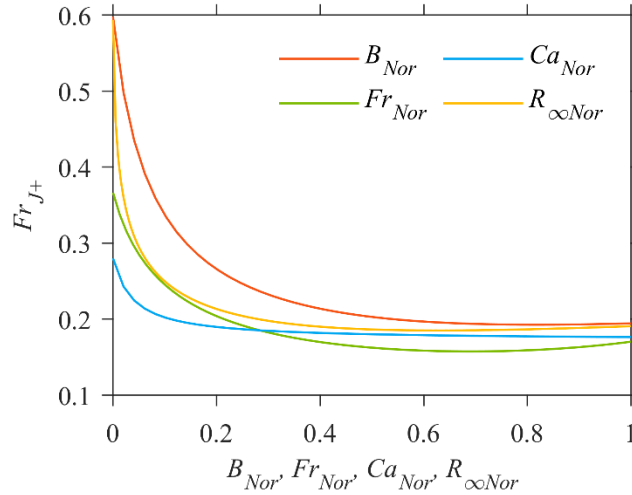


Figure 5-13: Dependence of Fr_{J+} on yield stress, gravity, surface tension and disk size. Here $Re = 50$, $Fr = 15$, $Ca = 2$, $B = 1$, $n = 1$ and $R_{\infty} = 8$ unless otherwise indicated in the figure.

Finally, we revisit some results of Zhou et al. (2007) on the planar jump in an open channel of relevance to the measurements of Ogihara & Miyazawa (1994), who examined the flow of Bingham fluids made of water and bentonite mixtures in a rectangular open channel. Figure 5-14 shows the dependence of the conjugate height ratio on the local Froude number upstream of the jump. The comparison between the theoretical results of Zhou *et al.* (2007) and the experimental data is included in the inset for reference. Zhou *et al.* observed that the experimental data are scattered, which may be due to the difficulty to measure the conjugate depths in the hydraulic jump. Their theoretical results as well as ours suggest a linear growth of the conjugate depth ratio with Fr_{J-} .

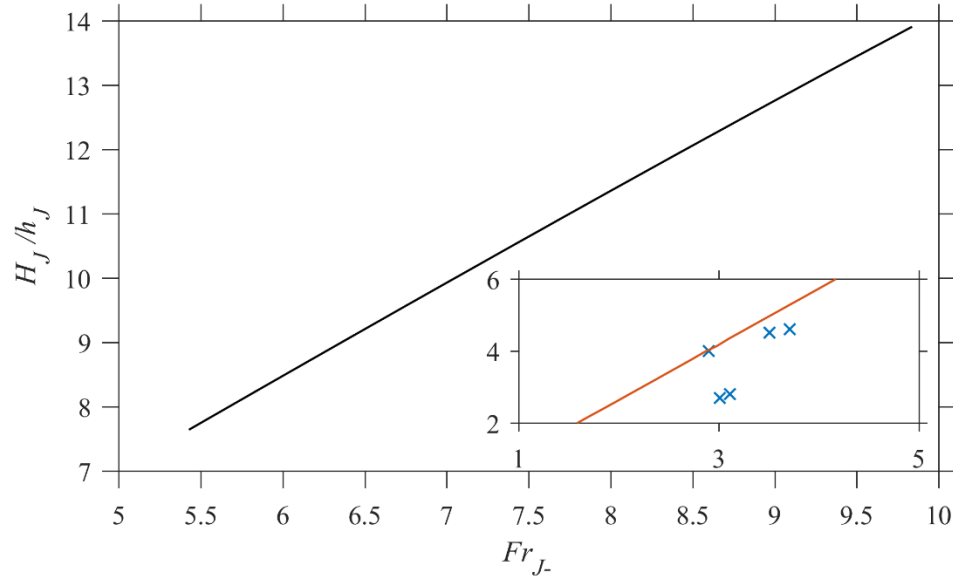


Figure 5-14: The dependence of the conjugate height ratio H_J/h_J on the local upstream Froude number Fr_{J-} . Here $Re = 601 - 1203$, $B = 0.2 - 0.1$, $Ca = 0.6 - 1.2$, $R_\infty = 30$ and $n = 1$. Inset shows the theoretical result of Zhou *et al.* (2006) in red line and the measurements of Ogihara & Miyazawa (1994) in blue \times symbols.

Figure 5-15 shows the dependence of the critical height on the Froude number, corresponding to the range of flow rate from the measurements of Ogihara & Miyazawa (1994) in the inset, which includes the theoretical result of Zhou *et al.* (2007). Our curve exhibits essentially a linear growth with flow rate with a decreasing slope in the higher Fr range. The trend is similar for both theory and experiment.

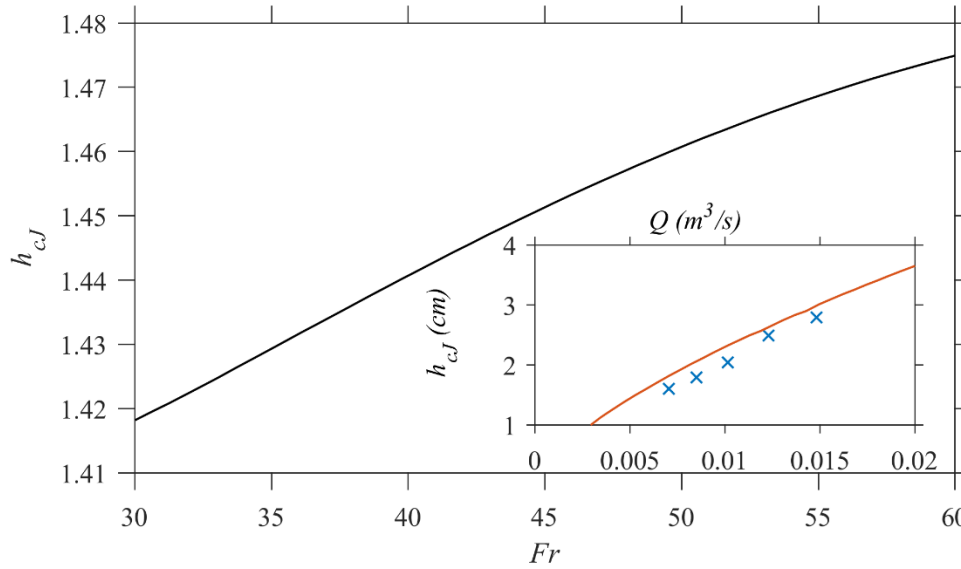


Figure 5-15: The dependence of the critical height on the flow rate or Froude number. Here $Re = 601 - 1203$, $B = 0.2 - 0.1$, $Ca = 0.6 - 1.2$, $R_\infty = 30$ and $n = 1$. Inset shows the theoretical result of Zhou *et al.* (2006) in red line and the measurements of Ogihara & Miyazawa (1994) in blue \times symbols.

5.6 Concluding remarks and discussion

In this study, we examined theoretically the spread of a jet impacting on a circular disk and the hydraulic jump structure of a viscoplastic fluid of the Heschel-Bulkley type. The supercritical flow is assumed to be of sufficient strength for inertia and viscous forces to dominate gravity. A depth-averaged approach is used to cast the conservation equations in weak form. The velocity profile is imposed in the fully-yielded region that satisfies conditions at the disk and the fake yield surface. The subcritical flow is assumed to be inertialess with dominant gravity and viscous effects. The jump is treated as a shock, where the balance of mass and momentum is established in the radial direction, including the effect of surface tension across the jump.

In contrast to the Newtonian flow, the viscoplastic flow does not require two separate formulations in the supercritical region, namely formulations in the developing boundary-layer and the fully-viscous sub-regions as suggested originally by Watson (1964). We show that the supercritical formulation for the fully-yielded and pseudo-plug layers is uniformly

valid in the radial direction between the impingement zone and the jump. Consequently, and importantly, a viscoplastic jet does not experience the discontinuity in the film height, pseudo-plug layer velocity gradient, and shear stress, predicted for a Newtonian film at the transition radial location along the disk (see Wang & Khayat 2018, 2019 and the references therein). We note that the viscoplastic formulation, which is valid over the entire supercritical region, is practically applicable for a non-yield stress (power-law or Newtonian) fluid by fixing the Bingham number to a small value (figures 5-2a, 5-2d and 5-2g).

We find that a larger yield stress leads to a lower pseudo-plug layer velocity and a higher wall shear stress (figure 5-3). The jump is found to occur closer to impingement, with growing height, as the yield stress increases; the subcritical region becomes increasingly invaded by the pseudo-plug flow layer (figures 5-7 and 5-9). In contrast, the influence of the power-law rheology (shear-rate dependence of the viscosity) is much weaker, except for a fluid with a small yield stress. The jump radius exhibits a maximum when varying the level of gravity, with increasing jump height immediately downstream of the jump (figure 5-10). The effect of gravity diminishes with increasing yield stress. We find that the location and height of the jump are increasingly influenced by surface tension as the yield stress increases (figure 5-11). We also assessed the influence of the disk radius, and found that a jump would not occur if the disk is smaller than a critical size. However, plasticity tends to enhance the formation of the jump compared to a Newtonian jet (figure 5-12). For a sufficiently large disk, the jump would occur in the impingement zone. We did not explore the flow details in the limits of small or a large disk. We suspect the thin-film approach breaks down if the film extent is too small (as in a transient moving film). For a large disk, the flow would likely behave as in the case of a surging fluid until steady conditions are reached.

The subcritical flow requires the value of the film and shear-layer heights at the edge of the disk. The value of the edge thickness or equivalent condition remains unaddressed in the Newtonian literature, and several different approaches have been proposed, such as posing a constant subcritical film height, and imposing an infinite slope (Kasimov 2008; Dhar *et al.* 2020). However, here we adopted the most likely plausible condition (Duchesne

et al. 2014; Ipatova *et al.* 2021) by assuming the edge thickness to be essentially equal to the capillary length as in expression (5.4.6). This is equivalent to balancing the gravity and surface tension forces at the edge of the disk based on the Young-Laplace law. We also derived an estimate of the edge thickness when inertia and gravity are in balance for a Bingham fluid. Following Higuera (1994), we also determined the order of magnitude of the distance from the edge where inertia effects become important. For a Newtonian fluid, the influence of surface tension was found greater than that of inertia (Wang & Khayat 2018, 2019).

The interplay between the yield stress and power-law rheology was found to be inconsistent, depending on the level of the yield stress, particularly downstream of the jump. As figure 5-7 indicates, the location and height of the jump remain relatively insensitive to the power-law rheology, except for very small yield stress. In contrast, the flow in the fully-yielded layer is very much influenced by the power-law index. The shear layer diminishes in thickness with increasing n , leaving an increasingly thicker pseudo-plug layer. Given our approximation of the jump as a shock makes it difficult to see what the real profile looks like. In this regard, what would the type of the smooth jump be? Would the Newtonian classification still hold (Bush & Aristoff 2003)? Given the small thickness at the edge of the disk, the jumps in figure 5-7 would likely correspond to type I, containing an eddy or a separation bubble near the disk, whose inner edge is located very close to the position of the abrupt change on the surface. Whether $n < 1$ or $n > 1$, figure 5-7 suggests that the eddy would be confined to a height closer to the disk due to the yield stress. This jump type is likely to lose its stability if the downstream thickness is increased, such as when a rim is imposed at the edge of the disk. In this case, what state will the jump transit to? Would wave-breaking occur as in the type II jump, where the flow develops an additional eddy? This roller is not likely to form beneath the film surface, as for a Newtonian fluid, given the relatively thick pseudo-plug layer. Capturing the vortex flow below a smooth jump has been challenging for a Newtonian fluid (Watanabe *et al.* 2003; Rojas *et al.* 2013), and is worth investigating for the viscoplastic case. In the present study, we adopted the generalized parabolic velocity profile for the Herschel-Bulkley model. In order to capture the vortex structure, a higher-order polynomial or spectral representation is needed that satisfies additional boundary conditions such as the momentum equation at

the disk. This, in turn, brings about a change in the class of the averaged governing system from parabolic to elliptic, thus transforming the problem from an initial-value to a two-point boundary-value problem. In this case, we expect the resulting upstream influence (Higuera 1994) to pose additional or different challenges for a viscoplastic fluid.

Additional interesting potential studies of relevance are worth mentioning here. First, many viscoplastic fluids can suffer an apparent slip along the solid surface, which is caused by a thin dilute layer near the wall (Piau & El-Kissi 1994; Jalaal *et al.* 2015; Muravleva 2019). The existence of an apparent slip can result in a lower wall shear stress and a large spread distance, as well as other consequences. It should be noted that the slip for a viscoplastic fluid on a smooth surface is not a true slip, but an apparent slip, which means that the fluid slips at the surface of a thin-fluid film near the solid (Cloitre & Bonnecaze 2017; Wang *et al.* 2021); a thin-dilute layer exists near the wall for a viscoplastic fluid. In fact, this apparent slip can be suppressed by manipulating the roughness of the wall surface, since the roughness can disrupt the thin-lubricated or thin-dilute layer. However, in order to inhibit slip by surface roughness, surface features that are much larger than the particle size or the largest dominating heterogeneity are created (Ballesta *et al.* 2013; Zakhari & Bonnecaze 2021). To describe the slip characteristic of the system, an effective slip length is normally used due to the complexity of the actual flow system (Niavarani & Priezjev 2009; Tsai *et al.* 2009; Dubov *et al.* 2018). In this case, it would be interesting to study the influence of roughness on the impinging viscoplastic jet and the resulting hydraulic jump. In fact, the influence of microdecorated surfaces on the thin-film Newtonian flow has already been investigated by Dressaire *et al.* (2010), who found that the patterned surface roughness modified the shape of the hydraulic jump. This modification resulted from the apparent slip between the liquid of the main flow and the liquid trapped in the microtextured surface.

Second, another interesting aspect is the influence of wettability on the flow of a viscoplastic fluid. For a Newtonian liquid droplet on an ideal flat solid surface, the wettability can be characterized by Young's equation, whereas the Wenzel model and Cassie-Baxter model can describe the wettability of a droplet on a surface with roughness (Lu, Wang & Duan 2016). For the dynamic wetting, it is usually characterized by the

relationship between the dynamic contact angle and the contact line velocity or the spreading radius versus the spreading time. There are already several studies focusing on the influence of the yield stress on the contact angle. Jalaal *et al.* (2021) investigated the effect of the yield stress on the spreading of a viscoplastic droplet on a chemically treated glass (to suppress any slip) both experimentally and theoretically. They found that the yield stress prohibits the spreading of the yield stress fluid, as the droplet converges to a final equilibrium shape once the driving stresses inside the droplet fall below the yield stress. In fact, Jørgensen (2016) also found a similar feature for the spreading of the viscoplastic droplet. These aspects can potentially be incorporated for a more accurate estimate of the thickness of the film as it drains at the edge of the disk (see figure 5-1), as well as when studying the transient formation of the hydraulic jump as it spreads before reaching the edge of the disk and the steady state.

Third, the present approach is based on a leading-order shallow-water formulation, where normal stress components are neglected. However, we suspect that the extensional and shear flows are of comparable strengths in the vicinity of the jump, and higher-order corrections are needed (Balmforth & Craster 1999; Balmforth & Liu 2004; Liu *et al.* 2019). Finally, a considerable effort has been devoted to the treating of the transient flow of viscoplastic fluid films, such as the expansion of lava domes (Balmforth *et al.* 2000), the evolution of extruded inclined domes (Balmforth *et al.* 2002), the transient spreading after a dam collapse (Liu *et al.* 2016, 2018), and the evolution of roll waves (Balmforth & Liu 2004), just to name a few. These studies can be of close relevance to the jump and vortex formation for an impinging viscoplastic jet.

Clearly, and in conclusion, there are many aspects left out in the present study of fundamental importance. The study should constitute the corner stone for future endeavours to elucidate the rich phenomena brought about by yield stress and fluid rheology for jet impingement and hydraulic jump of viscoplastic fluids.

5.7 References

- ACRIVOS, A., SHAH, M. & PETERSEN, E. E. 1960 Momentum and heat transfer in laminar boundary-layer flows of non-Newtonian fluids past external surface. *AIChE J.* **6**, 312 – 317.
- ANCEY, C. 2007 Plasticity and geophysical flows: a review. *J. Non-Newtonian Fluid Mech.* **142**, 4–35.
- AVEDISIAN, C. & ZHAO, Z. 2000 The circular hydraulic jump in low gravity. *Proc. R. Soc. London, Ser. A* **456**, 2127–2151.
- BAAYOUN, A., KHAYAT, R. E. & WANG, Y. 2022 The transient spread of a circular liquid jet and hydraulic jump formation. *J. Fluid Mech.* **947**:A34.
- BALLESTA P., KOUMAKIS N., BESSELING R., POON W.C.K. & PETEKIDIS G. 2013 Slip of gels in colloid–polymer mixtures under shear. *Soft Matter* **9**, 3237–3245.
- BALMFORTH, N.J., BURBIDGE, A.S., CRASTER, R.V., SALZIG, J. & SHEN, A. 2000 Viscoplastic models of isothermal lava domes. *J. Fluid Mech.* **403**, 37–65.
- BALMFORTH, N.J. & CRASTER, R.V. 1999 A consistent thin-layer theory for Bingham plastics. *J. Non-Newtonian Fluid Mech.* **84**, 65–81.
- BALMFORTH, N.J., CRASTER, R.V., PERONA, P., RUST, A.C. & SASSI, R. 2007b Viscoplastic dam breaks and the Bostwick consistometer. *J. Non-Newtonian Fluid Mech.* **142**, 63–78.
- BALMFORTH, N.J., CRASTER, R.V., RUST, A.C. & SASSI, R. 2007a Viscoplastic flow over an inclined surface. *J. Non-Newtonian Fluid Mech.* **139**, 103–127.
- BALMFORTH, N.J., CRASTER, R.V. & SASSI, R. 2002 Shallow viscoplastic flow on an inclined plane. *J. Fluid Mech.* **470**, 1–29.
- BALMFORTH, N.J., DUBASH, N. & SLIM, A. 2010. Extensional dynamics of viscoplastic filaments II. Drips and bridges. *J. Non-Newton. Fluid Mech.* **165**, 1147–60.

- BALMFORTH, N.J., FRIGAARD, I.A. & OVARLEZ, G. 2014 Yielding to Stress: Recent developments in viscoplastic fluid mechanics. *Annu. Rev. Fluid Mech.* **46**, 121–46.
- BALMFORTH, N.J. & HEWITT, I.J. 2013. Viscoplastic sheets and threads. *J. Non-Newton. Fluid Mech.* **193**, 28–42
- BALMFORTH, N.J. & LIU, J.J. 2004 Roll waves in mud. *J. Fluid Mech.* **519**, 33–54.
- BAONGA, J. B., GUALOUS, H. L. & IMBERT, M. 2006 Experimental study of hydrodynamic and heat transfer of free liquid jet impinging a flat circular heated disk. *Appl. Therm. Engng.* **26**, 1125–1138.
- BARNES, H. A. 1999 The yield stress—a review or “panta roi”—everything flows? *J. Non-Newtonian Fluid Mech.* **81**, 133–178.
- BAUER, H., BOESE, N. & STERN, N. 1995 Viscoplastic flow and shear thickening in concentrated diblock copolymer solutions. *Colloid Polym. Sci.* **273**:480-489.
- BENILOV, E. S. 2015 Hydraulic jumps in a shallow flow down a slightly inclined substrate. *J. Fluid Mech.* **782**, 5–24.
- BHAGAT, R. K., JHA, N. K., LINDEN, P. F., & WILSON, D. I. 2018 On the origin of the circular hydraulic jump in a thin liquid film. *J. Fluid Mech.* **851**, R5.
- BHAGAT, R. K. & LINDEN, P. F. 2020 The circular capillary jump. *J. Fluid Mech.* **896**, A25.
- BIRD, R. B., GANCE, D. & YARUSSO, B. J. 1983 The rheology and flow of viscoplastic materials. *Rev. Chem. Eng.* **1**, 1-70.
- BIRD, R. B., ARMSTRONG, R.C. & HASSAGER, O. 1987 Dynamics of Polymeric Liquids, Volume 1: Fluid Mechanics, 2nd edn. Wiley-Interscience.
- BOHR, T., DIMON, P. & PUTZKARADZE, V. 1993 Shallow-water approach to the circular hydraulic Jump. *J. Fluid Mech.* **254**, 635-648.

- BOHR, T., ELLEGAARD, C., HANSEN, A.E. & HAANING, A. 1996 Hydraulic jumps, flow separation and wave breaking: An experimental study. *Physica B* **228**, 1–10.
- BONN, D., ANDERSEN, A. & BOHR, T. 2009 Hydraulic jumps in a channel. *J. Fluid Mech.* **618**, 71-87.
- BUSH, J. W. M. & ARISTOFF, J. M. 2003 The influence of surface tension on the circular hydraulic jump. *J. Fluid Mech.* **489**, 229–238.
- BUSH, J. W. M., ARISTOFF, J. M. & HOSOI, A. E. 2006 An experimental investigation of the stability of the circular hydraulic jump. *J. Fluid Mech.* **558**, 33–52.
- CHAMBON, G., GHEMMOUR, A., & NAAIM, M. 2014 Experimental investigation of viscoplastic free-surface flows in a steady uniform regime. *J. Fluid Mech.* **754**, 332-364.
- CLOITRE, M. & BONNECAZE, R.T. 2017 A review on wall slip in high solid dispersions. *Rheol Acta* **56**, 283–305.
- CRAIK, A., LATHAM, R., FAWKES, M. & GIBBON, P. 1981 The circular hydraulic jump. *J. Fluid Mech.* **112**, 347–362.
- DE BRUYN, J.R., HABDAS, P. & KIM, S. 2002. Fingering instability of a sheet of yield-stress fluid. *Phys. Rev. E* **66**, 031504.
- DE SOUZA MENDES, P. R. 2009. Modeling the thixotropic behavior of structured fluids. *J. Non-Newtonian Fluid Mech.* **164**, 66-75.
- DENIER, J. P. & DABROWSKI, P. P. 2004 On the boundary-layer equations for power-law fluids. *Proc. R. Soc. Lond. A* **460**, 3143 – 3158.
- DHAR, M., DAS, G., & DAS, P. K. 2020 Planar hydraulic jumps in thin film flow. *J. Fluid Mech.* **884**. A11
- DRESSAIRE, E., COURBIN, L., CREST, J. & STONE, H. A. 2010 Inertia dominated thin-film flows over microdecorated surfaces. *Phys. Fluids* **22**, 073602.

- DUBOV, A. L., NIZKAYA, T. V., ASMOLOV, E. S., & VINOGRADOVA, O. I. 2018 Boundary conditions at the gas sectors of superhydrophobic grooves. *Phys. Rev. Fluids* **3**, 014002.
- DUCHESNE, A., LEBON, L. & LIMAT, L. 2014 Constant Froude number in a circular hydraulic jump and its implication on the jump radius selection. *Europhys. Lett.* **107**, 54002.
- DUCHESNE, A., ANDERS, A. & BOHR, T. 2019 Surface tension and the origin of the circular hydraulic jump in a thin liquid film. *Phys. Rev. Fluids* **4**, 084001.
- DUCHESNE, A., & LIMAT, L. 2022. Circular hydraulic jumps: where does surface tension matter? *J. Fluid Mech.* **937**, R2.
- ENGMANN, J., SERVAIS, C. & BURBIDGE, A.S. 2005. Squeeze flow theory and applications to rheometry: a review. *J. Non-Newton. Fluid Mech.* **132**,1–27.
- ESTELLE, P. & LANOS, C. 2012 High torque vane rheometer for concrete: Principle and validation from rheological measurements. *Appl. Rheol.* **22**, 12881.
- GERMAN, G. & BERTOLA, V. 2010a. Formation of viscoplastic drops by capillary breakup. *Phys. Fluids* **22**, 033101
- GERMAN, G. & BERTOLA, V. 2010b. The free-fall of viscoplastic drops. *J. Non-Newton. Fluid Mech.* **165**, 825–28.
- HEIRMAN, G., HENDRICKX, R., VANDEWALLE, L., FEYS, D., VAN GEMERT, D., DE SCHUTTER, G., DESMET, B & VANTOMME, J. 2009 Integration approach of the Couette inverse problem of powder type self-compacting concrete in a wide-gap concentric cylinder rheometer. Part II. Influence of mineral additions and chemical admixtures on the shear thickening flow behaviour. *Cement Concrete Res.* **39**, 171–181.
- HEIRMAN, G., VANDEWALLE, L., VAN GEMERT, D. & WALLEVIK, O. 2008 Integration approach of the Couette inverse problem of powder type self-compacting concrete in a wide-gap concentric cylinder rheometer. *J. Non-Newtonian Fluid Mech.* **150**, 93–103.

- HIGUERA, F. J. 1994 The hydraulic jump in a viscous laminar flow. *J. Fluid Mech.* **274**, 69–92.
- HOGG, A. J., & PRITCHARD, D. 2004 The effects of hydraulic resistance on dam-break and other shallow inertial flows. *J. Fluid Mech.* **501**, 179–212.
- HSU, T. T., WALKER, T. W., FRANK, C. W. & FULLER, G. G. 2011 Role of fluid elasticity on the dynamics of rinsing flow by an impinging jet. *Phys. Fluids* **23**, 033101.
- HUANG, X. & GARCÍA, M. H. 1998 A Herschel–Bulkley model for mud flow down a slope. *J. Fluid Mech.* **374**, 305–333.
- IPATOVA, A., SMIRNOV, K.V. & MOGILEVSKIY, E.I., 2021 Steady circular hydraulic jump on a rotating disk. *J. Fluid Mech.* **927**, A24.
- JALAAL, M., BALMFORTH, N. J. & STOEBER, B. 2015 Slip of spreading viscoplastic droplets, *Langmuir* **31**, 12071–12075.
- JALAAL, M., STOEBER, B. & BALMFORTH, N.J. 2021 Spreading of viscoplastic droplets. *J. Fluid Mech.* **914**, A21.
- JIANG, L. & LEBLOND, P. H. 1993 Numerical modeling of an underwater Bingham plastic mudslide and the waves it generates. *J. Geophys. Res.* **98**, 10 303–10 317.
- JØRGENSEN, L. 2016. Wetting of yield-stress fluids: capillary bridges and drop spreading (Doctoral dissertation, Université de Lyon).
- KAMRIN, K. & MAHADEVAN, L. 2012. Soft catenaries. *J. Fluid Mech.* **691**, 165–77.
- KANEKO, K., TAMENORI, A., ALLEBORN N., DURST F. 2007 Numerical and experimental investigation of wet chemical etching of silicon wafers. *ECS Trans.* **2**, 295.
- KASIMOV, A. R. 2008 A stationary circular hydraulic jump, the limits of its existence and its gasdynamic analogue. *J. Fluid Mech.* **601**, 189–198.

- KATE, R. P., DAS, P. K. & CHAKRABORTY, S. 2007 Hydraulic jumps due to oblique impingement of circular liquid jets on a flat horizontal surface. *J. Fluid Mech.* **573**, 247–263.
- KHAYAT, R. E. 2016 Impinging planar jet flow and hydraulic jump on a horizontal surface with slip. *J. Fluid Mech.* **808**, 258–289.
- KOBLITZ, A. R., LOVETT, S. & NIKIFORAKIS, N. 2018 Viscoplastic squeeze flow between two identical infinite circular cylinders. *Phys. Rev. Fluids* **3**, 023301-023316.
- KONERU, S.R., MANOHAR, R. 1968 Stagnation point flows of non-Newtonian power law fluids. *J. Appl. Maths. Phys. (ZAMP)* **19**, 84–88.
- LANDAU, L.D. & LIFSHITZ, E.M. 1987 Chapter X - One-dimensional gas flow. In *Fluid Mechanics*, 2nd edn (ed. L.D. Landau & E.M. Lifshitz), pp. 361–413 (Pergamon Press).
- LU, G., WANG, X.D. & DUAN, Y.Y. 2016 A critical review of dynamic wetting by complex fluids: from Newtonian fluids to non-Newtonian fluids and nanofluids. *Adv. Colloid Interface Sci.* **236**, 43-62.
- LI, Y., MU, J., XIONG, C., SUN, Z. & JIN, C. 2021 Effect of visco-plastic and shear-thickening/thinning characteristics on non-Newtonian flow through a pipe bend. *Phys. Fluids* **33**, 033102.
- LIENHARD, J. 2006 Heat transfer by impingement of circular free-surface liquid jets. In 18th National & 7th ISHMT-ASME Heat and Mass Transfer Conference, pp. 1–17. IIT.
- LIU, K.F. & MEI, C.C. 1989 Slow spreading of a sheet of Bingham fluid on an inclined plane. *J. Fluid Mech.* **207**, 505–529.
- LIU, K. & MEI, C.C. 1994 Roll waves on a layer of a muddy fluid flowing down a gentle slope—A Bingham model. *Phys. Fluids* **6**, 2577–2590.
- LIU, X. & LIENHARD, J. 1993 The hydraulic jump in circular jet impingement and in other thin liquid films. *Exp. Fluids* **15**, 108–116.

- LIU, Y., BALMFORTH, N. J., HORMOZI, S. 2018 Axisymmetric viscoplastic dambreaks and the slump test, *J Non-Newtonian Fluid Mech.* **258**, 45-57.
- LIU, Y., BALMFORTH, N. J., HORMOZI, S., & HEWITT, D. R. 2016 Two-dimensional viscoplastic dambreaks. *J Non-Newtonian Fluid Mech.* **238**, 65–79.
- LIU, Y., BALMFORTH, N. J., HORMOZI, S. 2019. Viscoplastic surges down an incline. *J Non-Newtonian Fluid Mech.* **268**, 1–11.
- MAITI, M.K. 1965 Axially-symmetric stagnation point flow of power law fluids. *J. Appl. Maths. Phys. (ZAMP)* **16**, 594–598.
- MATSON, G. P. & HOGG, A. J. 2007 Two-dimensional dam break flows of Herschel–Bulkley fluids: The approach to the arrested state. *J Non-Newtonian Fluid Mech.* **142**, 79–94.
- MEI, C.C. & M. YUHI 2001 Slow flow of a Bingham fluid in a shallow channel of finite width. *J. Fluid Mech.* **431**, 135–159.
- MOHAJER, B. & LI, R. 2015 Circular hydraulic jump on finite surfaces with capillary limit. *Phys. Fluids* **27**, 117102
- MULLAI VENTHAN, S., NISHA, M. S., SENTHIL KUMAR, P., & JAYAKARAN AMALRAJ, I. 2022 Heat transfer effect of SiC-GN hybrid nanocomposite with viscoplastic fluid in aircraft jet engine hoses. *Sustainable Energy Technologies and Assessments*, 52.
- MURAVLEVA, L. 2019 Axisymmetric squeeze flow of a Herschel–Bulkley medium. *J Non-Newtonian Fluid Mech.* **271**, 104147.
- NG, C.-O. & MEI, C. C. 1994 Roll waves on a shallow layer of mud modelled as a power-law fluid. *J. Fluid Mech.* **263**, 151–184.
- NGUYEN, Q.D. & BOGER, D.V. 1992 Measuring the Flow Properties of Yield Stress Fluids. *Annu. Rev. Fluid Mech.* **24**, 47–88.

- NIAVARANI, A., & PRIEZJEV, N. V. 2009 The effective slip length and vortex formation in laminar flow over a rough surface. *Phys. Fluids* **21**, 052105.
- OGIHARA, Y. & MIYAZAWA, N. 1994 Hydraulic Characteristics of Flow over Dam and Hydraulic Jump of Bingham Fluid. *J. Hydraul. Coastal Environ. Eng. Proc. Jpn. Soc. Civil Engineers* 485(II-26), 21–26 (in Japanese).
- OLDROYD, J. G. 1947 Two-dimensional plastic flow of a Bingham solid: a plastic boundary-layer theory for slow motion. *Proc. Camb. Phil. Soc.* **43**, 383–395.
- ORON, A., DAVIS, S.H. & BANKOFF, S.G. 1999 Long-scale evolution of thin liquid films. *Rev. Mod. Phys.* **69**, 931–980.
- OZAR, B., CETEGEN, B. M., & FAGHRI, A. 2003 Experiments on the flow of a thin liquid film over a horizontal stationary and rotating disk surface. *Exp. Fluids* **34**, 556–565.
- REAY, D. 2013 *Process Intensification*, 2nd, edn. Elsevier.
- PIAU, J. M. & EL-KISSI, N. 1994 Measurement and modelling of friction in polymer melts during macroscopic slip at the wall. *J Non-Newtonian Fluid Mech.* **54**, 121–142.
- PRINCE, J. F., MAYNES, D. & CROCKETT, J. 2012 Analysis of laminar jet impingement and hydraulic jump on a horizontal surface with slip. *Phys. Fluids* **24**, 102103.
- PRINCE, J. F., MAYNES, D. & CROCKETT, J. 2014 Jet impingement and the hydraulic jump on horizontal surfaces with anisotropic slip. *Phys. Fluids* **26**, 042104.
- RABIDEAU, B.D., LANOS, C, & COUSSOT P. 2009. An investigation of squeeze flow as a viable technique for determining the yield stress. *Rheol. Acta* **48**, 517–26
- RAHMANI, Y., HABIBI, M., JAVADI, A. & BONN D. 2011. Coiling of yield stress fluids. *Phys. Rev. E* **83**, 056327.
- RAYLEIGH, O. M. 1914 On the theory of long waves and bores. *Proc. R. Soc. Lond.* **A 90**, 324–328.

- RAZIS, D., KANELLOPOULOS, G., & VAN DER WEELE, K. 2021 Continuous hydraulic jumps in laminar channel flow. *J. Fluid Mech.* **915**, A8.
- ROBERTS, A. J. & LI, Z. 2006 An accurate and comprehensive model of thin fluid flows with inertia on curved substrates. *J. Fluid Mech.* **553**, 33–73.
- ROJAS, N., ARGENTINA, M. & TIRAPEGUI, E. 2013 A progressive correction to the circular hydraulic jump scaling. *Phys. Fluids* **104**, 187801.
- RUYER-QUIL, C. AND MANNEVILLE, P. 1998 Modeling film flows down inclined planes. *Eur. Phys. J. B* **6**, 277–292.
- RUYER-QUIL, C. & MANNEVILLE, P. 2000 Improved modeling of flows down inclined planes. *Eur. Phys. J. B* **15**, 357–369.
- SCHLICHTLING, H. & GERSTEN, K. 2000 *Boundary-Layer Theory*, 8th edn. Springer.
- SHU J. & ZHOU J. 2006 Characteristics of a hydraulic jump in Bingham fluid. *J. Hydraul. Res.* **44**, 421-426.
- STEVENS, J. & WEBB, B. W. 1992 Measurements of the free surface flow structure under an impinging free liquid jet. *Trans. ASME J. Heat Transfer* **114**, 79–83.
- TANI, I. 1949 Water jump in the boundary layer. *J. Phys. Soc. Japan* **4**, 212–215.
- TSAI, P., PETERS, A. M., PIRAT, C., WESSLING, M., LAMMERTINK, R. G., & LOHSE, D. 2009 Quantifying effective slip length over micropatterned hydrophobic surfaces. *Phys. Fluids* **21**, 112002.
- UGARELLI, R. & FEDERICO, V. D. 2007 Transition from supercritical to subcritical regime in free surface flow of yield stress fluids. *Geophys. Res. Lett.* **34**, L21402.
- UTRACKI, L. A. 1988 The rheology of two phase flows. In *Rheological Measurement*, ed. A. A. Collyer, D. W. Clegg, pp. 479-594. London: Elsevier.

- WALKER, T. W., HSU, T. T., FRANK, C. W. & FULLER, G. G. 2012 Role of shear-thinning on the dynamics of rinsing flow by an impinging jet. *Phys. Fluids* **24**, 093102.
- WALTON, I. C. & BITTLESTON, S. H. 1991 The axial flow of a Bingham plastic in a narrow eccentric annulus. *J. Fluid Mech.* **222**, 39–60.
- WANG, R., CHAI, J., LUO, B., LIU, X., ZHANG, J., WU, M., WEI, M. & MA, Z. 2021 A review on slip boundary conditions at the nanoscale: recent development and applications. *Beilstein J. Nanotechnol.* **12**, 1237–1251.
- WANG, Y. & KHAYAT, R. E. 2018 Impinging jet flow and hydraulic jump on a rotating disk. *J. Fluid Mech.* **839**, 525–560.
- WANG, Y. & KHAYAT, R. E. 2019 The role of gravity in the prediction of the circular hydraulic jump radius for high-viscosity liquids. *J. Fluid Mech.* **862**, 128–161.
- WANG, Y., & KHAYAT, R. 2020 The influence of heating on liquid jet spreading and hydraulic jump. *J. Fluid Mech.* **883**, A59.
- WANG, Y. & KHAYAT, R. E. 2021 The effects of gravity and surface tension on the circular hydraulic jump for low-and high-viscosity liquids: A numerical investigation. *Phys. Fluids* **33**, 012105.
- WATANABE, S., PUTKARADZE, V. & BOHR, T. 2003 Integral methods for shallow free-surface flows with separation. *J. Fluid Mech.* **480**, 233–265.
- WATSON, E. 1964 The spread of a liquid jet over a horizontal plane. *J. Fluid Mech.* **20**, 481–499.
- WHITE, F. 2006 *Fundamentals of Fluid Mechanics*. McGraw-Hill.
- YAHIA, A. 2011 Removal of a viscous film from a rigid plane surface by an impinging liquid jet. *Cement Concrete Res.* **41**, 230-235.

YAMAMURA, S., FUJIWARA, K., HONDA, K., YOSHIDA, H., HORIGUCHI, N., KANEKO, A., & ABE, Y. 2022 Experimental study of liquid spreading and atomization due to jet impingement in liquid–liquid systems. *Phys. Fluids* **34**, 082110.

ZAKHARI, M. E., & BONNECAZE, R. T. 2021 Slip of soft permeable particles near a wall. *Soft Matter* **17**, 4538-4549.

ZHAO, J. & KHAYAT, R. E. 2008 Spread of a non-Newtonian liquid jet over a horizontal plate. *J. Fluid Mech.* **613**, 411–443.

ZHOU J., SHU J. & STANSBY, P. K. 2007 Hydraulic jump analysis for a Bingham fluid. *J. Hydraul. Res.* **45**, 455-562.

ZHOU, G. & PROSPERETTI, A. 2022 Hydraulic jump on the surface of a cone. *J. Fluid Mech.* **951**, A20.

Chapter 6

6 Conclusion and recommendations for future works

6.1 Conclusion

In this thesis, the impinging axisymmetric jet of either a Newtonian or a viscoplastic fluid and the hydraulic jump of either a circular or a polygonal shape on a flat solid disk is examined theoretically. The polygonal hydraulic jump is induced by either the non-circularity of the disk or the azimuthal dependence film thickness at the disk edge. The thin-film approach and Kármán–Pohlhausen approach are adopted as the theoretical methods.

In Chapter 2, a composite mean-field thin-film approach consisting of subdividing the flow domain into three regions of increasing gravity strength (a developing boundary layer near impact, an intermediate supercritical viscous layer leading up to the edge of the jump and a region comprising the jump and subcritical flow) for the circular hydraulic jump of Newtonian fluid is proposed. Unlike the existing models (Watanabe *et al.* 2003; Roberts & Li 2006), the approach does not require any empirically or numerically adjusted boundary conditions. The model is validated extensively against the existing experimental measurements, numerical simulations of the boundary-layer equations and Navier-Stokes equations. The jump location is assumed to coincide with the change of concavity of the film surface, which is a reasonable assumption as the predicted jump radius is very close to the critical radius based on the local Froude number. It is found that a larger flow rate, smaller viscosity, and lower gravity level lead to a larger jump radius. In addition, the flow in the supercritical region is insensitive to the gravity level but is greatly affected by the viscosity of the fluid. Moreover, it is found that the existence of the jump is not necessarily commensurate with the presence of a recirculation zone.

In Chapter 3, based on the proposed composite approach, the characteristics of the circular hydraulic jump of Newtonian fluid are further investigated. The approach is further validated against both experiments and numerical simulations of Navier-Stokes equations. Although the flow in the supercritical region and jump radius is insensitive to the disk

radius, the flow in the subcritical region and vortex structure are found to be significantly affected by the disk size; the jump length and height, as well as the vortex size, decrease with the decrease of disk radius. The interplay between flow rate and disk size shows that the monotonicity of the jump height, jump length and vortex length with flow rate does not hold as the disk size becomes smaller than a critical value. By imposing the film thickness at the disk edge as the boundary condition, the approach is used to examine the influence of film edge thickness. It is found that the jump radius is pushed closer to the impingement as the edge film thickness increase, accompanied by a higher jump height, a steeper jump and a stronger recirculation zone. By keeping the dominant terms in the momentum balance equation across the jump, and assuming subcritical lubrication flow, a scaling law that takes the influence of disk size into account is proposed theoretically:

$$r_J \left[\ln(r_\infty / r_J) \right]^{1/8} \approx \frac{2}{3} Fr^{1/4} Re^{3/8}.$$

For a free-draining flow scenario, the film thickness at the disk edge is found to comprise a static component (capillary length), and a dynamic thickness component. The dynamic thickness component ($h_\infty \sim (Fr / r_\infty)^{2/3}$) is established by minimizing the Gibbs free energy of the flow at the disk edge, and is also the consequence of the flow becoming supercritical near the disk edge. By assuming negligible film slope and curvature at the leading edge of the jump and maximum height at the trailing edge, the jump length is found to be related to the jump radius as

$$L_J \sim Re \left(Fr^2 / r_J^5 \right)^{1/3}.$$

The vortex length follows the same behaviour. The energy loss and conjugate depth ratio exhibit a maximum with the flow rate, which originates from the descending and ascending branches of the film thickness in the supercritical region. The presence of the jump is not necessarily commensurate with that of a recirculation; the existence of the vortex closely depends on the upstream curvature and steepness of the jump. The surface separating the regions of existence/non-existence of the recirculation is given by the universal relation $Re^{10/3} Fr^2 = 9r_\infty^9 / 50$. The jump can be washed off the edge of the disk, particularly at low viscosity and small disk size.

In Chapter 4, the polygonal hydraulic jump of a Newtonian fluid induced by the azimuthal-dependent edge condition is studied theoretically. In contrast to the spontaneous non-

circular hydraulic found by Ellegaard *et al.* (1998), the loss of axial symmetry in the current thesis is induced by disk non-circularity or periodic edge film thickness. The jump is assumed to be shock-like, where the mass and momentum balance equation is used to determine the radius of the jump. To take the azimuthal flow in the subcritical region into consideration, the balance of mass and momentum is established in both the radial and azimuthal directions, including the non-axisymmetric effect of surface tension across the jump. It is found that the geometry of a non-circular disk has little influence on the shape of the jump, except when the jump occurs close to the disk edge, but the subcritical flow field can be highly non-axisymmetric even for an apparently circular jump. For a jet impinging on a circular disk with a variable film thickness at the disk edge, a small azimuthal variation in the edge thickness leads to a significant loss of axial symmetry. The nonlinearities in the balance equations across the jump cause an increase in the number of peaks and valleys as the disk radius decreases. Flow reversal occurs in the polar plane at alternating valleys.

In Chapter 5, the spread of a jet impacting on a circular disk and the hydraulic jump of a viscoplastic fluid of the Herschel-Bulkley type are examined theoretically. The depth-averaging approach is employed in the supercritical region, and the assumed velocity profile in this region is motivated by both the equilibrium uniform flow and the lubrication approximations (Balmforth & Liu 2004). The subcritical flow is assumed to be inertialess of the lubrication type. The jump is treated as a shock, where the balance of mass and momentum is established in the radial direction, including the effect of surface tension across the jump. In contrast to the Newtonian jet, which requires separate formulations in the developing-boundary layer and fully-viscous layers, the supercritical formulation for the fully-yielded and pseudo-plug layers is uniformly valid between the impingement zone and the jump. Consequently, a viscoplastic jet does not experience the discontinuity in the film height, pseudo-plug layer velocity gradient and shear stress, exhibited by a Newtonian film at the transition location. The jump is found to occur closer to impingement, with growing height, as the yield stress increases; the subcritical region becomes invaded by the pseudo-plug layer. The viscosity does not influence sensibly the jump location and height except for small yield stress; only the yielded layer is found to remain sensitive to the power-law rheology for any yield stress. In particular, shear thickening can cause the fully-

yielded layer to drop in height despite the jump in the film surface. It is also found that the jump would not occur if the disk was smaller than a critical size, but the yield stress tends to enhance the formation of the jump compared to a Newtonian jet. An almost constant local downstream Froude number also exists for a viscoplastic fluid. Finally, the current model can reduce to the limiting cases of Bingham, power-law and Newtonian fluids.

6.2 Recommendations for future works

For the proposed composite mean-field thin-film approach, the effect of surface tension is not included in this approach. Bush & Aristoff (2003) has established a corrected theory of Waston (1964), which takes the surface tension effects into account. They found that the surface tension effects become important when the jump radius is small. In addition, as shown in the current thesis, the surface tension effects also become important at the disk edge (see also Higuera 1994). Moreover, Askarizadeh *et al.* (2019) found that there are two different regimes in the jump formation: gravity- and capillary-dominant flow regimes. In this case, a model that includes the surface tension effects is work that is worth to be done in the future.

For the polygonal hydraulic jump induced by the azimuthally dependent edge conditions, the jump is assumed to be shock-like. In this case, the flow structure at the jump level is unclear. To gain a more comprehensive understanding of the flow features of the polygonal hydraulic jump, the approach proposed in Chapter 2 can be extended to the polygonal hydraulic jump. In this case, the flow characteristics, especially, the vortex structure at the jump level can be analyzed in detail.

For the impinging jet and hydraulic jump of viscoplastic fluid of Heschel-Bulkley type, the jump is also assumed to be shock-like, the boundary layer condition at the disk is no-slip, but many viscoplastic fluids can suffer an apparent slip along the solid surface, which is caused by a thin dilute layer near the wall (Piau & El-Kissi 1994; Jalaal *et al.* 2015; Muravleva 2019). In this case, it is worth exploring the slip effect on the flow and hydraulic jump.

Appendices

Appendix A: The thin-film equations and boundary conditions

In this appendix, we follow closely the treatment of Balmforth *et al.* (2000) to derive equations (5.2.2a-5.2.2b) and (5.2.3a-5.2.3b) from the full conservation equations. These equations govern the motion of the thin film flow of a yield-stress fluid. Consequently, we assume the film thickness to be small relative to its (horizontal) length. We therefore need to rescale the dimensionless variables in section 5.5.2 to assess their accurate weight in the equations and boundary conditions, leading up to the formulation in that section. In dimensional form, the conservation of mass and momentum for axisymmetric flow are

$$u_r + \frac{u}{r} + w_z = 0, \quad (\text{A1a})$$

$$\rho(uu_r + wu_z) = -p_r + \tau_{rr,r} + \tau_{rz,z} + \frac{\tau_{rr} - \tau_{\theta\theta}}{r}, \quad (\text{A1b})$$

$$\rho(uw_r + ww_z) = -p_z - \rho g + \tau_{zr,r} + \tau_{zz,z} + \frac{\tau_{rz}}{r}. \quad (\text{A1c})$$

A subscript for the velocity components u and w as well as a comma for the deviatoric stress components τ_{ij} denote partial differentials. In addition to $u(r, z=0) = w(r, z=0) = 0$, equations (A1) are solved subject to the kinematic and dynamic conditions at the free surface $z = h(r)$:

$$w = uh', \quad n_r t_r \tau_{rr} + (n_r t_z + n_z t_r) \tau_{rz} + n_z t_z \tau_{zz} = 0, \quad (\text{A2a, b})$$

$$-p + n_r^2 \tau_{rr} + 2n_r n_z \tau_{rz} + n_z^2 \tau_{zz} = -\sigma(\nabla \cdot \mathbf{n}). \quad (\text{A2c})$$

Here σ is the constant surface tension, \mathbf{t} and \mathbf{n} are the tangent and normal unit vectors at the surface, and $\sigma(\nabla \cdot \mathbf{n})\mathbf{n}$ is the normal curvature force per unit area associated with the local curvature of the free surface, $\nabla \cdot \mathbf{n}$. We thus have:

$$n_r = -\frac{h'}{\sqrt{1+h'^2}}, n_z = \frac{1}{\sqrt{1+h'^2}}, \quad t_r = \frac{1}{\sqrt{1+h'^2}}, t_z = \frac{h'}{\sqrt{1+h'^2}}, \quad (\text{A3a, b})$$

$$\nabla \cdot \mathbf{n} = -\frac{1}{r} \left(\frac{rh'}{\sqrt{1+h'^2}} \right)'. \quad (\text{A3c})$$

For a Herschel-Bulkley fluid, the constitutive model is conveniently reproduced from (2.1):

$$\tau_{ij} = \left(K\dot{\gamma}^{n-1} + \frac{\tau_0}{\dot{\gamma}} \right) \dot{\gamma}_{ij}, \quad \text{for } \tau \geq \tau_0, \quad (\text{A4a})$$

$$\dot{\gamma}_{ij} = 0, \quad \text{for } \tau < \tau_0. \quad (\text{A4b})$$

Here, we recall $\tau = \sqrt{\tau_{rz}^2 + \frac{1}{2}(\tau_{rr}^2 + \tau_{\theta\theta}^2 + \tau_{zz}^2)}$ and $\dot{\gamma} = \sqrt{\dot{\gamma}_{rz}^2 + \frac{1}{2}(\dot{\gamma}_{rr}^2 + \dot{\gamma}_{\theta\theta}^2 + \dot{\gamma}_{zz}^2)}$

are the second invariants of τ_{ij} and $\dot{\gamma}_{ij}$, respectively. We also have

$$\dot{\gamma}_{rr} = 2u_r, \quad \dot{\gamma}_{rz} = \dot{\gamma}_{zr} = u_z + w_r, \quad \dot{\gamma}_{zz} = 2w_z, \quad \dot{\gamma}_{\theta\theta} = 2u/r. \quad (\text{A6a-d})$$

Thus, we take the jet radius a as the length scale in the vertical direction for r , and the radius of the disk R as the length scale in the vertical direction for z . In this case, the jet radius is assumed to be small relative to R so that $\varepsilon \equiv a/R \ll 1$ becomes the small perturbation parameter in the problem. The radial velocity component u and pressure p remain scaled by the jet velocity W and $\rho g a$, respectively, while the vertical velocity component w is rescaled by εW . In this case, we take $\mu W/R$ as the scale for τ_{rr} , $\tau_{\theta\theta}$ and

τ_{zz} , and $\mu W/a$ for $\tau_{rz} = \tau_{zr}$, where we recall $\mu \equiv K \left(\frac{W}{a} \right)^{n-1}$. In this case, equation (A1a)

and condition (A2a) retain their original form in terms of the rescaled variables, and equations (A1b) and (A1c) are recast as:

$$\varepsilon \text{Re}(uu_r + ww_z) = -\varepsilon \frac{\text{Re}}{\text{Fr}^2} p_r + \varepsilon^2 \tau_{rr,r} + \tau_{rz,z} + \frac{\varepsilon^2}{r} (\tau_{rr} - \tau_{\theta\theta}), \quad (\text{A8a})$$

$$\varepsilon^2 \operatorname{Re}(uw_r + ww_z) = -\frac{\operatorname{Re}}{\operatorname{Fr}^2}(p_z + 1) + \varepsilon \left(\tau_{zr,r} + \tau_{zz,z} + \frac{\tau_{rz}}{r} \right). \quad (\text{A8b})$$

The dimensionless deviatoric normal and shear stress components are:

$$\tau_{rr} = 2 \left(\dot{\gamma}^{n-1} + \frac{\mathbf{B}}{\dot{\gamma}} \right) u_r, \quad \tau_{zz} = 2 \left(\dot{\gamma}^{n-1} + \frac{\mathbf{B}}{\dot{\gamma}} \right) w_z, \quad (\text{A9a, b})$$

$$\tau_{\theta\theta} = 2 \left(\dot{\gamma}^{n-1} + \frac{\mathbf{B}}{\dot{\gamma}} \right) \frac{u}{r}, \quad \tau_{rz} = \tau_{zr} = \left(\dot{\gamma}^{n-1} + \frac{\mathbf{B}}{\dot{\gamma}} \right) (u_z + \varepsilon^2 w_r), \quad (\text{A9c, d})$$

where $\dot{\gamma} = \sqrt{(u_z + \varepsilon^2 w_r)^2 + 2\varepsilon^2 \left(u_r^2 + \frac{u^2}{r^2} + w_z^2 \right)}$ is scaled by W/a . On using (A9),

conditions (A2b) and (A2c) become

$$-\varepsilon^2 h' (\tau_{rr} - \tau_{zz}) + (1 - \varepsilon^2 h'^2) \tau_{rz} = 0, \quad (\text{A10a})$$

$$-\frac{\operatorname{Re}}{\operatorname{Fr}^2} (1 + \varepsilon^2 h'^2) p + \varepsilon^3 h'^2 \tau_{rr} - 2\varepsilon h' \tau_{rz} + \varepsilon \tau_{zz} = \frac{\varepsilon^2}{\operatorname{Ca}r} (1 + \varepsilon^2 h'^2) \left(\frac{rh'}{\sqrt{1 + \varepsilon^2 h'^2}} \right)'. \quad (\text{A10b})$$

Various levels of approximation can be envisaged, depending on the local values of Re , Fr and Ca . If inertia and gravity are of equal strengths, then for impinging jet flow in the supercritical region, we generally have $\operatorname{Re} = O(\varepsilon^{-1})$ or larger and $\operatorname{Fr} = O(1)$ or smaller.

On the other hand, in the subcritical region, Re is typically of $O(1)$, and $\operatorname{Fr} = O(\sqrt{\varepsilon})$, then inertia effects can be neglected.

Clearly, (A10a) indicates that $\tau_{rz}(r, z = h) = O(\varepsilon^2)$. In this case, (A10b) indicates that

unless the Bond number $\operatorname{Bo} \equiv \frac{\operatorname{Ca} \operatorname{Re}}{\operatorname{Fr}^2} = O(\varepsilon^2)$ or smaller, surface tension effects are

negligible. Consequently, (A10b) reduces to $p(r, z = h) = \varepsilon \frac{\operatorname{Fr}^2}{\operatorname{Re}} \tau_{zz}(r, z = h) = O(\varepsilon^2)$ in

the supercritical and subcritical regions, and we recover the hydrostatic pressure equation: $p_z = -1$, leading to $p(r, z) = h - z$. When substituted into (A8a), we see that the equation reduced to

$$\varepsilon \operatorname{Re}(uu_r + wu_z) = -\varepsilon \frac{\operatorname{Re}}{\operatorname{Fr}^2} h' + \tau_{rz,z}, \quad (\text{A11})$$

after neglecting terms of $O(\varepsilon^2)$. We therefore conclude that equations (5.2.2) are recovered when terms of $O(\varepsilon^2)$ and smaller are neglected, with negligible surface tension effects, as well as the vanishing of the shear stress at the film surface or (5.2.5b).

Curriculum Vitae

Name: Wenxi Wang

Post-secondary Education and Degrees: Northwestern Polytechnical University
Xi'an, China
2006-2010 B.Eng.

Huazhong University of Science and Technology
Wuhan, China
2010-2013 M.E.Sc.

The University of Western Ontario
London, Ontario, Canada
2021-2023 Ph.D.

Honours and Awards: Merit Student and Second-Class Scholarship
2007, 2008, 2009

First Class Scholarship
2010-2013

National Scholarship
2013

Related Work Experience Senior Mechanical Engineer
POWERCHINA Central China Electric Power Engineering Corp. Ltd.
2013-2020

Teaching Assistant
The University of Western Ontario
2021-2023

Publications:

Wang, W., Baayoun, A. & Khayat, R.E.* 2023 A coherent composite approach for the continuous circular hydraulic jump and the vortex structure. *Journal of Fluid Mechanics*. 966, A15.

Wang, W., Khayat, R.E.* & de Bruyn J.R. 2023 The viscoplastic circular hydraulic jump. *Physics of Fluids*. 35, 063115.

Floryan, J.M.*, Wang, W. & Bassom, A.P. 2023 The reduction of pressure losses in thermally modulated vertical channels. *Journal of Fluid Mechanics*. 954, A38.

Wang, W. & Khayat, R.E.* 2022 The influence of azimuthally varying edge conditions on the hydraulic jump. *Acta Mechanica*. 233, 3679-3698.

Floryan, J.M.*, Wang, W., Panday, S. & Bassom, A.P. 2022 Natural convection and pattern interaction in a two-dimensional vertical slot. *Journal of Fluid Mechanics*. 946, A20.

Xie, M., He, Q., Wang, W.* & Wang, L.-P. 2013 An exact solution of interception efficiency over a circular-arc fiber collector. *Computers & Fluids*. 88, 354-362.

Xie, M., He, Q., Wang, W.* 2013 Interception efficiency of particle laden flow over a finite flat plate in potential flow regimes. *Thermal Science*. 17, 1343-1348.

Wang, W., Xie, M.* & Wang, L.-P. 2012 An exact solution of interception efficiency over an elliptical fiber collector. *Aerosol Science and Technology*. 46, 843-851.

Wang, W., He, Q., Chen, N., Zhou, Y. & Xie, M.* 2012 A solution for potential flow over an arc fiber. *Thermal Science*. 16, 1564-1568.

Wang, W., He, Q., Chen, N. & Xie, M.* 2012 A simple moment model to simulate the effect of diffusion on the coagulation of nano-particle due to Brownian motion in the free molecule regime. *Thermal Science*. 16, 1331-1338.

Zhou, Y. Zheng, Y.*, Wang, W. & Zheng, C. 2012 An experimental investigation on hydrogasification of coal chars in a fixed bed reactor under high pressure. *Advanced Materials Research*. 524-527, 863-870.

Conference Articles and Abstracts:

(Abstract, Presented) Wang, W. & Floryan, J.M.* Natural Convection in Vertical Slots. 2022 Canadian Society of Mechanical Engineering International Congress.

(Abstract, Presented) Wang, W. & Khayat, R.E.* Non-circular hydraulic jump for impinging jet flow for high-viscosity liquids. 2021 Canadian Society of Mechanical Engineering International Congress.

* Corresponding author